MOLECULAR SIMULATIONS OF ASSEMBLY OF FUNCTIONALIZED SPHERICAL NANOPARTICLES

by

AREZOU SEIFPOUR

B.S., University of Colorado, 2004

A thesis submitted to the

Faculty of the Graduate School of the

University of Colorado in partial fulfillment

of the requirement for the degree of

Doctor of Philosophy

Department of Chemical and Biological Engineering

2013

This thesis entitled:

Molecular simulations of assembly of functionalized spherical nanoparticles

written by Arezou Seifpour

has been approved for the Department of Chemical and Biological Engineering

_____

Arthi Jayaraman, Ph.D.

_____

Wounjhang Park, Ph.D.

Date_____

The final copy of this thesis has been examined by the signatories, and we find that both the content and the form meet acceptable presentation standards of scholarly work in the above mentioned discipline.

Abstract

Seifpour, Arezou (Ph.D., Chemical and Biological Engineering)

Molecular simulations of assembly of functionalized spherical nanoparticles

Thesis directed by Professor Arthi Jayaraman

Precise assembly of nanoparticles is crucial for creating spatially engineered materials that can be used for photonics, photovoltaic, and metamaterials applications. One way to control nanoparticle assembly is by functionalizing the nanoparticle with ligands, such as polymers, DNA, and proteins, that can manipulate the interactions between the nanoparticles in the medium the particles are placed in. This thesis research aims to design ligands to provide a new route to the programmable assembly of nanoparticles.

We first investigate using Monte Carlo simulation the effect of copolymer ligands on nanoparticle assembly. We first study a single nanoparticle grafted with many copolymer chains to understand how monomer sequence (e.g. alternating ABAB, or diblock A_xB_x) and chemistry of the copolymers affect the grafted chain conformation at various particle diameters, grafting densities, copolymer chain lengths, and monomer-monomer interactions in an implicit small molecule solvent. We find that the size of the grafted chain varies non-monotonically with increasing blockiness of the monomer sequence for a small particle diameter. From this first study, we selected the two sequences with the most different chain conformations—alternating

and diblock—and studied the effect of the sequence and a range of monomer chemistries of the copolymer on the characteristics of assembly of multiple copolymer-functionalized nanoparticles. We find that the alternating sequence produces nanoclusters that are relatively isotropic, whereas diblock sequence tends to form anisotropic structures that are smaller and more compact when the block closer to the surface is attractive and larger loosely held together clusters when the outer block is attractive.

Next, we conduct molecular dynamics simulations to study the effect of DNA ligands on nanoparticle assembly. Specifically we investigate the effect of grafted DNA strand composition (e.g. G/C content, placement and sequence) and bidispersity in DNA strand lengths on the thermodynamics and structure of assembly of functionalized nanoparticles. We find that higher G/C content increases cluster dissociation temperature for smaller particles. Placement of G/C block inward along the strand decreases number of neighbors within the assembled cluster. Finally, increased bidispersity in DNA strand lengths leads a distribution of inter-particle distances in the assembled cluster.

For my mother and sister.

Acknowledgements

Many people have contributed significantly to the completion of this thesis. First and foremost, I would like to thank my research advisor, Dr. Arthi Jayaraman. I am indebted to her for her patience, advice, and support for me. I appreciate her being my mentor and taking the time to offer guidance both on research matters as well as personal. Additionally, I would like to thank my thesis committee, Drs. Christine Hrenya, Wounjhang Park, Ivan Smalyukh, and Mark Stoykovich for their insightful feedback over the years.

I would like to thank the National Science Foundation (CBET 0930940) for the financial support of this thesis research.

I am grateful to the Jayaraman group members, who have all helped me throughout my research (and who have each forced me to try new software or programming languages along the way): postdoctoral fellows Drs. Nitish Nair, Steven Dahl and Eric Jankowski; graduate students Robert Elder, Tyler Martin, Charles Starbird, and Hilary Marsh; and undergraduate students Phil Spicer, Chris McKinney and Paul Dodd.

As he would expect, I thank Robert Elder a separate time for becoming one of my best friends and making graduate school a very enjoyable time for me. Someday, we will turn the Robertisms into a lucrative business venture. I thank all of the friends I have made in the department for the many good memories here in Boulder, in particular, the times spent in the North.

I would especially like to thank my sister for her unyeilding love and support.

Finally, I would like to thank my mother, who had the foresight to bring her two young daughters to this country where they would have an opportunity to excel. She sacrificed everything for us and meanwhile had the energy to offer love, friendship and support. I am immensely grateful for all that she has done for me.

TABLE OF CONTENTS

List of Tables

List of Figures

Chapter 1

Introduction

1.1 Overview

Encoding particles with information on how to arrange themselves into complex architectures is the central theme underlying materials assembly. To assemble the particles, their surfaces are chemically modified with ligands, e.g. polymers, DNA and proteins, to change the effective inter-particle interactions. The quest for the optimal ligand needed for a given particle arrangement is not simply to determine which ligands induce the functionalized nanoparticles to attract or repel one another, rather in engineering 'smart' ligands which have additional assembly instructions such as dimensionality of the assembled nanoparticle structure (e.g. 1D nanowires to 2D sheets to 3D gels or crystals) or the inter-particle distances within the assembled cluster (e.g. compact clusters versus large loosely held-together clusters) etc., to achieve tighter control over the final structure (e.g. coordination number). The catalogue of possible ligands is endless. For example, within the family of polymers one could choose homopolymers or copolymers composed of combinations of different monomers of varying molecular weight in a host of solvents. In the case of DNA, strands of a given length can have many sequences of A, T, G and C bases. Predicting *a priori* the assembly that results from a specific ligand can be challenging since how the particles arrange themselves depends on a complex balance of entropic and enthalpic driving forces. In addition, synthesizing each system in the laboratory to investigate what particle arrangement results from functionalizing the particles with a given ligand and placing them in a certain medium can be a time-consuming and costly process. Computational

tools can aid in scanning the parameter space of available ligands both rapidly and at lower cost. This thesis research aims to investigate two of such ligands, namely copolymers and single stranded DNA, using molecular simulation to determine the effect the ligands have on the assembly of the spherical nanoparticles at various conditions such as grafting density, sequence and chemistry of ligand, particle size, length of the ligand, and concentration of particles.

In Chapter 2, we describe our Monte Carlo simulation study of copolymer chains grafted onto a single nanoparticle to determine how the conformation of the grafted copolymer changes due to the sequence and chemistry (or monomer-monomer interactions) of the copolymer at varying particle diameters, grafting densities, and chain lengths (molecular weight) of the grafted copolymer in an implicit small molecule solvent. The conformations of the grafted copolymers lead the nanoparticle surface to be either covered with grafted monomers or exposed. The extent to which a particle surface is covered (exposed) determines how repulsive (attractive) the nanoparticles are to one another, dictating the inter-particle interactions. Understanding the effect of chemistry and sequence on the conformation of grafted copolymers is a first step towards designing copolymer-grafted nanoparticles with tailored effective inter-particle interactions that will then allow for better control of assembly of nanoparticles. Copolymer functionalization is an attractive route for directing nanoparticle assembly because unlike homopolymer grafts where the effect of the medium is homogenous throughout the homopolymer grafted chain, in a copolymer the presence of two different monomer chemistries could allow us to control the solvent effects non-homogeneously along the chain and thus the variation in the monomer aggregation on the particle surface, changing the effective inter-particle interactions. We used lattice Monte Carlo simulation to study AB copolymers with alternating, multiblock, or diblock sequences, where either A monomers or B monomers have monomer-monomer attractive

interactions. Our focus was to show the nontrivial effect of monomer sequence on the conformations of the grafted copolymers at various particle diameters, grafting densities, copolymer chain lengths, and monomer-monomer interactions. When copolymers are grafted on a spherical particle and one set of like monomers has an attractive interaction, either (i) all the grafted chains aggregate to bring attractive monomers from all grafted chains together (intrachain and interchain monomer aggregation) if the favorable enthalpy gained by doing so can offset the conformational entropic loss, or (ii) each grafted chain folds onto itself to bring attractive monomers along each chain together (pure intrachain monomer aggregation) if the entropic loss from stretching of chains for interchain aggregation cannot be overcome by the enthalpic gain. The implication of this on a system of multiple grafted particles is that the conformations and spatial organization of monomers in the two scenarios (both intra- and interchain versus purely intrachain monomer aggregation) will affect the effective interactions between two copolymer grafted particles. We found on the smallest spherical particle we studied that the radius of gyration varies non-monotonically with increasing blockiness of the monomer sequence, and the copolymers have both intrachain and interchain monomer aggregation. At larger particle diameters, however, the grafted chains transition to being mostly intrachain monomer aggregation and the radius of gyration varies monotonically with monomer sequence.

For our next study described in Chapter 3, we select from the first study two of the sequences with disparate chain conformations—alternating and diblock—and investigate the role of sequence and chemistry of the copolymer graft on the assembly of multiple copolymer-functionalized nanoparticles. We use lattice Monte Carlo simulations to study diblock or alternating AB copolymer-grafted spherical nanoparticles placed in an implicit solvent to establish how nanoparticles functionalized symmetrically with diblock and alternating

copolymers at low to medium grafting density assemble into nanoclusters of different sizes, shapes and structures at varying chemistries, particle sizes, concentration of grafted particles and grafted copolymer chain length. We have studied a range of monomer chemistries by varying strengths of like-monomer (A-A and/or B-B) attractive interactions in the presence of relatively strong or negligible unlike-monomer (A-B) repulsive interaction. We observe that while the alternating sequence produces clusters that are relatively isotropic regardless of whether A-A or B-B monomers are attractive in the presence of negligible unlike-monomer repulsions, the diblock sequence produces clusters that are smaller and more compact when inner block monomers (A-A) are attractive and larger loosely held together clusters when outer block monomers (B-B) are attractive. In the presence of strong A-B repulsions the alternating sequence leads to either particle dispersion or smaller clusters than those at negligible A-B repulsions while the diblock sequence exhibit similar cluster characteristics in the presence and absence of A-B repulsions. Additionally, diblock copolymer grafted particles tend to assemble into anisotropic shapes despite the isotropic grafting of the copolymer chains on the particle surface. We find that increasing particle size makes it more entropically unfavorable for grafted chains to interact with adjacent grafted chains on the same particle leading to cluster formation only in cases when the like-monomer attraction strength was strong enough to overcome the entropic loss from stretching grafts during inter-particle contacts. In the dilute concentration regime a small increase in the particle concentration does not change the cluster characteristics confirming that the structure within a cluster is primarily governed by the copolymer functionalization imparting a "valency" to the nanoparticle "atom." This work illustrated how copolymer functionalization and tuning the grafted copolymer sequence is an exciting route experimentalists can take to tailor self-assembly of nanoparticles into target nanostructures.

In Chapter 4, we shift our focus to DNA ligands, where we exploit the specificity of DNA hybridization through Watson-Crick base pairing to give the additional measure of control of directionality over the nanoparticle assembly. In this study, we use molecular dynamics simulations to study a system of a single population of DNA-functionalized nanoparticles that assemble (without linkers) in an implicit solvent through hybridization of grafted strands which are of a self-complementary sequence. In other words, when all particles in a system are grafted with the same sequence, for the particles to assemble, the DNA strands should bind in a head to tail manner. Thus, the sequence must be such that when placed in reverse, it is complementary to itself (e.g. since G bases hybridize with C bases, *particle*-G-G-C-C can bind in a head to tail manner with C-C-G-G-*particle*). Our goal is to understand the effect of chemical heterogeneity in the DNA strands on the assembly of multiple DNA-functionalized nanoparticles. Specifically, we determine the effect of the composition (G/C content) and placement of the G/C block within the grafted strands on the structure and thermodynamics of the assembly at varying grafting density and particle sizes. We tune the strength of the binding between two DNA strands by varying the G/C content or by incorporating "non-hybridizing" spacer bases in the strand between the G/C bases. It is important to find the optimal G/C content which is sufficient to drive nanoparticles to assemble, yet not too high causing "stuck" or metastable assembled structures. The optimal G/C content is not easy to predict *a priori* as it is depends in a complex manner on nanoparticle shape and size, grafting density, nanoparticle concentration, etc. One cannot easily predict how the enthalpic drive (G/C content) for nanoparticle assembly is balanced by the entropic loss (particle translation, strand conformation) of a given system simply from analysis of the building block itself. In addition to the G/C content, the placement of G/C in the strand, i.e. the length of contiguous G/C or sequence of G/C with respect other bases in the

strand also affects the structure of the nanoparticle assembly and the cluster dissociation temperature, primarily by affecting the entropy losses term in the free energy of cluster formation. We find that at constant grafting density and G/C content, nanoparticles assemble more readily when the G/C blocks are placed on the outer (far from the particle surface) or middle portions of the strands than in the inner portion (closest to the particle surface) because of entropic frustration in the latter case. Also, at constant G/C content, as the G/C placement along the strand shifts closer to the particle surface the "valency" of the particle decreases. As particle size decreases at constant grafting density and G/C placement the minimum G/C content needed for assembly increases.

In Chapter 5, we continue using molecular dynamics simulations to study the assembly of DNA-functionalized nanoparticles with equal number of short and long DNA strands on each nanoparticle to understand the effect of increasing bidispersity in strand lengths on the structure and thermodynamics of the assembled clusters. We vary short to long or bidisperse strand length ratios along with the grafting density and the length of the G/C segment per strand in each system. At constant number of grafts and number of G/C beads, as bidispersity in strand lengths increases the average number of nanoparticles that assemble into a cluster as well as the radius of gyration of the cluster increases and the average number of neighbors a nanoparticle has in a cluster also increases. When number of G/C beads is constant and thus the enthalpic drive for assembly is constant, the presence of long strands in the bidisperse systems helps alleviate the entropic losses seen in tightly packed particles by hybridizing with the longer strands on neighboring particles and increasing the inter-particle spacing. Inter-particle spacing in the clusters assembled from particles with bidisperse strand lengths depends on the relative frequency of the three possible ssDNA:ssDNA hybridization between particles, e.g. short strand

hybridizing to another short strand (short-short), short strand hybridizing to a long strand partially (short-long), or long strand hybridizing to another long strand (long-long). In the case of small number of grafts there are fewer short-short hybridization and mostly short-long and long-long hybridization. In the case of larger number of grafts there are negligible short-short hybridization and higher frequency of long-long hybridization versus short-long. As the number of grafts increase, long strands hybridize to other long strands in preference to short-long hybridization so that particle surface separation is increased to minimize entropic loss. While higher number of grafts systems have negligible short to short strand connections, particles are able to have short inter-particle distance via partial hybridization of strands. At high number of G/C beads, an increase in number of grafts causes a sharp increase in the number of nanoparticles that cluster.

In Chapter 6, we conclude by summarizing this thesis, noting limitations and challenges of this work, and providing directions for future work in this project. In the study on copolymer functionalization, we maintained particle-particle interactions and particle-monomer interactions as athermal to isolate the effect of grafted monomer chemistry on the nanoparticle assembly. Evaluating the role of particle-monomer interactions is important and has been the focus of a recent study by Martin, McKinney and Jayaraman. Analogous to the limitation of our copolymer work, in the study on DNA functionalization, we have not modeled non-specific interactions between the bases and the surface, which could have an effect on the structure and thermodynamics of the assembled clusters. Additionally we have not included electrostatic interactions to mimic purely a high salt concentration condition where electrostatic interactions are screened. Changing salt concentration will need explicit electrostatic interactions, and tuning the strand flexibility. Some of the future directions could involve tackling these limitations.

Lastly, this thesis has focused only on spherical particles; therefore, a natural next step would be to study mixtures of DNA-functionalized particles of various shapes (e.g. prisms, octahedral, and rhombic dodecahedra) to produce assemblies with unique 3D shapes.

Chapter 2

Effect of monomer sequences on conformations of copolymers grafted on spherical nanoparticles: A Monte Carlo simulation study

Adapted from: *J. Chem. Phys.* **132** 164901 (2010)

2.1 Introduction

Precise assembly and ordering of nanoparticles mediated by a solvent or a polymer matrix is extremely important for creating spatially engineered materials that can be used for photonics, metamaterials, photovoltaic, and electronics applications. One way to produce highly ordered nanoparticles assembly is by functionalizing the nanoparticle surface with ligands, such as polymers,[1-19] DNA,[20-28] and proteins,[29-32] that can then manipulate the interfacial interactions between the nanoparticles and the medium the particles are placed in, and thus control their assembly. Past theoretical and experimental work on *homopolymer* functionalized nanoparticles[1-11, 13-18] has established that the chemistry of the grafted polymers, nanoparticles and the medium (solvent or polymer matrix) play a critical role in dictating the spatial organization of the nanoparticles. For example, experimental studies[16-18] have achieved migration of the polymer grafted nanoparticles from one domain in the matrix to another domain simply by thermally changing the composition of grafted homopolymers on the nanoparticle, and thus the compatibility of the grafted polymer and matrix. Another important parameter that dictates the effective inter-particle interactions and therefore the particle assembly is the polymer grafting density, defined as the number of grafted polymers per unit surface area. The grafting density

and molecular weight dictate the conformations of the grafted copolymers. At high grafting density,[33-37] the grafted polymers extend due to crowding, and form a brush like conformation on the particle surface. A particle carrying a polymer brush on its surface can disperse (assemble) in medium that acts as a good (bad) solvent for the polymer brush; for example homopolymer grafted particles placed in a homopolymer matrix, where matrix chemistry is identical to the grafted polymer, disperse (aggregate) if the molecular weight of matrix homopolymer is lower (higher) than that of grafted homopolymer.[38, 39] At low grafting density[7, 12-15, 40-46] the grafted polymers do not face any crowding from monomers of adjacent chains and as a result do not stretch into brush like conformations. The surface of the nanoparticle that is exposed versus the surface of nanoparticle covered by the grafted monomers dictates interparticle interactions. Such homopolymer-grafted nanoparticles at low grafting densities have been shown to assemble into a variety of nanostructures. Glotzer and coworkers have conducted detailed studies of polymer-tethered nanoparticles of various shapes[13-15, 42, 46-48] and demonstrated the presence of gyroid-phase in mono-tethered spherical particles. Jayaraman and Schweizer[40, 41] used Polymer Reference Interaction Site Model (PRISM) theory with spherical nanoparticles with one-four homopolymer grafted chains to obtain order-disorder transition curves. Szleifer and coworkers[49] have used single-chain mean field theory to show the effect of surface curvature and surface geometries on homopolymers grafted on spherical and cylindrical particles, at athermal conditions. While most of the above studies establish the effect of various molecular parameters on behavior of *homopolymer* grafted nanoparticles either in solvent or in a polymer matrix, the behavior of *copolymer* grafted nanoparticles in a solvent or polymer matrix remains largely unexplored.

This paper focuses on AB copolymer chains grafted on spherical nanoparticles placed in an implicit small molecule solvent, and establishes the effect of *monomer sequence* on the conformations of the grafted copolymers at various particle diameters, copolymer chain length, at low grafting densities. A and B monomers in an AB copolymer can be distributed in regular (non-random) sequences, such as that found in diblock copolymers, multi-block copolymers and alternating copolymers, or in random, yet correlated, sequences, such as that found in blocky random copolymers and purely random copolymers. This study is restricted to non-random monomer sequences, e.g. alternating, multiblock and diblock. The motivation for this study stems from the behavior of proteins consisting of hydrophobic (say A) and polar (say B) residues placed in water, where the composition and sequence of the residues dictates the secondary structure of the proteins.[50] Just like proteins, conformations of *free* (ungrafted) copolymers in a solvent depend on the chemical composition and monomer sequence[51-54] and the solvent quality.[55, 56] Molecular simulations[56] have shown that the monomer sequence of a copolymer containing "sticky" monomers dictates the pathway to copolymer collapse. Copolymers with uniform monomer distribution abruptly formed a compact, nearly collapsed ordered intermediate core-shell state, while copolymers with random distribution formed intermediates with "fluffy" monomer shells over a wider temperature range. Monte Carlo simulations[57] of copolymers with varying sequences—alternating and diblock—grafted on *flat* surfaces at moderate to high surface grafting density show that if all parameters (temperature, grafting density, and interaction energies) are kept constant, the monomer sequence affects the coil-to-globule transition temperature, with the alternating copolymer having the sharpest coil-to-globule transition. In contrast to copolymers grafted on flat surfaces (zero curvature) heteroarm star polymers[58-62] have copolymer chains grafted to a small core (infinite curvature). Most of the past work on heteroarm

star polymers has focused only on arms with diblock copolymer sequence, and provide great insight into the conformations of the block copolymer arms tethered to the star core. Atomic force microscopy studies on polystyrene-poly(vinyl pyridine) star block copolymers[63] show that the solvent-block interactions dictate the overall conformation of the star polymer. If the solvent-inner block interactions and solvent-outer block interactions are comparable, then the star polymer takes on a uniform spherical shape, while increasing difference in solvent-inner block and solvent-outer block interactions leads to a "Janus-like" conformation. Molecular simulations on heteroarm star polymers[58, 59, 61] also confirm this behavior that the insoluble blocks collapse in strongly selective solvents, and the soluble and insoluble blocks separate to form an overall Janus-like structure. Since the core of the star polymer is negligible, it allows for the polymer arms grafted to the small core to more freely adopt energetically favorable conformations than polymers grafted to a solid spherical particle of non-negligible diameter where the excluded volume of the spherical particle inhibits certain conformations. This motivates us to study the conformations of copolymers with various sequences grafted onto solid spherical nanoparticle with a non-negligible curvature (or diameter), and contrast that to the past work on heteroarm star polymers (negligible diameter or infinitely high curvature) and copolymer chains grafted on flat surfaces (zero curvature).

In this paper we use lattice Monte Carlo simulations to study copolymers grafted on a spherical nanoparticle surface, and understand the effect of various molecular parameters, such as monomer sequence and molecular weight (or chain length) of the grafted copolymer, particle size (or curvature), and chemistry (or monomer-monomer interactions) on the conformations of the grafted copolymers. We observe that the monomer sequence, particle diameter and grafting density dictate whether (a) the grafted chains aggregate to bring attractive monomers from

multiple grafted chains together (inter-chain and intra-chain monomer aggregation) if the enthalpy gained by doing so offsets the entropic loss caused by stretching of chains, or (b) each grafted chain folds onto itself to bring its attractive monomers together (purely intra-chain monomer aggregation) if the entropic loss from inter-chain aggregation cannot be overcome by the enthalpic gain. For six copolymers of chain length N=24 grafted on a spherical particle of diameter D=4, inter-chain and intra-chain monomer aggregation occurs where the radius of gyration varies non-monotonically with increasing blockiness of the monomer sequence. At larger particle diameters the grafted chains transition to purely intra-chain monomer aggregation. The radius of gyration varies monotonically with monomer sequence for intra-chain monomer aggregation because as the sequence becomes blockier (like-monomers are grouped together), the copolymer chain has to fold less compactly to maximize the enthalpically favorable contacts while maintaining high conformation entropy. The radius of gyration of alternating and diblock copolymers scale with chain length, N, through a power law, $<R_g^2>^{1/2}=\alpha N^{\nu}$, with the prefactor, α, and scaling exponent, ν, varying with monomer sequence and monomer-monomer attraction strength. Understanding how these molecular parameters affect conformations of grafted copolymers is simply the first step towards designing copolymer- or protein-grafted nanoparticles with tailored effective interparticle interactions that will then allow for better control of assembly of nanoparticles in a solvent or a polymer matrix.

The paper is organized as follows. In section 2.2 we describe our model, simulation method and parameters used to quantify conformations of the copolymer grafted nanoparticle. In section 2.3 we present conformations of the grafted copolymers as a function of monomer sequence, grafted chain length, particle size, and grafting density, and contrast the copolymer

grafted nanoparticles to star copolymers and copolymers grafted on flat surfaces. We conclude with a discussion about the observed results and the future directions.

2.2 Method

2.2.1 Model

We model an AB copolymer grafted nanoparticle (Figure 2.1) as a hard sphere particle of diameter D with a finite number of grafted symmetric AB copolymers with a chosen monomer sequence.

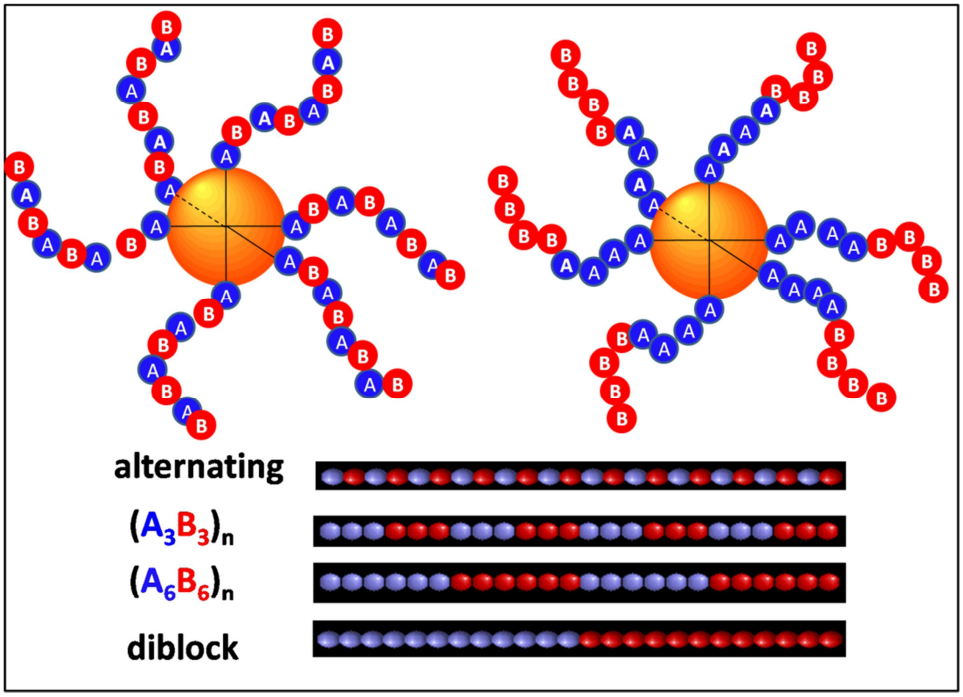

Figure 2.1 A schematic of model of AB copolymer grafted particles with alternating and diblock sequence for grafted chain length N=8. Also shown are the various monomer sequences—alternating or -(A_1B_1)n, multiblocks: -$(A_3B_3)_n$, -$(A_6B_6)_n$, and diblock or -$(A_{n/2}B_{n/2})$—for the grafted chain length N=24.

Figure 2.1 shows a schematic of two such copolymer grafted nanoparticles, one with alternating monomer sequence and another with a diblock monomer sequence for chain length equal to 8

monomers. The symmetric AB copolymers used in this paper have chain length, N =24 to 96, and one of four sequences (bottom panel of Figure 2.1)—alternating or $(A_1B_1)_{N/2}$, multiblock $(A_3B_3)_{N/6}$ and $(A_6B_6)_{N/12}$, and diblock or $(A_{N/2}B_{N/2})$ sequence. Each grafted copolymer chain is modeled as a freely jointed chain on a cubic lattice with each monomer bead of size d of the order 1 nanometer. Since we work with a cubic lattice, in case of six grafted copolymer chains the first monomer is placed symmetrically 1d away from the six poles of the spherical nanoparticle; in case of fourteen grafted chains, the chains are grafted *symmetrically* 1d away from six poles and 1.4d away from the centers of the surfaces representing the octants of the sphere. In all systems the AB copolymer chains are grafted such that the first monomer grafted to the particle surface is an A monomer. The identities of the second, third and higher monomers in each grafted chain depend on the chosen sequence. We also note that since we work with a cubic lattice the nanoparticle sphere is modeled as a collection of beads that are placed less than or equal to D/2 distance from the location of the central bead of the nanoparticle.

The interaction potentials, $U_{ij}(r)$ between one set of like-monomers is chosen to be attractive, while all other interactions are maintained as athermal. A real system that our model polymer and interactions mimic is a polymer made of hydrophobic (A) and hydrophilic (B) residues placed in water/organic solvent. When such a polymer is placed in water, corresponding to our system when U_{AA} is attractive, the A-A attractions (hydrophobic interactions) will dominate the physics of the system. The attractive interactions are modeled as square well potentials, characterized by a well depth ε_{ij}, between an i^{th} bead and its j^{th} nearest non-bonded neighbor (where j=1, 2, … 18) on the cubic lattice. AB copolymers are characterized by Flory Huggins interaction parameter $\chi_{AB} \sim z[\varepsilon_{AB}\text{-}1/2(\varepsilon_{AA} + \varepsilon_{BB})]/kT$, where ε_{ij} is the *attractive* well depth between i and j beads and z is the coordination number. The higher the value of χ_{AB}, larger

is the effective repulsion between the A and B monomers. . We consider the following cases for this study: 1) ε_{ij}=0 kT for all i and j (purely athermal), 2) ε_{AA}=-0.2 kT and ε_{ij}=0 kT for all other i and j, 3) ε_{BB}=-0.2 kT and ε_{ij}=0 kT for all other i and j, 4) ε_{AA}=-0.5 kT and ε_{ij}=0 kT for all other i and j, 5) ε_{BB}=-0.5 kT and ε_{ij}=0 kT for all other i and j. 6) ε_{AA}=-1 kT and ε_{ij}=0 kT for all other i and j, and 7) ε_{BB}=-1 kT and ε_{ij}=0 kT for all other i and j. We note that in case of free (ungrafted) copolymers in a solvent we expect cases 2 and 3 to have identical χ_{AB} and cases 5 and 6 to have identical χ_{AB}; when copolymers are grafted to a surface the monomers near the surface could have a different environment compared to the monomers away from the surface, depending on the grafting density and chemistries involved, therefore the χ_{AB} may not be the same for cases 2 and 3, and cases 5 and 6.

2.2.2 Monte Carlo simulation

We use lattice Monte Carlo simulation for this study since it is extremely fast and provides a good mimic for large scale conformations of polymer chains. The first step of our simulation is to grow the initial configuration of the copolymer grafted nanoparticle. We fix the center of the nanoparticle of the desired size at the center of the simulation box. We then fix the first monomers of the grafted chains at the predetermined symmetric sites on the sphere (as described in the previous section). Next, the second monomer of each grafted chain is grown in one of the five lattice sites adjacent to the first monomer of that grafted chain. During this growth process if an i^{th} monomer cannot be grown because all neighboring sites of $(i-1)^{th}$ monomer are occupied by other monomers, then all the monomers are subjected to local moves till a vacancy is created. This is repeated until all the grafted chains are grown to the desired chain length, N.

After the initial configuration is ready the simulation proceeds in three stages: initialization, equilibration, and production. In the initialization stage the system runs through 100000 Monte Carlo (MC) steps; a MC time step is defined as N random monomer moves, where N is the grafted copolymer chain length. In one monomer move, we first randomly pick a monomer (with the exception of the first bead that is fixed) on a randomly picked grafted chain, and then move that monomer using a randomly chosen move- "crankshaft", "kink" and "end" (last bead only) [64]. The center of the particle is fixed at the center of the simulation box through the simulation. After attempting N such randomly picked moves, the moves are accepted or rejected based on the Metropolis algorithm[65]; since attractive interactions are not turned on until the equilibration stage, all the initialization-stage moves are made under athermal conditions and accepted if no overlaps occur during the move. This initialization stage helps us avoid any bias that might arise due to the nature of the initial configuration of the grafted chains. In the equilibration stage, attractive interactions are turned on (except for the purely athermal system where there are no attractive interactions), and the system goes through 40 million MC steps with N moves in each MC step, and the moves during each MC step is accepted or rejected according to Metropolis algorithm.[65] We collect data on the thermodynamic property of interest over 1000 MC steps and calculate the block averages for every 100 000 MC steps. After the 40 million MC steps we check if the system has equilibrated; equilibration is said to be achieved when 5 consecutive block averages of energy, U, are within 5% of each other. Once the system has reached equilibrium, in the production stage we collect the ensemble average of the block averages of the equilibrated system. For each system we repeat 10 trials of simulation where the 10 trials are marked with different random number seeds. We obtain error bars for every data

point presented in the results sections from the ensemble averages collected from 10 such simulations.

2.2.3 Analysis

To quantify the equilibrium conformations of the grafted chains we calculate average radii of gyration of the grafted copolymers. In each simulation we obtain the ensemble average for squared radius of gyration, $\langle Rg^2 \rangle$, where Rg^2 is calculated as follows.

$$R_g^2 = \frac{1}{N*M} \sum_{j=1}^{M} \sum_{i=1}^{N} (x_{i,j} - x_{cm,j})^2 + (y_{i,j} - y_{cm,j})^2 + (z_{i,j} - z_{cm,j})^2$$

where N is the length of the grafted copolymer chain, i the monomer number, M is the number of grafted chains, j is the chain number, and $x_{cm,j}$, $y_{cm,j}$ and $z_{cm,j}$ are the coordinates of the center of mass of the j^{th} grafted chain. For each chain we first calculate the center of mass coordinates ($x_{cm,j}$, $y_{cm,j}$ and $z_{cm,j}$), then calculate the square of the displacement of each monomer from the center of mass, and average that over the number of monomers in each chain. After this is repeated for all grafted chains, we obtain the average radius of gyration per chain. The radius of gyration values presented in the next section are the square root of this ensemble average, $\langle Rg^2 \rangle^{1/2}$.

To understand the spatial organization of the monomers on the particle surface we collect data on the average number of graft monomers (both A and B), N(r), present within the spherical region r-0.5 and r+0.5 with r being the radial distance from the nanoparticle surface. We also track the ensemble average number of favorable contacts, i.e. the number of monomer contacts that contribute to the energy of the systems. In addition, we also visualize the conformations of the grafted chains by collecting spatial coordinates of all components in these systems. These

simulation snapshots help in interpreting the trends seen in the radius of gyration and monomer profiles.

2.2.4 Parameters

In a copolymer grafted spherical nanoparticle there are a large number of molecular parameters that could affect the conformations of the grafted copolymers. The first and the main focus of this study is varying monomer sequence in the grafted copolymers, which we choose from alternating or $(A_1B_1)_{N/2}$, multiblocks: $(A_3B_3)_{N/6}$, $(A_6B_6)_{N/12}$, and diblock or $(A_{N/2}B_{N/2})$ copolymer sequences (Figure 2.1). The next parameter is the particle diameter, D=4, 8 and 12; since D is scaled in terms of monomer diameter and the monomer diameter is of the order of 1 nm, the particle diameters D=4, 8 and 12 correspond to 4 nm, 8 nm and 12 nm, respectively. The third parameter is the grafting density, defined as number of chains per unit particle surface area. For six grafted chains on the particle diameter D=4, 8 and 12 nm, the surface grafting density is 0.12, 0.03, and 0.01 chains/nm^2, respectively. Since varying particle diameter with six grafted chains leads to variation in curvature and grafting density, to study the sole effect of curvature on the conformations, we maintain a constant grafting density by grafting 2, 6 and 14 chains on particle size D=4, 8 and 12, respectively. We also consider varying lengths of the grafted copolymers N=24, 48, 72 and 96; the length is chosen to be an even multiple of the block length in order to maintain symmetric composition of the grafted copolymers (equal number of A and B beads in each copolymer chain). In the next section we present the results showing the effect of varying each of the above parameters on the conformations of the grafted copolymers.

2.3 Results

2.3.1 Effect of monomer sequence and monomer-monomer interactions

In Figure 2.2a we present the effect of various monomer sequences at purely athermal interactions and at monomer-monomer (A-A or B-B) attractive interaction strengths of 0.2 kT, 0.5 kT and 1 kT, on the radius of gyration of six copolymers of length N=24 grafted on a nanoparticle of diameter D=4 nm.

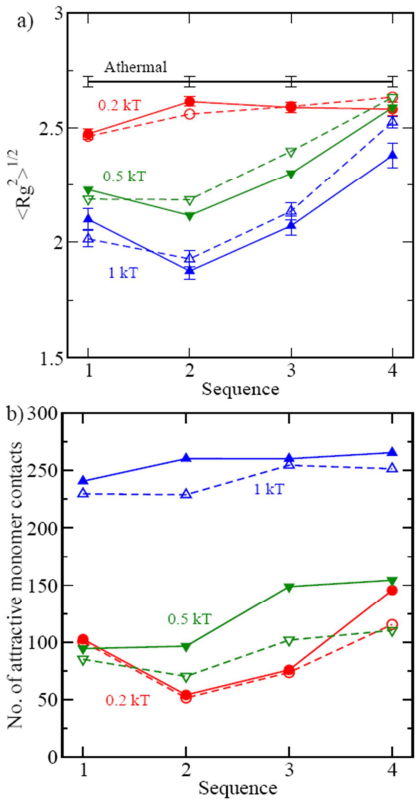

Figure 2.2 a) Radius of gyration and b) number of attractive monomer contacts as a function of monomer sequence for six AB copolymers of length N=24 grafted on a spherical nanoparticle of diameter D=4, at athermal interactions (no symbols solid line), and monomer-monomer attractive interaction strength=0.2 kT (circles), 0.5 kT (down triangle) and 1 kT (up triangle). Open symbols-dashed lines correspond to systems where A monomers are attractive and filled symbols-solid lines correspond to systems where B monomers are attractive. Monomer sequence 1 refers to alternating, 2 refers to $(A_3B_3)_4$, 3 refers to $(A_6B_6)_2$, and 4 refers to diblock copolymer.

The error bars are shown in all figures, and in most cases the size of the error bars is approximately the size of the symbols used. In case of purely athermal interactions, for all monomer sequences the ensemble average radius of gyration, $\langle Rg^2 \rangle^{1/2}$ is ~2.7 nm. This is because at purely athermal conditions the simulation cannot distinguish energetically between A

and B monomers, and treats all grafted copolymers as grafted *homopolymers*. When the monomers (A-A or B-B) have weak attractive interactions of strength 0.2 kT, the radius of gyration of all four sequences is less than the purely athermal case because the grafted copolymers change conformations to bring attractive monomers together to maximize favorable enthalpic contacts. As the like-monomer attractive interaction strength is increased to 0.5 kT and then 1 kT, the radius of gyration, R_g decreases further, because the copolymer chains collapse more to allow the attractive monomers to aggregate more strongly and maximize the favorable interactions. Furthermore, for attraction strength=0.5 kT or 1 kT, R_g of the grafted copolymers when A-A interactions are attractive (dashed lines), R_g (ε_{AA}), is different from the average R_g when B-B interactions are attractive (solid lines), R_g (ε_{BB}). The monomer sequence dictates whether R_g (ε_{AA}) is higher than R_g (ε_{BB}) or vice versa. For all cases the chains are grafted by the A monomer. For all monomer sequences the grafted copolymer chains maximize favorable attractive monomer contacts by either coiling up to bring attractive monomers within one grafted chain together (intra-chain monomer aggregation) or by stretching to bring attractive monomers on themselves and other grafted chains together (intra-chain and inter-chain monomer aggregation). The choice between purely intra-chain monomer contacts and combination of intra- and inter-chain monomer contacts is dictated by the placement and number of the grafts, and the sequence of attractive monomers along the copolymer chain which can either facilitate or deter the attractive monomers aggregation. We will start this discussion with the diblock copolymer sequence, followed by alternating and multiblock sequences.

At monomer attraction strength $\geq$ 0.2 kT the diblock copolymers have the highest radius of gyration as compared to other sequences (Figure 2.2a) because the sequence along the copolymer favorably places attractive like-monomers together, and facilitates aggregation of

attractive monomers without the grafted chains having to lose many conformations (entropy). This is confirmed by the highest value of average number of attractive monomer contacts for diblock copolymer at all monomer attraction strengths (Figure 2.2b). The number of attractive monomer contacts plotted in Figure 2.2b includes all attractive monomer contacts, intra-chain and inter-chain, that contribute to the energy of the system. The grafted diblock copolymers exhibit both intra- and inter-chain attractive monomer aggregation for attraction strength 1 kT because the enthalpic gain by doing so can easily overcome the conformational entropic loss (as seen in simulation snapshots). The entropic loss of conformations is also dictated by how far the *attractive* monomers are from the particle surface; therefore in case of diblock copolymers whether ε_{AA} is attractive i.e. block closer to the particle surface is attractive, or ε_{BB} is attractive i.e. block farther from the particle surface is attractive, plays a major role in deciding how easily the grafted chains can form inter-chain contacts. When the outer block is attractive ($\varepsilon_{BB}>0$), the six grafted chains are able to easily bring their B monomers together, as compared to when the inner block is attractive ($\varepsilon_{AA}>0$). This is confirmed in Figure 2.2b by the higher number of favorable contacts for $\varepsilon_{BB}>0$ versus that for $\varepsilon_{AA}>0$, for all attraction strengths. The copolymers need to stretch more to bring attractive A monomers on all chains together than to bring attractive B monomers together, leading to the radius of gyration being slightly higher for ε_{AA} attractive case as compared to ε_{BB} attractive case. These conformations agree with the past work on heteroarm star polymers containing AB diblock copolymers arms,[62] which show that if the A monomers that formed the block closer to the star core (inner block) were attractive they collapsed to form an A-core while the outer block formed by the B monomers dangled away in the corona of the star polymer, and if the B monomers forming the outer block were attractive they aggregated to form B domains on the outer rim of the star polymer. It was also seen that if

the arms were long enough all the aggregated B-domains collapsed together, analogous to our inter-chain aggregation.

In contrast to the diblock copolymer, the alternating copolymer has a frustrated symmetric sequence that inherently separates every like-monomer along the copolymer chain. Therefore the alternating copolymers have to aggregate more compactly to bring attractive monomers together. This is confirmed by the lower radius of gyration (more compact) in Figure 2.2a, and also a lower number of favorable intra- and inter-chain monomer contacts in Figure 2.2b for alternating sequence as compared to the diblock sequence. Also, unlike diblock copolymer, for the alternating copolymers simulation snapshots show that the chain conformations and spatial arrangement of monomers around the particle surface are similar at ε_{AA}=1 kT and ε_{BB}=1 kT. To quantify the spatial arrangement of monomers on particle surface for alternating and diblock copolymers in Figure 2.3 we present the average number of monomers N(r) at various radial distances *r* from the particle surface.

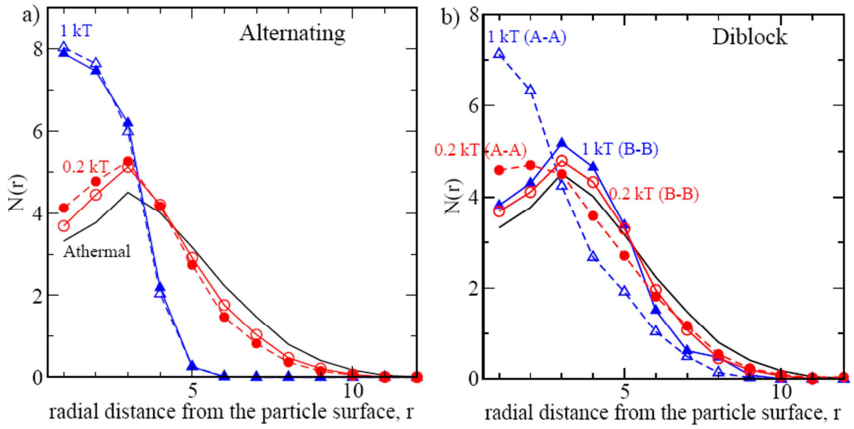

Figure 2.3 Average number of monomers N(r) at increasing radial distance from the surface of the particle, r, for particle diameter D=4 with six a) alternating copolymer and b) diblock copolymer grafted chains of length N=24 at athermal interactions(black solid line), and monomer-monomer attractive interaction strength = 0.2kT (circles) and 1kT (triangles). Open symbols- dashed lines correspond to systems where A monomers are attractive and filled symbols- solid lines correspond to systems where B monomers are attractive.

For alternating copolymers (Figure 2.3a) as the strength of attraction increases, the accumulation on the surface increases, with the accumulation on the surface being only slightly higher for ε_{AA}>0 kT versus ε_{BB}>0 kT. In contrast, in the case of diblock copolymer grafted nanoparticles (Figure 2.3b), when A monomers (the block closer to the surface) are attractive, the accumulation of monomers on the surface is significantly higher as compared to when B monomers (block away from the surface) are attractive. This difference is more prominent for attraction strength ~1 kT. This can have implications on the assembly of such grafted-nanoparticles. The attractive A monomers that crowd the nanoparticle surface shield the surface from direct nanoparticle-nanoparticle contacts. The attractive B monomers (Figure 2.3b solid lines), that accumulate away from the surface, leave the particle surface exposed for direct particle-particle contacts. This can control the structure and inter-particle spacing within the assembled nanoparticle clusters.

With regards to the multiblock cases, $(A_3B_3)_n$ and $(A_6B_6)_n$, despite the expectation that the multi-block copolymers would exhibit behavior that lies in between those of the alternating and diblock copolymers, we see an interesting non-monotonic trend in R_g (Figure 2.2a) for attraction strength greater than 0.2 kT. As stated earlier, the sequence on the grafted copolymers dictates a) how compactly the monomers can be brought together within the grafted copolymer (intra-chain) or between some or all grafted copolymers (intra- and inter-chain) and b) whether the system has purely intra chain attractive monomer aggregation or both intra- and inter-chain attractive monomer aggregation. For the -(A_3B_3)- sequence, at ε_{BB}=1 kT while the number of favorable contacts (Figure 2.2b) is comparable to corresponding diblock copolymer case, the R_g is much lower than diblock sequence. At ε_{AA}=1 kT both the number of favorable contacts and R_g are lower for the -(A_3B_3)- sequence than the diblock sequence. We conjecture that a subtle

balance of the entropy and enthalpy dictates the amount of inter-chain contacts and how much the chains have to stretch to achieve those contacts. At monomer attraction strength of 0.5 kT both the R_g (ε_{AA}=0.5 kT) and R_g (ε_{AA}=0.5 kT), and the corresponding number of attractive monomer contacts are lower than the values for diblock copolymers. The -(A_3B_3)- sequence shifts towards purely intra-chain contacts as the monomer attraction strength decreases, evident from a lower number of attractive contacts for 0.5 kT and 0.2 kT versus 1 kT. For the -(A_6B_6)- sequence, the trends are similar to -(A_3B_3)- with the absolute values of R_g and number of contacts always higher for the -(A_6B_6)- sequence. This is because the attractive monomers are favorable placed closer together in the -(A_6B_6)- sequence than the -(A_3B_3)- sequence, and the chains can stretch less to bring more attractive monomers together in the -(A_6B_6)- sequence than the -(A_3B_3)- sequence.

We expect that as particle size increases (next section) at constant graft length N=24 or as the grafted chain length decreases at constant particle diameter D=4, all four sequences will prefer purely intra-chain aggregation versus a combination of intra- and inter-chain aggregation because the grafted chains will not be long enough to wrap around the particle surface to allow inter-chain aggregation. With only intra-chain monomer aggregation, we expect the effect of monomer sequence on bringing together attractive monomers within a grafted chain or the "folding" of the grafted chains to exhibit a monotonic trend in R_g versus sequence. In the next section, we present the results for increasing particle size at constant graft length.

2.3.2 Effect of particle size (curvature) and grafting density

Figure 2.4 a and b present the average radius of gyration of the six copolymers of length N=24 grafted on particles of size D=8 and D=12, respectively, as a function of monomer sequence and increasing attractive interaction strength.

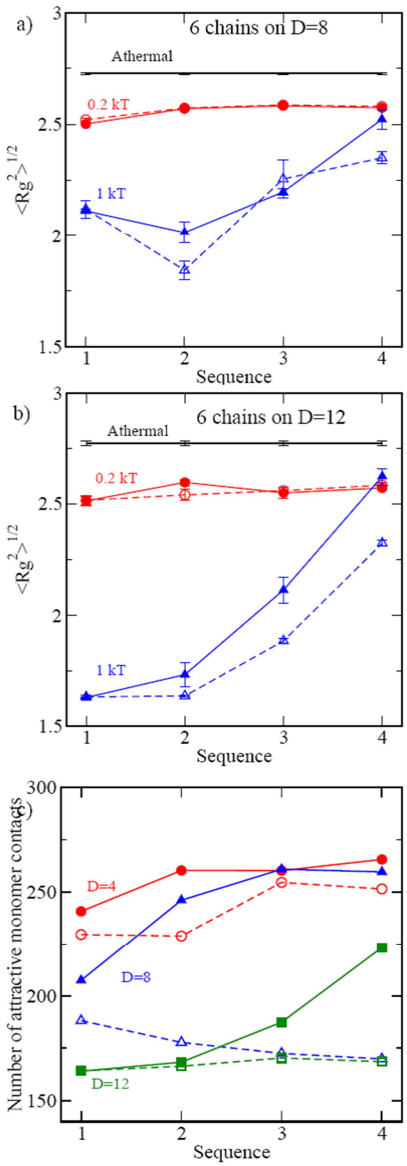

Figure 2.4 Radius of gyration, R_g, as a function of monomer sequence for AB copolymers of length N=24 grafted on a spherical nanoparticle of diameter a) D= 8 and b) 12, at athermal interactions (black solid line), and monomer-monomer attractive interaction strength = 0.2kT (circles) and 1kT (triangles). c) Number of attractive monomer contacts for D=4 (circles), D=8 (triangles) and 12 (squares) at monomer attractive interaction strength=1kT. Open symbols-dashed lines correspond to systems where A monomers are attractive and filled symbols- solid lines correspond to systems where B monomers are attractive.

For purely athermal interactions and for weak attractive interaction strength of 0.2 kT we do not see any effect of D on the radius of gyration. At 1 kT, $R_g(\varepsilon_{AA}=1\ kT) > R_g\ (\varepsilon_{BB}=1\ kT)$ for D=4 (Figure 2.2a), while $R_g(\varepsilon_{AA}=1\ kT) < R_g\ (\varepsilon_{BB}=1\ kT)$ for D=12 (Figure 2.4b). For D=8 diblock and $-(A_3B_3)-$ copolymers exhibit $R_g(\varepsilon_{AA}=1\ kT) < R_g\ (\varepsilon_{BB}=1\ kT)$ while $-(A_6B_6)-$exhibits $R_g(\varepsilon_{AA}=1$

kT) > R_g (ε_{BB}=1 kT) (Figure 2.4a). Monomer sequence plays a critical role in the transition from D=4-like conformations to D=12-like conformations. As mentioned in the previous section for D=4, the monomer sequence dictates if grafted chains bring attractive monomers on all chains together (intra- and inter-chain) or by purely intra-chain contacts (when each chain folds onto itself). For particle size D=12 the enthalpic gain is unable to overcome entropic loss of stretch since the chains of constant length N=24 have to stretch more when grafted on D=12 than on D=4; therefore the chains prefer to fold onto themselves and have intra-chain contacts only. The monotonic dependence of Rg on varying monomer sequence at D=12 (Figure 2.4b) when there is only intra-chain monomer aggregation is because the monomer sequence becomes blockier, going from A_1B_1 (alternating) to A_3B_3 to A_6B_6 to $A_{12}B_{12}$ (diblock), the copolymer needs to be less compact (higher radius of gyration) to maximize attractive monomer contacts. Figure 2.4c shows that the number of favorable contacts for D=12 is lower than the corresponding system on D=4 and D=8, proving the chains exhibit purely intra-chain aggregation. For D=8 and ε_{AA}=1 kT the number of contacts is in between those of D=4 and D=12 for alternating copolymer, but as the sequence becomes blockier, the number of contacts for D=8 approaches the D=12 limit (Figure 2.4c). The behavior is completely different for D=8 and ε_{BB}=1 kT, whereas the sequence becomes blockier the number of contacts for D=8 approaches the D=4 limit. This is because the chains are grafted such that A monomers are always placed closer to the surface than the B monomers; so each grafted chain has to stretch more (loses more conformational entropy) to bring A monomers from multiple chains together than to bring B monomers from multiple chains together. Therefore, for all sequences other than alternating sequence, on D=8 particle at ε_{BB}=1 kT the grafted chains exhibit intra- and inter-chain aggregation (higher contacts) and at ε_{AA}=1 kT the grafted chains exhibit purely intra-chain aggregation (fewer contacts). This behavior is also

seen in the simulation snapshots presented in **Figure 2.5** for alternating and diblock copolymers grafted on increasing particle sizes, D=4, 8 and 12 for monomer attractive strength of 1 kT.

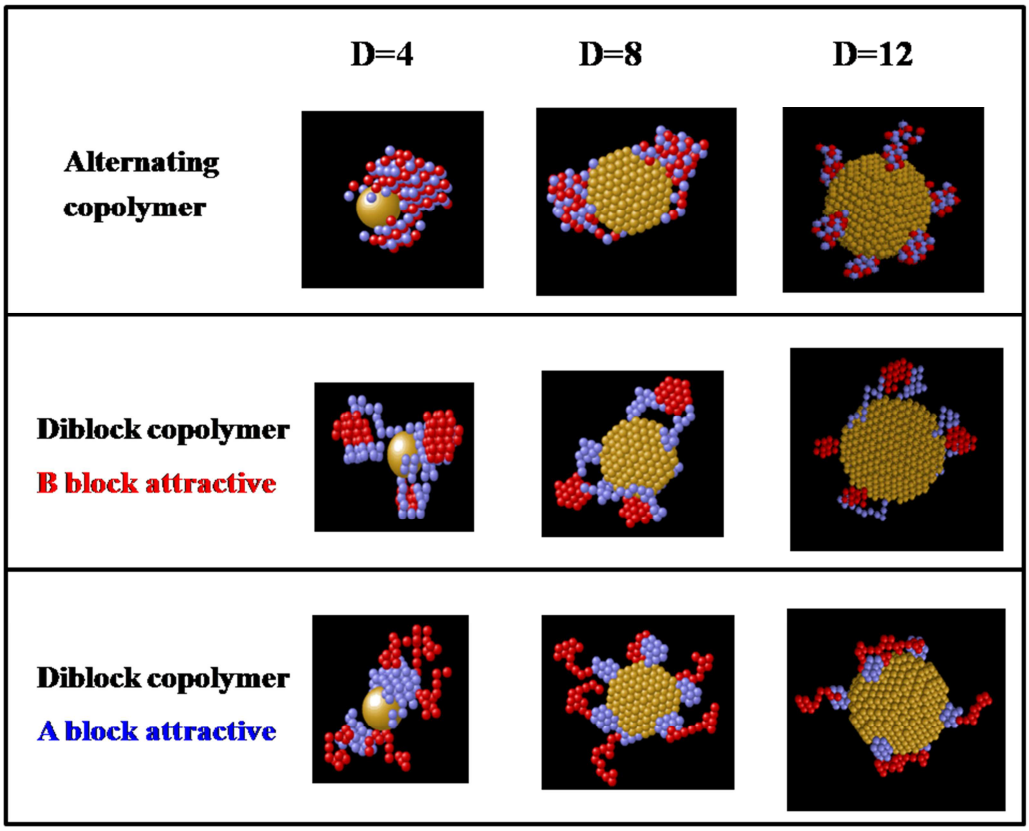

Figure 2.5 Representative simulation snapshots (best seen in color) for alternating and diblock AB copolymers of length N=24 grafted on a spherical nanoparticle of diameter D=4, 8 and 12 at ε_{AA} or ε_{BB}=1 kT. For alternating sequence we show snapshots only for ε_{AA}=1 kT because the chain conformations are similar for both ε_{AA}=1 kT and ε_{BB}=1 kT. D=4 exhibits intra- and inter-chain monomer aggregation, and D=12 exhibits mainly intra-chain aggregation only. D=8 shows purely intra-chain aggregation for diblock copolymer and A block attractive, and a combination of intra- and inter-chain aggregation for alternating and diblock and B block attractive.

All the results presented so far are for six chains grafted on nanoparticles with increasing diameter. When we increase the particle diameter at constant number of grafted chains, we are simultaneously decreasing the curvature of the grafting surface and the grafting density. Decreasing grafting density leads to *increasing* the overall volume available around each chain

as the chains are grafted farther apart. Decreasing curvature leads to *decreasing* overall volume available to each chain (see supplementary information). The available volume around each chain is important because the higher the volume around each chain the higher the number of conformations the chain can sample thus a higher conformational entropy. Since decreasing curvature and decreasing grafting density cause opposite effects on the available volume around each chain, it is important to study how curvature alone affects the radius of gyration of the grafted chains while the *grafting density* is maintained constant.

We present in Figure 2.6 ensemble average R_g for increasing particle size (decreasing curvature) at constant grafting density of approximately σ=0.03-0.04 chains/nm^2 for grafted chain length N=24. Figure 2.6a is for two chains grafted on D=4 particle, Figure 2.6b is for six chains grafted on D=8 particle, and Figure 2.6c is for fourteen chains grafted on D=12 particle. At this low grafting density, changing the curvature at constant grafting density does not affect the R_g at athermal interactions or weak monomer attraction strength 0.2 kT. This will not be the case at high "brush-like" grafting densities (high σ), where even if the area per chain ($1/\sigma$) is small, it can be compensated by the higher volume per chain possible at high curvatures, thus leading to a significant difference in R_g with increasing curvature. At attractive monomer strength of 1 kT the effect of changing curvature on the radius of gyration of the grafted copolymers has a non-trivial dependence on the monomer sequence of the grafted chain.

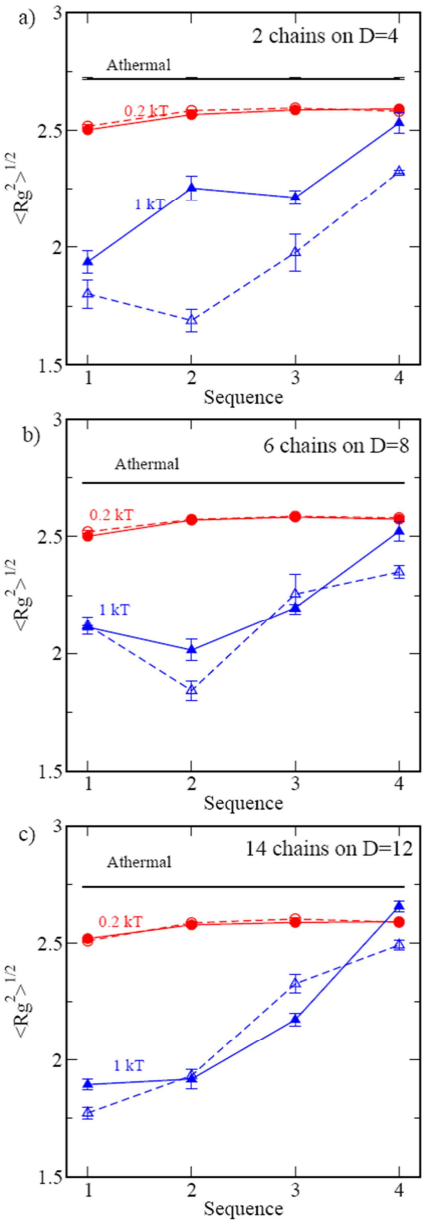

Figure 2.6 Radius of gyration, R_g, as a function of monomer sequence (x-axis) for AB copolymers of length N=24 grafted on spherical nanoparticles of size D=4, 8, and 12nm, at grafting density 0.03-0.04 chains/nm^2 and at athermal interactions (black solid line), and monomer-monomer attractive interaction strength = 0.2kT (circles) and 1kT (triangles). Open symbols-dashed lines correspond to systems where A monomers are attractive and filled symbols-solid lines correspond to systems where B monomers are attractive.

For diblock copolymers, at constant grafting density as curvature decreases the R_g increases slightly, but at all curvatures $R_g(\varepsilon_{BB}=1\ kT) > R_g(\varepsilon_{AA}=1\ kT)$. For A_6B_6 sequence, as curvature decreases $R_g(\varepsilon_{BB}=1\ kT)$ does not change, but $R_g(\varepsilon_{AA}=1\ kT)$ increases, such that there is a reversal in dependence of R_g on ε_{BB} and ε_{AA} around D=8. For the A_3B_3 sequence as the curvature decreases $R_g(\varepsilon_{BB}=1\ kT)$ decreases but $R_g(\varepsilon_{AA}=1\ kT)$ increases, such that at the lowest curvature considered here (D=12) $R_g(\varepsilon_{BB}=1\ kT)$ becomes equal to $R_g(\varepsilon_{AA}=1\ kT)$. For alternating copolymer as curvature decreases both $R_g(\varepsilon_{BB}=1\ kT)$ and $R_g(\varepsilon_{AA}=1\ kT)$ increase, exhibiting a maximum around D=8 and then decrease. Decreasing curvature at constant grafting density A) decreases volume available to each chain forcing the chain to extend more, leading to higher R_g, and B) allows for chains to more easily (less stretching) bring attractive monomers (especially those away from the surface) on multiple chains together, leading to lower R_g.. The monomer sequence and whether the A monomers (closer to the surface) or B monomers (away from the surface) are attractive dictate the balance the two scenarios.

To understand the effect of changing grafting density at constant curvature we compare the results for D=4 particle in Figure 2.4a (0.12 chains/nm^2) and Figure 2.6a (0.04 chains/nm^2), and for D=12 particle Figure 2.4c (0.01 chains/nm^2) and Figure 2.6c (0.03 chains/nm^2). Decreasing grafting density leads to increasing distances between the chains grafted on the surface, which in turn should reduce the *inter-chain* attractive monomer aggregation because the chains have to stretch more to aggregate with another grafted chain, making it entropically unfavorable for inter-chain aggregation. Therefore, decreasing grafting density leads to purely intra-chain attractive monomer aggregation, where the radius of gyration is dictated mainly by how a sequence facilitates the folding of the chains that maximizes favorable enthalpy while maintaining a higher entropy. For both cases, D=4 and D=12, decreasing grafting density makes

$R_g(\varepsilon_{BB}=1\ kT) > R_g(\varepsilon_{AA}=1\ kT)$ because when $\varepsilon_{BB}=1$ kT the A monomers closest to the surface do not provide any energetic gain by being part of the folded compact coil, and act as spacers that keep the coiled up globule away from the particle surface, thus leading to larger R_g when $\varepsilon_{BB}=1$ kT than when $\varepsilon_{AA}=1$ kT.

So far the chains were grafted on spherical particles ranging in particle diameter (D) from 4 to 12 or in curvature from 1/4 to 1/12. As the curvature increases to infinity we will reach the star copolymer limit[62] and based on the agreement between the D=4 results for diblock copolymers with the results on heteroarm star polymers[62] we expect the star copolymer trends for other copolymer sequences to be similar to that at D=4. As the curvature decreases to zero we approach the flat surface limit. In Figure 2.7 we present the effect of monomer sequences and grafting density on the conformations of N=24 chains grafted on a *flat surface*. Note that the results on the flat surface presented in Figure 2.7 are at the same grafting density as that of six grafted chains on D=4, 8 and 12, respectively (Figure 2.4) in order to fairly compare the results from curved surfaces (chains grafted on particles) to that from a flat surface. The two significant differences between the curved surfaces (Figure 2.4) and the flat surfaces (Figure 2.7) are: 1) in most cases differentiation in R_g at $\varepsilon_{BB}=1$ kT (solid lines) and $\varepsilon_{AA}=1$ kT (dashed lines) is reduced on a flat surface than in the corresponding system on spherical particles, and 2) if the radius of gyration varies non-monotonically with monomer sequence in case of spherical particle the corresponding flat surface results show a monotonic dependence on monomer sequence.

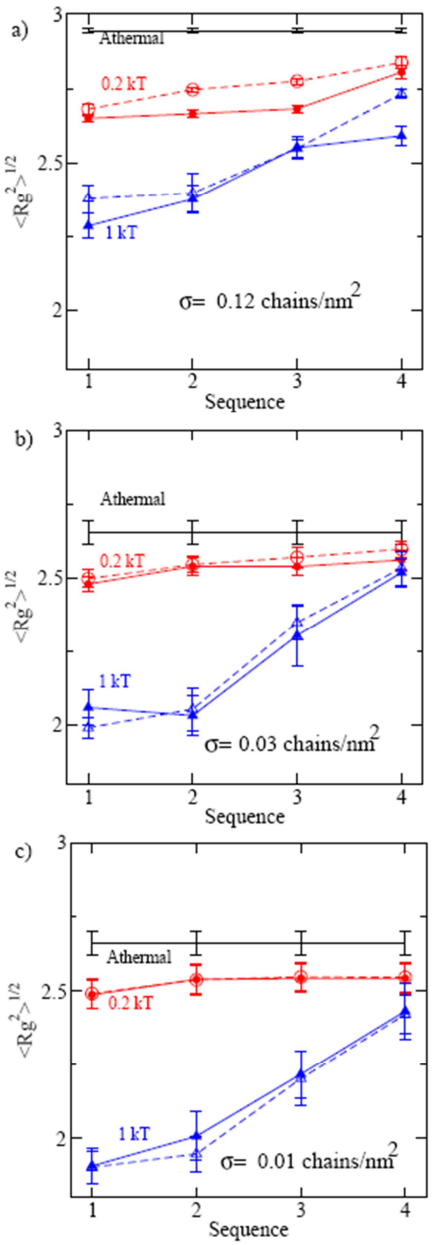

Figure 2.7 Radius of gyration, R_g, as a function of monomer sequence for AB copolymers of length N=24 grafted on a flat surface at decreasing grafting density, at athermal interactions (black solid line), and monomer-monomer attractive interaction strength=0.2 kT (circles) and 1 kT (triangles). Open symbols-dashed lines correspond to systems where A monomers are attractive and filled symbols-solid lines correspond to systems where B monomers are attractive.

At *athermal conditions*, if the grafting density is higher than the critical grafting density, $\sigma^* = 1/(\pi R^2_{g,athermal,onechain})$, where the grafted chains begin to touch each other, the higher volume per chain provided by the curved surface as compared to flat surfaces at that grafting density (see supplementary information) becomes important in dictating the R_g of the grafted chain. For N=24, the athermal single chain has an ensemble average R_g~2.75 nm, and σ^*=0.042 chains/nm^2. A surface grafting density of 0.12 chains/nm^2 is greater than σ^* for N=24, and therefore the lower available volume per chain in case of flat surface leading to chains being more extended, causes the R_g to be higher for the flat surface (Figure 2.7a) than for D=4 (Figure 2.4a) at purely athermal interactions. A surface grafting density of 0.03 chains/nm^2 is lower than the $\sigma^*$of 0.042 chains/nm^2, therefore the R_g of the grafted chain is not affected by the difference in available volume per chain on a D=8 spherical nanoparticle and on a flat surface. We expect as curvature decreases and at grafting lower than σ^*=0.042 chains/nm^2, the corresponding curved and flat surface R_g should be same. But at grafting density of 0.01 chains/ nm^2 the radius of gyration of chains grafted on D=12 (Figure 2.4c) is slightly higher and not equal to that on a flat surface (Figure 2.7c). Perhaps the higher error bar in case of flat surface suggests that the difference is not significant compared to the noise in the data.

At weak attractive monomer interaction strength of 0.2 kT (circles) the trends of radius of gyration with varying sequences is similar for curved surfaces and flat surfaces at the lower grafting densities of 0.03 and 0.01 chains/nm^2. At 0.12 chains/nm^2 we observe two main differences between the chains grafted on spherical particles (Figure 2.4a) and on flat surfaces (Figure 2.7a): i) the values of radius of gyration are higher for the flat surface than spherical particles (as seen at the athermal conditions), and ii) for flat surface the $R_g(\varepsilon_{AA}$=0.2 kT) is slightly higher than $R_g(\varepsilon_{BB}$=0.2 kT) for all sequences, while for spherical particles the monomer

sequence dictates whether $R_g(\varepsilon_{AA}=0.2$ kT) is higher or lower than $R_g(\varepsilon_{BB}=0.2$ kT); for -(A_3B_3)- sequence $R_g(\varepsilon_{AA}=0.2$ kT) is slightly higher than $R_g(\varepsilon_{BB}=0.2$ kT); for diblock $R_g(\varepsilon_{AA}=0.2$ kT) is slightly lower than $R_g(\varepsilon_{BB}=0.2$ kT); for alternating and –(A_6B_6)- sequences $R_g(\varepsilon_{AA}=0.2$ kT) is equal to $R_g(\varepsilon_{BB}=0.2$ kT). At attractive monomer interaction strength of 1 kT and surface grafting density 0.12 chains/nm^2 the radius of gyration of chains on flat surfaces is higher than those on D=4 particle for all sequences, by approximately the same amount as the athermal and 0.2 kT cases. This can be explained based on chains stretching on flat surface due to excessive crowding.

2.3.3 Effect of grafted copolymer chain length

In Figure 2.8 we plot the effect of grafted chain length on the radius of gyration for athermal (Figure 2.8a), alternating copolymer at $\varepsilon_{AA}=1$ kT (Figure 2.8b) and diblock copolymer at $\varepsilon_{AA}=1$ kT (Figure 2.8c). The four values of chain lengths used for these results were N=24, 48, 72 and 96. We plot log(R_g) versus log (N) and capture from the linear fits on the data, the exponent ν and prefactor α of the relationship $\langle R_g^2\rangle^{1/2}=\alpha N^{\nu}$. Like the scaling relationship developed for athermal star polymers $\langle R_g^2\rangle \sim N^{2\nu} f^{2(1-\nu)}$ where N is the arm length and f is the number of arms of the star, we expect that the R_g will scale with N and grafting density (number of grafted chains per unit surface area). In addition as seen in previous sections, R_g is also affected by the monomer sequence, strength of monomer-monomer attraction and placement of the attractive monomer with respect to particle surface. We have focused this discussion simply on how R_g scales with graft length N for each monomer sequence, and expect the prefactor and exponent to capture the collective effects of the remaining molecular parameters on R_g and how it scales with chain length.

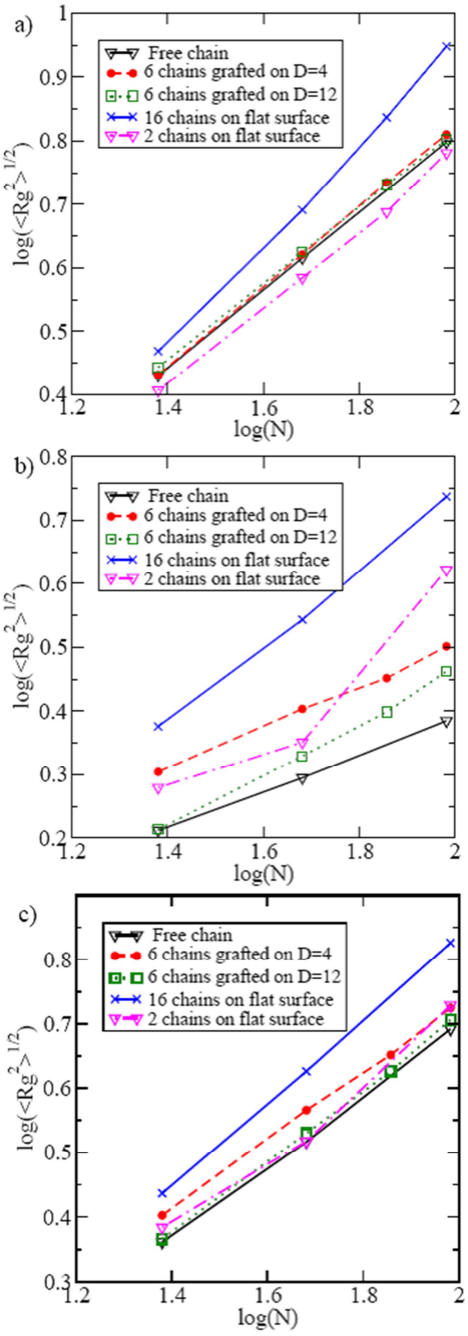

Figure 2.8 $\log(R_g)$ as a function of log(N), where N is the length of the grafted or free copolymer at a) athermal conditions, b)alternating copolymers at A-A monomer-monomer attraction strength is 1 kT, and c) diblock copolymers at A-A monomer-monomer attraction strength is 1 kT.

The data was obtained from five systems: (I) a single free chain, (II) six chains on spherical particle D=4, (III) six chains on spherical particle D=12, (IV) 16 chains grafted on a flat surface (same grafting density as six chains on D=4) and (V) 2 chains grafted on a flat surface (same grafting density as six chains on D=12). In Table 2.1 we have tabulated these exponents and prefactors obtained using linear fits to the data points in the plot of log R_g versus log N.

Table 2.1 The exponent and prefactor in $\langle R_g^2 \rangle^{1/2}=\alpha N^{\nu}$, where N is the grafted chain length for systems:I=free chain,II=six chains grafted on D=4 particle, III=six chains grafted on D=12 particles, IV=sixteen chains grafted on a flat surface with grafting density same as II, V= two chains grafted on a flat surface with grafting density same as III. Empty cells indicate that the data did not fit the scaling relationship.

	I		II		III		IV		V	
	ν	α	ν	α	ν	α	ν	α	ν	α
Athermal	0.61	0.66	0.63	0.65	0.60	0.68	0.79	0.53	0.61	0.64
Alternating (ε_{AA}=1 kT)	0.28	0.85	0.32	0.87	0.41	0.70	0.60	0.63	-	-
Alternating (ε_{BB}=1 kT)	0.28	0.84	0.30	0.91	0.44	0.67	0.63	0.60	-	-
Diblock (ε_{AA}=1 kT)	0.55	0.67	0.53	0.72	0.57	0.64	0.65	0.63	-	-
Diblock (ε_{BB}=1 kT)	0.54	0.69	0.53	0.70	0.50	0.75	0.57	0.69	-	-

All linear fits had a residual value greater than R^2=0.99, showing a good fit. In cases where the linear fits of log R_g versus log N data had a residual value <0.95 we concluded that the system does not fit the $\langle R_g^2 \rangle^{1/2}=\alpha N^{\nu}$ relationship.

At purely athermal interactions (Figure 2.8a and Table 2.1 row 1), for free polymer the radius of gyration scales with N through an exponent of 0.61, which agrees with the scaling exponent of 3/5 for unperturbed self-avoiding walks.[66] The exponent of free chain is similar to the six chains grafted on particle D=4, and on particle D=12. The chains grafted on flat surfaces at a high grafting density (same as that for six chains grafted on particle D=4) have a different exponent and prefactor from that of free chain and chains grafted on spherical particles at the same grafting density. On flat surfaces as grafting density decreases (IV to V) below the critical grafting density, σ^*, the scaling relationship approaches that of free polymers.

For *free* alternating copolymers (rows 2 and 3 and column I) the exponent at monomer attraction strength ε_{AA}=1 kT (also Figure 2.8b) and ε_{BB}=1 kT is close to the exponent of 1/3 for dense polymer globule formed in a bad solvent. There is no difference between the exponents at monomer attraction strength ε_{AA}=1 kT and ε_{BB}=1 kT for free alternating copolymer chains, as expected the corresponding χ_{AB} are equal. For alternating copolymers *grafted* on D=4 particles (row 2 and 3 and column II), the exponents are close to those seen at free copolymers, with a marginal difference in the exponents at monomer attraction strength ε_{AA}=1 kT and ε_{BB}=1 kT. This suggests that how R_g scales with N for the free copolymers is similar to that for the copolymers grafted on a highly curved surface because the volume available per chain is similar for free copolymers and copolymers grafted on small spherical particles. As the curvature of the surfaces decreases from D=4 to D=12 to flat (column II to III to IV), the exponent deviates from the corresponding collapsed free copolymer (column I), and the difference in exponents at monomer attraction strength ε_{AA}=1 kT (row 2) and ε_{BB}=1 kT (row 3) also increases. At lower grafting density, two chains on flat surfaces (system V), the data did not fit the $\langle R_g^2 \rangle^{1/2}=\alpha N^{\nu}$ relationship (Figure 2.8b). Although the grafting density for 16 chains grafted on a flat surface

(column IV) is equal to 6 chains grafted on a D=4 particle (column II), the exponents are not the same, implying that at the range of grafting densities considered in this paper (not a brush), the curvature plays a bigger role than the grafting density in deciding the scaling exponent. Interestingly, the exponents for all attractive cases on flat surface (column IV row 2 and 3) approach the "athermal free chain" value of 0.60, while the corresponding flat surface results at athermal conditions (column IV row 1) is ~0.80.

For the diblock copolymer systems (Table 2.1 rows 4 and 5) the exponents for the free chains and chains grafted on D=4 (column II) are approximately the same, as seen for alternating copolymers. For chains grafted on surfaces with low curvature, D=12 and flat surface (columns III and IV) the difference between the exponents at monomer attraction strength ε_{AA}=1 kT and ε_{BB}=1 kT is larger for the diblock copolymer systems than the corresponding alternating copolymer system. This is not surprising considering that in case of diblock copolymers the block of A monomers is closer to the surface than the other block of B monomers, while in alternating copolymers the A and B monomers are placed alternately from the surface. For a grafted diblock copolymer, the volume available to the block A (the block closer to the surface) is much less than the volume available for block B (the block away from the surface), leading to different scaling behavior.

In case of the multiblock sequences -(A_3B_3)- and –(A_6B_6)-, the R_g data at attractive interaction strength of 1 kT for all five systems lead to a non-linear log(R_g) versus log(N) graph.

2.4 Discussion

We have presented a detailed study on AB copolymer chains grafted on spherical particles to show the non-trivial effect of monomer sequence, on the conformations of AB copolymers

grafted on spherical particles of varying diameters. We have compared the conformations of copolymers grafted on spherical nanoparticles to that of free copolymers, heteroarm star copolymers (copolymer arms tethered to a small core) and copolymers grafted on flat surfaces to establish the effect of curvature on the dependence of grafted chain conformations on monomer sequence. When copolymers are grafted on a spherical particle and one set of like-monomers have an attractive interaction either (i) all the grafted chains aggregate to bring attractive monomers from all grafted chains together (intra-chain and inter-chain monomer aggregation) if the favorable enthalpy gained by doing so can offset the conformational entropic loss, or (ii) each grafted chain folds onto itself to bring attractive monomers along each chain together (pure intra-chain monomer aggregation) if the entropic loss from stretching of chains for inter-chain aggregation cannot be overcome by the enthalpic gain. The implication of this on a system of multiple copolymer grafted particles is that the conformations and spatial organization of monomers in the two scenarios (both intra- and inter-chain versus purely intra-chain monomer aggregation) will affect the effective interactions between two copolymer grafted particles. For example, in the case of intra- and inter chain monomer aggregation the attractive monomers form a crowded layer around the nanoparticle surface (snapshots in Figure 2.5), either symmetrically (as in diblock) or in an anisotropic fashion (as in alternating). This crowded monomer layer near the surface could cause a repulsive potential of mean force close to the particle surface when two identical copolymer grafted particles approach each other. Furthermore, the asymmetric crowding of monomers on one side of the particle could lead to a directional anisotropic effective particle interactions.

At a constant chain length, whether the copolymer grafted nanoparticle exhibit pure intra-chain folding or a combination of the intra-chain and inter-chain monomer aggregation is

dictated by the monomer sequence, particle diameter and grafting density. For six copolymers of chain length N=24 grafted on a spherical particle of diameter D=4, the latter dominates because the grafted chains are long enough and the particle small enough for the chains to find attractive monomers on other grafted chains. For N=24 and D=4 the radius of gyration, which quantifies the conformations, varies non-monotonically with the monomer sequence going from alternating to diblock, with the smallest radius of gyration seen for -(A_3B_3)- sequence. The monomer sequence also dictates whether the radius of gyration for attractive A monomers is higher or lower than the radius of gyration for attractive B monomers. The trends seen for diblock copolymer sequence match those seen in previous work on star block copolymers (analogous to a copolymer grafted particle where the particle size is infinitely small).

As the particle diameter is increased, while maintaining the same grafted chain length, the six grafted chains transition to purely intra-chain monomer aggregation because the conformational entropic loss from the chains trying to stretch around the large particle to find attractive monomers on other grafted chains is high, and cannot be overcome by the enthalpic gain. The monomer sequence dictates the critical particle diameter where the copolymer chains change from intra- and inter-chain aggregation to pure intra-chain aggregation, because the monomer sequence affects the balance of enthalpic gain by bringing monomers from multiple chains versus the conformational entropic penalty in doing so. When the grafted chains exhibit purely intra-chain monomer aggregation, the radius of gyration varies monotonically with monomer sequence, with the lowest radius of gyration for the alternating copolymer and the highest radius of gyration for the diblock copolymers. This is because as the sequence becomes blockier (the like monomers are grouped together), the chain has to fold less compactly to maximize the enthalpically favorable contacts while maintaining high conformation entropy.

The radius of gyration of alternating and diblock copolymers scale with chain length through a power law, $<R_g^2>^{1/2}=\alpha N^{\nu}$, while the multiblock sequences do not follow that relationship. For a constant sequence, the scaling exponents obtained from plots of log (R_g) as a function of log N are similar for free copolymers and chains grafted on highly curved surface (spherical particles), and completely different for chains grafted on flat surface and curved surface at same grafting density. These results demonstrate that at the low grafting densities considered here, the available volume per chain, dictated by the curvature of the grafting surface, is more critical than the grafting density in affecting the size of the copolymer chain, at a constant monomer sequence. It is important to note that we work at the low to medium grafting density rather than the brush-like high grafting density because we expect that the effect of the monomer sequence on the chain conformation will diminish at brush-like grafting densities where the excluded volume interactions will dominate the conformations the chains adopt.

It is important we point to the potential impact of this work and some of the limitations of this study. Although the motivation of this work came from the effect of peptide sequence on the folding of proteins, and the use of polypeptides and proteins for guiding assembly of nanoparticle, the model we have used to mimic a protein is a simple AB copolymer which does not include the complexities in real proteins, such as side chain structure in the residues, competition or cooperativity of hydrogen bonding and hydrophobicity, electrostatic interactions, etc. This work is simply meant to be the first step towards understanding the complex protein driven assembly of nanoparticles and to present the basic physics behind how *monomer sequences* affect conformations of proteins grafted on spherical nanoparticles. The conformations the grafted copolymers adopt can predict the effective interactions and inter-particle spacing between two such copolymer grafted particles, thus guiding us in assembly of

multiple copolymer grafted nanoparticles. However, we only focus on a single copolymer grafted particle in this paper. In case of single copolymer grafted particle the conformations of each grafted chains are affected only by the other chains in the same particle. During assembly of many such copolymer grafted particles the conformations of chains on one particle could also be affected by the chains on another particle because attractive monomers on chains grafted on multiple particles could aggregate leading to particle assembly. Understanding the effect of molecular parameters on assembly of multiple polymer grafted particles is the focus of our next study and will be presented in a future publication. In addition to providing guidelines for designing new materials through assembly of such grafted nanoparticles, we expect this work to impact the biomedical field because copolymer grafted nanoparticles can be used for drug delivery[67 68, 69]. One can create drug or protein carriers by grafting on nanoparticles stimuli-responsive polymers, such as thermosensitive polymers (e.g.poly(4-vinylpyridine)) or pH-sensitive polymers (e.g.poly(*N*-isopropylacrylamide)), that can exhibit sharp changes to variation in temperature, light, salt concentration or pH. Stimuli sensitive copolymers grafted particles can then load or trap drugs or proteins in one environment e.g. when the like-monomers collapse due to strong attraction, and release the drugs at the target site when the environment neutralizes the monomer attraction leading to open conformations. Although we do not address the dynamics of conformational changes, and in turn the kinetics of drug or protein release, this work is useful in predicting how varying monomer sequences in the stimuli responsive copolymers are capable of different conformational changes and in turn different mechanisms of loading, delivery and release.

2.5 REFERENCES

1. T. A. Witten and P. A. Pincus, *Macromolecules*, 1986, **19**, 2509-2513.
2. C. F. Laub and J. T. Koberstein, *Macromolecules*, 1994, **27**, 5016-5023.
3. A. Jayaraman and K. S. Schweizer, *Macromolecules*, 2009, **42** pp 8423-8434.
4. S. T. Milner, T. A. Witten and M. E. Cates, *Macromolecules*, 1989, **22**, 853-861.
5. J. U. Kim and M. W. Matsen, *Macromolecules*, 2008, **41**, 4435-4443.
6. M. Himmi, M. Benhamou, A. Bettachy and M. Daoud, *Journal of Molecular Liquids*, 2003, **102**, 347-363.
7. K. T. Marla and J. C. Meredith, *Journal of Chemical Theory and Computation*, 2006, **2**, 1624-1631.
8. V. Causin, B. X. Yang, C. Marega, S. H. Goh and A. Marigo, *Journal of Nanoscience and Nanotechnology*, 2008, **8**, 1790-1796.
9. N. Tsubokawa, *Polymer Journal*, 2007, **39**, 983-1000.
10. C. Li, J. Han, C. Y. Ryu and B. C. Benicewicz, *Macromolecules*, 2006, **39**, 3175-3183.
11. V. Goel, T. Chatterjee, L. Bombalski, K. Yurekli, K. Matyjaszewski and R. Krishnamoorti, *Journal of Polymer Science Part B-Polymer Physics*, 2006, **44**, 2014-2023.
12. E. R. Chan, L. C. Ho and S. C. Glotzer, *Journal of Chemical Physics*, 2006, **125**, 064905.
13. C. R. Iacovella, M. A. Horsch, Z. Zhang and S. C. Glotzer, *Langmuir*, 2005, **21**, 9488-9494.
14. X. Zhang, E. R. Chan and S. C. Glotzer, *Journal of Chemical Physics*, 2005, **123**, 184718.
15. M. A. Horsch, Z. Zhang and S. C. Glotzer, *Nano Letters*, 2006, **6**, 2406-2413.
16. P. J. Costanzo and F. L. Beyer, *Macromolecules*, 2007, **40**, 3996-4001.
17. J. J. Chiu, B. J. Kim, E. J. Kramer and D. J. Pine, *Journal of the American Chemical Society*, 2005, **127**, 5036-5037.
18. B. J. Kim, G. H. Fredrickson and E. J. Kramer, *Macromolecules*, 2008, **41**, 436-447.
19. V. Pryamitsyn, V. Ganesan, A. Z. Panagiotopoulos, H. Liu and S. K. Kumar, *Journal of Chemical Physics*, 2009, **131**, 221102.
20. S. Y. Park, K. R. A. Lytton-Jean, B. Lee, S. Weigand, G. C. Schatz and C. A. Mirkin, *Nature*, 2008, **451**, 553-556.
21. P. L. Biancaniello, A. J. Kim and J. C. Crocker, *Physical Review Letters*, 2005, **94**.
22. D. B. Lukatsky, B. M. Mulder and D. Frenkel, *Journal of Physics-Condensed Matter*, 2006, **18**, S567-S580.
23. N. C. Harris and C. H. Kiang, *Physical Review Letters*, 2005, **95**.
24. A. A. Lazarides and G. C. Schatz, *Journal of Physical Chemistry B*, 2000, **104**, 460-467.
25. A. J. Kim, P. L. Biancaniello and J. C. Crocker, *Langmuir*, 2006, **22**, 1991-2001.
26. A. V. Tkachenko, *Physical Review Letters*, 2002, **89**.
27. V. Talanquer, *Journal of Chemical Physics*, 2006, **125**, 194701.
28. W. J. Parak, T. Pellegrino, C. M. Micheel, D. Gerion, S. C. Williams and A. P. Alivisatos, *Nano Letters*, 2003, **3**, 33-36.
29. M. M. Stevens, N. T. Flynn, C. Wang, D. A. Tirrell and R. Langer, *Advanced Materials*, 2004, **16**, 915-918.

30. S. Si, A. Kotal and T. K. Mandal, *Journal of Physical Chemistry C*, 2007, **111**, 1248-1255.
31. J. M. Slocik, F. Tam, N. J. Halas and R. R. Naik, *Nano Letters*, 2007, **7**, 1054-1058.
32. S. Si and T. K. Mandal, *Langmuir*, 2007, **23**, 190-195.
33. M. K. Corbierre, N. S. Cameron, M. Sutton, K. Laaziri and R. B. Lennox, *Langmuir*, 2005, **21**, 6063-6072.
34. B. J. Kim, J. Bang, C. J. Hawker and E. J. Kramer, *Macromolecules*, 2006, **39**, 4108-4114.
35. Q. Lan, L. F. Francis and F. S. Bates, *Journal of Polymer Science Part B-Polymer Physics*, 2007, **45**, 2284-2299.
36. K. R. Shull, *Journal of Chemical Physics*, 1991, **94**, 5723-5738.
37. S. E. Harton and S. K. Kumar, *Journal of Polymer Science Part B-Polymer Physics*, 2008, **46**, 351-358.
38. P. Akcora, H. Liu, S. K. Kumar, M. J., Y. Li, B. C. Benicewicz, L. S. Schadler, D. Acehan, A. Z. Panagiotopoulos, V. Pryamitsyn, V. Ganesan, J. Ilavsky, P. Thiyagarajan, R. H. Colby and J. F. Douglas, *Nature Materials*, 2009, **8**, 354-359.
39. G. D. Smith and D. Bedrov, *Langmuir*, 2009, **published online**.
40. A. Jayaraman and K. S. Schweizer, *J. Chem. Phys.*, 2008, **128**, 164904.
41. A. Jayaraman and K. S. Schweizer, *Langmuir*, 2008, **24**, 11119-11130.
42. E. R. Chan, X. Zhang, C. Y. Lee, M. Neurock and S. C. Glotzer, *Macromolecules*, 2005, **38**, 6168-6180.
43. M. A. Horsch, Z. L. Zhang and S. C. Glotzer, *Physical Review Letters*, 2005, **95**, 056105.
44. J. Y. Lee, A. C. Balazs, R. B. Thompson and R. M. Hill, *Macromolecules*, 2004, **37**, 3536-3539.
45. A. Striolo, *Small*, 2007, **3**, 628-635.
46. C. R. Iacovella, A. S. Keys, M. A. Horsch and S. C. Glotzer, *Phys. Rev. E.*, 2007, **75**, 040801.
47. S. C. Glotzer, M. A. Horsch, C. R. Iacovella, Z. L. Zhang, E. R. Chan and X. Zhang, *Current Opinion in Colloid & Interface Science*, 2005, **10**, 287-295.
48. Z. Zhang, M. A. Horsch, M. H. Lamm and S. C. Glotzer, *Nano Letters*, 2003, **3**, 1341-1346.
49. M. A. Carignano and I. Szleifer, *Journal of Chemical Physics*, 1995, **102**, 8662-8669.
50. K. A. Dill, S. Bromberg, K. Z. Yue, K. M. Fiebig, D. P. Yee, P. D. Thomas and H. S. Chan, *Protein Science*, 1995, **4**, 561-602.
51. A. C. Balazs and M. T. Demeuse, *Macromolecules*, 1989, **22**, 4260-4267.
52. A. C. Balazs, I. C. Sanchez, I. R. Epstein, F. E. Karasz and W. J. Macknight, *Macromolecules*, 1985, **18**, 2188-2191.
53. J. J. Semler, Y. K. Jhon, A. Tonelli, M. Beevers, R. Krishnamoorti and J. Genzer, *Advanced Materials*, 2007, **19**, 2877-2883.
54. J. J. Semler and J. Genzer, *Journal of Chemical Physics*, 2006, **125**, 014902.
55. A. K. Dasmahapatra, G. Kumaraswamy and H. Nanavati, *Macromolecules*, 2006, **39**, 9621-9629.
56. A. K. Dasmahapatra, H. Nanavati and G. Kumaraswamy, *Journal of Chemical Physics*, 2007, **127**, 234901.
57. A. Sikorski and P. Romiszowski, *Physica a-Statistical Mechanics and Its Applications*, 2005, **357**, 364-370.

58. Y. Chang, W. C. Chen, Y. J. Sheng, S. Y. Jiang and H. K. Tsao, *Macromolecules*, 2005, **38**, 6201-6209.
59. J. Havrankova, Z. Limpouchova and K. Prochazka, *Macromol Theor Simul*, 2003, **12**, 512-523.
60. M. Stepanek, P. Matejicek, J. Humpolickova, J. Havrankova, K. Podhajecka, M. Spirkova, Z. Tuzar, C. Tsitsilianis and K. Prochazka, *Polymer*, 2005, **46**, 10493-10505.
61. J. Havrankova, Z. Limpouchova, M. Stepanek and K. Prochazka, *Macromolecular Theory and Simulations*, 2007, **16**, 386-398.
62. Y. J. Sheng, C. H. Nung and H. K. Tsao, *Journal of Physical Chemistry B*, 2006, **110**, 21643-21650.
63. A. Kiriy, G. Gorodyska, S. Minko, M. Stamm and C. Tsitsilianis, *Macromolecules*, 2003, **36**, 8704-8711.
64. D. Frenkel and B. Smit, *Understanding Molecular Simulations: From Algorithms to Applications*, Academic Press, 2001.
65. N. Metropolis, A. W. Rosenbluth, M. N. Rosenbluth, A. H. Teller and E. Teller, *Journal of Chemical Physics*, 1953, **21**, 1087-1092.
66. M. Rubinstein and R. H. Colby, *Polymer Physics*, Oxford University Press, 2008.
67. D. Trombly and V. Ganesan, *Journal of Polymer Science Part B-Polymer Physics*, 2009, **47**, 2566-2577.
68. Y. Y. Yuan, X. Q. Liu, Y. C. Wang and J. Wang, *Langmuir*, 2009, **25**, 10298-10304.
69. S. Chen, Y. Li, C. Guo, J. Wang, J. H. Ma, X. F. Liang, L. R. Yang and H. Z. Liu, *Langmuir*, 2007, **23**, 12669-12676.

2.6 Supplementary Information

2.6.1 Volume available per chain that is grafted on spherical particle and flat surface

The surface grafting density, σ, is defined as number of chains per unit surface area. In other words the surface area available per chain is 1/ σ. If a curved surface and a flat surface have the same grafting density (and therefore the same area available per chain, shown in Figure 2.9 by the shaded region around the grafting site) the volume available per chain can be compared.

For a flat surface the volume available per chain, V, is equal to height of the chain times the surface area (1/ σ), assuming it is a cylindrical space around each chain. Since the grafting

densities in this paper are low, at athermal conditions we can approximate the height to be about twice the R_g of an unperturbed self-avoiding walk. This leads to $V= 2Rg/\sigma$.

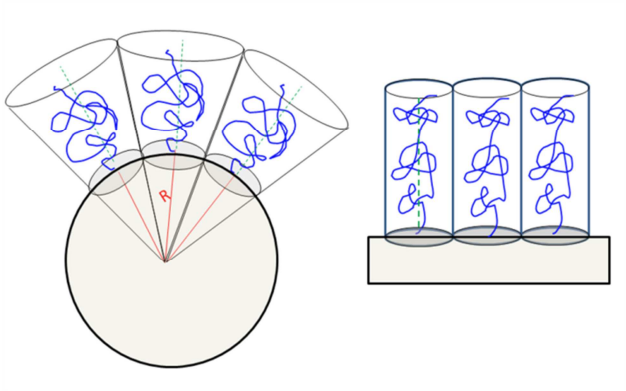

Figure 2.9 Schematic of volume occupied by chains for curved (left) and flat (right) surfaces at the same grafting density.

For spherical particles the volume available to each chain, V, is the volume of the shell around the spherical particle (the shell thickness is the height of the grafted chain) divided by number of grafted chains, assuming symmetric grafting as done in our simulations. We can approximate the height to be about twice the R_g of an unperturbed self-avoiding walk, since we work at low grafting densities. The number of grafted chains is grafting density, σ, times the surface area of the particle, $4\pi R^2$. This leads to $V= [(R+2R_g)^3-R^3]/[3R^2\sigma]$.

We have tabulated the volume per chain, V, (nm^3/chain) for N=24 (whose $R_{g,free\ athermal}$~2.75) at athermal conditions grafted on spherical particles with increasing diameter D or grafted on flat surface in Table S.2.1. If a curved surface (say, D=4) and a flat surface have same grafting density (~0.11 chains/nm^2), the volume available per chain decreases with decreasing curvature (curved to flat).

Table S.2.1 Volume per chain, V, (nm^3/chain) for N=24 for varying grafting density, σ, and diameter, D, or flat surface.

σ	D	A=1/ σ	V
0.11	4	9.09	313.54
0.03	4	33.33	1149.65
0.03	8	33.33	553.88
0.01	12	100	910.97
0.01	2000	100	416.98
0.01	Flat	100	396.00
0.11	Flat	9.09	49.50

At constant curvature (say D=4) with decreasing grafting density the available volume per chain, V, increases, and so does the surface area per chain A (or the inter-chain spacing).

As the curvature decreases (or D increases) the available volume approaches the flat surface limit.

Chapter 3

Assembly of copolymer functionalized nanoparticles: a Monte Carlo simulation study

Adapted from: *Soft Matter* **7** 5952-5964 (2011)

3.1 Introduction

Precise assembly and ordering of nanoparticles mediated by a solvent or a polymer matrix is extremely important for creating spatially engineered materials that can be used for photonics, metamaterials, photovoltaic, and electronics applications. One way to produce precise nanoparticle assembly is by functionalizing the nanoparticle surface with ligands, such as polymers,[1-24] DNA,[25-41] and proteins,[42-45] that can then manipulate the interfacial interactions between the nanoparticles and the medium the particles are placed in, and thus control their assembly. Past theoretical and experimental work on *homopolymer* functionalized nanoparticles has established that the *chemistry* of the grafted polymers, nanoparticles and the medium (solvent or polymer matrix) is one parameter that controls the spatial organization of the nanoparticles. For example, experimental studies[16-18] have achieved migration of the polymer grafted nanoparticles from one domain in a polymer matrix to another domain simply by thermally changing the composition of grafted homopolymers on the nanoparticle, and thus the compatibility of the grafted polymer and matrix. Another important parameter that dictates the effective inter-particle interactions and therefore the particle assembly is the *polymer grafting density*, defined as the number of grafted polymers per unit surface area on the particle. At high grafting density the grafted polymers extend due to crowding, and form a brush like

conformation on the particle surface. A particle carrying a polymer brush on its surface can disperse (assemble) in medium that acts as a good (bad) solvent for the polymer brush. Additionally the *molecular weight of the graft* could also play a role in deciding whether the grafted particles disperse or aggregate. For example homopolymer grafted particles placed in a homopolymer matrix, where matrix chemistry is identical to the grafted polymer, disperse (aggregate) if the molecular weight of matrix homopolymer is lower (higher) than that of grafted homopolymer.[46, 47] At low grafting density[7, 12-15, 48-54] the grafted polymers do not face any crowding from monomers of adjacent chains and as a result do not stretch into brush like conformations, and the inter-particle interactions are governed by how much of nanoparticle surface is exposed versus covered by the grafted monomers. Such homopolymer-grafted nanoparticles at low grafting densities have been shown to assemble into a variety of nanostructures. Glotzer and coworkers have conducted detailed simulation studies of polymer-tethered nanoparticles of various shapes[13-15, 50, 54-58] and demonstrated the presence of gyroid-phase in mono-tethered spherical particles. Jayaraman and Schweizer[3, 48, 49, 59, 60] have used Polymer Reference Interaction Site Model (PRISM) theory on spherical nanoparticles grafted with few homopolymer grafted chains to obtain order-disorder transition curves in dense solutions and melts of grafted particles and to understand phase behavior of these lightly grafted particles in a dense homopolymer matrix. While most of the above studies establish the effect of various molecular parameters on behavior of *homopolymer* grafted nanoparticles either in solvent or in a polymer matrix, the behavior of *copolymer* grafted nanoparticles (with more than just one graft) has been studied to a much smaller extent.[61-65] This is surprising considering recent synthetic advances to make copolymer-grafted nanoparticles through atom transfer radical

polymerization (ATRP)[11] and Z-supported reversible addition−fragmentation chain transfer (RAFT) polymerization.[66]

Copolymer functionalization is an attractive route for directing nanoparticle assembly because unlike homopolymer grafts where the effect of the medium (solvent or matrix) is homogeneous throughout the homopolymer grafted chain, in a copolymer the presence of two different monomer chemistries could allow us to control the solvent effects non-homogeneously along the chain and thus spatial variation in effective inter-particle interactions. This was proven in recent work by Jayaraman and coworkers,[65] who used Monte Carlo simulations to study copolymers of varying monomer sequences grafted onto *a single* solid spherical nanoparticle and showed the non-trivial effect of monomer sequence, particle diameter, grafted chain length and grafting density on the grafted copolymer *conformations.* They showed that monomer sequence, particle diameter, grafted chain length and grafting density dictate if (a) the grafted chains aggregate to bring attractive monomers from multiple grafted chains together (inter-chain and intra-chain monomer aggregation) if the enthalpy gained by doing so offsets the entropic loss caused by the stretching of the chains, or (b) each grafted chain folds onto itself to bring the attractive monomers together (purely intra-chain monomer aggregation) if the entropic loss from inter-chain aggregation cannot be overcome by the enthalpic gain, but the energetically favorable intra-chain contacts compensate for the loss of conformational entropy accompanying the monomer aggregation. A follow up study by Nair and Jayaraman[64] showed how this complex interplay of monomer sequence, particle diameter, grafted chain length and grafting density affects effective inter-particle interactions. They developed a self-consistent PRISM theory-MC simulation method to study potential of mean force (PMF) between copolymer –grafted nanoparticles at infinitely dilute concentration in a polymer matrix. This study showed that the

monomer sequence (alternating and diblock) in the grafted chains dictates how the attractive monomers aggregate and how those aggregates help or hinder matrix-induced direct contacts between the grafted particles, and thus the strength and location of attraction or repulsion in the PMF between two grafted particles. While alternating copolymer-grafted particles exhibit a PMF similar to athermal homopolymer-grafted particles, diblock copolymer-grafted particles exhibit interesting behavior different from homopolymer-grafted particles. For the diblock copolymer-grafted particles if the monomers in the block closer to the surface are attractive the PMF is repulsive at contact and weakly attractive at larger inter-particle distances; if the monomers in the outer block are attractive the PMF is attractive at contact and repulsive at larger inter-particle distances. Since these two studies have established that grafting copolymers on nanoparticles and varying monomer sequence affects grafted chain conformations, and in turn helps tune the magnitude, nature and location of attraction or repulsion in the PMF, which is needed for the tailored assembly of these functionalized nanoparticles, we are now motivated to investigate this tailored *assembly of copolymer grafted nanoparticles*.

In this paper we use lattice Monte Carlo simulations to study diblock or alternating copolymer grafted spherical nanoparticles placed in an implicit solvent with the goal to establish how nanoparticles functionalized symmetrically with diblock and alternating copolymers at low – medium grafting density and varying chemistries, particle sizes, concentration of grafted particles and grafted copolymer chain length assemble into nanoclusters of different sizes, shapes and structures. We observe that while the alternating sequence produces clusters that are relatively isotropic regardless of whether A-A or B-B monomers are attractive in the presence of negligible unlike monomer repulsions, diblock sequence produces clusters that are smaller and more compact when inner block monomers (A-A) are attractive and larger loosely held together

clusters when outer block monomers (B-B) are attractive. The monomer sequence dictates the role of like-monomer attractions in the presence of strong unlike A-B repulsions. For example, in the alternating case strong A-B repulsions lead to either particle dispersion or smaller clusters as compared to negligible A-B repulsions but for diblock case strong A-B repulsions and negligible A-B repulsions exhibit similar cluster characteristics. Diblock copolymers with strong inner block (A-A) attractions lead to anisotropic clusters like nanowires which are of interest for optical applications.[67-69] We also investigate how the cluster characteristics are affected by varying particle diameters, grafting densities (low-medium), copolymer chain lengths, and copolymer grafted particle concentrations. We find that increasing particle size makes it more entropically unfavorable for grafted chains to interact with adjacent grafted chains on the same particle leading to cluster formation only in cases when the like-monomer attraction strength was strong enough to overcome the entropic loss from stretching grafts during inter-particle contacts. Particle size and graft length affect the balance of enthalpic gain and entropic losses coming from inter-grafted particle contacts and/or inter- and intra- grafted chain contacts in the same grafted particle, and in turn affect the shape and size of the clusters. For example, at constant graft length and when A-A attractions are stronger than B-B attractions, diblock copolymer grafted particles form long “caterpillar-like” structures with large particle diameters and short trimer or tetramer nanowires with smaller particle diameters. Upon increasing particle concentration, while staying in the dilute concentration regime, the structure within the cluster quantified by the coordination numbers, does not change, confirming that the assembly is primarily governed by the copolymer functionalization imparting a ”valency” to the nanoparticle “atom”, with the valency depending on the monomer sequence and the monomer-monomer interactions within the functionalization. This work illustrates how copolymer functionalization

and monomer sequence is a new design knob that experimentalists could use to tailor nanoparticle self-assembly.

The paper is organized as follows. In section 3.2 we provide details of our model, the simulation method and analysis techniques. In section 3.3 we present the results showing the effect of varying monomer sequence and chemistry, particle size, grafted chain length and concentration of copolymer grafted particles on the shape, size and structure of the aggregates assembled from the copolymer grafted nanoparticles. We conclude with a discussion on the observed general trends, limitations of this work, some future directions and the impact of this computational work on experimental work in this area.

3.2 Method

3.2.1 Model

We model the system of AB copolymer grafted nanoparticles as hard sphere particles of diameter D each with six grafted symmetric AB copolymers. Each grafted copolymer chain is modeled as a freely jointed chain on a cubic lattice with monomer beads of size d of the order 1 nm, and the first monomer is placed symmetrically 1d away from the six poles of the spherical nanoparticle. The symmetric AB copolymers used in this paper have one of two sequences—alternating or $(A_1B_1)_{N/2}$, and diblock or $(A_{N/2}B_{N/2})$ sequence. In all systems the AB copolymer chains are grafted such that the first monomer grafted to the particle surface is an A monomer. The identities of the second, third and higher monomers in each grafted chain depend on the chosen monomer sequence.

Particle-particle and particle-grafted monomer interactions are maintained as hard-sphere interactions. The monomer-monomer interaction potential, $U_{ij}(r)$, between the i^{th} and j^{th} non-

bonded grafted monomers is described by a square well or square shoulder potential described in equation (1):

$$U_{ij}(r) = \begin{cases} \infty & r < d \\ \varepsilon_{ij} & d < r < \sqrt{2}d \\ 0 & \sqrt{2}d < r \end{cases} \quad (\mathbf{1})$$

where r is the center-center distance between monomer beads, d is the diameter of the bead and $\sqrt{2}d$ is the range of interaction, and ε_{ij} is the strength of interaction. Attractive interactions are characterized by a negative ε_{ij} and repulsive interactions are denoted by a positive ε_{ij}. The ε_{AB}, ε_{AA}, and ε_{BB} we have chosen to mimic varying chemistries are tabulated in Table 3.1.

	ε_{AB} (kT)	ε_{AA} (kT)	ε_{BB} (kT)
(1)	1.0	-0.2	-0.2
(2)	1.0	-0.5	-0.5
(3)	1.0	-1.0	-1.0
(4)	0	0	-0.2
(5)	0	0	-0.5
(6)	0	0	-1.0
(7)	0	-0.2	0
(8)	0	-0.5	0
(9)	0	-1.0	0
(10)	1.0	0	-0.2
(11)	1.0	0	-0.5
(12)	1.0	0	-1.0
(13)	1.0	-0.2	0
(14)	1.0	-0.5	0
(15)	1.0	-1.0	0

Table 3.1 Chemistry of AB copolymer grafted chains. This is also the legend for x-axis values in the figures showing <N>, $\langle R_{g,cluster}^2 \rangle^{1/2}$ and metal fill fraction for various chemistries.

We choose these interactions to isolate the effect of monomer-monomer interactions on the nanoparticle assembly.

3.2.2 Monte Carlo Simulation

We use lattice Monte Carlo simulation to study the assembly of the grafted nanoparticles. In the first step of the simulation we grow the initial configuration by creating a particle sphere in a random position inside the simulation box. We then fix the first monomers of the grafted chains at the predetermined symmetric sites on the sphere followed by placing the second monomer of each grafted chain in one of the five unoccupied lattice sites adjacent to the first monomer of that grafted chain. During this growth process if an i^{th} monomer cannot be grown because all neighboring sites of $(i-1)^{th}$ monomer are occupied by other monomers, then all the monomers are subjected to local moves until a vacancy is created. This is repeated until all the grafted chains are grown to the desired chain length, N_{graft}. This process is followed for all copolymer grafted particles within the simulation box while ensuring no overlaps. After the initial configuration is grown, the simulation proceeds to the initialization stage. The initialization stage helps us avoid any bias that might arise due to the nature of the initial configuration. In the initialization stage the system is subjected to 100,000 Monte Carlo (MC) steps with purely hard-sphere interactions between all beads in the system. An MC time step is defined either as $N_{graft}*N_g$ random monomer moves, where N_{graft} is the grafted copolymer chain length and N_g is the number of grafts (=6 in this study), or one copolymer grafted nanoparticle translate or rotate move. In one monomer move, we randomly pick a monomer (with the exception of the first bead that is fixed) on a randomly picked grafted chain of a randomly selected nanoparticle, and then move that monomer using a randomly chosen move—"crankshaft", "kink" and "end" (for last bead only). In one single copolymer grafted nanoparticle move, one copolymer grafted nanoparticle is randomly chosen and the particle along with its constituent chains is translated or rotated. The moves are accepted or rejected based on the Metropolis algorithm;[70] since interaction potentials are not

turned on until the equilibration stage, all initialization-stage moves are made under athermal conditions and accepted as long as no overlaps occur during the move.

The initialization stage is followed by the equilibration stage. In the equilibration stage the system goes through 20 million MC steps with a temperature annealing schedule[71] going from dimensionless temperature $T_{initial}$=3 to T_{final}=1 with a temperature decrement of 0.9 at every i^{th} stage ($T_i = T_{i-1}$x0.9), and 3 million MC steps per temperature stage. This annealing schedule was chosen after rigorous testing to ensure equilibrium is reached at each temperature stage, and the resulting configurations at temperature are independent of small variations in the annealing schedule (e.g. 3million or 4million MC steps per stage). The moves during the equilibration stage include the monomer moves (47.5%) and grafted particle moves (47.5%) described above and cluster moves (5%). A cluster move is defined as a move of a collection of copolymer grafted nanoparticles, where every grafted particle is making at least one monomer contact with a monomer of another grafted particle in the cluster. During a cluster move we translate randomly picked clusters and accept the move only when the cluster move does not lead to an overlap or formation of a new cluster.[72] If there are no clusters in the configuration the chosen cluster move is rejected. We collect data on the thermodynamic property of interest over 10,000 MC steps and calculate the block averages for every 100,000 MC steps. Once the system has reached T_{final}=1 and an equilibrium—when 40 consecutive block averages of energy are within 10% of each other—we collect the ensemble average of the block averages of the equilibrated system. For each system we repeat 10 trials of simulation where the 10 trials are marked with different random number seeds used in the growth of the initial configuration. We obtain error bars for every data point presented in the results section from the ensemble averages collected from 10 such simulations.

3.2.3 Analysis

To characterize the shape, size and structure of the assembled clusters we calculate the ensemble average of the following parameters. To quantify the equilibrium conformations of the grafted chains we calculate the average radius of gyration of the grafted copolymer, R_g^2:

$$R_g^2 = \frac{1}{M}\sum_{j=1}^{M}\sum_{i=1}^{N_j}\frac{\left(x_{i,j} - x_{cm,j}\right)^2 + \left(y_{i,j} - y_{cm,j}\right)^2 + \left(z_{i,j} - z_{cm,j}\right)^2}{N_j} \quad (2)$$

where M is the number of grafted chains, i is the monomer number, N_j is the length of the j^{th} grafted copolymer chain (=N_{graft}), and $x_{cm,j}$, $y_{cm,j}$ and $z_{cm,j}$ are the coordinates of the center of mass of the j^{th} grafted chain. The grafted chain radius of gyration values presented in Sec. III are the square root of the ensemble average, $<R_g^2>^{1/2}$. We also calculate the radius of gyration of the cluster, $R_{g,cluster}^2$, analogous to equation (2) with M being the number of clusters at the time step when the $R_{g,cluster}^2$ is calculated, i is the nanoparticle index in the j^{th} cluster, N_j is the number of nanoparticles in the j^{th} cluster and $x_{cm,j}$, $y_{cm,j}$ and $z_{cm,j}$ are the coordinates of the center of mass of the j^{th} cluster.

For the design of metamaterials or negative index of refraction materials it is important to obtain simultaneous negative permittivity and negative permeability, which are in turn dictated by the metal fill fractions in the nanoparticle cluster.[67, 73] Therefore we use the $(R_{g,cluster}^2)^{1/2}$ to calculate the metal fill fraction in each cluster at that time step:

$$\text{Metal Fill Fraction} = \frac{(\bar{N})\cdot\frac{4}{3}\pi\left(\frac{D}{2}\right)^3}{\frac{4}{3}\pi\left(\left(R_{g,cluster}^2\right)^{\frac{1}{2}} + \frac{D}{2}\right)^3} \quad (3)$$

where $\overline{N}$ is the average number of nanoparticles in the clusters at that time step and D/2 is the nanoparticle radius. To quantify the structure within the cluster we also calculate the distribution of coordination number, Z, for the nanoparticles within each cluster during the simulation. This distribution of Z within a cluster characterizes the structure and isotropy within each cluster. For example, a system with clusters that show peak frequency of low Z suggests that either a) the clusters are small and thus the nanoparticles within the cluster only have few neighbors or b) the clusters are large and anisotropic with the constituent nanoparticles having neighbors only in certain directions. One can interpret unambiguously which of the above is true by also studying the size of the clusters, quantified by the ensemble average number of nanoparticles in the clusters, <N>. While the ensemble average number of nanoparticles in the clusters,<N>, is calculated only when clusters are formed and ignores the single grafted particles not participating in clusters, the coordination number distribution takes into account all grafted particles in the system whether or not they are part of a cluster.

In addition to the above quantitative characterization we also visualize the assembly of the copolymer grafted nanoparticles by collecting spatial coordinates of all components in the systems. Some of these simulation snapshots are shown in Sec. III and in the supplementary file.

3.2.4 Parameters

We study two sequences in the grafted polymers— alternating or $(A_1B_1)_{Ngraft/2}$ and diblock or $(A_{Ngraft/2}B_{Ngraft/2})$ sequence. We study the effect of varying monomer chemistries by changing the like-monomer (A-A and/or B-B) interaction (ε_{AA} and ε_{BB}) and unlike monomer (A-B) (ε_{AB}) interaction strengths as shown in Table 3.1. We also vary the particle diameter, D/d=2, 4 and 12; since the monomer diameter, d, is ~1 nm these particle diameters correspond to ~2 nm, 4 nm and

12 nm, respectively. We keep the number of grafted chains fixed at six chains. Therefore by changing particle diameter, D=2, 4 and 12 nm, we not only understand the effect of changing curvature (1/2, 1/4 and 1/12) but also changing surface grafting density (0.48, 0.12 and 0.01 chains/nm^2), albeit in a coupled fashion. We study two dilute concentrations of copolymer grafted nanoparticles in the system c=0.0001 particles/nm^3 and 0.0002 particles/nm^3, by simulating 10 and 20 grafted particles, respectively, in a simulation box size of 100x100x100 nm^3.

3.3 Results

3.3.1 Effect of monomer sequence for varying chemistries

The results plotted in Figure 3.1 are for a solution containing 10 copolymer grafted particles in a 100x100x100 nm^3 simulation box, with particles of diameter D=4nm and six grafts of 24 monomers arranged in either an alternating or diblock sequence.

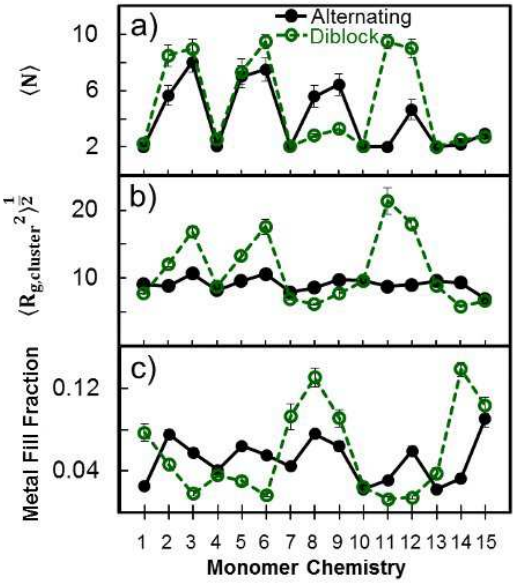

Figure 3.1 (a) Ensemble average number of particles in clusters <N>, (b) radius of gyration of the clusters, $\langle R_{g,cluster}^2 \rangle^{1/2}$ and (c) metal fill fraction within the clusters formed from the assembly of 10 copolymer grafted particles (in a 100x100x100 nm^3 simulation box) with particle diameter D=4nm and six grafts of 24 monomers arranged in either an alternating (black solid lines) or diblock sequence (green dashed lines). X-axis denotes the monomer chemistries and the values correspond to the rows in Table 3.1.

We have systematically studied the effect of varying chemistries (shown in Table 3.1 and indicated in the x-axis of Figure 3.1) to elucidate how increasing strength of like-monomer (A-A and/or B-B) attraction affects the cluster formation and cluster characteristics, in the presence of either a relatively strong or a negligible unlike-monomer (A-B) repulsion.

We first discuss results for monomer chemistries where the strength of A-A and B-B attraction strength are similar, varying from 0.2 kT – 1 kT, in the presence of a relatively strong A-B repulsion strength (1 kT) (x-axis values 1-3 correspond to row 1-3 of Table 3.1). As both pairs of like-monomer attractions increase, for alternating (black solid) and diblock (green dashed) sequences the copolymer functionalized nanoparticles assemble into clusters of increasing size, as seen from increasing <N> and increasing $<R_{g,cluster}^2>^{1/2}$ in Figure 3.1a and Figure 3.1b for x-axis values 1-3. An increase in cluster size with increasing like-monomer attraction is expected because as the like-monomer attraction strength increases the copolymer grafted nanoparticles assemble together more readily to make enthalpically favorable attractive monomer contacts. At weak attraction strength (0.2 kT) both alternating- and diblock- grafted particles rarely form clusters as seen from the peak frequency for Z=0 in Figure 3.2a and when they do form clusters they form dimers as seen from <N>~2 (Figure 3.1). This is because the A-A and B-B attraction strength is unable to overcome A-B repulsion and also unable to compensate for the entropic loss from bringing these grafted particles together. With increasing like-monomer (A-A and B-B) attraction strength, the attractive interaction between like-monomers is able to overcome the strong repulsive interactions between the unlike monomers (A-B) and overcome the entropic loss from assembly.

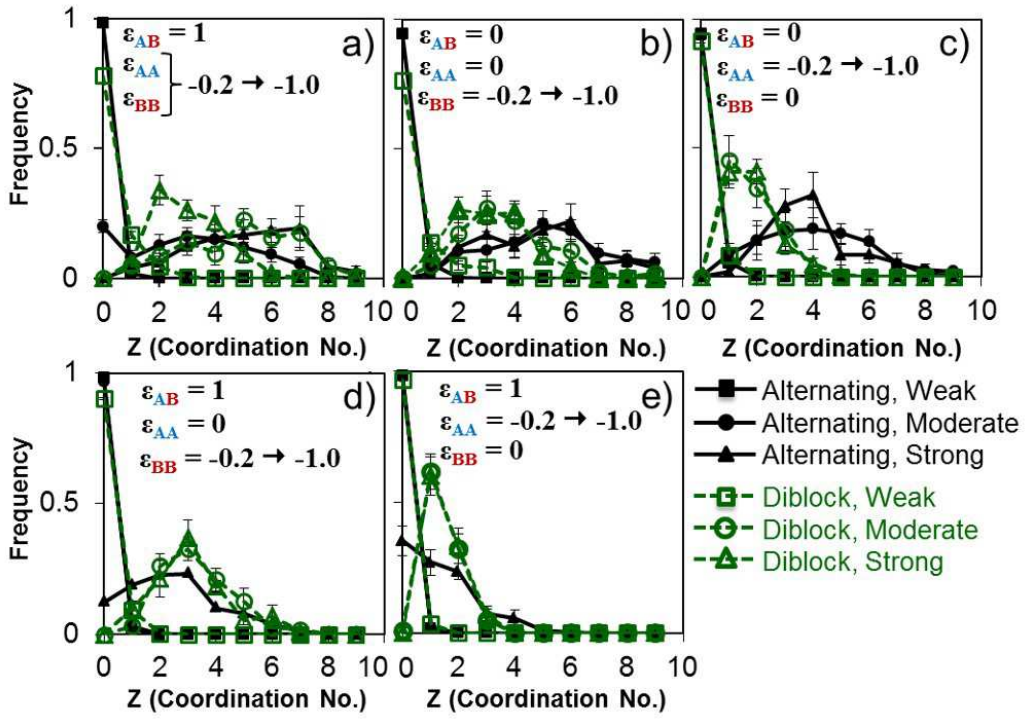

Figure 3.2 Histogram of frequency of coordination numbers, Z, within clusters formed from the assembly of 10 copolymer grafted particles (in a 100x100x100 nm^3 simulation box) with particle diameter D=4nm and six grafts of 24 monomers arranged in either an alternating (black solid lines) or diblock sequence (green dashed lines) with varying monomer chemistries corresponding to a) rows 1-3, b) rows 4-6, c) rows 7-9, d) rows 10-12, and e) rows 13-15 in Table 3.1. The symbols for weak, moderate and strong attraction strength are square, circle and triangle, respectively.

Therefore at moderate to high attraction strengths (0.5 and 1 kT), we observe larger clusters both for diblock and alternating grafted particles. However the clusters formed with diblock copolymer grafts are larger than those formed with alternating copolymer grafts, as evident from clusters of diblock copolymer grafted nanoparticles having larger <N> and/or larger $<R_{g,cluster}^2>^{1/2}$ for similar <N> than those for alternating copolymer grafted particles (Figure 3.1a and Figure 3.1b). This is because in the alternating case the frustrated alternating A monomer-B monomer placement forces the chains to pack more compactly to bring A-A and B-B attractive monomers together. In contrast, as the diblock sequence topologically places A and B monomers

separately in two blocks, the chain does not have to be compact and is a little more stretched than alternating copolymers to avoid unfavorable A-B contacts and yet make attractive A-A and B-B contacts. This is also confirmed in Supplementary Table S.1 which tabulates the radius of gyration of the grafted chains. The $<R_{g,chain}^2>^{1/2}$ values (rows 2 and 3) for alternating copolymer is lower than the corresponding values of the diblock copolymer. Clearly, for a constant chemistry the monomer sequence affects the grafted chain conformations, and in turn the size of the assembled cluster. Next we discuss how the sequence affects the *shape* of the cluster and *structure* within the cluster.

For *alternating* sequence, as strength of like-monomer attraction increases (Figure 3.2a black solid lines), the coordination number Z within each cluster shifts to higher values. An increase in <N> (Figure 3.1a) and a corresponding shift in the coordination numbers to higher values suggest that the clusters are becoming larger and isotropic as like-monomer attraction increases. This is confirmed by the simulation snapshots shown in Figure 3.3 (top row). However, the metal fill fraction in Figure 3.1c does not increase monotonically for x-axis values 1-3 (black solid); the fill fraction is the highest for moderate strength (0.5 kT). We conjecture that at larger like-monomer attractions (1 kT), monomers along the alternating copolymer grafts on different particles are strongly pulled together and aggregate within the cluster leading to increased spacing between nanoparticles at 1 kT than at 0.5 kT thus leading to lower metal fill fraction for 1 kT than 0.5 kT. In contrast to the alternating sequence, for *diblock* sequence, as strength of like monomer attraction increases from 0.5 kT to 1 kT the Z shifts to smaller values (Figure 3.2a green dashed lines). Since the <N> is approximately the same for both 0.5 kT and 1 kT in Figure 3.1a, we believe that at 1 kT attraction the clusters are anisotropic while clusters seen at 0.5 kT are isotropic.

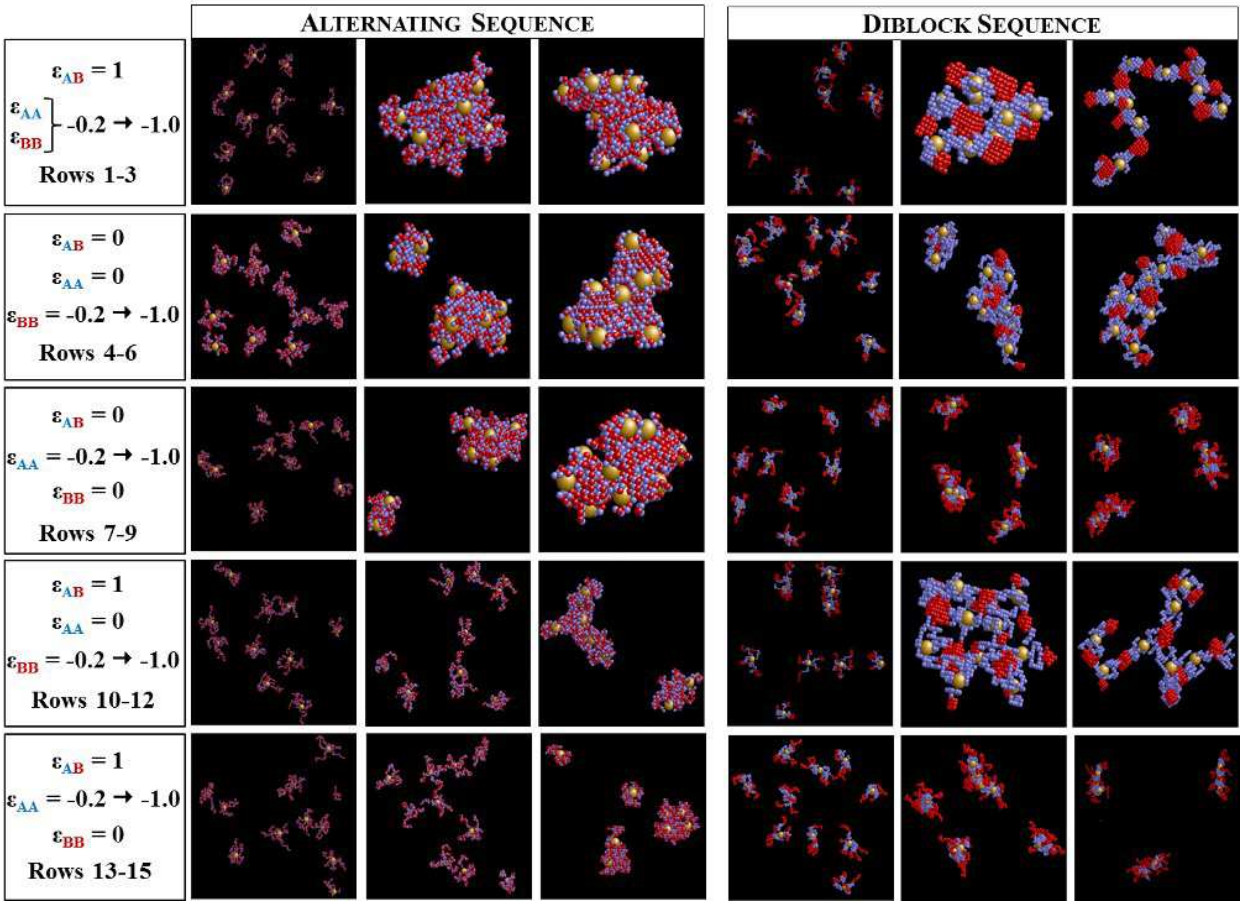

Figure 3.3 Simulation snapshot from one of the trials showing representative equilibrium clusters formed from the assembly of 10 copolymer grafted particles (in a 100x100x100 nm^3 simulation box) with particle diameter D=4 nm and six grafts of 24 monomers arranged in either an alternating or diblock sequence. The rows in the figure, as labeled, correspond to the varying monomer chemistries in Table 3.1.

This is confirmed from the anisotropic cluster shapes for 1 kT monomer attraction in Figure 3.3 (top row last image). We note that for these anisotropic cluster shapes the metal fill fraction is inaccurate as the metal fill fraction is calculated assuming a spherical cluster shape, which is not true for these anisotropic clusters. To ensure these highly anisotropic structures are indeed equilibrium structures we studied from multiple *independent* trials both the simulation snapshots and cluster characteristics data. In supplementary figure S.3.1 we show five of the ten independent trials for the chemistries that lead to the most anisotropic structures; the similarity in

structures for all five trials of the same system confirms that the structures seen in Figure 3.3 are equilibrium structures. Additionally we note that each of these trials starts at a very high temperature where all functionalized nanoparticles are well dispersed and the system is cooled slowly through gradual temperature decrements (see Sec. IIB) further ensuring that the assembled clusters are not kinetically trapped metastable structures.

So far we have examined a system where both pairs of like-monomer, A-A and B-B, attractions are equal in strength, and there is significant A-B repulsion (rows 1-3 in Table 3.1). Next we mimic a chemistry where *one pair of like-monomer* (A-A or B-B) attraction dominates and the other like-monomer attraction is negligible, in the presence of a relatively negligible or strong unlike monomer-monomer (A-B) repulsion.

When B-B monomers attraction is much stronger than A-A monomers attractions and A-B repulsion (rows 4-6 in Table 3.1), as B-B monomer attraction strength increases, for both sequences the cluster sizes increase as seen from increasing <N> and increasing $<R_{g,cluster}^2>^{1/2}$ in Figure 3.1a and Figure 3.1b for x-axis values 4-6. At weak B-B attractions (0.2 kT) for both sequences the grafted particles *rarely form clusters* (Z peaks at 0 in Figure 3.2b) and when they do form clusters they form dimers with a high $<R_{g,cluster}^2>^{1/2}$ suggesting loosely held together dimers. At moderate B-B attractions (0.5 kT) for both sequences the <N> is approximately the same (x-axis value 5 in Figure 3.1a) but the diblock copolymer grafted nanoparticles have a larger $<R_{g,cluster}^2>^{1/2}$ (Figure 3.1b) and lower metal fill fraction (Figure 3.1c) than the alternating copolymer grafted particles. This is because while both alternating and diblock grafted particles assemble by bringing B monomers on various particles together, the diblock sequence has the B-monomers conveniently placed as the outer block in the graft which facilitates assembly by

bringing attractive B-monomers together without much loss of conformational entropy of the A-block. On the other hand in the alternating sequence when the B-monomers are brought together the attached adjacent A monomers are also dragged along leading to tighter clusters. This can be confirmed by the simulation snapshots in Figure 3.3 (second row) showing loosely held together clusters for diblock copolymer grafted particles versus alternating copolymer grafted particles. Additionally, the ensemble average $<R_{g,chain}^2>^{1/2}$ for diblock copolymer chains is higher than alternating copolymer chains shown in Supplementary Table S.1. (rows 4-6 for alternating and diblock). The coordination number distribution for 0.5 kT for alternating and diblock cases (Figure 3.2b) show a shift to slightly higher values for alternating compared to diblock, suggesting more isotropic clusters for alternating sequence than diblock sequence. At stronger B-B attractions (1kT) the trends seen at 0.5 kT continue but the sequence effects are magnified, which is most likely because of the reduced loss of conformational entropy seen in case of diblock sequence as compared to alternating sequence.

When A-A monomers attraction is much stronger than the B-B attraction and A-B repulsion (rows 7-9 in Table 3.1), at weak A-A attractive strengths (0.2kT) both the alternating and diblock form dimers evident from $<N>\sim2$ (Figure 3.1a for x-axis values 7). However, at moderate (0.5 kT) and strong (1 kT) A-A attractions the alternating case leads to clusters with higher $<N>$ and $<R_{g,cluster}^2>^{1/2}$ but lower metal fill fractions than the corresponding diblock cases. This is opposite to the trends seen when B-B monomers are stronger than A-A and A-B interactions (rows 4-6). This is because in the diblock grafted particles since the A-block is closer to the particle surface it is less easily accessible for making contacts with A-blocks on another particle, leading to lower $<N>$, and when it does form inter-particle A-A contacts the particles have to come closer together within the cluster causing higher metal fill fractions. This

means when A-A monomers are attractive, and A-B repulsion and B-B attraction are negligible, diblock copolymer grafted particles lead to tightly packed smaller clusters with some anisotropy, also seen from Z shifted to lower values than the Z distribution of the alternating copolymer grafted particles (Figure 3.2c). This also leads us to conclude that for diblock copolymer grafted particles there are drastic differences between the cluster characteristics when A-A attraction (attractive inner block) dominates as compared to when B-B attraction (attractive outer block) dominates. In contrast, for the alternating case due to the frustrated alternating A monomer-B monomer sequence there is no significant effect of type (A-A or B-B) like-monomer attraction. Simulation snapshots in Figure 3.3 also confirm all of the above trends.

Next we discuss the effect of increasing the strength of one pair of like-monomer attractions in the presence of *a significant A-B repulsion*. When the B-B attraction increases in the presence of strong A-B repulsion (1 kT) and negligible A-A interactions (rows 10-12 in Table 3.1), for alternating sequence the presence of significant A-B repulsion reduces the cluster size, evident from a lower <N> and lower $<R_{g,cluster}^2>^{1/2}$ (Figure 3.1a and Figure 3.1b, x-axis values 10 -12) than those seen with negligible A-B repulsion (x-axis values 4-6). The peaks at Z=0 in Figure 3.2d also suggest that for B-B attractions strengths ≤ 0.5 kT the strong A-B repulsion (1 kT) dominates, favoring the dispersion of alternating copolymer grafted nanoparticles. In contrast, for the diblock sequence, since the diblock sequence separates the A and B monomers topologically, the effect of A-B repulsion on the resulting nanoparticle assembly is minimal. This is confirmed by similar values of <N> for diblock sequence (Figure 3.1a x-axis values 10-12 and 4-6) and similar Z- distribution (Figure 3.2d and Figure 3.2b) both in the presence of strong A-B repulsion and negligible A-B repulsion. The only effect that the strong A-B repulsion has on the assembly of diblock copolymer grafted particles is that it stretches grafted chains, evident from

higher $<R_{g,\,chain}^2>^{1/2}$ in Supplementary Table S.1. in the presence of strong A-B repulsion (rows 10-12) as compared to negligible A-B repulsion (rows 4-6); the stretching of the grafted chains increases the spacing between the nanoparticles in the cluster resulting in lower metal fill fraction and slightly higher $<R_{g,\,cluster}^2>^{1/2}$ for interaction parameters 10-12 as compared to 4-6.

When the A-A attraction increases in the presence of strong A-B repulsion (1kT) and negligible B-B interactions (rows 13-15 in Table 3.1) both sequences form small clusters, evident from low <N> and low $<R_{g,cluster}^2>^{1/2}$. While the propensity to form clusters is low for both sequences, the reasoning behind why that is so is completely different for both sequences. The reasoning for alternating copolymer is similar to that discussed for rows 10-12, and for diblock copolymer is similar to that discussed for rows 7-9.

As seen in most of the cases so far, much of the trends for varying monomer sequence and monomer chemistry can be explained on how the placement of monomers (sequence) facilitates bringing attractive monomer pairs together while keeping the repulsive monomer pairs apart, and in turn how that balances the enthalpic gain from favorable monomer contacts and conformational entropic loss. Since the alternating sequence has A and B monomers placed adjacent to each other within each of the grafted chains, we see similar trends whether the A-A interactions are attractive or the B-B interactions are attractive; in both cases the presence of strong A-B repulsion drastically reduces the assembly as compared to negligible A-B repulsion. On the other hand, since the diblock sequence separates the two monomers into blocks the trends are similar both in the presence of strong A-B repulsion and negligible A-B repulsion but there are large differences in assembled structures when the inner block (A monomers) is attractive and outer block (B monomers) is attractive. Additionally, the anisotropy in the cluster shapes is

similar in the presence of strong and negligible A-B repulsion (Figure 3.3 diblock column fifth and third row, respectively), suggesting that the like-monomer attraction strength, and not the A-B repulsion, dictates the shape of the cluster formed with diblock functionalization.

While the above results are for six grafts of length 24 monomers on particle size of 4nm, to understand the effect of changing particle size (and thus the curvature and grafting density) on the assembly of alternating and diblock copolymer grafted particles, we present the results for particle diameters D=2 nm and D=12 nm in the next section.

3.3.2 Effect of particle diameter

In Figure 3.4 we plot the <N>, $<R_{g,cluster}^2>$ and metal fill fraction as a function of interaction parameters (x-axis values correspond to the row numbers in Table 3.1) for alternating (left column) and diblock (right column) copolymer grafted nanoparticles for *varying particles sizes* D=2 nm (black squares solid line), 4 nm (violet circles dashed line) and 12 nm (orange diamonds dotted line). We discuss alternating sequence first followed by the diblock sequence.

For alternating sequence when the monomer interactions are such that both A-A and B-B attractions are equal in the presence of strong A-B repulsion (x-axis values 1-3 in Figure 3.4a) the D=12 nm particles assemble only when the like monomer attraction strength is strong (1 kT), while the D=2 nm and D=4 nm particles can assemble even for moderate attraction strengths (0.5 kT). To understand the basis for these trends we first explain how particle size and graft chain length affect the chain conformations in a *single* polymer grafted particle.[65]

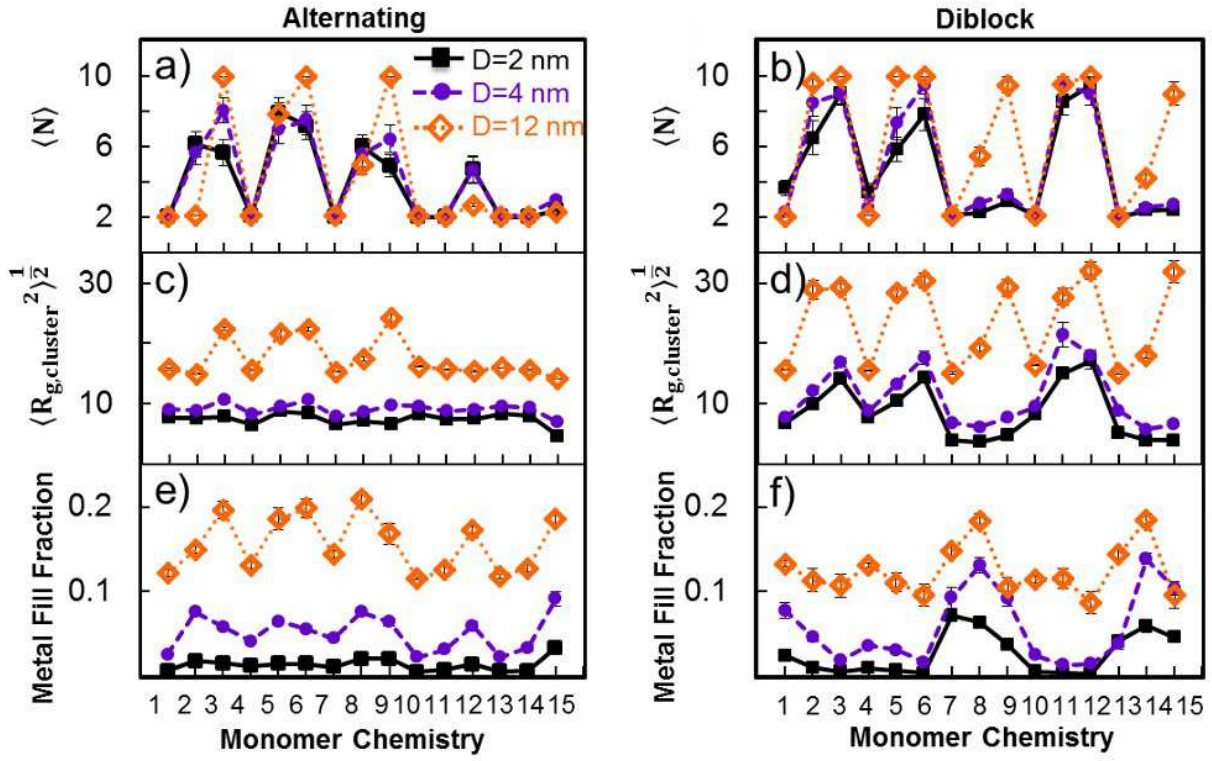

Figure 3.4 (a) Ensemble average number of particles in clusters <N>, (b) radius of gyration of the clusters, $\langle R_{g,cluster}^2 \rangle^{1/2}$ and (c) metal fill fraction within the clusters formed from the assembly of 10 copolymer grafted particles in a 100x100x100 nm^3 simulation box with six grafts of 24 monomers arranged in either an alternating (left panel) or diblock sequence (right panel) and particle diameters D=2nm (solid black square), 4nm (dashed purple circles) and 12nm (dotted orange diamonds). X-axis denotes the monomer chemistries and the values correspond to the rows in Table 3.1.

For alternating sequence when the monomer interactions are such that both A-A and B-B attractions are equal in the presence of strong A-B repulsion (x-axis values 1-3 in Figure 3.4a) the D=12 nm particles assemble only when the like monomer attraction strength is strong (1 kT), while the D=2 nm and D=4 nm particles can assemble even for moderate attraction strengths (0.5 kT). To understand the basis for these trends we first explain how particle size and graft chain length affect the chain conformations in a *single* polymer grafted particle.[65] In the case of single copolymer grafted particle with low grafting density (not a grafted polymer brush) as the N_{graft}/D decreases the attractive monomers on the same graft aggregate together (intra-grafted chain

contacts) much more than between grafts on the same particle (inter-grafted chain contacts) because the spacing between the grafts is too large making it either impossible due to far placement or entropically unfavorable for inter-grafted chain contacts to occur. In case of multiple grafted particles in addition to the intra-grafted chain and inter-grafted chain contacts found in the single grafted particle, there are *inter-grafted particle contacts*. For D=12nm and N_{graft} =24 the inter-grafted chain contacts within a grafted particle are less likely as the grafts are not long enough or the particle is too big for the graft to make contacts with another graft on the same particle (as seen in simulation snapshots in Supplementary figure S.3.2), and instead favorable monomer contacts come from either inter-grafted *particle* contacts inducing assembly and/or from *intra*-grafted *chain* contacts in the same particle. For inter-grafted particle contacts to happen, the entropic loss from chain stretching during inter-grafted particle contacts has to be overcome by the enthalpic gain from the favorable inter-grafted particle monomer contacts; for D=12 and N_{graft}=24 this only happens when the like-monomer attraction strength is strong (1 kT).

When only one-pair of like-monomers (A-A or B-B) are attractive with *negligible A-B repulsion* (x-axis values 4-9 in Figure 3.4a), all particle diameters assemble at moderate like-monomer attraction strength (0.5 kT). It should be noted that although <N> is approximately the same for all three particle sizes the $<R_{g,cluster}^2>^{1/2}$ is higher for clusters formed from larger particles because of the larger particle diameter involved in the $<R_{g,cluster}^2>^{1/2}$ calculation. When one pair of like-monomers is attractive in the presence of *significant A-B repulsion* (x-axis values 10-15 in Figure 3.4a) alternating sequence does not favor cluster formation for most particle sizes because the A-B repulsive interactions and conformational entropic loss cannot be overcome by the favorable attractive contacts from a single pair of like monomers.

Supplementary figures S.3.3 and S.3.4 show the Z histograms for D=2 nm and D=12 nm alternating grafted particles (black solid lines). We note that the coordination numbers within the clusters exhibit surprisingly similar trends with increasing strength of attraction and between the various set of interactions.

For diblock sequence at almost all chemistries as the particle size D increases <N> increases. Additionally, for all particle diameters the cluster characteristics are dominated by the strength and type (A-A or B-B) of like-monomer interaction and the role of A-B repulsion (strong or negligible) is minimal. There are also clear differences between the three particle sizes. While for D=2 nm and 4 nm particles the cluster size <N> depends strongly on the type (inner or outer block) of like-monomer attraction at all attraction strengths, for D=12 the effect of type (A-A or B-B) like monomer attraction on <N> is not as drastic. The reasoning behind this trend is based on how the particle size and graft length affect the balance of enthalpic gain and entropic losses coming from inter-grafted particle contacts and/or inter- and intra- grafted chain contacts in the same grafted particles. For D=12 nm, as stated before, the particle is so large that the grafts in the same particle are unable to make inter-grafted chain contacts within the same particle irrespective of type of attraction; thus one of the driving forces behind the differences observed between A-A (inner block) or B-B (outer block) attractions is eliminated. Therefore in both cases (A-A or B-B attraction) the particles can only form inter-grafted particle contacts, which is slightly easier to form when outer block (B-B) attraction dominates. Supplementary figures S.3.3 and S.3.4 show the Z histograms for D=2 nm and D=12 nm diblock grafted particles (green dashed lines), respectively. We note that the coordination numbers within the clusters exhibit surprisingly similar trends for various particle sizes with increasing strength of attraction and between the various set of interactions.

Interestingly, for diblock copolymer grafted particles we observe a variety of highly anisotropic cluster shapes for D=12 nm (Figure 3.5 top and middle rows), as seen for D=4 nm (Figure 3.3 and also Figure 3.5 bottom row).

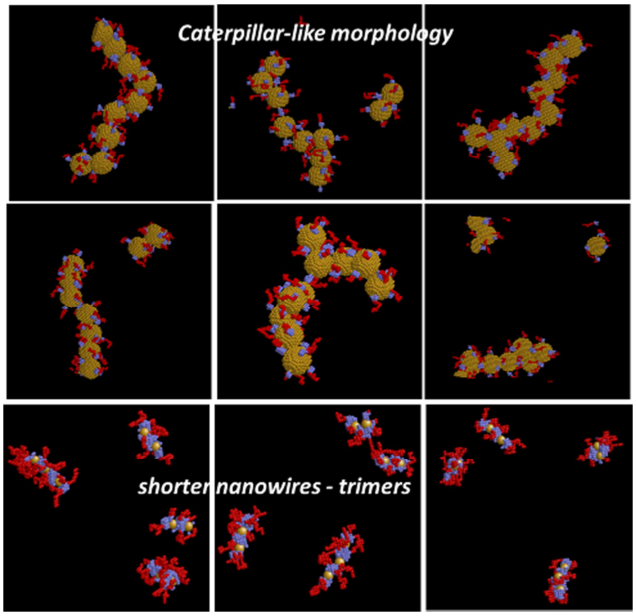

Figure 3.5 Simulation snapshots from three trials showing clusters formed from the assembly of 10 copolymer grafted particles (in a 100x100x100 nm^3 simulation box) with particles diameter D=12nm (top and middle) and D=4nm (bottom) with six grafts of 24 monomers arranged in diblock sequence. The monomer chemistries correspond to row 15 (top), row 9 (middle) and row 15 (bottom).

Figure 3.5 top and middle rows show snapshots from three trials (out of the 10 trials) of D=12 nm systems that exhibit one such anisotropic cluster shape that we characterize as "caterpillar-like" or nanowires. Supplementary figure S.3.2 shows the morphologies of cluster assembled with D=12 nm grafted particles for all chemistries. These anisotropic morphologies shown here in Figure 3.5 top and middle row are only seen when the inner A block is strongly attractive either in the presence of negligible or strong A-B repulsion (row 15 and 9 in Table 3.1). These anisotropic structures are of tremendous interest because these string-like structures are useful

for designing metamaterials.[67, 73-75] This anisotropy is also seen for the same chemistry for D=4nm particles (Figure 3.5 bottom row), but the length of the strings or "caterpillars" is much smaller for D=4 than D=12, and restricted mostly to trimers. In contrast, when the outer B block is attractive we do not see these anisotropic structures and observe more isotropic web-like cluster formation. These isotropic structures are not surprising considering that for large particles of size D=12 with only six grafts of length 24 monomers and "sticky" outer blocks, we are essentially designing patchy particles. Past theoretical and computational work by Sciortino and co-workers and Glotzer and co-workers on patchy particles with sticky interactions has characterized both their equilibrium nanostructures[76] and provided some valuable understanding on formation of "stable equilibrium gels".[77] In contrast to this past work, where the authors have assigned patchy spots on the particle surface to impart directionality in interactions and assembly, we have shown here how an experimentalist could engineer some patchy particles using copolymer functionalization.

3.3.3 Effect of length of graft

We discuss next how the assembly of copolymer grafted particles is affected with varying graft length N_{graft}. In Figure 3.6 we plot the $<N>$, $<R_{g\ cluster}^2>^{1/2}$ and metal fill fraction as a function of interaction parameters (x-axis values correspond to the row numbers in Table 3.1) for 10 alternating (left column) and diblock (right column) copolymer grafted nanoparticles of diameters D=4 nm with grafts of length N_{graft}=48 (black squares solid line), 24 (violet circles dashed line) and 8 (orange diamonds dotted line).

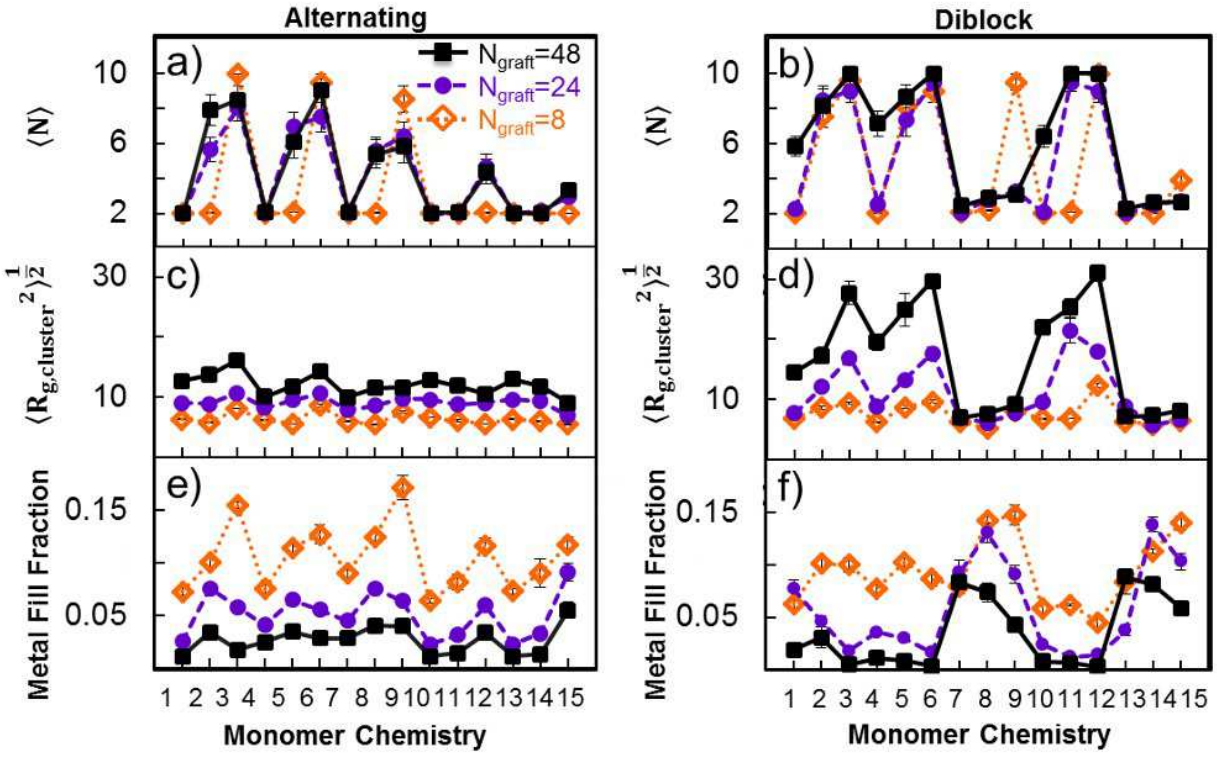

Figure 3.6 (a) Ensemble average number of particles in clusters <N>, (b) radius of gyration of the clusters, $\langle R_{g,cluster}^2 \rangle^{1/2}$ and (c) metal fill fraction within the clusters formed from the assembly of 10 copolymer grafted particles (in a 100x100x100 nm^3 simulation box) with six grafts of 48 (solid black square), 24 (dashed purple circles) and 8 (dotted orange diamonds) monomers arranged in either an alternating (left panel) or diblock sequence (right panel) on particle diameters D=4 nm. X-axis denotes the monomer chemistries and the values correspond to the rows in Table 3.1.

For alternating grafted particles, as the grafted chain length N_{graft} increases, at constant D and monomer interactions, the number of particles in a cluster <N> increases and the corresponding size of the cluster $\langle R_{g,cluster}^2 \rangle^{1/2}$ also increases. This is expected because for longer grafts it is easier to make enthalpically favorable contacts with the long grafts on other grafted particles. As expected for all interactions the metal fill fraction decreases with increasing N_{graft}; this is because the number and volume of monomers that are placed between the particles increases with increasing N_{graft} thus reducing the metal fill fraction in a cluster. For diblock grafted particles, we see a more rich behavior with increasing N_{graft} at constant D, with the trends

being dependent strongly on which block of the diblock copolymer is attractive. When the outer block is more attractive than inner block (x-axis values 4-6 and 10-12), the longer grafts form clusters much more readily than the shorter grafts even at low attraction strength (0.2 kT). This is because longer grafts have a longer inner block that presents the longer outer block more readily to outer blocks on other grafted particles. When the inner block is more attractive than the outer block (x-axis values 7-9 and 13-15), either the shorter grafts form clusters more readily than the longer grafts (e.g. x-axis values 9 and 15) or all lengths have equally low propensity to form clusters. When the inner block is attractive, the particle cores have to be closer together to bring attractive monomers together, which in turn can confine the outer blocks and lead to loss of conformational entropy. Therefore only the shortest graft at the highest attraction strength is capable of gaining favorable enthalpy that can overcome the entropy loss of the confined outer B block. Longer grafts lose more conformational entropy and no amount of attractive monomer contacts can overcome the entropic loss. Irrespective of the interaction set, the size of the cluster $<R_{gcluster}^2>^{1/2}$ always increases with increasing N_{graft} due to larger number of monomers in a cluster for the longer grafts. Metal fill fractions also tend to be the highest for the smaller graft because of less number and thereby less volume of monomers between the metal particle cores. Simulation snapshots of clusters formed by D=4 nm particles with N_{graft} =24 and 48 at varying chemistries are shown in supplementary figure S.3.5.

The question we pose next is the following. Could the trends in <N> and Z histogram as a function of monomer interactions be similar whether we increase N_{graft} at constant D or decrease D at constant N_{graft}? To answer this, we compare first the trends in <N> with increasing N_{graft}/D in Figure 3.6 to that in Figure 3.4. For alternating copolymer grafted particles as N_{graft} increases from 8 to 48 for D=4 nm (Figure 3.6a), we observe qualitatively similar trends in <N>,

average number of particles in the clusters, as that seen for decreasing D from 12 to 2 nm for constant N_{graft} =24 (Figure 3.4a). The only minor difference is that for x-axis values of 3 and 6, when N_{graft} =24 the D=2 nm case (highest N_{graft}/D in Figure 3.4a) has a lower <N> than D=4 and 12 nm, while when D=4 nm the N_{graft}=48 case (highest N_{graft}/D in Figure 3.6a) has <N> comparable to N_{graft} =8. We show the coordination number distribution for alternating copolymer grafted particles in supplementary figure S.3.6 with the top panel in Figure S.3.6 showing decreasing D at constant N_{graft} and the bottom panel showing increasing N_{graft} at constant D. There are only minor differences in the trends in structure with varying chemistries whether we increase D at constant N_{graft} or decrease N_{graft} for constant D. For diblock copolymer grafted particles we see similarity in results whether N_{graft} increases from 8 to 48 for constant D=4 nm (Figure 3.6b), or D decreases from 12 to 2 for constant N_{graft} =24 (Figure 3.4b). The only noticeable difference is that when B-B interaction is weak (0.2 kT) and either equal to A-A attraction or much stronger than A-A (x-axis values 1, 4 and 10) we see that N_{graft}=48, D=4 nm (highest N_{graft}/D in Figure 3.6b) forms cluster much more easily than the corresponding N_{graft}=24, D=2 nm system (highest N_{graft}/D in Figure 3.4b). The metal fill fractions and Z distributions (supplementary figure S.3.7) are remarkably same as N_{graft} increases from 8 to 48 for D=4 nm or as D decreases from 12 to 2 nm at constant N_{graft} =24. These results suggest that if the monomer sequence and monomer chemistry is fixed, the ratio of N_{graft}/D balances the entropic and enthalpic contributions that govern the cluster formation, shape, size and structure.

3.3.4 Effect of changing number of grafted particles at dilute concentration

In this section we present the results for cluster formation for 20 grafted particles of size D=2, 4 and 12 nm with graft length of 24 monomers placed in a 100x100x100 nm^3 volume. In Figure 3.7 we plot the <N>, $<R_{g\ cluster}^2>^{1/2}$ and metal fill fraction as a function of interaction parameters (x-

axis values correspond to the row numbers in Table 3.1) for alternating (left column) and diblock (right column) copolymer grafted nanoparticles of diameters D=2 (black squares solid line), 4 (violet circles dashed line) and 12 (orange diamonds dotted line).

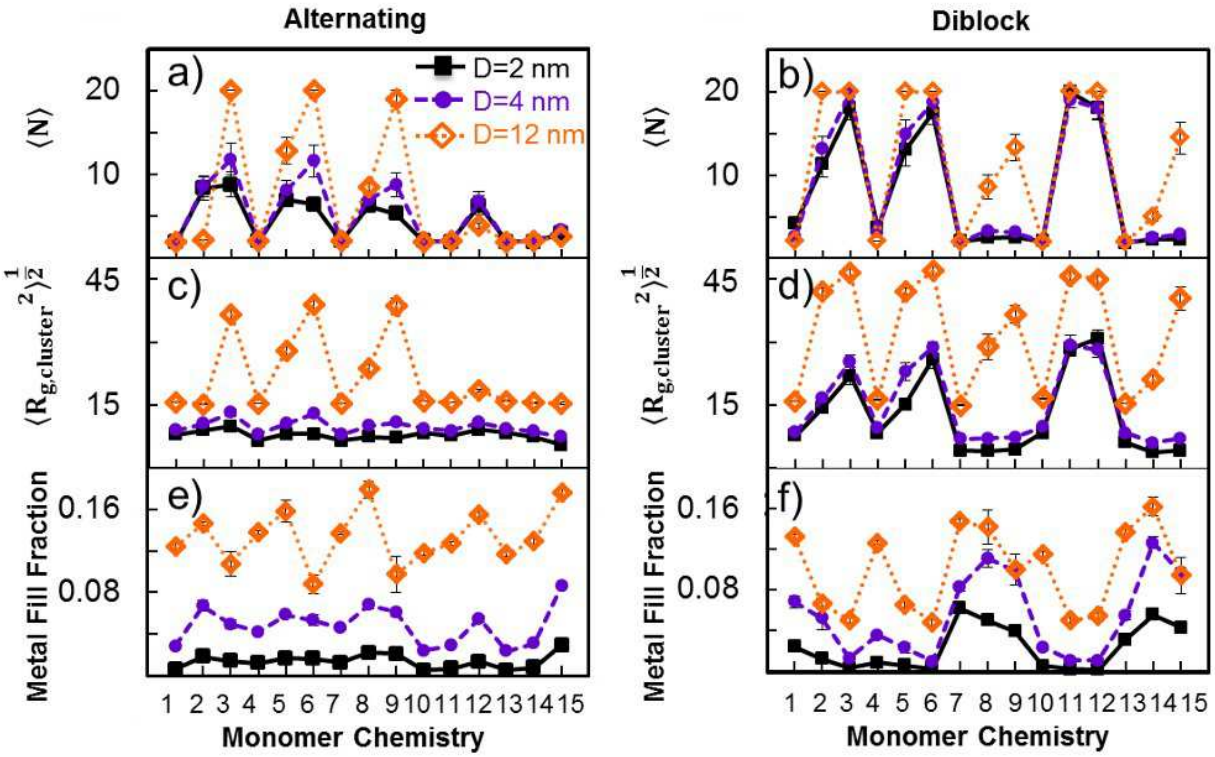

Figure 3.7 Same as Figure 3.4 but for 20 copolymer grafted particles in a 100x100x100 nm^3 simulation box.

For both diblock and alternating copolymer grafted particles at all particle diameters how <N> and $\langle R_{g,cluster}^2 \rangle^{1/2}$ change with varying monomer interactions (x-axis) and particle diameter D is same for 20 grafted particles (Figure 3.7) as it is for 10 grafted particles (Figure 3.1). The absolute values of <N> and $\langle R_{g,cluster}^2 \rangle^{1/2}$ at each monomer interaction for 20 grafted particles in Figure 3.7 is higher than the corresponding values for 10 grafted particles in Figure 3.1. This is particularly true for monomer interactions where the attraction strength between like monomers is strong, leading to all particles in the solution aggregating to form a cluster. To compare the internal

structure of the clusters formed by assembly of the 20 grafted particles and 10 grafted particles we compare the Z distribution of the clusters for 20 grafted particles (see supplementary figures S.3.8, S.3.9 and S.3.10) with the corresponding results discussed before for 10 grafted particles (Figure S.3.3, Figure 3.2 and Figure S.3.4). For a few monomer interactions, especially those with strong like-monomer interactions, the Z distribution for the 20 polymer grafted particles is shifted slightly to higher neighbors, but for the majority of the interaction sets considered here we see very similar trends in Z distribution with monomer chemistry, suggesting similarity in the *structure* within the clusters formed by 20 and 10 grafted particles. This suggests that the structure within the nanoclusters is a function of the characteristics of the grafted copolymers and not the number of grafted particles. This is remarkable as it confirms that by tailoring the copolymer functionalization we are able to control assembly, in a reproducible manner. By designing the copolymer functionalization, the monomer sequence, chemistry and grafting density, we have imparted in essence a "valency" to the nanoparticle "atom". These results also confirm that the "valency" solely depends on the monomer sequence and the monomer-monomer interactions within the functionalization and less on number of "atoms" available to "bond", as long as we remain in the same concentration regime. We note that both 10 and 20 grafted particles in a simulation box 100x100x100 nm^3 represent dilute concentrations, and we expect higher concentrations could change these trends due to increased crowding effects which should reduce the role of grafted chain conformational entropy on the grafted particle assembly.

3.4 Conclusions

We have conducted Monte Carlo simulations to study copolymer grafted spherical nanoparticles placed in an implicit solvent to establish that functionalizing nanoparticles with copolymers at low grafting density and varying monomers sequence and chemistries, particle sizes, and grafted

copolymer chain length allows us to tune the assembly of nanoparticles into nanoclusters of varying sizes, shapes and structures. The insight from this computational work could guide experimentalists trying to design clusters of functionalized particles targeted, say towards metamaterial synthesis where controlling shape and structure of the cluster is more important that having crystalline order.[67, 68]

The effects of monomer-monomer interactions on the assembly of copolymer functionalized nanoparticles is dependent on whether the grafted copolymer has an alternating or diblock monomer sequence and on how the chemistry of the monomers affects the gain in enthalpy and loss in conformational entropy of the grafted chains during nanoparticle assembly. Alternating sequence produces clusters that are relatively isotropic regardless of whether A-A or B-B monomers are attractive in the presence of negligible unlike monomer repulsions. Strong A-B repulsions lead to either particle dispersion or smaller clusters as compared to negligible A-B repulsions. In contrast, diblock sequence produces clusters that are compact and small when inner block monomers (A-A) are attractive, and clusters that are loosely held together and large when outer block monomers (B-B) are attractive. The characteristics of clusters formed with diblock copolymer grafted particles do not change whether the A-B repulsions are strong or negligible compared to the like-monomer attractions. While alternating copolymers lead to isotropic structures, diblock copolymers with strong A-A attractions lead to anisotropic clusters, e.g. long or short nanowires. The size of the anisotropic clusters depends on the graft length and particle size. We find that increasing particle size makes it more entropically unfavorable for chains to form inter-graft contacts on the same particle leading to cluster formation only in cases when the like-monomer attraction strength is strong enough to overcome the entropic loss from stretching grafts during inter-particle contacts. Particle size and graft length affect the balance of

enthalpic gain and entropic losses coming from inter-grafted particle contacts and/or inter- and intra- grafted chain contacts in the same grafted particles. Upon increasing particle concentration, while staying in the dilute concentration regime, we find the trends of cluster structure is similar to the lower particle concentration case confirming that the structure within a cluster is primarily governed by the copolymer functionalization imparting a "valency" to the nanoparticle atom, rather than the number of particles to "bond" with.

It is important to discuss some of the limitations of this work. While in experiments there are competing particle-particle attractive interactions, we chose to keep particle-particle interactions and particle-monomer interactions to be athermal, so as to isolate the effect of grafted monomer chemistry on the nanoparticle assembly. If one chooses particle and monomer chemistry such that particle-particle interactions dominate over monomer-monomer interactions we expect grafted chain sequence and chemistry to play a smaller role than presented in this paper. Additionally, by keeping the number of grafts fixed at six grafts and changing particle diameter we have not decoupled the role of curvature and grafting density. By changing particle diameter, D=2, 4 and 12 nm, we understand the coupled effect of changing curvature (1/2, 1/4 and 1/12) and changing surface grafting density (0.48, 0.12 and 0.01 chains/nm^2). It would be of interest to isolate the effect of curvature and grafting density. Since there is growing interest in densely grafted diblock copolymer functionalized particles, how the microphase separation of the densely grafted diblock copolymer chains induces or hinders particle assembly would be an interesting investigation. Lastly, the coarse-grained model used here is simple and assume similar monomer sizes and similar flexibility in backbones for the two blocks (in case of diblock copolymer). To better link to poly-peptide or protein grafted particle assembly[78] we will need to incorporate size variations in monomers and electrostatic interactions.

The highlight of this work is that it illustrates how tuning copolymer sequence in the polymer functionalization is an exciting route for experimentalists to use for assigning a desired "patchiness" or "valency" to nanoparticles. This computational work is timely considering the growing advances in synthetic chemistry that allows one to create polymers with controlled monomer sequences and graft nanoparticles with a variety of ligands. Combining this new tuning parameter, copolymer sequence, with varying particle shapes (e.g. tetrapods) or copolymer composition (e.g. asymmetric diblock copolymers) or grafting pattern (e.g. Janus-like grafting) will provide endless opportunities to obtain target nanostructures.

3.5 References

1. T. A. Witten and P. A. Pincus, *Macromolecules*, 1986, 19, 2509-2513.
2. C. F. Laub and J. T. Koberstein, *Macromolecules*, 1994, 27, 5016-5023.
3. A. Jayaraman and K. S. Schweizer, *Macromolecules*, 2009, 42 pp 8423-8434.
4. S. T. Milner, T. A. Witten and M. E. Cates, *Macromolecules*, 1989, 22, 853-861.
5. J. U. Kim and M. W. Matsen, *Macromolecules*, 2008, 41, 4435-4443.
6. M. Himmi, M. Benhamou, A. Bettachy and M. Daoud, *Journal of Molecular Liquids*, 2003, 102, 347-363.
7. K. T. Marla and J. C. Meredith, *Journal of Chemical Theory and Computation*, 2006, 2, 1624-1631.
8. V. Causin, B. X. Yang, C. Marega, S. H. Goh and A. Marigo, *Journal of Nanoscience and Nanotechnology*, 2008, 8, 1790-1796.
9. N. Tsubokawa, *Polymer Journal*, 2007, 39, 983-1000.
10. C. Li, J. Han, C. Y. Ryu and B. C. Benicewicz, *Macromolecules*, 2006, 39, 3175-3183.
11. V. Goel, T. Chatterjee, L. Bombalski, K. Yurekli, K. Matyjaszewski and R. Krishnamoorti, *Journal of Polymer Science Part B-Polymer Physics*, 2006, 44, 2014-2023.
12. E. R. Chan, L. C. Ho and S. C. Glotzer, *Journal of Chemical Physics*, 2006, 125, 064905.
13. C. R. Iacovella, M. A. Horsch, Z. Zhang and S. C. Glotzer, *Langmuir*, 2005, 21, 9488-9494.
14. X. Zhang, E. R. Chan and S. C. Glotzer, *Journal of Chemical Physics*, 2005, 123, 184718.
15. M. A. Horsch, Z. Zhang and S. C. Glotzer, *Nano Letters*, 2006, 6, 2406-2413.
16. P. J. Costanzo and F. L. Beyer, *Macromolecules*, 2007, 40, 3996-4001.
17. J. J. Chiu, B. J. Kim, E. J. Kramer and D. J. Pine, *Journal of the American Chemical Society*, 2005, 127, 5036-5037.
18. B. J. Kim, G. H. Fredrickson and E. J. Kramer, *Macromolecules*, 2008, 41, 436-447.

19. V. Pryamitsyn, V. Ganesan, A. Z. Panagiotopoulos, H. Liu and S. K. Kumar, *Journal of Chemical Physics*, 2009, 131, 221102.
20. P. Akcora, S. K. Kumar, V. G. Sakai, Y. Li, B. C. Benicewicz and L. S. Schadler, *Macromolecules*, 2010, 43, 8275-8281.
21. J. A. Fan, C. H. Wu, K. Bao, J. M. Bao, R. Bardhan, N. J. Halas, V. N. Manoharan, P. Nordlander, G. Shvets and F. Capasso, *Science*, 2010, 328, 1135-1138.
22. X. M. Jiang, B. Zhao, G. J. Zhong, N. X. Jin, J. M. Horton, L. Zhu, R. S. Hafner and T. P. Lodge, *Macromolecules*, 2010, 43, 8209-8217.
23. S. Ojha, B. Beppler, H. C. Dong, K. Matyjaszewski, S. Garoff and M. R. Bockstaller, *Langmuir*, 2010, 26, 13210-13215.
24. D. M. Trombly and V. Ganesan, *Journal of Chemical Physics*, 2010, 133.
25. S. Y. Park, K. R. A. Lytton-Jean, B. Lee, S. Weigand, G. C. Schatz and C. A. Mirkin, *Nature*, 2008, 451, 553-556.
26. P. L. Biancaniello, A. J. Kim and J. C. Crocker, *Physical Review Letters*, 2005, 94, 058302.
27. D. B. Lukatsky, B. M. Mulder and D. Frenkel, *Journal of Physics-Condensed Matter*, 2006, 18, S567-S580.
28. N. C. Harris and C. H. Kiang, *Physical Review Letters*, 2005, 95, 046101-046104.
29. A. A. Lazarides and G. C. Schatz, *J. Phys. Chem. B*, 2000, 104, 460-467.
30. A. J. Kim, P. L. Biancaniello and J. C. Crocker, *Langmuir*, 2006, 22, 1991-2001.
31. A. V. Tkachenko, *Physical Review Letters*, 2002, 89, 148303.
32. V. Talanquer, *Journal of Chemical Physics*, 2006, 125, 194701.
33. W. J. Parak, T. Pellegrino, C. M. Micheel, D. Gerion, S. C. Williams and A. P. Alivisatos, *Nano Letters*, 2003, 3, 33-36.
34. S. C. Glotzer and J. A. Anderson, *Nature Materials*, 2010, 9, 885-887.
35. M. R. Jones, R. J. Macfarlane, B. Lee, J. A. Zhang, K. L. Young, A. J. Senesi and C. A. Mirkin, *Nature Materials*, 2010, 9, 913-917.
36. C. H. Kiang, *Physica A*, 2003, 321, 164-169.
37. J. Largo, F. W. Starr and F. Sciortino, *Langmuir*, 2007, 23, 5896-5905.
38. J. C. Crocker, *Nature*, 2008, 451, 528-529.
39. H. D. Hill, R. J. Macfarlane, A. J. Senesi, B. Lee, S. Y. Park and C. A. Mirkin, *Nano Letters*, 2008, 8, 2341-2344.
40. D. Nykypanchuk, M. M. Maye, D. van der Lelie and O. Gang, *Nature*, 2008, 451, 549-552.
41. M. E. Leunissen, R. Dreyfus, R. J. Sha, T. Wang, N. C. Seeman, D. J. Pine and P. M. Chaikin, *Soft Matter*, 2009, 5, 2422-2430.
42. M. M. Stevens, N. T. Flynn, C. Wang, D. A. Tirrell and R. Langer, *Advanced Materials*, 2004, 16, 915-918.
43. S. Si, A. Kotal and T. K. Mandal, *Journal of Physical Chemistry C*, 2007, 111, 1248-1255.
44. J. M. Slocik, F. Tam, N. J. Halas and R. R. Naik, *Nano Letters*, 2007, 7, 1054-1058.
45. S. Si and T. K. Mandal, *Langmuir*, 2007, 23, 190-195.
46. P. Akcora, H. Liu, S. K. Kumar, M. J., Y. Li, B. C. Benicewicz, L. S. Schadler, D. Acehan, A. Z. Panagiotopoulos, V. Pryamitsyn, V. Ganesan, J. Ilavsky, P. Thiyagarajan, R. H. Colby and J. F. Douglas, *Nature Materials*, 2009, 8, 354-359.
47. G. D. Smith and D. Bedrov, *Langmuir*, 2009, 25, 11239-11243.

48. A. Jayaraman and K. S. Schweizer, *J. Chem. Phys.*, 2008, 128, 164904.
49. A. Jayaraman and K. S. Schweizer, *Langmuir*, 2008, 24, 11119-11130.
50. E. R. Chan, X. Zhang, C. Y. Lee, M. Neurock and S. C. Glotzer, *Macromolecules*, 2005, 38, 6168-6180.
51. M. A. Horsch, Z. L. Zhang and S. C. Glotzer, *Physical Review Letters*, 2005, 95, 056105.
52. J. Y. Lee, A. C. Balazs, R. B. Thompson and R. M. Hill, *Macromolecules*, 2004, 37, 3536-3539.
53. A. Striolo, *Small*, 2007, 3, 628-635.
54. C. R. Iacovella, A. S. Keys, M. A. Horsch and S. C. Glotzer, *Phys. Rev. E.*, 2007, 75, 040801.
55. S. C. Glotzer, M. A. Horsch, C. R. Iacovella, Z. L. Zhang, E. R. Chan and X. Zhang, *Current Opinion in Colloid & Interface Science*, 2005, 10, 287-295.
56. Z. Zhang, M. A. Horsch, M. H. Lamm and S. C. Glotzer, *Nano Letters*, 2003, 3, 1341-1346.
57. C. L. Phillips, C. R. Iacovella and S. C. Glotzer, *Soft Matter*, 2010, 6, 1693-1703.
58. C. R. Iacovella and S. C. Glotzer, *Nano Letters*, 2009, 9, 1206-1211.
59. A. Jayaraman and K. S. Schweizer, *Macromolecules*, 2008, 41, 9430-9438.
60. A. Jayaraman and K. S. Schweizer, *Mol Simulat*, 2009, 35, 835-848.
61. T. L. Chantawansri, A. W. Bosse, A. Hexemer, C. H. D., C. J. Garcia-Cervera, E. J. Kramer and G. H. Fredrickson, *Physical Review E*, 2007, 75, 031802.
62. J. U. Kim and M. W. Matsen, *Physical Review Letters*, 2009, 102, 078303.
63. X. M. Zhu, L. Q. Wang, J. P. Lin and L. S. Zhang, *Acs Nano*, 2010, 4, 4979-4988.
64. N. Nair and A. Jayaraman, *Macromolecules*, 2010, 43, 8251-8263.
65. A. Seifpour, P. Spicer, N. Nair and A. Jayaraman, *Journal of Chemical Physics*, 2010, 132, 164901.
66. Y. L. Zhao and S. Perrier, *Macromolecules*, 2006, 39, 8603-8608.
67. C. C. DuFort and B. Dragnea, in *Annual Review of Physical Chemistry, Vol 61*, 2010, vol. 61, pp. 323-344.
68. G. Mattei, P. Mazzoldi and H. Bernas, in *Materials Science with Ion Beams*, 2010, vol. 116, pp. 287-316.
69. H. M. Xiong, M. Y. Sfeir and O. Gang, *Nano Letters*, 2010, 10, 4456-4462.
70. N. Metropolis, A. W. Rosenbluth, M. N. Rosenbluth, A. H. Teller and E. Teller, *Journal of Chemical Physics*, 1953, 21, 1087-1092.
71. S. Kirkpatrick, C. D. Gelatt and M. P. Vecchi, *Science*, 1983, 220, 671-680
72. D. Frenkel and B. Smit, *Understanding molecular simulation : from algorithms to applications*, Academic, San Diego, Calif. ; London, 2002.
73. W. Park and J. Kim, *Mrs Bulletin*, 2008, 33, 907-911.
74. V. M. Shalaev, W. S. Cai, U. K. Chettiar, H. K. Yuan, A. K. Sarychev, V. P. Drachev and A. V. Kildishev, *Optics Letters*, 2005, 30, 3356-3358.
75. V. A. Tamma, J. H. Lee, Q. Wu and W. Park, *Applied Optics*, 2010, 49, A11-A17.
76. Z. L. Zhang and S. C. Glotzer, *Nano Letters*, 2004, 4, 1407-1413.
77. F. Sciortino, E. Bianchi, J. F. Douglas and P. Tartaglia, *Journal of Chemical Physics*, 2007, 126, 194903.
78. M. Kar, P. S. Vijayakumar, B. L. V. Prasad and S. Sen Gupta, *Langmuir*, 26, 5772-5781.

3.6 Supplementary Information

Table S.3.1 Radius of gyration $\langle R_{g,chain}^2 \rangle^{1/2}$ (in nm) of the alternating (top) and diblock (bottom) chains grafted on particles of size D=2 nm, 4 nm and 12 nm, and varying interaction parameters (also rows in Table 3.1 in the main text).

	D=2nm			D=4nm			D=12nm	
ALTERNATING	**Average**	**Error**		**Average**	**Error**		**Average**	**Error**
Interactions								
1	2.934	0.004		2.905	0.006		2.892	0.003
2	2.442	0.011		2.438	0.007		2.397	0.004
3	2.334	0.011		2.433	0.028		1.834	0.011
4	2.505	0.004		2.495	0.003		2.501	0.003
5	2.341	0.022		2.392	0.020		2.058	0.006
6	2.325	0.020		2.386	0.018		1.848	0.013
7	2.509	0.003		2.510	0.002		2.503	0.003
8	2.346	0.016		2.347	0.013		2.050	0.004
9	2.270	0.013		2.353	0.025		1.825	0.016
10	3.043	0.003		3.016	0.005		3.001	0.004
11	2.821	0.005		2.801	0.005		2.797	0.003
12	2.309	0.013		2.328	0.017		2.140	0.007
13	3.055	0.003		3.009	0.006		3.004	0.005
14	2.844	0.007		2.806	0.006		2.805	0.005
15	2.325	0.007		2.316	0.012		2.130	0.008
DIBLOCK	**Average**	**Error**		**Average**	**Error**		**Average**	**Error**
Interactions								
1	2.881	0.008		2.812	0.004		2.771	0.004
2	2.959	0.025		2.893	0.020		2.670	0.018
3	2.743	0.015		2.729	0.013		2.499	0.017
4	2.604	0.008		2.583	0.004		2.597	0.003
5	2.779	0.018		2.813	0.020		2.807	0.020
6	2.674	0.021		2.680	0.027		2.758	0.018
7	2.683	0.002		2.625	0.002		2.573	0.004
8	2.758	0.009		2.718	0.009		2.456	0.005
9	2.751	0.014		2.687	0.012		2.408	0.006
10	2.954	0.005		2.928	0.004		2.914	0.005
11	2.974	0.014		2.989	0.019		2.997	0.012
12	2.916	0.018		2.904	0.021		2.928	0.010
13	3.002	0.005		2.957	0.005		2.904	0.003
14	3.018	0.010		2.985	0.011		2.766	0.003
15	2.999	0.016		2.925	0.013		2.681	0.005

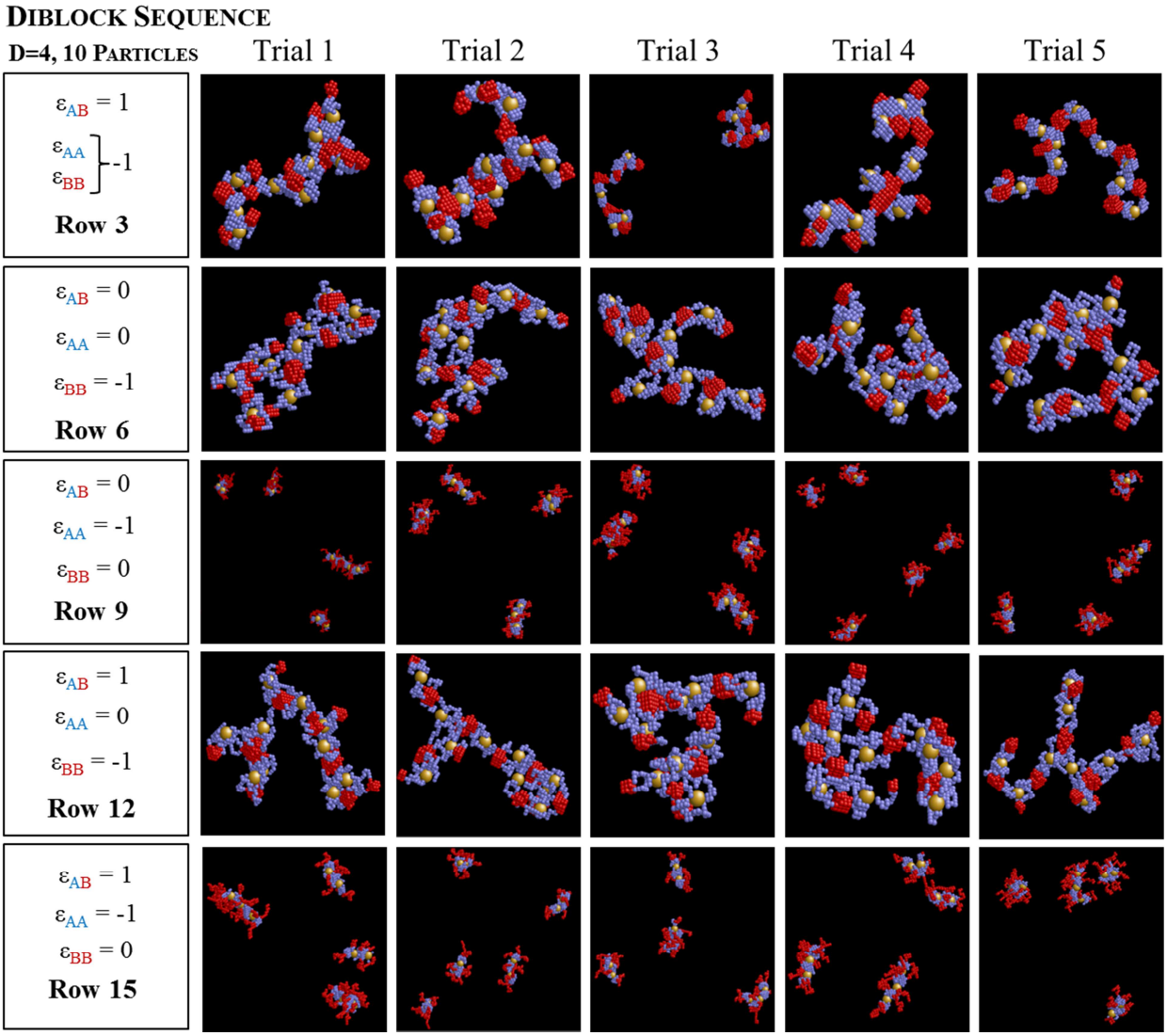

Figure S.3.1 Simulation snapshots from five trials showing representative equilibrium clusters formed from the assembly of **10 copolymer grafted particles** (in a 100x100x100 nm^3 simulation box) with particle diameter **D=4 nm** and six grafts of **24 monomers** arranged in diblock sequence. The rows in the figure, as labeled, correspond to the rows in Table 3.1.

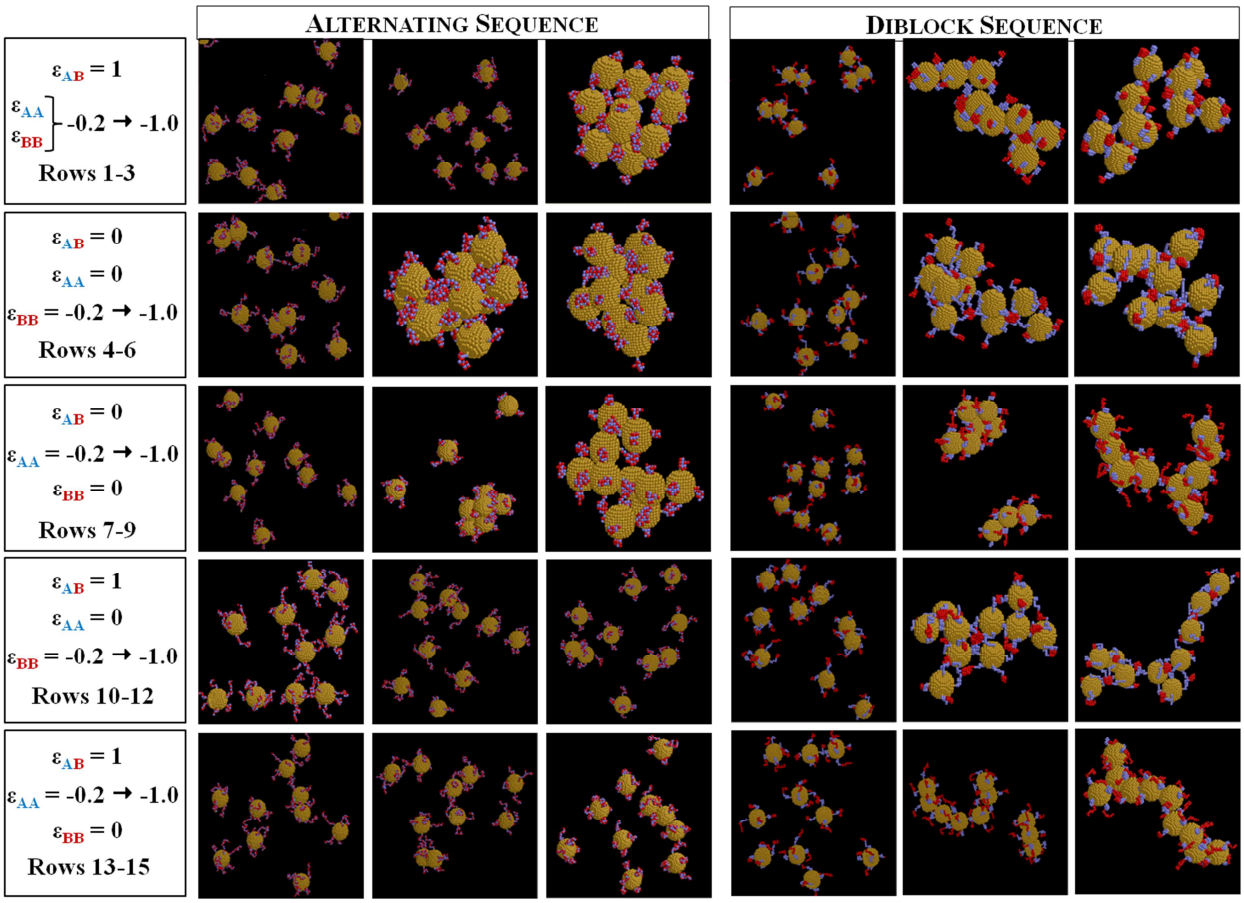

Figure S.3.2 Simulation snapshots from one trial showing representative equilibrium clusters formed from the assembly of **10 copolymer grafted particles** (in a 100x100x100 nm^3 simulation box) with particle diameter **D=12 nm** and six grafts of **24 monomers** arranged in alternating and diblock sequence. The rows in the figure, as labeled, correspond to the rows in Table 3.1.

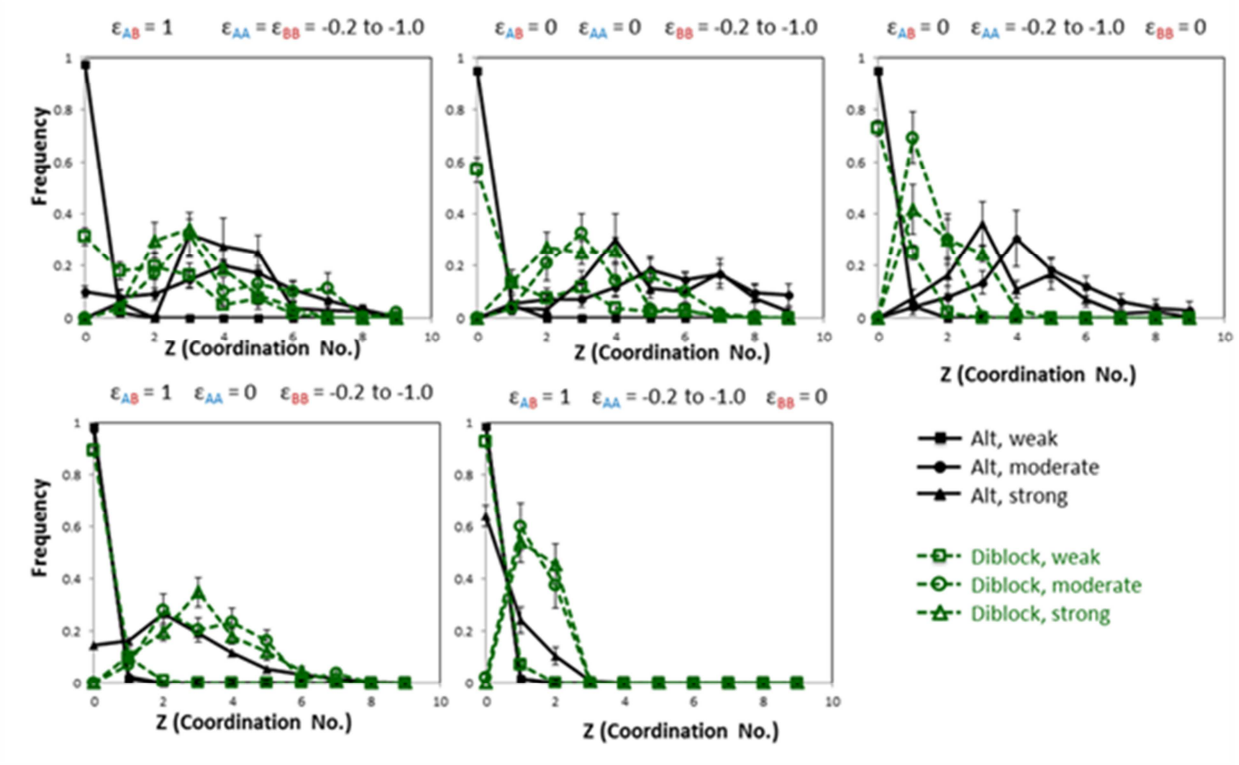

Figure S.3.3 Histogram of Z coordination numbers characterizing the structure within clusters formed from the assembly of **10 copolymer grafted particles** (in a 100x100x100 nm^3 simulation box) with particle diameter **D=2 nm** and six grafts of **24 monomers** arranged in either an alternating (solid lines) or diblock sequence (dashed lines) with varying monomer chemistries corresponding to a) rows 1-3, b) rows 4-6, c) rows 7-9, d) rows 10-12 and e) rows 13-15 in Table 3.1. The symbols for weak, moderate and strong attraction strength are square, circle and triangle, respectively.

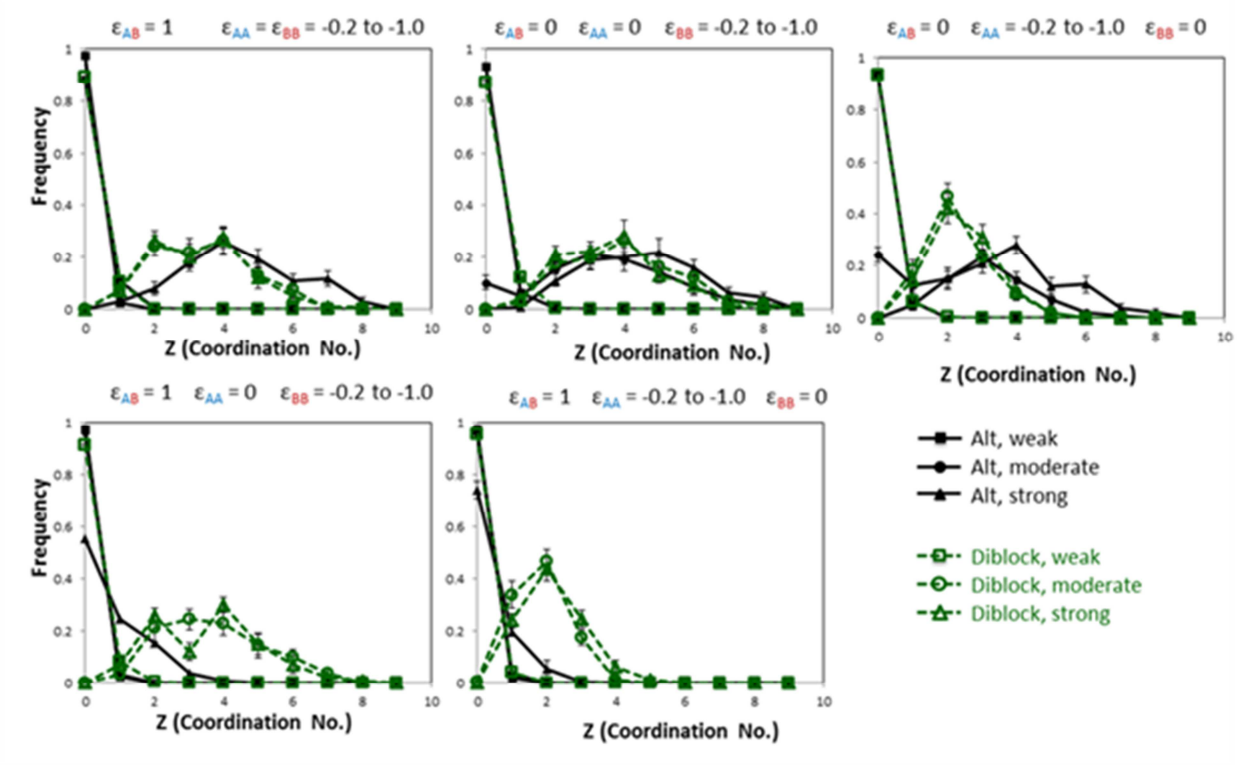

Figure S.3.4 Histogram of Z coordination numbers characterizing the structure within clusters formed from the assembly of **10 copolymer grafted particles** (in a 100x100x100 nm^3 simulation box) with particle diameter **D=12nm** and six grafts of **24 monomers** arranged in either an alternating (solid lines) or diblock sequence (dashed lines) with varying monomer chemistries corresponding to a) rows 1-3 b) rows 4-6, c) rows 7-9, d) rows 10-12 and e) rows 13-15 in Table 3.1. The symbols for weak, moderate and strong attraction strength are square, circle and triangle, respectively.

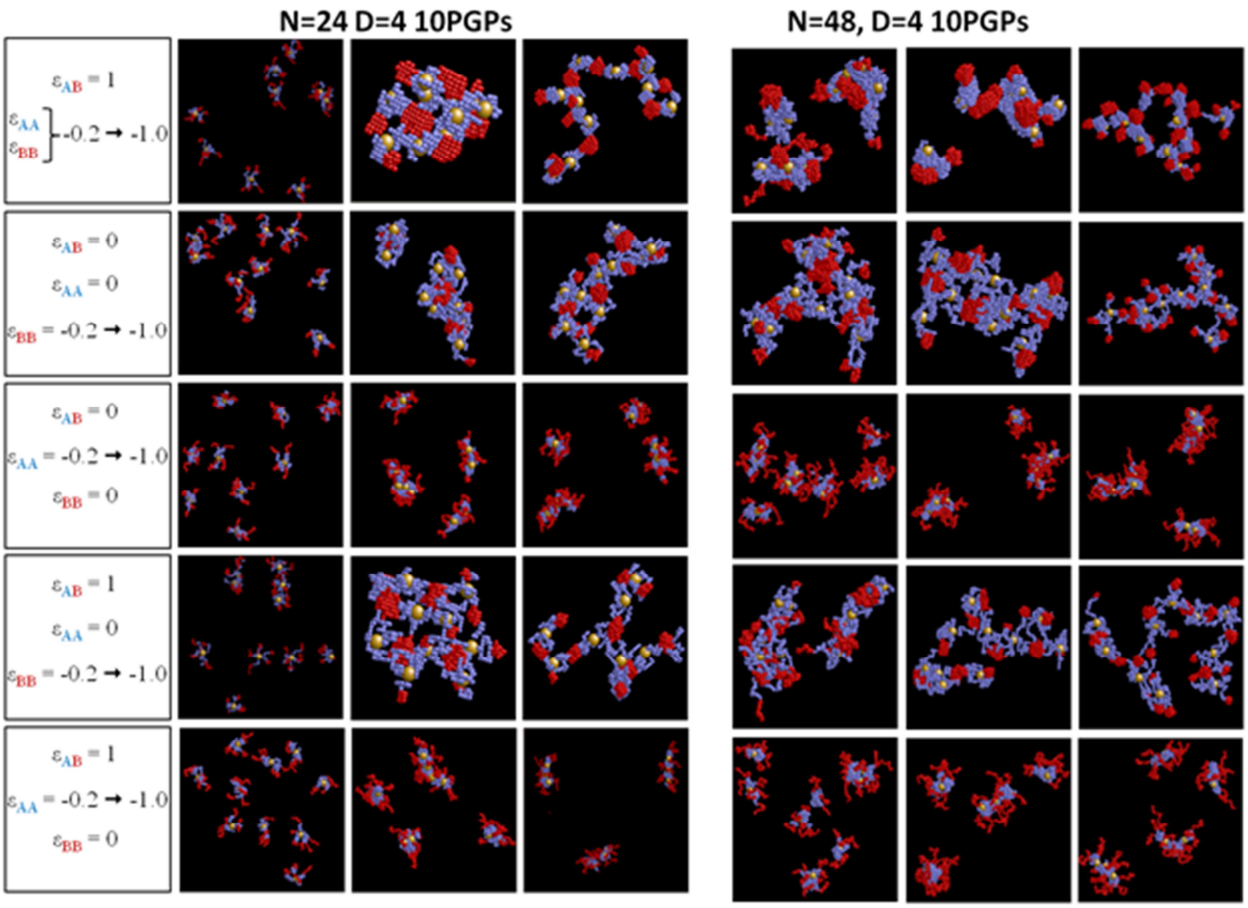

Figure S.3.5 Simulation snapshots from one trial showing representative equilibrium clusters formed from the assembly of **10 copolymer grafted particles** (in a 100x100x100 nm^3 simulation box) with particle diameter **D=4 nm** and six grafts of **24 monomers or 48 monomers** arranged in **diblock sequence**.

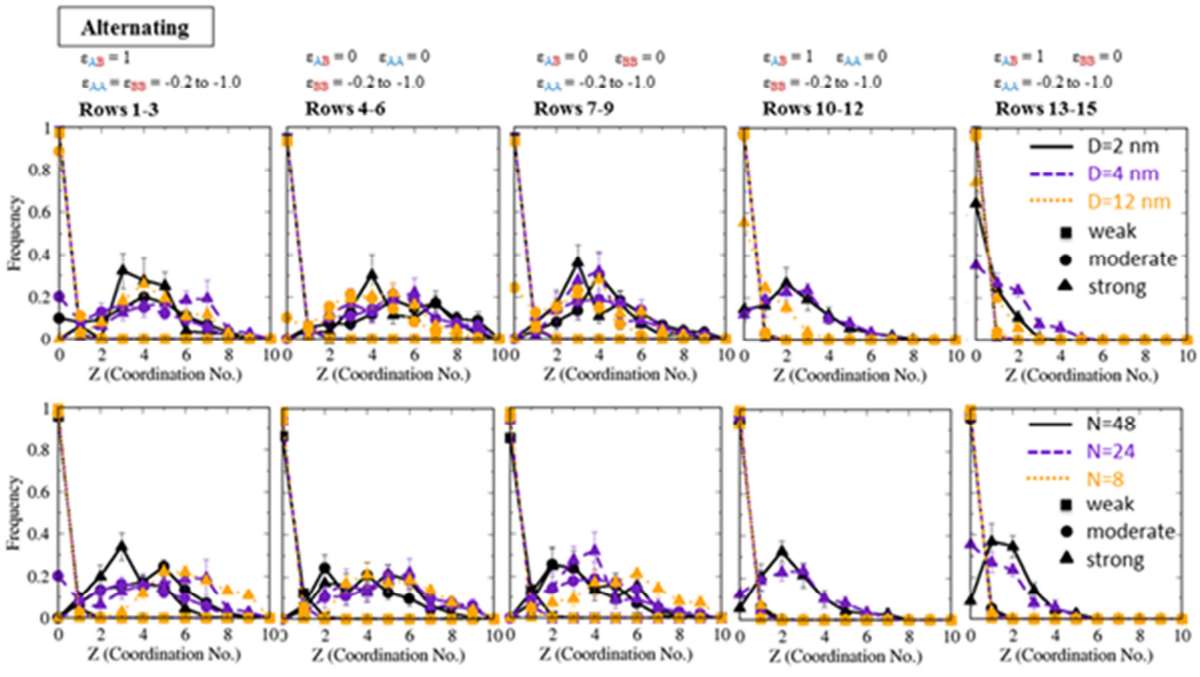

Figure S.3.6 Histogram of Z coordination numbers characterizing the structure within clusters formed from the assembly of **10 copolymer grafted particles** (in a 100x100x100 nm^3 simulation box) with varying particle diameter (top panel) and six grafts of varying length (bottom panel) arranged in **alternating** sequence with varying monomer chemistries corresponding to a) rows 1-3, b) rows 4-6, c) rows 7-9, d) rows 10-12 and e) rows 13-15 in Table 3.1. The symbols for weak, moderate and strong attraction strength are square, circle and triangle, respectively.

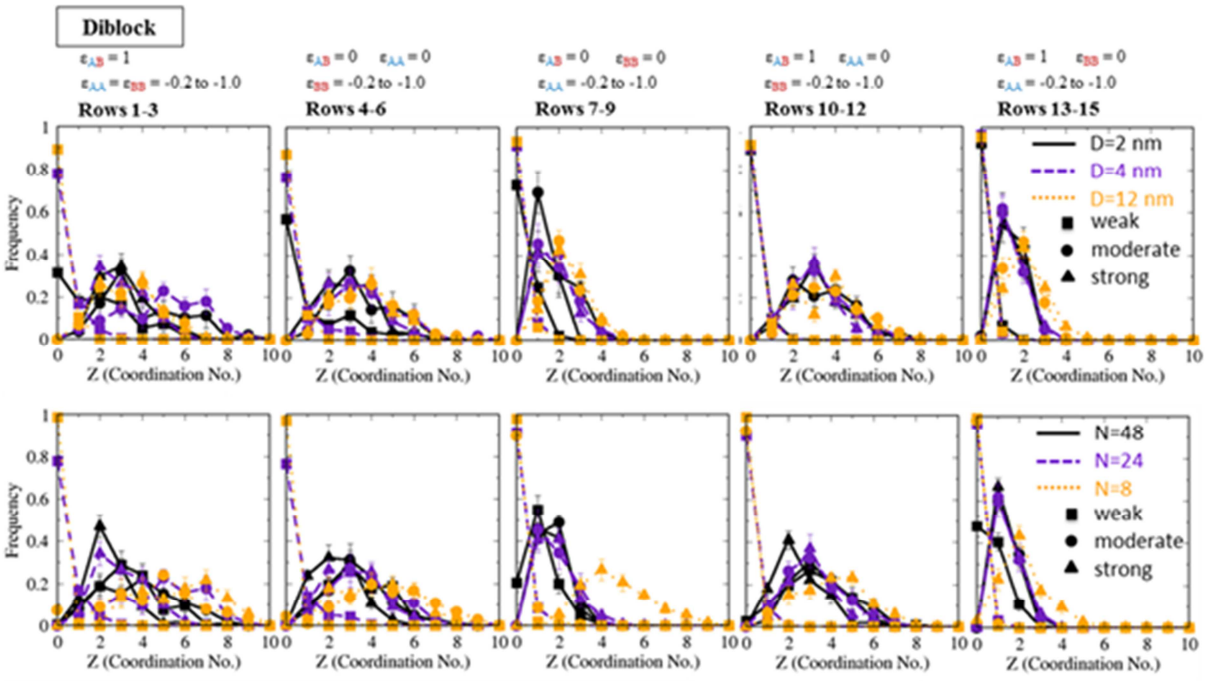

Figure S.3.7 Histogram of Z coordination numbers characterizing the structure within clusters formed from the assembly of **10 copolymer grafted particles** (in a 100x100x100 nm^3 simulation box) with varying particle diameter (top panel) and six grafts of varying length (bottom panel) arranged in **diblock** sequence with varying monomer chemistries corresponding to a) rows 1-3, b) rows 4-6, c) rows 7-9, d) rows 10-12 and e) rows 13-15 in Table 3.1. The symbols for weak, moderate and strong attraction strength are square, circle and triangle, respectively.

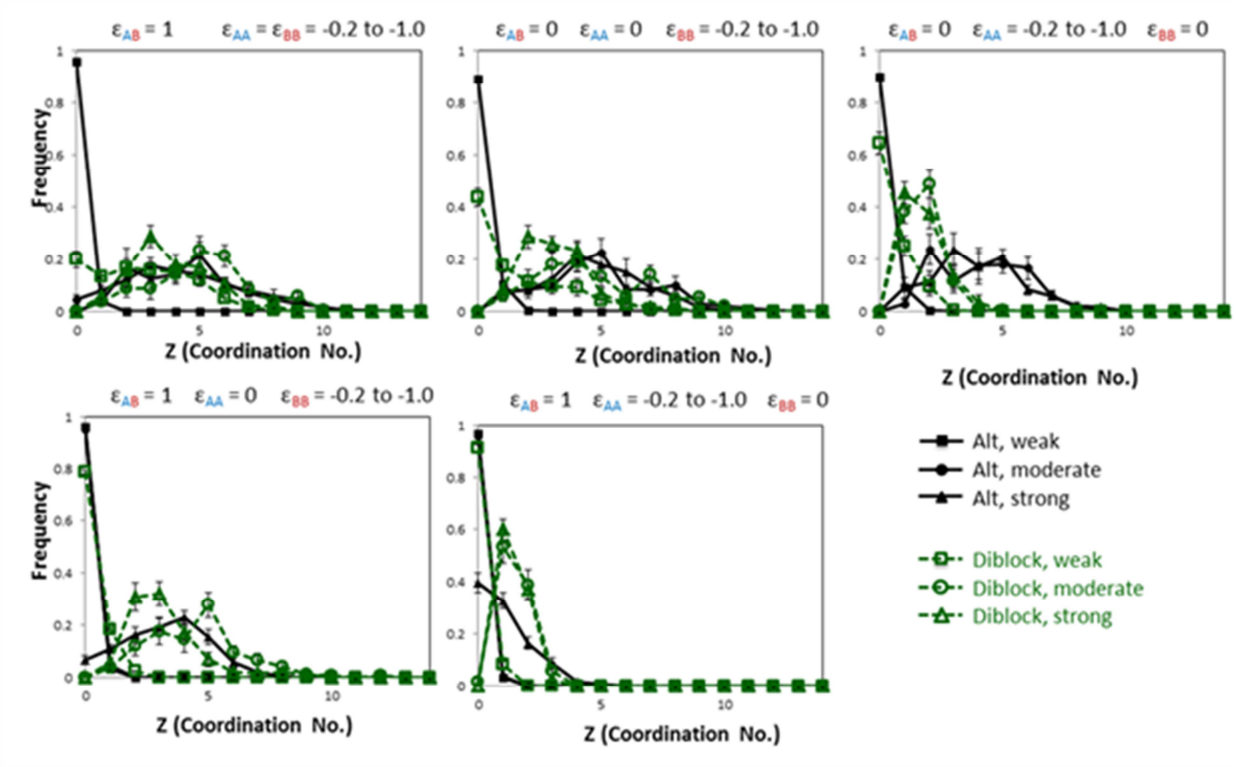

Figure S.3.8 Histogram of Z coordination numbers characterizing the structure within clusters formed from the assembly of **20 copolymer grafted particles** (in a 100x100x100 nm^3 simulation box) with particle diameter **D=2 nm** and six grafts of **24 monomers** arranged in either an alternating (solid lines) or diblock sequence (dashed lines) with varying monomer chemistries corresponding to a) rows 1-3, b) rows 4-6, c) rows 7-9, d) rows 10-12 and e) rows 13-15 in Table 3.1. The symbols for weak, moderate and strong attraction strength are square, circle and triangle, respectively.

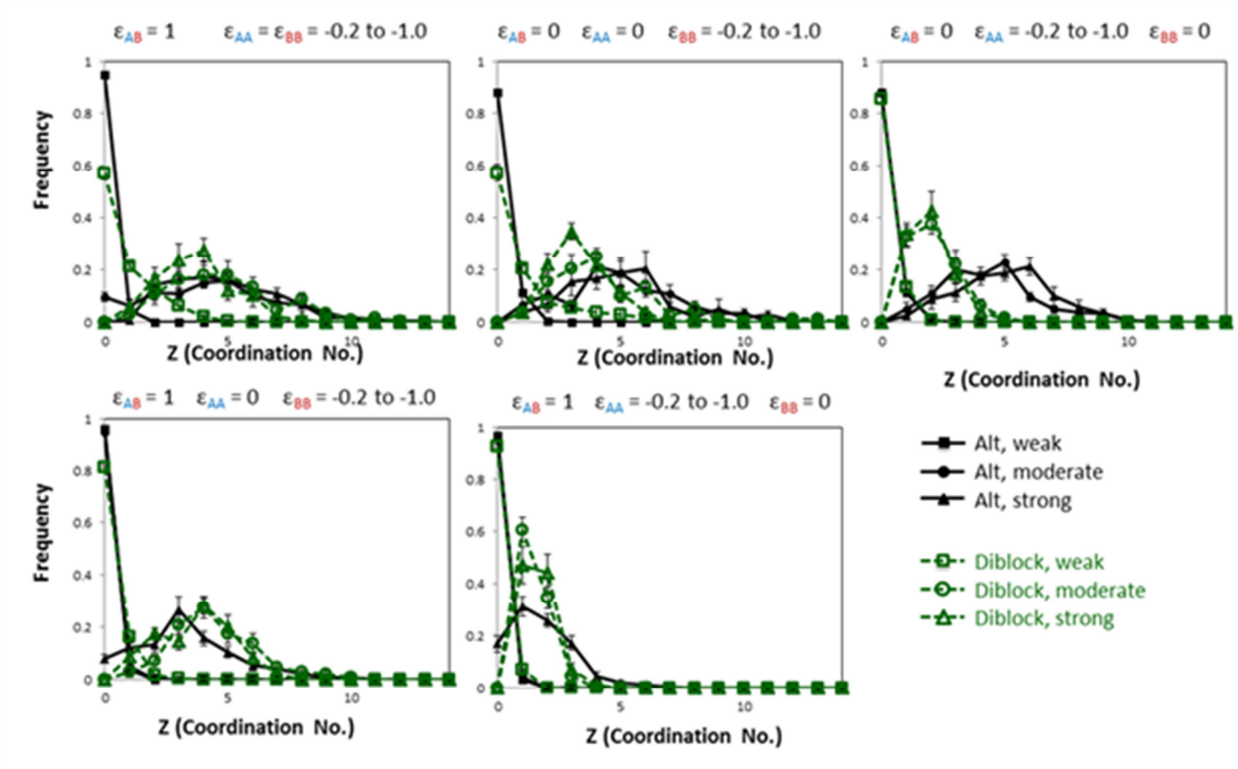

Figure S.3.9 Histogram of Z coordination numbers characterizing the structure within clusters formed from the assembly of **20 copolymer grafted particles** (in a 100x100x100 nm^3 simulation box) with particles diameter **D=4 nm** and six grafts of **24 monomers** arranged in either an alternating (solid lines) or diblock sequence (dashed lines) with varying monomer chemistries corresponding to a) rows 1-3, b) rows 4-6, c) rows 7-9, d) rows 10-12 and e) rows 13-15 in Table 3.1. The symbols for weak, moderate and strong attraction strength are square, circle and triangle, respectively.

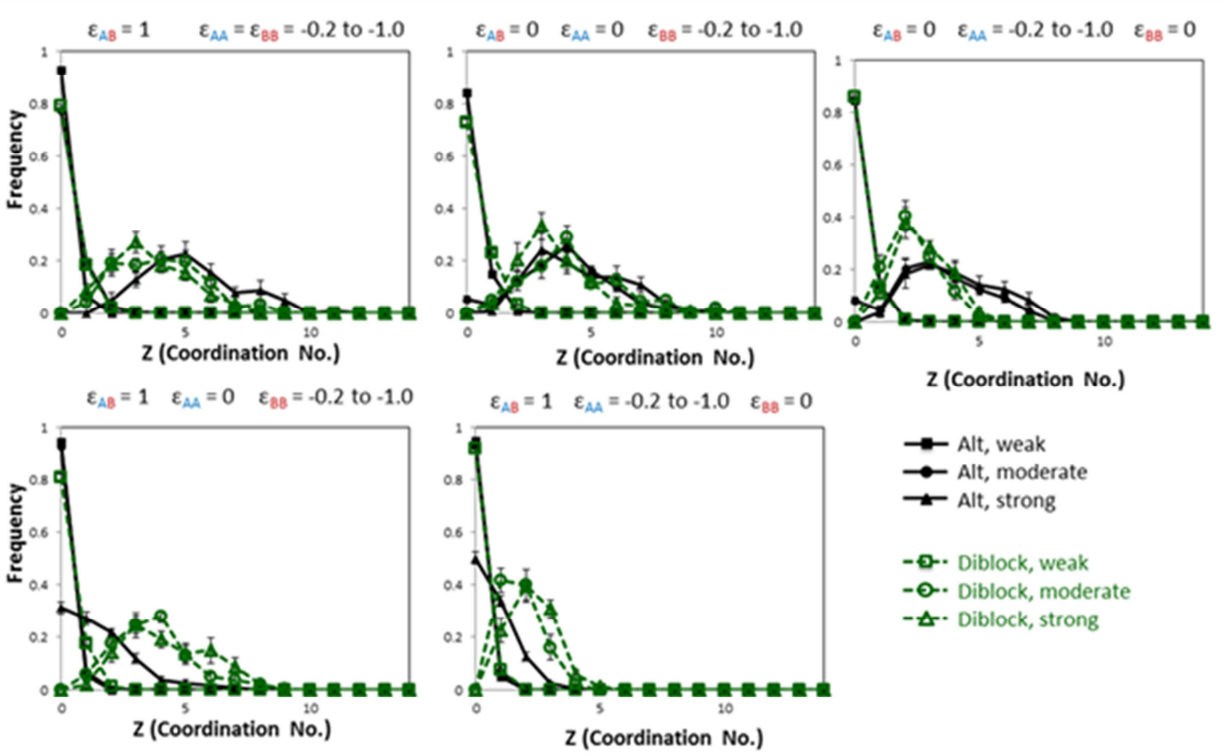

Figure S.3.10 Histogram of Z coordination numbers characterizing the structure within clusters formed from the assembly of **20 copolymer grafted particles** (in a 100x100x100 nm^3 simulation box) with particles diameter **D=12 nm** and six grafts of **24 monomers** arranged in either an alternating (solid lines) or diblock sequence (dashed lines) with varying monomer chemistries corresponding to a) rows 1-3, b) rows 4-6, c) rows 7-9, d) rows 10-12 and e) rows 13-15 in Table 3.1. The symbols for weak, moderate and strong attraction strength are square, circle and triangle, respectively.

Chapter 4

Molecular simulation study of the assembly of DNA-functionalised nanoparticles: effect of DNA strand sequence and composition

Adapted from: *Molecular Simulation* (2013)

4.1 Introduction

DNA functionalisation is an attractive route to programme an assembly of nanoparticles into target nanostructures because of the specificity and reversibility of DNA hybridization. A single DNA strand consists of nucleotides, each of which has a sugar, a phosphate group and a nitrogenous base (adenine (A), guanine (G), cytosine (C) or thymine (T)). According to Watson–Crick base pairing, complementary bases specifically form hydrogen bonds with each other (A with T and G with C). It is through this Watson–Crick base pairing that a sequence of nucleotides in a single-stranded DNA (ssDNA) hybridises specifically with another ssDNA with a complementary sequence of nucleotides. This hybridization leads to a double-stranded DNA (dsDNA) whose stability at a given temperature is known to be strongly dependent on the strand length and sequence. As the temperature increases above the melting temperature, the dsDNA separates into the two-constituent ssDNA. Using this thermoreversible and specific nature of hybridization of the ssDNA grafted on nanoparticles, one can assemble DNA-grafted nanoparticles into nanoclusters. Strands grafted on one particle hybridise with complementary strands on another particle either in a binary system in which one set of particles is grafted with strands that are complementary to the strands grafted on another set of nanoparticles[1-11] or in a

single population of particles in which the ssDNA sequence is self-complementary (e.g. ACGT).[12, 13] Alternatively, strands on two or more particles hybridise via free linker strands which when added to the system of DNA-grafted particles induce nanoparticle assembly.[14-22] Current synthetic capabilities allow for designing of DNA-functionalised nanoparticles[19, 23-25] and colloids[17, 26, 27] with the desired ssDNA sequence, length and composition to tailor nanoparticle/colloid assembly into target nano/microstructures. Many computational and experimental studies provide a fundamental understanding of the effect of various parameters (ssDNA length, sequence, grafting density, G/C content) on the thermodynamics and kinetics of colloidal and nanoparticle assembly. For example, past studies have established that as the length of the grafted ssDNA increases the hybridisation/melting temperature (T_m) of dsDNA increases and the assembly/dissociation transition temperature of nanoparticles (T_d) increases.[15, 22] As ssDNA strand length increases, the number of base pairs in the dsDNA increases, and in turn the higher enthalpic gain from the larger number of base pairs drives the T_m and T_d to shift to higher temperatures. Structurally, increasing length of the ssDNA increases the inter-particle spacing within the assembled structure. As grafting density, defined as the number of grafted strands per unit particle surface area, increases, T_d increases because the large enthalpic gain upon hybridization from increased number of complementary bases easily overcomes the loss in translational entropy of particles and conformational entropy of the densely grafted DNA strands upon hybridization. Similarly, as the particle size increases at constant grafting density the number of grafted strands increases, and as a result the T_d increases and melting transition sharpens.[5, 22, 28, 29]

With regard to strand content or composition, defined as percentage of strand that contains G or C bases, it is well understood that higher the percentage of G/C bases in the strand

stronger the hybridization between the complementary strands, because of the three hydrogen bonds in a G-C pair in contrast to two hydrogen bonds in an A-T pair. This increased enthalpic gain from G/C base pairing leads to higher T_m between the complementary single strands, and as a result higher T_d of the nanocluster assembled through hybridization of strands containing higher G/C content.[29] One could tune the strength of binding between two oligonucleotide strands by varying the G/C content or by incorporating 'non-hybridising' spacer bases in the strand between the G/C bases. It is important to find the optimal G/C content which is sufficient to drive nanoparticles to assemble, yet not too high leading to metastable structures.[30] The optimal G/C content is not easy to predict *a-priori* as it is depends in a complex manner on nanoparticle shape and size, grafting density, nanoparticle concentration, etc. In addition to the G/C content, the placement of G/C in the strand, i.e. the length of contiguous G/C or sequence of G/C with respect to other bases in the strand also affects the structure of the nanoparticle assembly and the cluster dissociation temperature, primarily by affecting the entropy losses term in the free energy of cluster formation. This aspect of G/C placement along the strand, and how it affects the assembly at varying particle sizes, grafting densities and G/C content, has not been studied well in the past.[21]

In this paper, we used molecular dynamics simulations to study a system of a single population of DNA-functionalised nanoparticles that assemble (without linkers) through hybridisation of complementary grafted strands in an implicit solvent. Our goal is to understand the effect of G/C content and placement within the grafted strands on the structure and thermodynamics of the assembly at varying grafting density and particle sizes. We first validated our coarse-grained model by replicating experimentally observed trends with increasing grafting densities. Consistent with experimental trends,[14] at a constant G/C content and G/C placement, as

grafting density increased, we observed that the melting temperature T_m and cluster dissociation temperature T_d of the assembly increased because the total number of G/C bonds between particles increased. Structurally, an increase in grafting density, within the low grafting density regime (σ=0.01 – 0.10 chains/nm^2) leads to an increase in the average number of neighbours within the final cluster or the 'valency' of the DNA grafted nanoparticle. At a constant grafting density and G/C content, nanoparticles assembled more readily when the G/C bases were placed on the outer (far from the particle surface) or middle portions of the strands than in the inner portion (closest to the particle surface) because of entropic frustration in the latter case. Moreover, at a constant G/C content, as the G/C placement along the strand shifted closer to the particle surface, the 'valency' of the particle decreased. As particle size decreased at constant grafting density and G/C placement, the minimum G/C content needed for assembly increases. Alternatively, when the G/C content (or the enthalpic contribution to hybridisation) is constant, smaller particles have a higher T_d than larger particles because the smaller particles experience a lower translational entropic loss upon assembly. Although much of the study was conducted at a constant dilute concentration of 10^{-5} particles/nm^3, as particle concentration is increased at 100% G/C content the number of neighbours or 'valency' increased at first and then plateaud. As particle concentration increased at a lower G/C content, the higher concentration drove further assembly of the particles.

The paper is organised as follows: in section 4.2, we provide details of our model and the simulation method as well as analysis techniques we used and parameters we studied. In section 4.3, we present the results of the assembly of DNA-functionalised nanoparticles as a function of G/C content and placement within the grafted strands at varying grafting density and particle

sizes. In section 4.4, we conclude with the key observed results, limitations of this work, and future directions.

4.2 Method

4.2.1 Model and Simulation

We modelled a system of DNA-functionalised nanoparticles in an implicit solvent using a coarse-grain model (Figure 4.1). This coarse-grain model is capable of capturing the timescale and length scale of DNA hybridization-driven assembly of many nanoparticles[12, 13] that atomistically detailed models would not be able to capture.

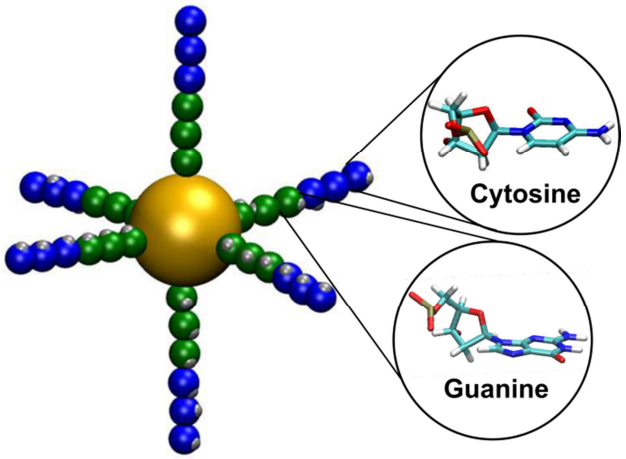

Figure 4.1 Schematic of our coarse grain model. In this model, a nucleotide on each strand is represented with one coarse-grained bead, and the hydrogen bonding sites on the bases are represented with sticky patches on the coarse-grained beads. Each nanoparticle is grafted with N_g number of DNA strands (N_g=6 in this figure) of a given length, N_{bases} (N_{bases}=6 in this figure).

In our model, hard spherical nanoparticles of diameter *D* are grafted with ssDNA strands at fixed locations and symmetrically on the nanoparticle surface. The strands were modelled as semi-flexible chains composed of N_{bases} number of 'monomer' beads of diameter σ_{mon}, where $\sigma_{mon} \sim 1$ nm because each 'monomer' bead represents a complete nucleotide (sugar, phosphate and A, C, G, or T base). Each monomer bead contains an attractive site that mimics hydrogen bonding. This attractive hydrogen bonding site is restricted to interact with another hydrogen bonding site on a complementary monomer bead, thus mimicking Watson–Crick base pairing. This model of DNA functionalised nanoparticles is adapted from a recent simulation study on DNA dendrimers.[12, 13] We note that although in those studies the DNA dendrimers are modelled with a tetrahedral hub to which ssDNA are bound, we modelled the nanoparticle as a hard core of a given diameter.

All non-bonded pair-wise interactions (nanoparticle–nanoparticle, nanoparticle–monomer, monomer–monomer, hydrogen bonding site–monomer, hydrogen bonding site–nanoparticle, and hydrogen bonding site–hydrogen site) were modelled using a truncated and shifted Lennard-Jones (LJ) potential:

$$U(r) = U_{LJ}(r) - U_{LJ}(r_c) - (r - r_c) \cdot \left. \frac{dU_{LJ}(r)}{dr} \right|_{r=r_c} \qquad (1)$$

where $U_{LJ} = 4 \cdot \varepsilon \cdot \left[\left(\frac{\sigma}{r}\right)^{12} - \left(\frac{\sigma}{r}\right)^{6} \right]$, σ is the sum of the radii of the interacting spheres, ε is the energetic well depth, r_c is the distance where the potential is truncated, and r represents the center-to-center distance between the coarse-grained beads of interest. All pair-wise interactions involving nanoparticle–nanoparticle, nanoparticle–monomer, monomer–monomer, hydrogen bonding site–monomer, hydrogen bonding site–nanoparticle, and non-complementary hydrogen bonding site–non-complementary hydrogen bonding site were modelled as repulsive interactions

with $r_c=2^{1/6}\cdot\sigma$. The pair-wise interactions between complementary hydrogen bonding sites include both the repulsive and attractive portion of the potential, with $r_c=2.5\cdot\sigma$. The reduced value of ε in Equation (1) is assigned as follows: $\varepsilon_{nanoparticle}=1$, $\varepsilon_{monomer}=1$, $\varepsilon_{hydrogen\ bonding\ site}=1$ for hydrogen bonding sites on monomer beads representing A or T nucleotides, and $\varepsilon_{hydrogen\ bonding\ site}=1.5$ for hydrogen bonding sites on monomer beads representing G or C nucleotides. All energies are represented in terms of ε_{mon} (LJ energy parameter for the monomer spheres), where ε_{mon} ~8 kT. The value of pair-wise interaction between two sites is the geometric average of the individuals forming the pair, $\varepsilon=(\varepsilon_1\varepsilon_2)^{1/2}$. The value of σ in Equation (1) is assigned as follows: $\sigma_{nanoparticle}=2\cdot\sigma_{mon}$ or $5\cdot\sigma_{mon}$, $\sigma_{monomer}=1$ and $\sigma_{hydrogen\ bonding\ site}=0.35\cdot\sigma_{mon}$ where σ_{mon} is the diameter of the monomer spheres and σ_{mon} ~1 nm.

Bonded interactions between various beads were simulated using a Finitely Extensible Non-linear Elastic (FENE) potential:

$$U_{FENE}=-\frac{K\cdot R_0^2}{2}\cdot\ln\left[1-\left(\frac{r}{R_0}\right)^2\right] \qquad (2)$$

where $K = (30*\varepsilon_{FENE})/\sigma^2$ and $R_0 = 1.5*\sigma$, K is the force constant, R_o is the maximum extension of the bond, ε_{FENE} is an energy parameter which is equal to ε_{mon}, and the values of σ and r depend on the type of beads involved in the bond. For a bond between a nanoparticle and the first monomer of a DNA strand, σ is defined as the radius of the monomer and r is defined as the distance between the centre of the monomer and the surface of the nanoparticle. For a bond between two monomers, σ is defined as the sum of the two monomer radii and r is defined as the distance between the monomer centers. Finally, a pseudo-bond between a hydrogen bonding site and the host monomer uses the σ equivalent to the diameter of the hydrogen bonding site and r is

defined as the centre-to-centre distance of the hydrogen bonding site and the host monomer. The equilibrium position of the hydrogen bonding sites is such that the surface of the hydrogen bonding site protrudes $0.02 \cdot \sigma_{mon}$ from the surface of the host monomer.

A three-body potential between bonded monomer beads along the ssDNA regulates the characteristic stiffness of the DNA strands:

$$U_{3-\text{body}} = \frac{1}{2} \cdot K \cdot (\theta - \theta_0)^2 \quad (3)$$

where K is a stiffness factor equal to $2\varepsilon_{3\text{-}body}$, where $\varepsilon_{3\text{-}body}$ is 10 times ε_{mon}, θ is the angle made by the three adjacent monomer beads, and θ_0 is the ideal angle equal to 180° for the preferred linear orientation of DNA. Hydrogen bonding sites are not subject to three-body interactions. A three-body interaction was also applied between the nanoparticle and the first two monomers of each chain to keep the monomer chains oriented perpendicular to the surface of the nanoparticle. Lastly, a three-body interaction was applied between the first monomer of each DNA graft, the nanoparticle, and the first monomer of every other DNA strand on the same nanoparticle, and the θ_0 value for the three-body interactions was set to force the DNA grafts to the desired relative positions on the surface of the nanoparticle which allowed us to ensure the grafts were placed symmetrically on the particle surface.

The above model was incorporated into a locally authored molecular dynamics simulation code in the canonical ensemble, in which the temperature was controlled via Nosé-Hoover thermostat.[31, 32] We refer the reader to the supplementary information for other details of the reduced model parameters and validation of the code.

4.2.2 Analysis

Thermodynamics. We characterised the thermodynamics of the DNA-functionalised nanoparticle assembly by calculating the hybridisation/melting curves of the grafted strands and the assembly/dissociation transition of the nanoparticles as a function of reduced temperature.

To calculate the hybridisation/melting of the grafted strands, at each temperature and each time step, we track the fraction of strands with 0–100% of G/C hybridised. Then, at each temperature we calculated the average fraction of strands that have at least half of the G/C in the strand hybridised ($f_{50\%}$). We then normalised $f_{50\%}$ by the maximum value of $f_{50\%}$, usually observed at the lowest temperature, and denote this as $f_{N,50\%}$. The melting curve is a plot of average $f_{N,50\%}$ as a function of temperature. We defined the melting point, T_m, as the temperature at which $f_{N,50\%} = 0.5$. We had an additional measure for determining T_m from computing the heat capacity at constant volume:

$$C_V = \left(\frac{\delta E}{\delta T}\right)_V = \frac{1}{k_B T^2}\langle (E - \langle E \rangle)^2 \rangle \qquad (4)$$

where T is the reduced temperature, E is the total energy of the system and k_b is the Boltzmann constant. We identified the T_m by locating a sharp increase in the plot of the heat capacity versus temperature . We found melting temperatures in each simulation trial and reported an average T_m as a mean of the T_m from these trials.

As the temperature was lowered and the strands hybridised, the functionalised particles assembled into a cluster. We defined a cluster as two or more particles with minimum of one base pair hybridised between DNA strands of adjacent nanoparticles. Free nanoparticles are those whose grafted ssDNA have not hybridised with any strand at that time step. We tracked the average number of free nanoparticles as a function of temperature. We defined the

assembly/dissociation transition temperature, T_d, as the temperature at which the number of free nanoparticles is half the total number of particles.

Structure. For each nanoparticle, we calculated a coordination number, Z, defined as the average number of particle neighbours the nanoparticle has within the cluster. Two particles are neighbours if they have at least one base pair hybridised between their DNA strands. The coordination number curve at each temperature is a distribution of the number of neighbours each nanoparticle has in a given system at that temperature. We averaged the coordination number distribution to obtain $\langle Z \rangle$ of the system at a specific temperature. To understand whether the average number of neighbours arises from multiple strands partially hybridising or a few strands completely hybridising we calculated the average number of strands per particle which were (partially or fully) hybridised at each temperature by multiplying the $f_{50\%}$, with the total number of strands on each particle for that system. We also calculated the nanoparticle–nanoparticle radial distribution function, $g(r)$ and nanoparticle–nanoparticle number profile, $N(r)$ in the simulation box. We calculated the average shape of the cluster at varying temperatures using relative shape anisotropy (RSA) parameter.[33] The RSA of a cluster is 0 when the particles are arranged perfectly isotropic (i.e. spherical symmetry) and 1 when the particles are perfectly anisotropic (i.e. rod-like) in their arrangement. We applied the RSA calculation to the coordinates of the particles of a cluster and not on the monomer beads of the DNA. We first translated the centre of mass of the particles' coordinates of a cluster to the origin and calculate the average radius of gyration tensor for a cluster containing N particles:

$$S = \frac{1}{N}\sum_{i=1}^{N} r_i r_i^{\boldsymbol{T}} \qquad (5)$$

where r_i is the translated coordinate vector of particle i, and $r_i^{\boldsymbol{T}}$ is the transpose of this coordinate

vector. Then S is diagonalised as:

$$\boldsymbol{S} = V^{\boldsymbol{T}} S\, V \qquad (6)$$

where V is a 3x3 matrix with columns that correspond to the three eigenvectors of S. The traceless part of $\boldsymbol{S}$ is then calculated:

$$\widehat{\boldsymbol{S}} = \boldsymbol{S} - \frac{1}{3} tr(\boldsymbol{S}) I \qquad (7)$$

where I is the 3x3 identity matrix, and tr($\boldsymbol{S}$) is the trace of $\boldsymbol{S}$. The RSA of the cluster of particles is then defined as

$$RSA = \frac{3}{2} \frac{tr(\widehat{\boldsymbol{S}}\widehat{\boldsymbol{S}})}{tr(\boldsymbol{S})^2} \qquad (8)$$

We note that as our systems were at significantly low concentration, these RSA calculations are conducted on small values of N (=10-20 particles). RSA calculations are significantly more reliable when applied to systems with large N. Therefore, we restricted our RSA analysis to trends within a system with changing temperatures, rather than placing quantitative or qualitative emphasis on RSA variation between systems with varying parameters.

We also calculated the mean square displacement (MSD) of the nanoparticle centres (not the strands) in each system at each temperature to understand the relative mobility of the particles in the system before and after cluster formation.

4.2.3 Parameters

We varied the G/C content of the strands from 100%, 83%, 67%, 50%, 33% to 17% in strands of length N_{bases}=12, as shown in Table 4.1.

Table 4.1 Grafted strand sequences with the left-most base grafted to the particle surface.

	Sequence		
G/C content (%)	Outer block G/C	Middle block G/C	Inner block G/C
100	GGGGGGCCCCCC	–	–
67	AAAAGGGGCCCC	AAGGGGCCCCAA	GGGGCCCCAAAA
50	AAAAAAGGGCCC	AAAGGGCCCAAA	GGGCCCAAAAAA
33	AAAAAAAAGGCC	AAAAGGCCAAAA	GGCCAAAAAAAA
17	AAAAAAAAAAGC	AAAAAGCAAAAA	GCAAAAAAAAAA

For a G/C content < 100%, the remaining bases are Adenine (A), serving as spacers. We also varied the G/C placement along the strand to the outer (away from the particle surface), middle, or inner portion of the strand relative to the particle surface, shown in Figure 4.2.

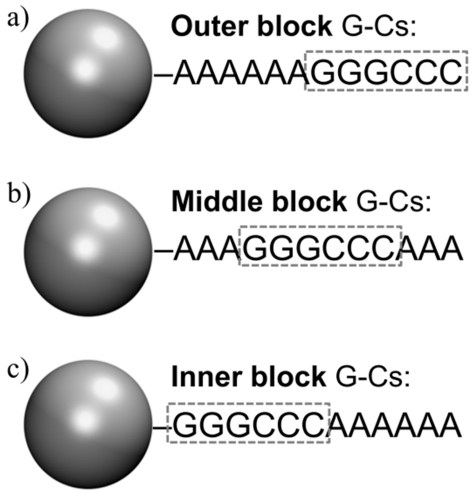

Figure 4.2 Schematic of oligonucleotide sequences with varying G/C placement indicated by grey-dashed box. We show only a single strand per particle for clarity.

We studied two particle diameters, D = $2 \cdot \sigma_{mon}$ and $5 \cdot \sigma_{mon}$ with σ_{mon} ~1 nm as described in the model section. We also varied the number of grafts on the particle surface and the concentration of DNA-functionalised nanoparticles (Table 4.2).

Table 4.2 Parameters varied: (a) number of grafts, N_g, and corresponding grafting density σ (chains/nm^2) for each particle size and (b and c) concentration of DNA-functionalised nanoparticles

(a) Number of grafts, N_g	Grafting Density, σ (chains/nm^2)	
	D=2 nm	D=5 nm
1	0.08	0.01
4	–	0.05
6	–	0.08
8	0.64	0.10
(b) Concentration, c (particles/nm^3) for N_g>1	Number of nanoparticles	Simulation box
0.00001	10	(100 nm)^3
0.00002	20	(100 nm)^3
0.00016	20	(50 nm)^3
0.00032	40	(50 nm)^3
(c) Concentration, c (particles/nm^3) for N_g=1	Number of nanoparticles	Simulation box
0.00013	2	(25 nm)^3
0.00064	10	(25 nm)^3

4.3 Results

4.3.1 Effect of number of grafted DNA strands at 100% G/C content

Figure 4.3 shows the effect of varying number of DNA strands (while maintaining low grafting density) on the thermodynamics and cluster structure for 10 particles in a (100 nm)^3 simulation box, with particles of diameter D=5 nm each with N_g=4, 6, or 8 number of strands of length N_{bases}=12 with 100% G/C content arranged in a diblock (G_6C_6) sequence. For all systems, as the temperature decreases the DNA-grafted nanoparticles assembled into a cluster. The normalised melting curves in Figure 4.3(a) show that as grafting density increases, the melting curves and T_m (identified by the vertical dashed lines in Figure 4.3(a)) shift to higher temperatures.

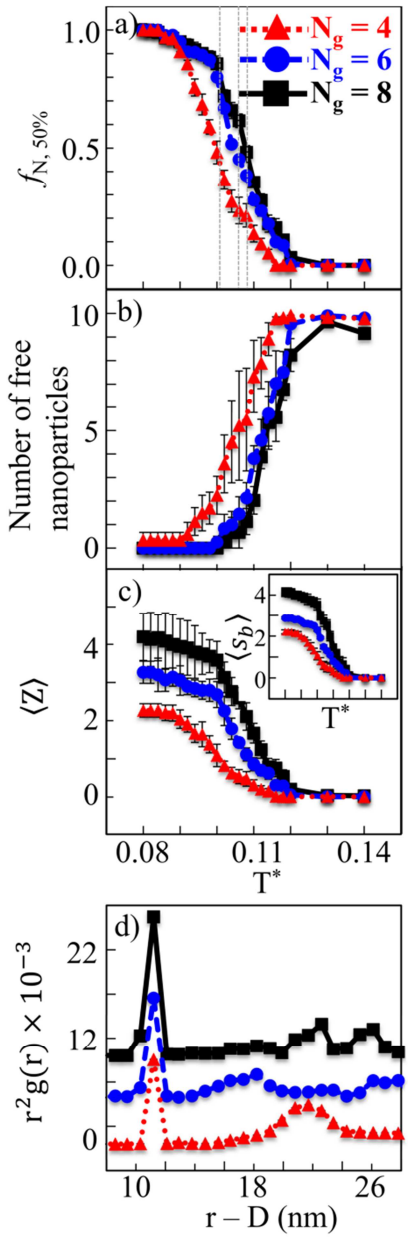

Figure 4.3 (a) Normalised melting curves, (b) number of free nanoparticles, (c) average coordination number, <*Z*>, and (inset) average number of strands bonded per particle, <s_b>, as a function of reduced temperature, T^*, for 10 particles, in (100 nm)^3 box, each of diameter D=5 nm and grafted with N_g=4 (red triangle, dotted line), 6 (blue circle, dashed line) and 8 (black square, solid line) strands of 12 bases each with a diblock (G_6C_6) sequence. Vertical dashed lines in part (a) indicate T_m for each system. (d) Radial distribution function at T_{low}=0.08. $r^2g(r)$ for N_g=6 and 8 are shifted by 5000 and 10000 units in the *y*-axis from $r^2g(r)$ for N_g=4 for clarity.

In the supplementary information (Table S.4.1), we tabulated the T_m determined from heat capacity data, and they showed agreement with the T_m in Figure 4.3(a). The shift to higher temperatures with increasing number of strands has been observed experimentally before (although at relatively higher grafting densities)[14] and can be explained as follows. As number of strands increase, there is a higher enthalpic gain from hybridisation of complementary bases, and a lower entropic loss from hybridisation due to higher crowding between the larger number of strands in the unhybridised state. The plot of the number of free nanoparticles as a function of temperature in Figure 4.3(b) shows that the temperature by which the number of free nanoparticles decreases abruptly, defined as the cluster assembly/dissociation transition temperature, T_d, corresponds to the T_m in these systems, as expected because the hybridisation of the grafted strands leads to assembly of particles.

Next, we characterised the structure within the assembled nanocluster as a function of number of strands. Figure 4.3(c) shows the average coordination number,$\langle Z \rangle$, within the system at each temperature. At a constant temperature below the T_d, the average number of neighbours for every particle,$\langle Z \rangle$, in the cluster increases with increasing grafting density. A neighbour to a particle is defined as another particle with minimum one base pair hybridised between their DNA strands. One could consider the number of neighbours of a particle as its effective 'valency'. Thus, there is an increase in 'valency' with the increasing number of strands, as one would expect; however the 'valency' is not equal to number of strands even at these low grafting densities. The inset in Figure 4.3(c) shows that the average number of strands hybridised (at least 50%) per particle,$\langle s_b \rangle$, correlates with $\langle Z \rangle$, confirming that the number of strands that hybridise dictate the number of neighbours in a cluster. The number of strands hybridised is less than the number of grafts available; the average number of strands hybridized per particle at T_{low}=0.08 for

N_g=4, 6, and 8 strands are 2.2 ± 0.1, 2.9 ± 0.1, and 4.1 ± 0.2 strands, respectively. This is because as the number of strands increases, so does the crowding, thus making it more difficult for a particle to have all N_g strands hybridise to form N_g neighbours.

As the temperature is reduced and as more particles join the clusters, the shape of the clusters shifts from anisotropic (high $\langle RSA \rangle$ at low $\langle N \rangle$) to isotropic (low $\langle RSA \rangle$ at high $\langle N \rangle$) (see supplementary information). We see that as number of strands increased, the shift in clusters from high to low temperature followed a similar path for $\langle RSA \rangle$ and $\langle N \rangle$, resulting in clusters at T_{low} generally composed of all of the nanoparticles and at a low $\langle RSA \rangle$ (relatively isotropic).

At T_{low}=0.08 (Figure 4.3(d)) for all three number of strands, the first peak in $r^2g(r)$ occurs at $r–D$ ~11 nm. This means particles that hybridise with each others' strands are spaced at approximately the length of the strands for strands with 100% G/C composition and diblock sequence (G_6C_6) because of the complete hybridisation between *surface*-G_6C_6 and complementary strand C_6G_6-*surface*. Additional results in supplementary information further confirmed that the strand length determines the inter-particle spacing within the clusters, as expected which is in agreement with some past work.[23] We have studied other G/C arrangements—(G_1C_1) and (G_2C_2)—in strands with 100% G/C content and shown their effect on inter-particle distances (see supplementary Figure S.4.6); however, for the remainder of this paper we focused only on diblock sequence.

4.3.2 Effect of G/C content and particle size

We next determined at constant number of strands the effect of G/C content (100%, 67%, 50%, 33% and 17% G/C) arranged in a diblock fashion with the G/C bases placed in the outermost section of the strand (Figure 4.2(a)). The remaining spacer portion of the strand made of Adenine

nucleotides do not hybridise during assembly. We studied 10 particles of diameter D=5 nm, N_{bases}=12 and N_g=8 (σ=0.10 chains/nm^2) in a (100 nm)^3 simulation box. From the normalised melting curve (Figure 4.4(a)) and the plot of number of free nanoparticles versus temperature (Figure 4.4(b)), we found that as the G/C content increases, the melting temperature, T_m, and cluster dissociation temperature, T_d, increased.

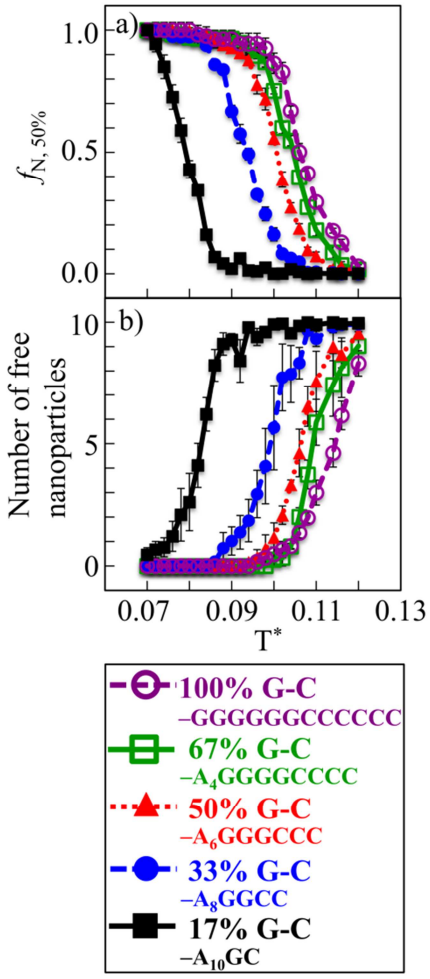

Figure 4.4 (a) Normalised melting curves and (b) number of free nanoparticles as a function of reduced temperature, T^*, for 10 particles, in (100 nm)^3 box, each of diameter D=5 nm and grafted with N_g=8 strands of 12 bases each with sequence shown in legend. Error bars are calculated from the average of three trials.

This was expected because as G/C content increases, there is a higher enthalpic drive for hybridisation and assembly. The trend in Figure 4.4(a) and (b) also suggests that at each temperature, there is a minimum G/C content needed for assembly and cluster formation. For example, at T^*=0.10, particles of size D=5 nm with 8 strands of length 12 bases require >33% G/C content for cluster formation. Past experimental work has also shown that there is a minimum G/C base pairing necessary to induce clustering.[30] At a temperature, the enthalpic gain(dependent on G/C content) has to overcome the entropic loss upon hybridisation and assembly for assembly to occur. Because the entropic losses are dependent on particle size, strand length, G/C placement in the strand and grafting density, the enthalpic gain needed for assembly is also expected to be dependent on the above parameters.

Next, we looked at the effect of G/C content as a function of particle size by comparing results from D=5 nm (Figure 4.4) and D=2 nm (Figure 4.5). First, the melting temperature increased on going from D=5 nm (Figure 4.4(a)) to D=2 nm (Figure 4.5(a)), at higher G/C contents. Similar trends were observed in the number of free particles plot (Figure 4.4(b) and Figure 4.5(b)). At a lower G/C content (e.g. 17% and 33% G/C content), we did not observe much difference between the two particle sizes. The fact that most of the differences are evident only at higher G/C content can be explained as follows: at a high G/C content, strands hybridise completely, and as a result, the particles in the cluster are tightly packed (lower inter-particle distances in Figure 4.6 and supplementary Tables S.4.3-S.4.4 and supplementary Figures S.4.7 and S.4.8) in the assembled state. In such conditions, the differences in translational entropy loss with varying particle size are significant. At a low G/C content, the hybridised portion of the strands is small leading to larger spacing between particles (Figure 4.6(a) and Figure 4.6(b)), and as a result the particles have greater mobility within clusters and within the system (see

supplementary information). In such conditions, the differences in translational entropy loss with varying particle size are negligible, leading to negligible differences in cluster dissociation temperature between the two particle sizes.

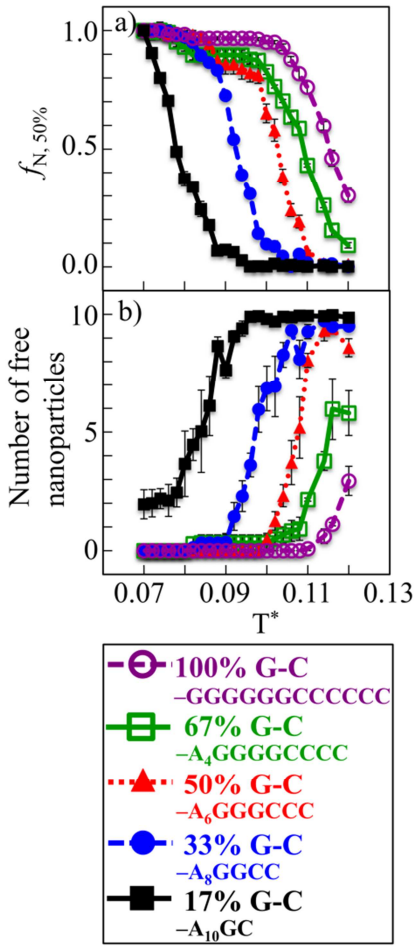

Figure 4.5 (a) Normalised melting curves and (b) number of free nanoparticles as a function of reduced temperature, T^*, for 10 particles, in $(100\ \text{nm})^3$ box, each of diameter D=2 nm and grafted with N_g=8 strands of 12 bases each with sequence shown in legend. Error bars are calculated from the average of three trials.

In the above discussion by keeping the number of strands the same and changing the particle size, we were also changing the grafting density. To eliminate the effect of grafting density and isolate the role of particle diameter on the G/C content effects, we investigated

hybridisation in systems with same number of particles as above (10 particles in the same simulation box size), but only a single strand.

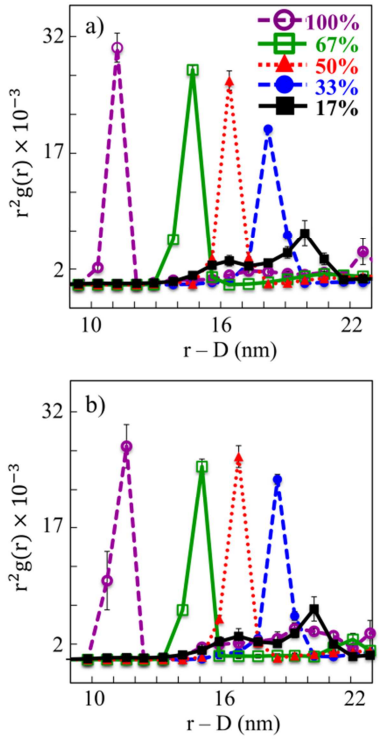

Figure 4.6 Radial distribution function at T^*=0.07 for 10 particles, in $(100\ nm)^3$ box, each of diameter (a) D=5 nm and (b) D=2 nm and grafted with N_g=8 strands of 12 bases with the following G/C contents: 100% (particle-G_6C_6) (purple open circles, dashed line), 67% (particle-$A_4G_4C_4$) (green open squares, solid line), 50% (particle-$A_6G_3C_3$) (red filled triangles, dotted line), 33% (particle-$A_8G_2C_2$) (blue filled circle, dashed line) and 17% (particle-$A_{10}GC$) (black filled square, solid line). Error bars are calculated from the average of 3 trials.

In Table 4.3 for 10 particles with a single DNA strand, at 100% GC we observed an increase in T_d or T_m with decreasing particle size, indicating that the entropic loss upon hybridisation is lower for smaller particles.

Table 4.3 Melting temperatures determined from the melting curves for the systems described in the first two rows. For N_g=8 systems, number of particles is 10, particle diameter is D=5 nm or D=2 nm, each grafted with N_g=8 strands of 12 bases with G/C content shown in the first column. Error bars are calculated from the average of 3 trials. For N_g=1 systems, number of particles shown in the second row each grafted with N_g=1 strand of 12 bases with G/C content shown in the first column. Error bars are calculated from the average of 25 trials. Simulation box sizes listed in supplementary information.

	D=5 nm			D=2 nm		
	10 NP, N_g=8	10 NP, N_g=1	2 NP, N_g=1	10 NP, N_g=8	10 NP, N_g=1	2 NP, N_g=1
100%	0.107 ± 0.002	0.125 ± 0.001	0.125 ± 0.003	0.115 ± 0.001	0.130 ± 0.001	0.131 ± 0.003
67%	0.105 ± 0.001	0.120 ± 0.001	0.120 ± 0.003	0.109 ± 0.000	0.120 ± 0.002	0.127 ± 0.005
50%	0.101 ± 0.001	0.112 ± 0.001	0.111 ± 0.002	0.102 ± 0.001	0.113 ± 0.001	0.122 ± 0.006
33%	0.093 ± 0.001	0.100 ± 0.002	0.098 ± 0.003	0.093 ± 0.001	0.101 ± 0.001	0.112 ± 0.007
17%	0.078 ± 0.001	0.081 ± 0.001	0.082 ± 0.001	0.078 ± 0.000	0.082 ± 0.001	0.090 ± 0.004

When the G/C content decreased, the increase in T_d or T_m becomes negligible. This agreed with the trends discussed above for systems with 10 particles but higher number of grafted strands.

If we decreased the number of particles to two particles with one DNA strand grafted on each particle (Table 4.3 and Figure 4.7) as particle size decreased, T_d or T_m increased for all G/C contents. We noted that in this system the two particles hybridised to form dimers. At this low particle limit, the differences in entropy loss upon dimer formation are significant for the two particle sizes, with the smaller particle losing less translational entropy upon dimer formation, and as a result having higher T_d or T_m than the larger particle.

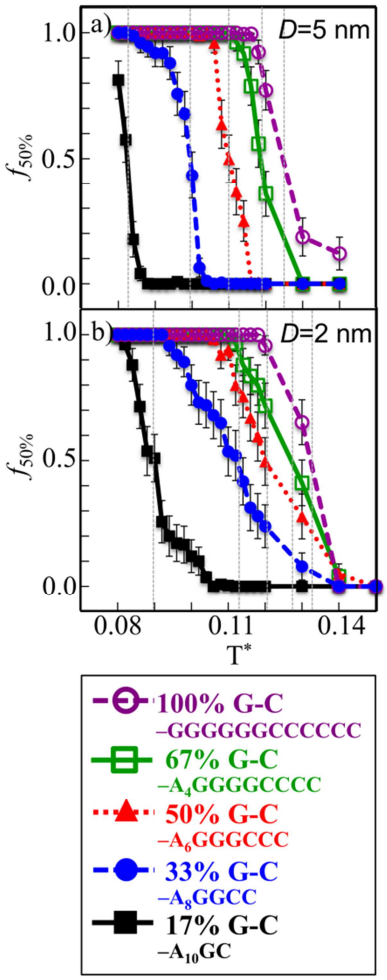

Figure 4.7 Melting curves as a function of reduced temperature, T^*, for 2 particles, each of diameter (a) D=5 nm and (b) D=2 nm, grafted with N_g=1 strand of 12 bases each with sequence shown in legend. Simulation box is (25 nm)^3 for all G/C contents except for 17% where the simulation box is (50 nm)^3. Vertical dashed lines indicate T_m for each system. Error bars are calculated from the average of 25 trials.

4.3.3 Effect of G/C placement along the strand

For G/C content below 100%, the placement of the G/C block along the strands can affect the thermodynamics and structural aspects of the assembly. The G/C diblock can be placed in three different ways (see Figure 4.2 and Table 4.1): inner block where G/C bases are placed closest to the particle surface (*particle*-GGGCCCA$_6$), middle block where the G/C bases are in the centre of the strand (*particle*-A$_3$GGGCCCA$_3$), and outer block where the G/C bases are placed farthest

from the particle surface (*particle*-$A_6GGGCCC$). Figure 4.8 shows the effect of G/C placement in a system of 10 particles of diameter D=5 nm with 8 grafts each of length 12 bases with 50% G/C content.

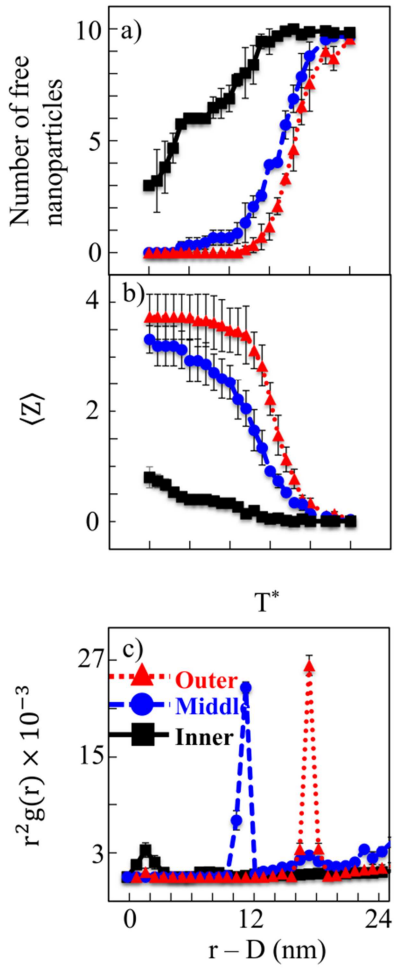

Figure 4.8 (a) Number of free nanoparticles, and (b) average coordination number, <*Z*>, as a function of reduced temperature for 10 particles, in $(100\ nm)^3$ box, each of diameter D=5 nm and grafted with N_g=8 strands of 12 bases with 50% G/C content placed in the outer block (particle-$A_6G_3C_3$) (red filled triangles, dashed line), middle block (particle-$A_3G_3C_3A_3$) (blue filled circle, dashed line) or inner block (particle-$G_3C_3A_6$) (black solid square, solid line). (c) Radial distribution function at T_{low}=0.07. Error bars are calculated from the average of three trials.

Supplementary figures show the corresponding results for 67%, 33% and 17% G/C content. We see similar trends for other G/C contents as 50% discussed below, with the nanoparticles having

a decreasing propensity for cluster formation with decreasing G/C content and the effect being enhanced as G/C placement is moved inward along a strand. For 50% G/C content, as we moved the G/C bases from the outer to middle to inner placement, we observed a decrease in propensity for cluster formation. This is seen in Figure 4.8(a) where for the inner-most placement, the number of free nanoparticles is non-zero at the lowest temperature (and melting temperature not observed in temperature range we studied, Table 4.4).

Table 4.4 Melting temperatures determined from the melting curves for the systems described in the first two rows. For N_g=8 systems, number of particles is 10, particle diameter is D=5 nm or D=2 nm, each grafted with N_g=8 strands of 12 bases of 50% G/C content with G/C placement shown in the first column. Error bars are calculated from the average of 3 trials. For N_g=1 systems, number of particles shown in the second row each grafted with N_g=1 strand of 12 bases of 50% G/C content and G/C placement shown in the first column. Error bars are calculated from the average of 25 trials. Simulation box sizes listed in supplementary information.

	D=5 nm			D=2 nm		
	10 NP, N_g=8	10 NP, N_g =1	2 NP, N_g =1	10 NP, N_g =8	10 NP, N_g =1	2 NP, N_g =1
Outer	0.101 ± 0.001	0.112 ± 0.001	0.111 ± 0.002	0.102 ± 0.001	0.113 ± 0.001	0.122 ± 0.006
Middle	0.096 ± 0.001	0.109 ± 0.001	0.115 ± 0.015	0.099 ± 0.001	0.110 ± 0.001	0.109 ± 0.002
Inner	--	--	--	--	--	--

This is because when the G/C bases are placed close to the particle surface (inner placement), the hybridisation to a complementary inner block on another particle is sterically hindered by the outer spacer nucleotides of the strands. In contrast, the middle and outer placements have significantly lower steric hindrance to cluster formation. In addition, in case of the inner placement the clusters that do form have <Z> ~ 1 (Figure 4.8(b)) in contrast to outer and middle block strands where the G/C bases' placement favors hybridisation with multiple neighbours. The radial distribution function in (Figure 4.8(c)) shows that the inter-particle distances between

nearest neighbours in the cluster increase as the G/C placement moves outward along the strand, as expected. In the few cases in which the inner G/C placement forms clusters, the particles are spaced almost at contact, with inter-particle distances ~1 nm. The middle block placement leads to the inter-particle distances of ~11 nm (base pairing 6 nucleotides + 6 nucleotide-long spacer). Similarly, outer G/C placement leads to an inter-particle spacing of ~16 nm (base pairing 6 nucleotides + 12 nucleotide-long spacer).

Clearly, the inner G/C placement and 50% G/C content showed the lowest propensity for assembly in Figure 4.8. Next, in Figure 4.9 we observed how this behaviour changed for other G/C contents for the inner placement. We found that melting temperature decreased as G/C content decreases (Figure 4.9(a)), because the enthalpic drive for assembly decreases with decreasing G/C content. From the number of free nanoparticles at lowest T^* (Figure 4.9(b)) we oberved that the systems with G/C content > 50% have higher propensity to form clusters, with cluster formation being minimal for 33-50% and absent entirely for 17%. As for the structure, we observed that at higher G/C contents, clusters have a higher number of neighbours (despite same number of grafted strands in all systems) (Figure 4.9(c)) and clearly defined inter-particle distances (Figure 4.9(d)), whereas the lower G/C contents were not able to form clusters (low or 0 number of neighbours in Figure 4.9(c)) and exhibited lack of order in nanoparticle organisation in Figure 4.9(d).

So far, we have discussed the effect of the G/C placement when the G and C nucleotides are positioned *contiguously* in the strand. Next, we present results in which the G and C bases are placed apart in the strand. The sequence (*particle*-$G_3A_6C_3$), in which the G and C bases are placed at the extremes of the strand, has decreased propensity for cluster formation compared with outer block placement of (*particle*-$A_6G_3C_3$) (supplementary Figure S.4.12).

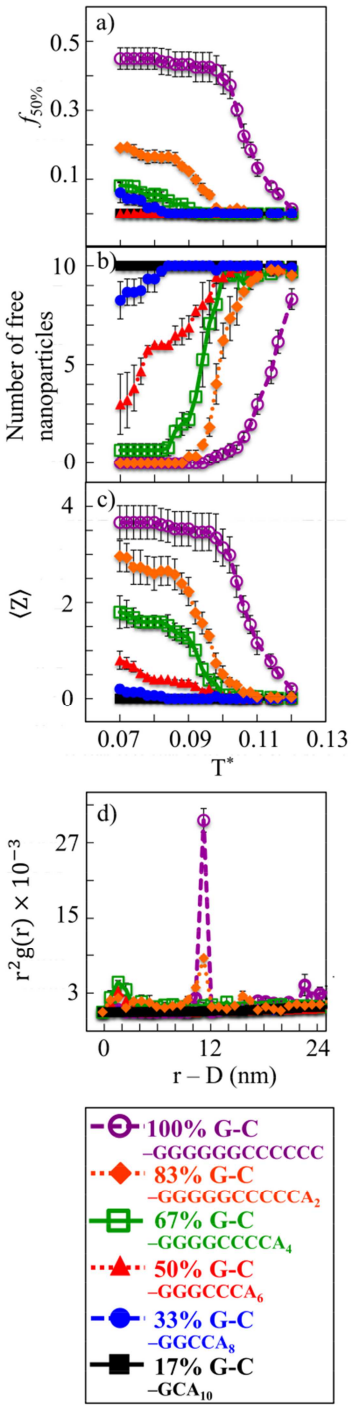

Figure 4.9 (a) Melting curves (not normalised), (b) number of free nanoparticles, and (c) average coordination number as a function of reduced temperature, T^*, for 10 particles, in $(100\ \text{nm})^3$ box, each of diameter D=5 nm and grafted with N_g=8 strands of 12 bases each with sequence shown in legend. (d) Radial distribution function at T_{low}=0.07. Error bars are calculated from the average of three trials.

In contrast, the system where the G_3C_3 contiguous block is in the middle of the strand (*particle*-$A_3G_3C_3A_3$) and the system where G and C bases are at the extremes of the strand (*particle*-$G_3A_6C_3$) hybridise similarly because both sequences require full alignment of strands for complete hybridisation of the G and C nucleotides (see supplementary Figure S.4.13). But the middle block G/C sequences have a higher cluster dissociation temperature than at the extremes strands because the extremes of strands sequences undergo a greater entropic loss upon hybridisation. The fact that the placement of the hybridising bases, together or a apart affects the cluster formation suggests that a minimum contiguous block of hybridising bases is necessary to favor strand hybridisation and as a result nanoparticle assembly.

4.3.4 Effect of particle concentration

Although all of the above results are at one dilute concentration, c=0.00001 particles/nm^3 (10 particles in a (100 nm)^3 simulation box), to examine how the above results are affected by changing to other dilute concentrations, we also simulated c=0.00002 particles/nm^3, c=0.00016 particles/nm^3 and c=0.00032 particles/nm^3 (see Table 4.2). Table 4.5 shows that as concentration increases, T_m and T_d increase. As concentration increased, the number of bases that can hybridise increased (higher enthalpic gain upon assembly) and the crowding increased (lower entropic loss upon assembly). The average number of neighbours and the average number of strands hybridized, however, appeared to reach a maximum (confirmed in N_g=4 system at the two highest concentrations). As one would expect, the inter-particle spacing is invariant with increasing concentration for all systems because the strand design, not how many particles are present, dictates how far nanoparticles are spaced in a cluster.

Table 4.5 Thermodynamic and structural aspects of various systems. Concentration, c, melting temperature, T_m, average coordination number, $\langle Z \rangle$, average number of strands bonded, $\langle s_b \rangle$, and inter-particle spacing are averages of 3 trials. For top portion of the table, D=5 nm particles are grafted N_g=4, 6 and 8, number of strands with N_{bases}=12 and 100% G/C in a diblock sequence. For outer and inner placement, D=5 nm particles are grafted N_g=8 with N_{bases}=12 G/C content is 50% in a diblock sequence.

	c (particles/nm^3)	T_m	$\langle Z \rangle$ at $T_{low} = 0.08$	$\langle s_b \rangle$ at $T_{low} = 0.08$	Inter-particle spacing
N_g=4	0.00001	0.100 ± 0.002	2.3 ± 0.2	2.2 ± 0.1	11.2 ± 0.0
	0.00002	0.104 ± 0.001	2.7 ± 0.2	2.7 ± 0.1	11.2 ± 0.0
	0.00016	0.115 ± 0.000	3.4 ± 0.2	3.2 ± 0.0	11.4 ± 0.0
	0.00032	0.116 ± 0.000	3.5 ± 0.3	3.2 ± 0.1	11.4 ± 0.0
N_g =6	0.00001	0.105 ± 0.001	3.3 ± 0.3	2.9 ± 0.1	11.2 ± 0.0
	0.00002	0.110 ± 0.001	3.3 ± 0.1	3.3 ± 0.5	11.2 ± 0.0
	0.00016	0.116 ± 0.000	4.5 ± 0.5	4.0 ± 0.0	11.4 ± 0.0
N_g =8	0.00001	0.107 ± 0.001	4.2 ± 0.6	4.1 ± 0.2	11.2 ± 0.0
	0.00002	0.110 ± 0.000	4.1 ± 0.7	4.1 ± 0.1	11.2 ± 0.0
	0.00016	0.118 ± 0.000	5.1 ± 0.2	4.7 ± 0.0	11.3 ± 0.1
Outer	0.00001	0.101 ± 0.002	3.2 ± 0.4	3.3 ± 0.1	16.4 ± 0.0
	0.00016	0.110 ± 0.000	6.0 ± 0.5	5.3 ± 0.1	16.7 ± 0.0
Inner	0.00001	--	0.6 ± 0.1	0.0 ± 0.0	0.7 ± 0.0
	0.00016	0.092 ± 0.002	2.2 ± 0.3	0.6 ± 0.1	1.0 ± 0.1

For 50% G/C content and outer block placement, the number of strands hybridised and nanoparticle neighbours increased. Placing the hybridising bases on the outer portion of the strand for a system with higher concentration increased the likelihood of bonding because enthalpically favourable contacts can form with minimal steric hindrance to the strands. For inner block placement of G/Cs, although the lowest concentration led to minimal cluster formation, an increase in concentration helped strands overcome the entropic loss of close packing by the enthalpic gain of hybridisation (see Table 4.5 and supplementary Figure S.4.14).

4.4 Conclusion

We have studied using molecular dynamics simulations systems of DNA-functionalised nanoparticles that assemble through hybridisation of the grafted DNA strands and demonstrated how the composition of the grafted DNA strand (G/C content and placement of the G/C along the strand) affects assembly thermodynamics and structure as a function of ssDNA grafting density and particle size. Given a particle diameter and grafting density, the following design rules can be followed to obtain a target cluster structure or target cluster association/dissociation temperature. To increase the inter-particle spacing within an assembled cluster: (i) at constant strand length, decrease the G/C content and place the G/C on the part of the strand farthest from the surface of the particle or (ii) at constant G/C content and outer most placement of G/C bases, increase the strand length. To reduce the sizes of the cluster or the propensity of cluster formation one could reduce G/C content and shift the G/C bases closer to the particle surface, placing the spacers on the outside portion of the strand. To increase the cluster dissociation temperature, one could increase the G/C content of the strands, or at a constant G/C content, shift the G/C blocks to the outer portion of the strand.

We noted a few limitations of the model used in this study. One limitation is that these systems mimic cases where the electrostatic interactions are completely screened, making it difficult for us to replicate experimental findings on the effect of salt concentration on the assembly. Furthermore, strand flexibility should increase in the prsence of higher salt concentration affecting how the ssDNA facilitates assembly, a feature we were not able to capture with this model. Following the model proposed by Sciortino and colleagues,[12, 13] we expected to capture the essential equilibrium features of DNA hybridisation-directed nanoparticle assembly in conditions in which electrostatic interactions are completely screened.[34]

Another limitation is that the DNA strands in our model are fixed at specific locations, whereas synthesis of DNA-functionalised gold nanoparticles using Au-thiol non-covalent binding will allow strands to move on the surface. Lastly, we have not modelled non-specific interactions between the bases and the surface which has been seen with thymine bases and gold surface.

Despite these limitations, our study provides valuable guidance to experimentalists on how G/C content and placement in ssDNA can be tailored for target assembly, in terms of both structure and thermodynamics. Understanding how to finely balance enthalpic and entropic driving forces for assembly/dispersion with changing parameters (particle size, grafting density, G/C content, G/C placement, particle concentration) is non-trivial, and our study provides valuable insight into this complex interplay of parameters.

4.5 References

1. C. W. Hsu, F. Sciortino and F. W. Starr, *Physical Review Letters*, 2010, **105**.
2. D. Nykypanchuk, M. M. Maye, D. van der Lelie and O. Gang, *Nature*, 2008, **451**, 549-552.
3. R. Dreyfus, M. E. Leunissen, R. J. Sha, A. V. Tkachenko, N. C. Seeman, D. J. Pine and P. M. Chaikin, *Physical Review Letters*, 2009, **102**.
4. R. Dreyfus, M. E. Leunissen, R. Sha, A. Tkachenko, N. C. Seeman, D. J. Pine and P. M. Chaikin, *Physical Review E*, 2010, **81**.
5. O. Padovan-Merhar, F. V. Lara and F. W. Starr, *Journal of Chemical Physics*, 2011, **134**.
6. B. M. Mognetti, M. E. Leunissen and D. Frenkel, *Soft Matter*, 2012, **8**, 2213-2221.
7. W. Dai, S. K. Kumar and F. W. Starr, *Soft Matter*, 2010, **6**, 6130-6135.
8. M. R. Jones, R. J. Macfarlane, B. Lee, J. A. Zhang, K. L. Young, A. J. Senesi and C. A. Mirkin, *Nature Materials*, 2010, **9**, 913-917.
9. E. Auyeung, J. I. Cutler, R. J. Macfarlane, M. R. Jones, J. S. Wu, G. Liu, K. Zhang, K. D. Osberg and C. A. Mirkin, *Nature Nanotechnology*, 2012, **7**, 24-28.
10. W. B. Rogers and J. C. Crocker, *Proceedings of the National Academy of Sciences of the United States of America*, 2011, **108**, 15687-15692.
11. T. Li, R. Sknepnek, R. J. Macfarlane, C. A. Mirkin and M. O. de la Cruz, *Nano Letters*, 2012, **12**, 2509-2514.

12. F. W. Starr and F. Sciortino, *Journal of Physics-Condensed Matter*, 2006, **18**, L347-L353.
13. J. Largo, F. W. Starr and F. Sciortino, *Langmuir*, 2007, **23**, 5896-5905.
14. R. C. Jin, G. S. Wu, Z. Li, C. A. Mirkin and G. C. Schatz, *Journal of the American Chemical Society*, 2003, **125**, 1643-1654.
15. J. J. Storhoff, A. A. Lazarides, R. C. Mucic, C. A. Mirkin, R. L. Letsinger and G. C. Schatz, *Journal of the American Chemical Society*, 2000, **122**, 4640-4650.
16. T. R. Prytkova, I. Eryazici, B. Stepp, S. B. Nguyen and G. C. Schatz, *Journal of Physical Chemistry B*, 2010, **114**, 2627-2634.
17. P. L. Biancaniello, A. J. Kim and J. C. Crocker, *Physical Review Letters*, 2005, **94**.
18. R. T. Scarlett, M. T. Ung, J. C. Crocker and T. Sinno, *Soft Matter*, 2011, **7**, 1912-1925.
19. S. Y. Park, A. K. R. Lytton-Jean, B. Lee, S. Weigand, G. C. Schatz and C. A. Mirkin, *Nature*, 2008, **451**, 553-556.
20. C. H. Kiang, *Physica A*, 2003, **321**, 164-169.
21. B. D. Smith, N. Dave, P. J. J. Huang and J. W. Liu, *Journal of Physical Chemistry C*, 2011, **115**, 7851-7857.
22. Y. Sun, N. C. Harris and C. H. Kiang, *Physica A*, 2005, **354**, 1-9.
23. C. A. Mirkin, R. L. Letsinger, R. C. Mucic and J. J. Storhoff, *Nature*, 1996, **382**, 607-609.
24. A. P. Alivisatos, K. P. Johnsson, X. G. Peng, T. E. Wilson, C. J. Loweth, M. P. Bruchez and P. G. Schultz, *Nature*, 1996, **382**, 609-611.
25. D. Nykypanchuk, M. M. Maye, D. van der Lelie and O. Gang, *Langmuir*, 2007, **23**, 6305-6314.
26. A. J. Kim, R. Scarlett, P. L. Biancaniello, T. Sinno and J. C. Crocker, *Nature Materials*, 2009, **8**, 52-55.
27. V. T. Milam, A. L. Hiddessen, J. C. Crocker, D. J. Graves and D. A. Hammer, *Langmuir*, 2003, **19**, 10317-10323.
28. D. B. Lukatsky and D. Frenkel, *Journal of Chemical Physics*, 2005, **122**.
29. N. Geerts and E. Eiser, *Soft Matter*, 2010, **6**, 4647-4660.
30. S. J. Hurst, H. D. Hill and C. A. Mirkin, *Journal of the American Chemical Society*, 2008, **130**, 12192-12200.
31. D. Frenkel and B. Smit, *Understanding Molecular Simulation: From Algorithms to Applications*, Academic Press, San Diego, 2002.
32. G. J. Martyna, D. J. Tobias and M. L. Klein, *Journal of Chemical Physics*, 1994, **101**, 4177-4189.
33. D. N. Theodorou and U. W. Suter, *Macromolecules*, 1985, **18**, 1206-1214.
34. J. C. Araque, A. Z. Panagiotopoulos and M. A. Robert, *Journal of Chemical Physics*, 2011, **134**.

4.6 Supplementary Information

4.6.1 Reduced model parameters used in the Molecular Dynamics code and method details

Table S.4.1 Summary of the typical properties for each sphere and interaction in reduced form. Note the mass of each sphere *m* is typically calculated directly from the volume of the sphere, assuming all spheres in the model have the same density.

Property	**Reduced form (as input into simulation)**
Mass of sphere (*m*)	$m^* = m/m_{mon}$
Radius of sphere (*r*)	$r^* = r/\sigma_{mon}$
LJ energy parameter for sphere (ε_{LJ})	$\varepsilon_{LJ}^* = \varepsilon_{LJ}/\varepsilon_{mon}$
Three body strength ($\varepsilon_{3\text{-}body}$)	$\varepsilon_{3-body}^* = \varepsilon_{3-body}/\varepsilon_{mon}$
FENE interaction strength (ε_{FENE})	$\varepsilon_{FENE}^* = \varepsilon_{FENE}/\varepsilon_{mon}$
Simulation domain size (*L*)	$L^* = L/\sigma_{mon}$
Temperature (*T*)	$T^* = T/(\varepsilon_{mon}/k_B)$
Time (*t*)	$t^* = t/\left(\sigma_{mon} \cdot (m_{mon}/\varepsilon_{mon})^{1/2}\right)$

Method details: to increase computational efficiency, a full linked-cell search is used for evaluating the LJ interactions on regular intervals. This linked-cell search also generates a list of possible interaction partners for each sphere. At intervening time steps, the partner list is used to evaluate LJ interactions rather than performing a full linked-cell search.

4.6.2 Validation of in-house code

To confirm that our locally authored code can replicate trends seen experimentally, we perform validation trials with the following parameters.

4.6.2.1 Effect of grafting density on melting temperature

Past work shows that as grafting density increases, the melting temperature, T_m, increases, while melting transition sharpens.[14]

We tested, in a simulation box $(100\ nm)^3$, 10 particles of diameter D=5 nm, 12 bases on each strand, diblock sequence of 100% G-C content and varied the number of grafts per particle: N_g=3, 4, 6, 8, or 12. The N_g=12 system best correlates to the experimental strand length/D ratio. Experimentally: D=13 nm particles are linked by strands composed of 30 bases, so strand length/D≈2. For this system: (strand length=12)/(D=5)≈2. The number of grafts per particle N_g=3, 4, 6, 8, 12 correspond to grafting densities: σ=0.03, 0.05, 0.08, 0.10 and 0.15 chains/nm^2, respectively.

We see in Figure S1 that as grafting density increases, melting temperature, T_m, increases and the melting transition breadth decreases.

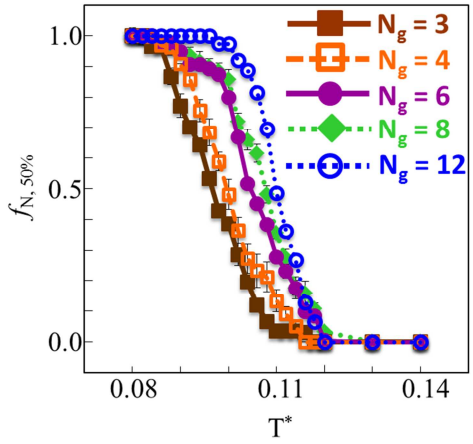

Figure S.4.1 Normalized melting curves as a function of reduced temperature, T^*, for 10 particles, in $(100\ nm)^3$ box, each of diameter D=5 nm and grafted with N_g=3, 4, 6, 8, or 12 strands of 12 bases each with a diblock G_6C_6 sequence. Error bars are calculated from the average of 3 trials.

As grafting density increases, there is a higher enthalpic gain from hybridization of complementary bases due to a higher number of strands, and a lower entropic loss from hybridization due to higher crowding between the strands at high grafting density in the unhybridized (melted) state.

4.6.2.2 Effect of strand length on melting temperature

Past work shows that as strand length increases, T_m increases.[15, 22] Strand length determines the number of possible G-C bonds between adjacent nanoparticles. As strands length increases, number of bases and thus G-C bonds increases, increasing the temperature needed for breaking the higher number of G-C bonds.

We tested, in a simulation box $(100\ \text{nm})^3$, 10 particles of diameter D=5 nm (Figure S2(a)), number of grafts per particle N_g=6, diblock sequence of 100% G-C content, and varied the number of bases per strand N_{bases} from 6 to 12 to 24.

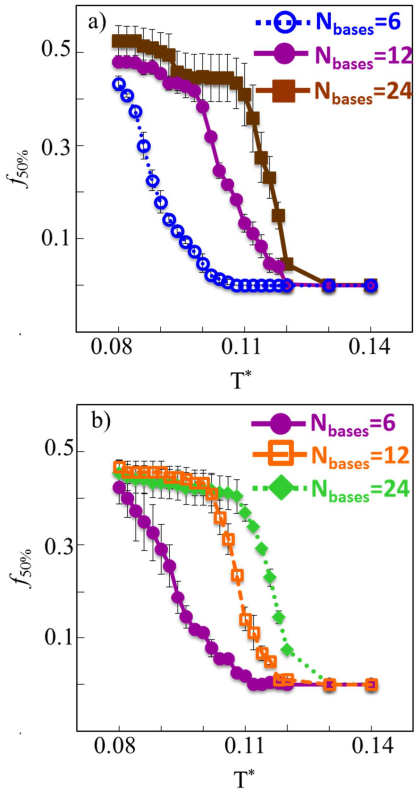

Figure S.4.2 Melting curves (not normalized) as a function of reduced temperature, T^*, for 10 particles, in $(100\ \text{nm})^3$ box, each of diameter (a) D=5 nm and (b) D=4 nm, and grafted with N_g=6 strands of 6, 12 or 24 bases each with a diblock G_6C_6 sequence. Error bars are calculated from the average of 3 trials.

The melting temperature increases as strand length increases. We perform the same test with particles of diameter D=4 nm (Figure S2(b)), in a box of $(100\ nm)^3$, number of grafts per particle N_g=6, diblock sequence of 100% G-C content, and varying number of bases per strand N_{bases} from 6 to 12 to 24. We confirm that the melting temperature increases as strand length increases for both systems we studied.

4.6.2.3 Effect of particle diameter on melting temperature breadth

As particle diameter increases, the melting transition becomes sharper.[22, 28]

At constant grafting density, an increased particle diameter results in increased number of grafts per particle. The increased grafts have enthalpic gain and melt at higher temperatures, per discussion of effect of grafting density. Additionally, the increased number of grafts is thought to induce cooperativity in melting, causing the melting transition to sharpen.

We tested 10 particles, in $(100\ nm)^3$, grafting density σ=0.033 chains/nm^2, N_{bases}=12, diblock sequence of 100% G-C content and varying particle size D=5 nm (3 grafts each) and D = 10 nm (10 grafts each). We see two important trends in Figure S3: 1) as particle size increases, the melting transition gets sharper and 2) as the number of grafts increases, T_m increases.

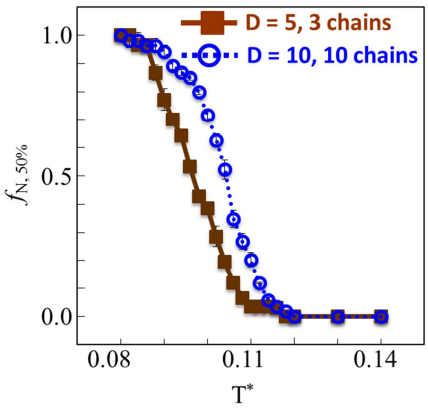

Figure S.4.3 Normalized melting curves as a function of reduced temperature, T^*, for 10 particles, in $(100\ nm)^3$ box, each of D=5 nm grafted with N_g=3 strands or D=10 nm grafted with N_g=10 strands (σ=0.033 chains/nm^2 for both systems) of 12 bases each with a diblock G_6C_6 sequence. Error bars are calculated from the average of 3 trials.

4.6.3 Melting curve prior to normalization for grafting density study

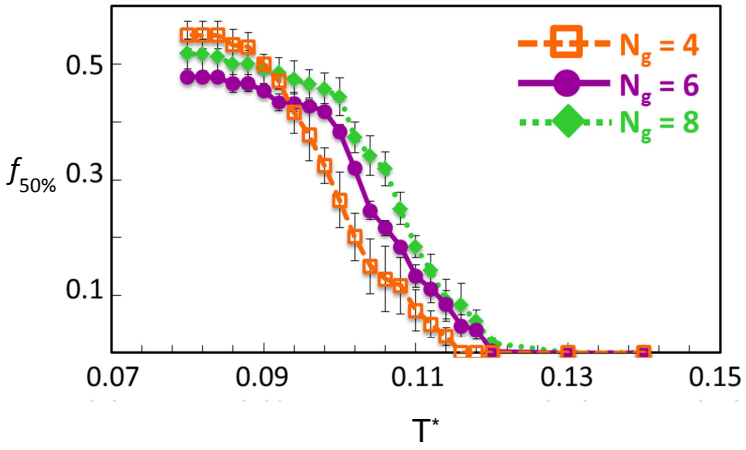

Figure S.4.4 Melting curves prior to normalization as a function of reduced temperature, T^*, for 10 particles, in $(100\ nm)^3$ simulation box, each of diameter D=5 nm and grafted with N_g=4, 6 and 8 strands of 12 bases each with a diblock (G_6C_6) sequence. Fraction of strands bonded, $f_{50\%}$, represents strands with minimum 50% G-C bonded. Error bars are calculated from the average of 3 trials.

4.6.4 Melting temperatures determined from melting curve and from heat capacity, C_v, for grafting density study

	T_m determined from melting curve	T_m determined from C_v
N_g=4	0.100 ± 0.002	0.094 ± 0.002
N_g=6	0.105 ± 0.001	0.105 ± 0.005
N_g=8	0.107 ± 0.001	0.105 ± 0.004

Table S.4.2 Melting temperature, T_m, determined from melting curve (2nd column) and heat capacity, C_v, (3rd column) for 10 particles, in (100 nm)^3 box, each of diameter D=5 nm and grafted with N_g=4, 6 and 8 strands of 12 bases each with a diblock (G_6C_6) sequence. Error bars are calculated from the average of 3 trials.

4.6.5 Inter-particle spacing determined by graft length

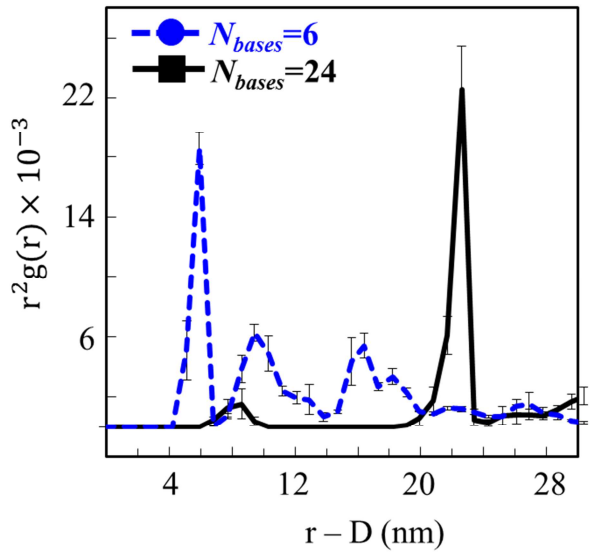

Figure S.4.5 Radial distribution function at T^*=0.08 for 10 particles, in (100 nm)^3 box, each of diameter D=5 nm and grafted with N_g=6 strands composed of 6 bases and 24 bases, each with a diblock sequence. For N_{bases}=6, r – D ~6 nm and for N_{bases}=24, r – D ~23 nm, confirming that strand length chosen determines inter-particle spacing.

4.6.6 Inter-particle spacing caused by various sequences

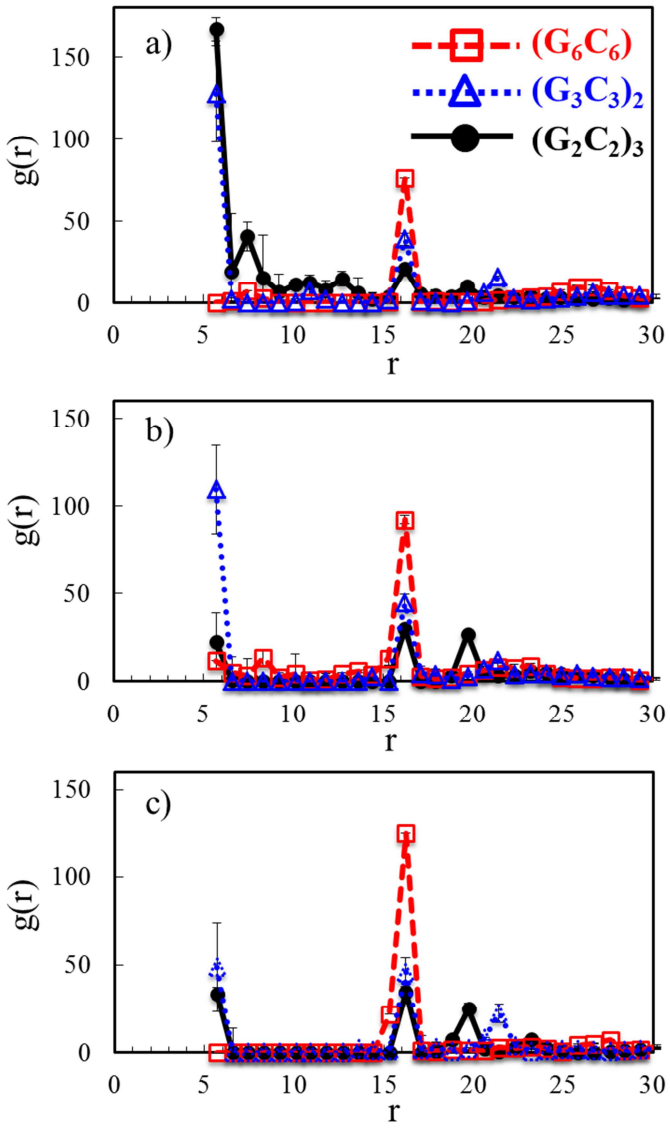

Figure S.4.6 Radial distribution function at T^*=0.08 for 10 particles, in $(100\ nm)^3$ box, each of diameter D=5 nm and grafted with (a) N_g=4, (b) N_g=6, and (c) N_g=8 strands composed of 12 bases and the following sequences: (G_6C_6) (red open square-dashed line), $(G_3C_3)_2$ (blue open triangle-dotted line), and $(G_2C_2)_3$ (black filled circle-solid line). For all grafting densities, the diblock (G_6C_6) sequence has one major peak at r ~16 nm, resulting in particles that are spaced according to the strand length (r – D = 11 nm, and strand length is 12). Remaining intermediate blockiness sequences (shown here are $(G_2C_2)_3$ and $(G_3C_3)_2$) have variable inter-particle spacing for each sequence and grafting density.

4.6.7 Inter-particle spacing for varying G-C content and strand end-to-end distances, $<R_{ee}>$

First neighbor peak from g(r) gives the inter-particle spacing, actual r – D, for each G-C content listed. We calculate the expected r – D by summing the G-C binding block and twice the A-spacer length. We show the strand end-to-end distance per temperature to show that when the expected inter-particle distance deviates from the actual inter-particle distance that strands typically remain as flexible in the cluster (at T_{low}) as they were before hybridization (at T_{high}). This happens most prominently with sequences that have a high number of spacers, i.e. 17%.

	Actual $r - D$ (nm)	Expected $r - D$ (nm)	Δ
100%	11.2 ± 0.0	12	0.8
67%	14.7 ± 0.0	16	1.3
50%	16.4 ± 0.0	18	1.6
33%	18.2 ± 0.0	20	1.8
17%	18.7 ± 1.2	22	3.3

Table S.4.3 First neighbor peak from g(r) gives the inter-particle spacing, actual $r - D$, for each G-C content listed for 10 particles in $(100\ \text{nm})^3$, D=5 nm, N_{bases}=12, outer block placement of G-C diblock of shown G-C content. We calculate the expected r – D by summing the G-C binding block and twice the A-spacer length. Error bars are calculated from the average of 3 trials.

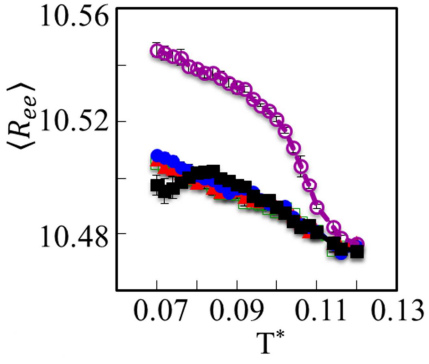

Figure S.4.7 Strand end-to-end-distance, $\langle R_{ee} \rangle$, per temperature for 10 particles in $(100\ \text{nm})^3$, D=5 nm, N_{bases}=12, outer block placement of G-C diblock of G-C content: 100% (purple open circles, dashed lines), 67% (green open squares, solid line), 50% (red filled triangle, dashed line), 33% (filled blue circle, dashed line), and 17% (black filled square, solid line). Error bars are calculated from the average of 3 trials.

Table S.4.4 First neighbor peak from g(r) gives the inter-particle spacing, actual $r - D$, for each G-C content listed for 10 particles in $(100\ \text{nm})^3$, D=2 nm, N_{bases}=12, outer block placement of G-C diblock of shown G-C content. We calculate the expected r – D by summing the G-C binding block and twice the A-spacer length. Error bars are calculated from the average of 3 trials.

	Actual r – D (nm)	Expected r – D (nm)	Δ
100%	11.3 ± 0.2	12	0.7
67%	15.1 ± 0.0	16	0.9
50%	16.8 ± 0.0	18	1.2
33%	18.6 ± 0.0	20	1.4
17%	19.1 ± 1.2	22	2.9

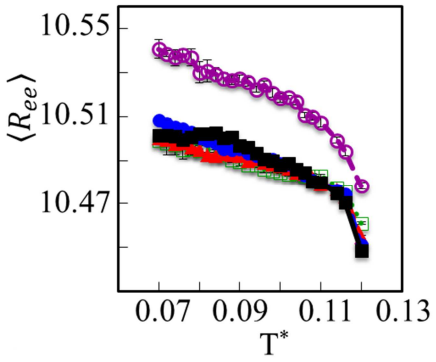

Figure S.4.8 Strand end-to-end-distance, $\langle R_{ee} \rangle$, per temperature for 10 particles in $(100\ \text{nm})^3$, D=2 nm, N_{bases}=12, outer block placement of G-C diblock of G-C content: 100% (purple open circles, dashed lines), 67% (green open squares, solid line), 50% (red filled triangle, dashed line), 33% (filled blue circle, dashed line), and 17% (black filled square, solid line). Error bars are calculated from the average of 3 trials.

4.6.8 Effect of G-C placement for 67%, 33%, and 17% G-C content

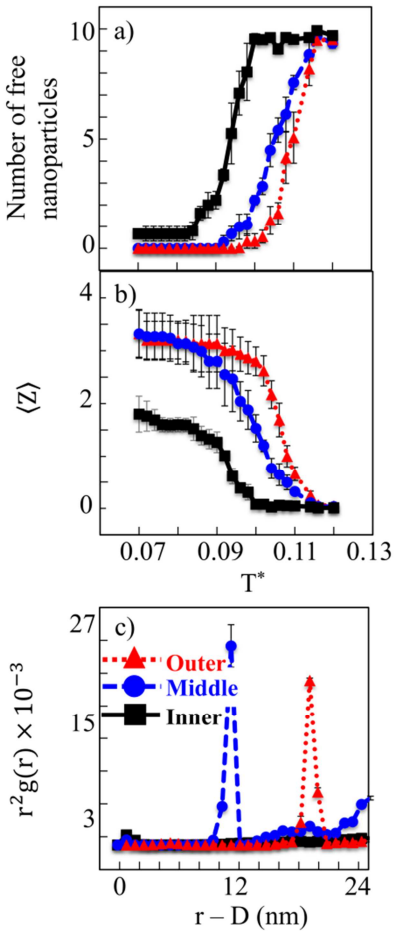

Figure S.4.9 (b) Number of free nanoparticles and (b) average coordination number, <Z>, as a function of reduced temperature for 10 particles, in $(100\ nm)^3$ box, each of diameter D=5 nm and grafted with N_g=8 strands of 12 bases with 67% G-C content placed in the outer block (*particle*-$A_4G_4C_4$) (red filled triangles, dashed line), middle block (*particle*-$A_2G_4C_4A_2$) (blue filled circle, dashed line) or inner block (*particle*-$G_4C_4A_4$) (black solid square, solid line). Vertical dashed lines indicate T_m for each system except for the inner block G-C system. (c) Radial distribution function at T_{low}=0.07. Error bars are calculated from the average of 3 trials.

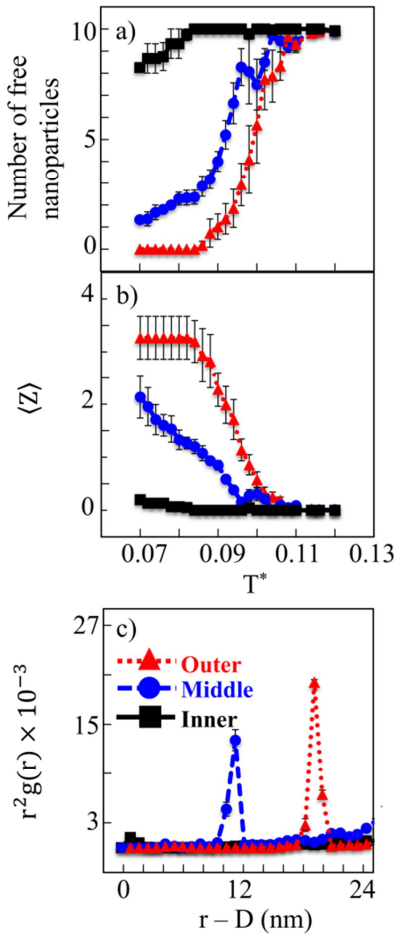

Figure S.4.10 (b) Number of free nanoparticles and (b) average coordination number, <Z>, as a function of reduced temperature for 10 particles, in $(100\ nm)^3$ box, each of diameter D=5 nm and grafted with N_g=8 strands of 12 bases with 33% G-C content placed in the outer block (*particle*-$A_8G_2C_2$) (red filled triangles, dashed line), middle block (*particle*-$A_4G_2C_2A_4$) (blue filled circle, dashed line) or inner block (*particle*-$G_2C_2A_8$) (black solid square, solid line). Vertical dashed lines indicate T_m for each system except for the inner block G-C system. (c) Radial distribution function at T_{low}=0.07. Error bars are calculated from the average of 3 trials.

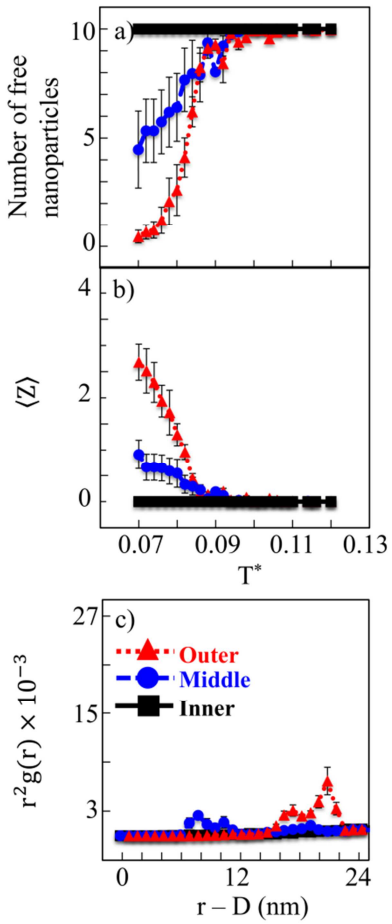

Figure S.4.11 (b) Number of free nanoparticles and (b) average coordination number, <Z>, as a function of reduced temperature for 10 particles, in $(100\ nm)^3$ box, each of diameter D=5 nm and grafted with N_g=8 strands of 12 bases with 17% G-C content placed in the outer block (*particle*-$A_{10}GC$) (red filled triangles, dashed line), middle block (*particle*-A_5GCA_5) (blue filled circle, dashed line) or inner block (*particle*-GCA_{10}) (black solid square, solid line). (c) Radial distribution function at T_{low}=0.07. Error bars are calculated from the average of 3 trials.

4.6.9 Effect of G-C binding block placement on assembly thermodynamics and structure: main paper Figure 4.8 with additional sequence

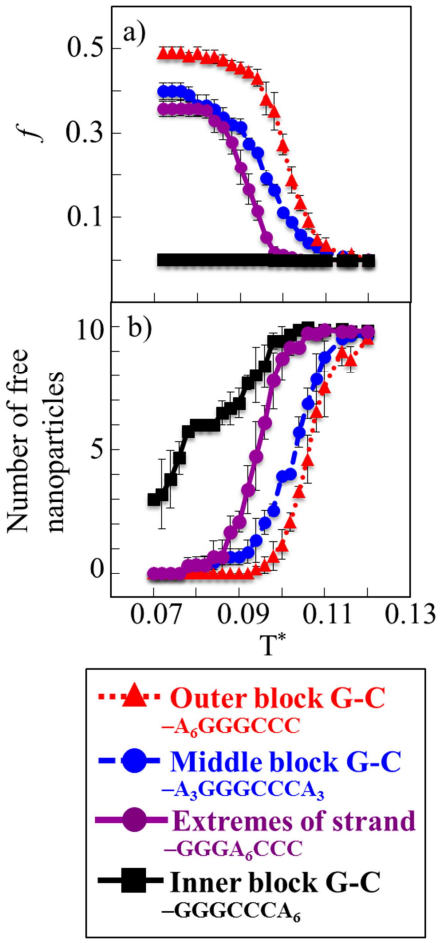

Figure S.4.12 (a) Melting curves (not normalized) and (b) number of free nanoparticles as a function of reduced temperature for 10 particles, in $(100\ \text{nm})^3$ box, each of diameter D=5 nm and grafted with N_g=8 strands of 12 bases with 50% G-C content placed in the outer block (*particle*-$A_6G_3C_3$) (red filled triangles, dashed line), middle block (*particle*-$A_3G_3C_3A_3$) (blue filled circle, dashed line), extremes of strand (*particle*-G3A6C3) (purple filled circle, solid line), or inner block (*particle*-$G_3C_3A_6$) (black solid square, solid line).

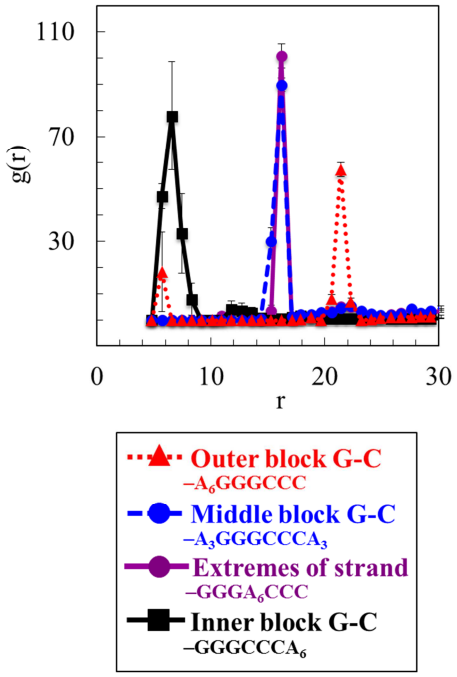

Figure S.4.13 Radial distribution function for 10 particles, in $(100\ nm)^3$ box, each of diameter D=5 nm and grafted with N_g=8 strands of 12 bases with 50% G-C content placed in the outer block (*particle*-$A_6G_3C_3$) (red filled triangles, dashed line), middle block (*particle*-$A_3G_3C_3A_3$) (blue filled circle, dashed line), extremes of strand (*particle*-G3A6C3) (purple filled circle, solid line), or inner block (*particle*-$G_3C_3A_6$) (black solid square, solid line). In the middle block and extremes of strand sequences, for the G-C diblock to hybridize with another strand, both strands must completely align, resulting in the same inter-particle distance.

4.6.10 Effect of concentration on assembly of G-C binding block placement systems

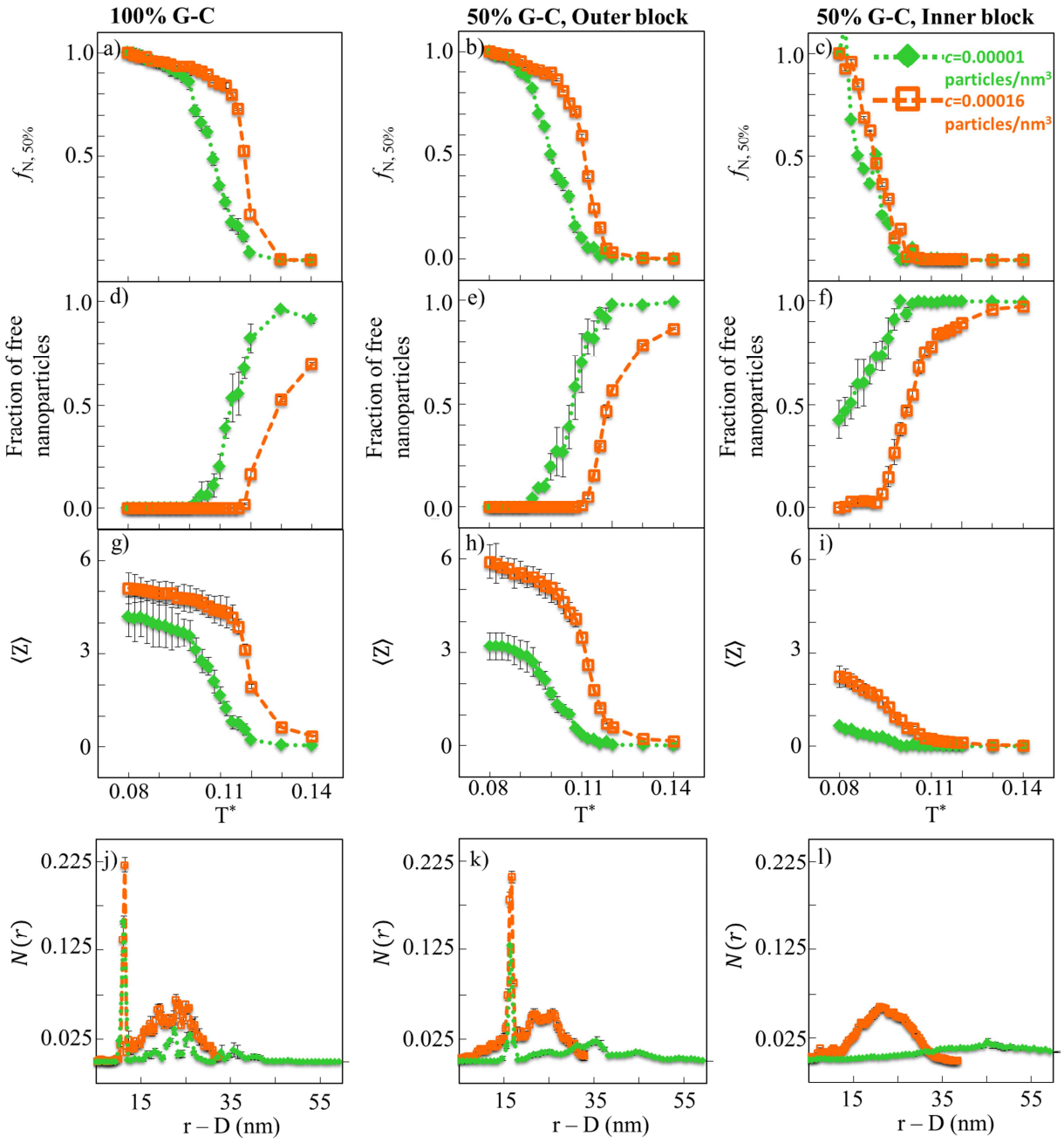

Figure S.4.14 Thermodynamic and structural aspects for (a, d, g, j) 100% G-C content, (b, e, h, k) 50% G-C, outer block, and (c, f, i, l) 50% G-C, inner block for concentration, c=0.00001 particles/nm^3 (10 particles in a (100 nm)^3 simulation box) (orange open squares, dashed line) and c=0.00016 particles/nm^3 (20 particles in a (50 nm)^3 simulation box) (green filled diamonds, dotted line). For all systems, particle size is D=5 nm grafted with N_g=8 strands of length N_{bases}=12. (a, b, c) Normalized melting curves, (d, e, f) fraction of free nanoparticles, and (g, h, i) average coordination number, $\langle Z \rangle$, versus reduced temperature and (j, k, l) nanoparticle-

nanoparticle concentration profile, $N(r)$, versus inter-particle distance r – D (nm). Error bars are calculated from the average of 3 trials. Note that for c=0.00016 particles/nm^3, the fraction of strands with 50% G-C bonded, prior to normalization, was less than 0.08 for all temperatures. Normalizing these values arbitrarily inflates the melting curve, making it appear a smooth melting transition, but analyzing fraction of free nanoparticles (<5 for the 10 particle case) and nanoparticle neighbors and inter-particle distance shows minimal cluster formation has occurred at the temperatures investigated and that the T_m for this system appears to be lower than the T_{low} simulated.

4.6.11 Relative Shape Anisotropy (RSA)

Relative shape anisotropy (RSA) shows the progression of cluster size and shape from T_{high} to T_{low}. For N_g=4, we see that at high temperature, dimers form which are necessarily anisotropic. As temperature is reduced and more nanoparticles begin to cluster, we see both a distribution in average number of nanoparticles per cluster, $\langle N \rangle$, as well as a decrease in $\langle RSA \rangle$. As more particles join the clusters, the shape of the clusters shifts from anisotropic (high $\langle RSA \rangle$ at low $\langle N \rangle$) to isotropic (low $\langle RSA \rangle$ at high $\langle N \rangle$). We see that as grafting density increases, the shift in clusters from high temperature to low follows a similar path for $\langle RSA \rangle$ and $\langle N \rangle$, resulting in clusters at T_{low} generally composed of all of the nanoparticles and at a low $\langle RSA \rangle$ (relatively isotropic).

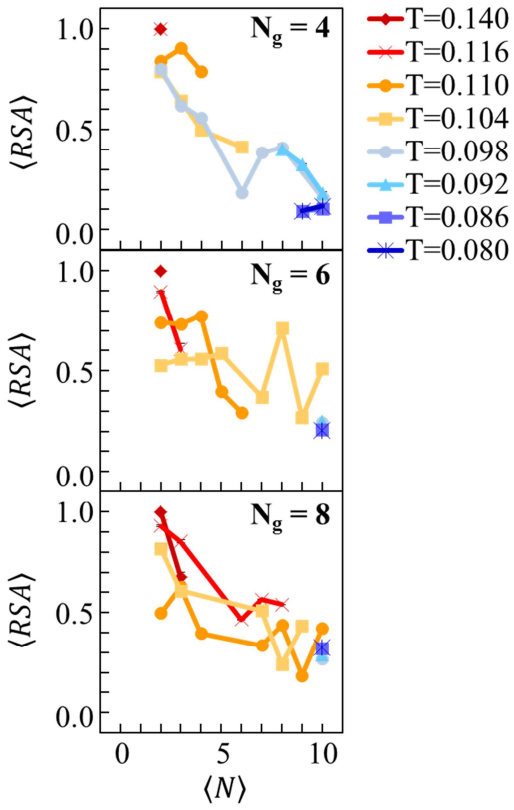

Figure S.4.15 Relative shape anisotropy <*RSA*> versus average number of nanoparticles per cluster <*N*> for 10 particles, in (100 nm)^3 box, each of diameter *D*=5 nm and grafted with (a) N_g=4, (b) N_g=6, and (c) N_g=8 strands of 12 bases each with a diblock (G_6C_6) sequence.

As G-C content decreases, there is less propensity for cluster formation with decreasing enthalpic drive. At higher G-C contents, clusters can form easily at the higher temperatures and form clusters of all 10 particles by the lowest temperature. At the lowest G-C content, clusters are seen rarely at the higher temperatures (and if so, of size 2 only) and only begin to form clusters of increasing size as temperature decreases. Anisotropy follows the previous discussion that clusters of small $\langle N \rangle$ form clusters of high $\langle RSA \rangle$ (more anisotropic) and clusters of high $\langle N \rangle$ tend to have lower values of $\langle N \rangle$ (more isotropic). We see a similar trend in progression of cluster formation for G-C content decreasing on particles of diameter 2 nm, showing that the G-C content determines how clusters come together, and of what size and anisotropy at certain temperatures.

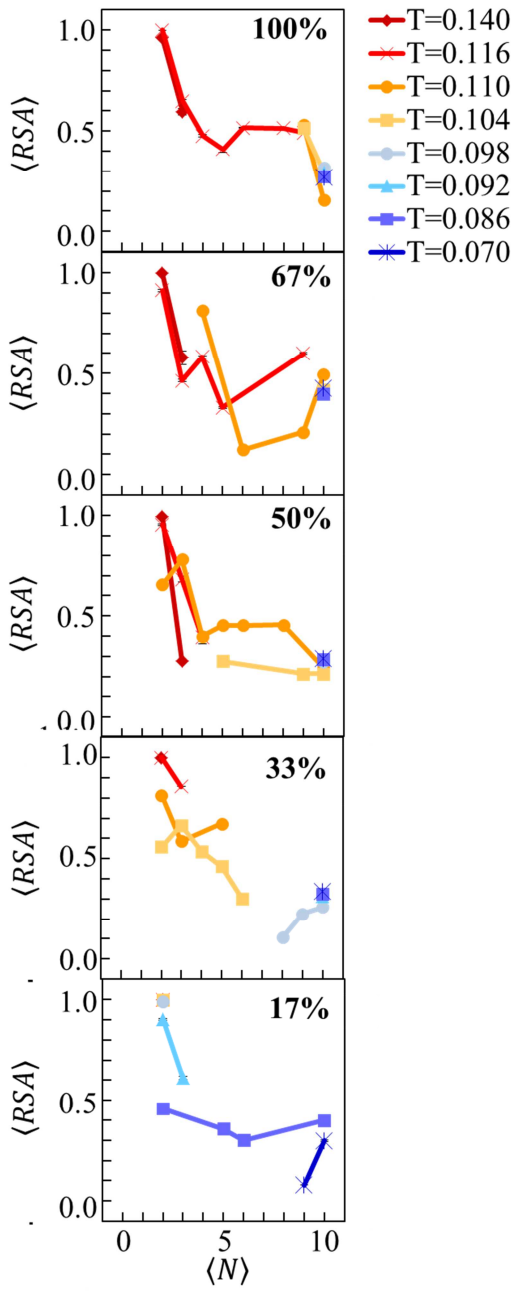

Figure S.4.16 Relative shape anisotropy <*RSA*> versus average number of nanoparticles per cluster <*N*> for 10 particles, in $(100\ \text{nm})^3$ box, each of diameter D=5 nm and grafted with N_g=8 strands of 12 bases each with a diblock sequence arranged in the outer block of the following G-C contents: (a) 100%, (b) 67%, (c) 50%, (d) 33% and (e) 17%.

As we move the G-C placement from the outer to the middle to the inner block, there is a decreased propensity for cluster formation. The outer and middle placements form larger clusters at the high temperatures and by mid-range temperatures have already formed clusters of $\langle N \rangle$ ~10. In contrast the inner placement, which had the least propensity for cluster formation forms mostly dimers throughout the simulation, if any cluster formation at all (see main paper Figure 8b), and by the lowest temperature, begins to form clusters of slightly higher $\langle N \rangle$ but of an $\langle RSA \rangle$ that remains relatively anisotropic. We find that a decrease in particle size (Figure S10) preserves these trends, with the exception that the inner block in the smaller particle case forms clusters at the lowest temperatures that are less anisotropic. Also for the smaller particle diameter, the middle placement of G-Cs facilitates small and large cluster formation at the lower temperatures, as opposed to the expected large and isotropic cluster formation we would expect.

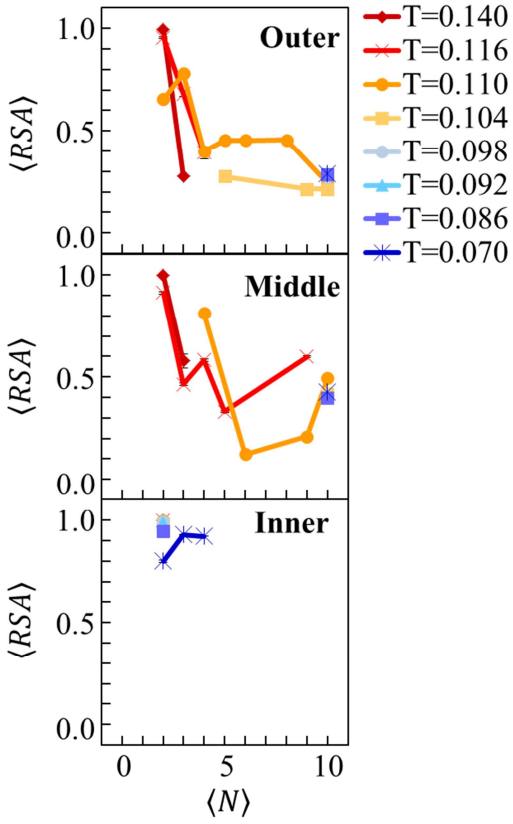

Figure S.4.17 Relative shape anisotropy <*RSA*> versus average number of nanoparticles per cluster <*N*> for 10 particles, in $(100\ nm)^3$ box, each of diameter D=5 nm and grafted with N_g=8 strands of 12 bases each with 50% G-C content arranged in a diblock fashion in the (a) outer block, (b) middle block, and (c) inner block.

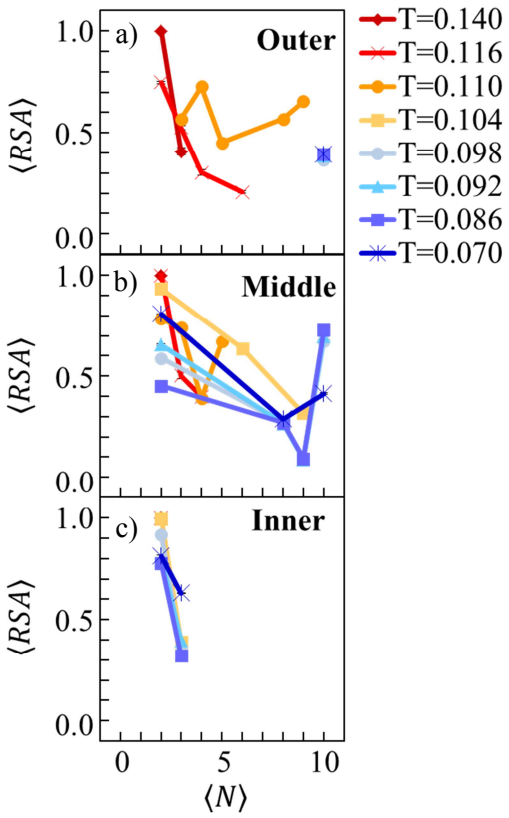

Figure S.4.18 Relative shape anisotropy <*RSA*> versus average number of nanoparticles per cluster <*N*> for 10 particles, in $(100\ \text{nm})^3$ box, each of diameter D=2 nm and grafted with N_g=8 strands of 12 bases each with 50% G-C content arranged in a diblock fashion in the (a) outer block, (b) middle block, and (c) inner block.

As we increase concentration at constant number of grafts (N_g=4) and graft length, we see that the increase in nanoparticles facilitates cluster formation at the higher temperatures. By the lowest temperature at the higher concentrations, clusters of all particles form with nearly the same anisotropy. At the highest concentration (c=0.00032 particles/nm^3), clusters already form at T_{high}, and accordingly, there is a decrease in anisotropy for the clusters at this temperature.

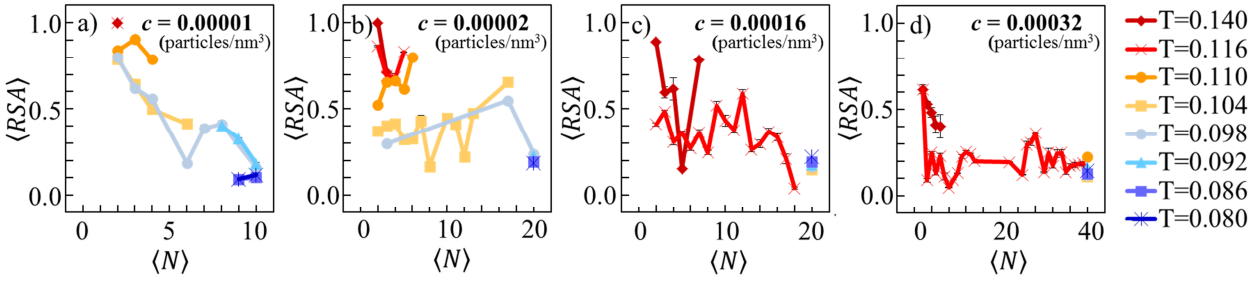

Figure S.4.19 Relative shape anisotropy <*RSA*> versus average number of nanoparticles per cluster <*N*> for particles of diameter D=5 nm and grafted with N_g=4 strands of 12 bases each with a diblock (G_6C_6) sequence with a) c=0.00001 particles/nm^3 (10 particles in a (100 nm)^3 box), b) c=0.00002 particles/nm^3 (20 particles in a (100 nm)^3 simulation box), c) c=0.00016 particles/nm^3 (20 particles in a (50 nm)^3 simulation box), and d) c=0.00032 particles/nm^3 (40 particles in a (50 nm)^3 simulation box).

When we increase concentration for N_g=6 grafts, we see a similar trend that the increase in concentration helps facilitate larger clusters that are more isotropic earlier in the simulation. By the lowest temperature, all nanoparticles cluster and form relatively isotropic clusters, with the exception of c=0.00002 particles/nm^3 where clusters in mid-range temperatures rearrange to be more isotropic than at the final temperature.

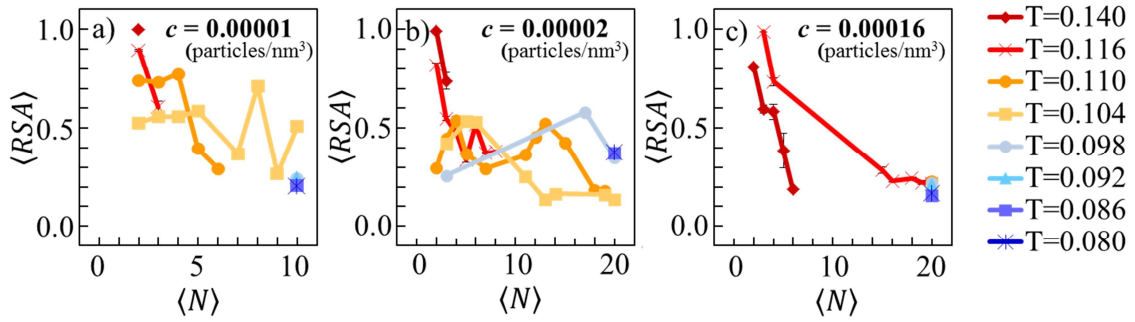

Figure S.4.20 Relative shape anisotropy <*RSA*> versus average number of nanoparticles per cluster <*N*> for particles of diameter *D*=5 nm and grafted with N_g=6 strands of 12 bases each with a diblock (G_6C_6) sequence with a) *c*=0.00001 particles/nm^3 (10 particles in a (100 nm)^3 box), b) *c*=0.00002 particles/nm^3 (20 particles in a (100 nm)^3 simulation box), and c) *c*=0.00016 particles/nm^3 (20 particles in a (50 nm)^3 simulation box).

The trends of <*RSA*> with increasing concentration for the N_g=8 system follow the previous discussion for N_g=4 and N_g=6. By the final temperature, clusters of all particles form with similar isotropy.

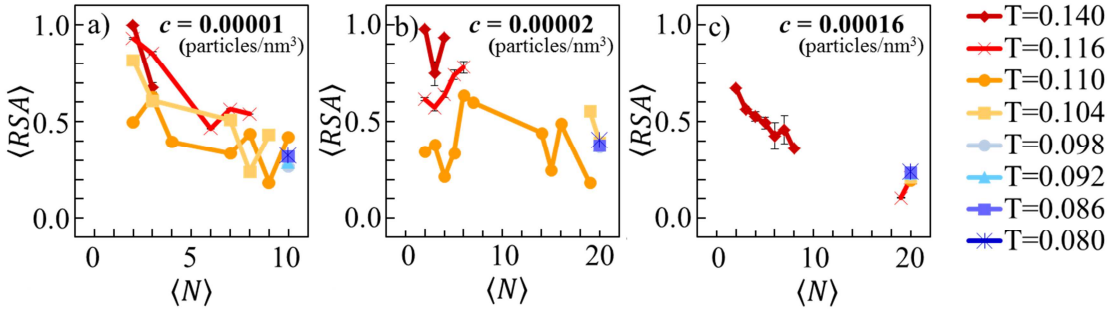

Figure S.4.21 Relative shape anisotropy <*RSA*> versus average number of nanoparticles per cluster <*N*> for particles of diameter *D*=5 nm and grafted with N_g=8 strands of 12 bases each with a diblock (G_6C_6) sequence with a) *c*=0.00001 particles/nm^3 (10 particles in a (100 nm)^3 box), b) *c*=0.00002 particles/nm^3 (20 particles in a (100 nm)^3 simulation box), and c) *c*=0.00016 particles/nm^3 (20 particles in a (50 nm)^3 simulation box).

When we increase concentration for the G-C binding placement, we find that for the outer block, the increase in concentration leads to larger clusters forming earlier in the simulation. By mid-range temperatures, clusters of high <*N*> form and continue to rearrange to become more isotropic. For the inner placement, an increase in concentration increases cluster formation. At the higher concentration, as temperature decreases, nanoparticles have a distribution of cluster sizes, but remain relatively anisotropic as inner placement causes steric hindrance for isotropic cluster formation.

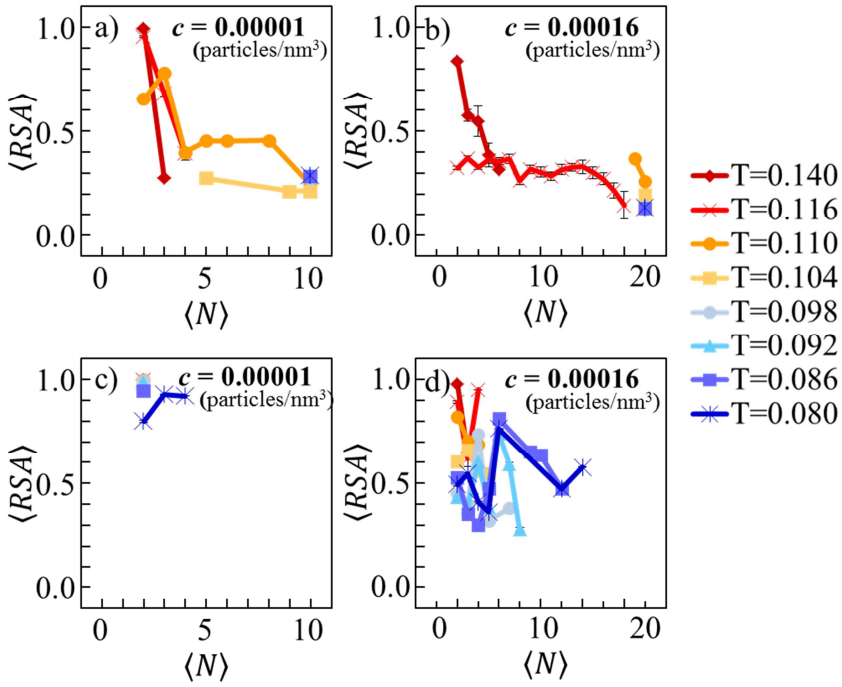

Figure S.4.22 Relative shape anisotropy <*RSA*> versus average number of nanoparticles per cluster <*N*> for particles of diameter *D*=5 nm and grafted with N_g=8 strands of 12 bases each with 50% G-C content arranged in a diblock fashion in the (a,b) outer block and (c,d) inner block with (a,c) *c*=0.00001 particles/nm^3 (10 particles in a (100 nm)^3 box) and (b,d) *c*=0.00016 particles/nm^3 (20 particles in a (50 nm)^3 simulation box).

4.6.12 Mean square displacement

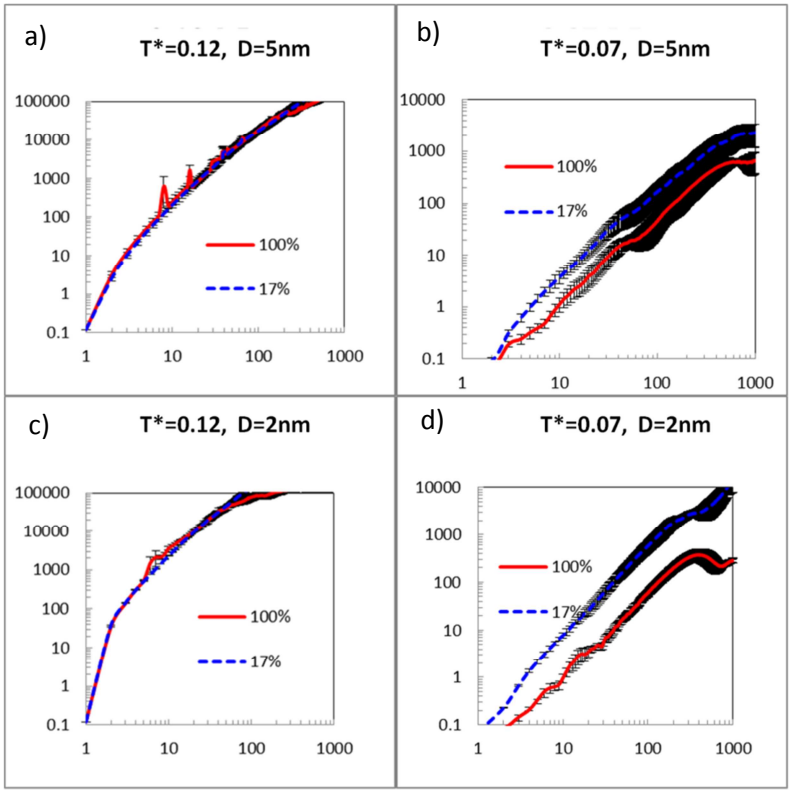

Figure S.4.23 Mean square displacement for 10 particles, in $(100\ \text{nm})^3$ box, each of diameter (a and b) D=5 nm or (c and d) D=2 nm and grafted with N_g=8 strands of 12 bases of 100% G/C content (solid red line) or 17% G/C content (dashed blue line) arranged in a diblock sequence.

4.6.13 Simulation box size for main paper tables

Table S.4.5 Simulation box size for systems listed in main paper Table 4.3.

	D=5 nm			*D*=2 nm		
	10 NP, N_g=8	10 NP, N_g=1	2 NP, N_g=1	10 NP, N_g=8	10 NP, N_g=1	2 NP, N_g=1
100%	$(100\ \text{nm})^3$	$(25\ \text{nm})^3$	$(25\ \text{nm})^3$	$(100\ \text{nm})^3$	$(25\ \text{nm})^3$	$(25\ \text{nm})^3$
67%	$(100\ \text{nm})^3$	$(25\ \text{nm})^3$	$(25\ \text{nm})^3$	$(100\ \text{nm})^3$	$(25\ \text{nm})^3$	$(25\ \text{nm})^3$
50%	$(100\ \text{nm})^3$	$(25\ \text{nm})^3$	$(25\ \text{nm})^3$	$(100\ \text{nm})^3$	$(25\ \text{nm})^3$	$(25\ \text{nm})^3$
33%	$(100\ \text{nm})^3$	$(50\ \text{nm})^3$	$(25\ \text{nm})^3$	$(100\ \text{nm})^3$	$(25\ \text{nm})^3$	$(25\ \text{nm})^3$
17%	$(100\ \text{nm})^3$	$(50\ \text{nm})^3$	$(50\ \text{nm})^3$	$(100\ \text{nm})^3$	$(50\ \text{nm})^3$	$(50\ \text{nm})^3$

Table S.4.6 Simulation box size for systems listed in main paper Table 4.4.

	D=5 nm			*D*=2 nm		
	10 NP, N_g=8	10 NP, N_g =1	2 NP, N_g =1	10 NP, N_g =8	10 NP, N_g =1	2 NP, N_g =1
Outer	$(100\ \text{nm})^3$	$(25\ \text{nm})^3$	$(25\ \text{nm})^3$	$(100\ \text{nm})^3$	$(25\ \text{nm})^3$	$(25\ \text{nm})^3$
Middle	$(100\ \text{nm})^3$	$(25\ \text{nm})^3$	$(25\ \text{nm})^3$	$(100\ \text{nm})^3$	$(25\ \text{nm})^3$	$(25\ \text{nm})^3$
Inner	$(100\ \text{nm})^3$	$(25\ \text{nm})^3$	$(25\ \text{nm})^3$	$(100\ \text{nm})^3$	$(25\ \text{nm})^3$	$(25\ \text{nm})^3$

Chapter 5

Molecular simulation study of the assembly of DNA-functionalised nanoparticles: effect of bidispersity in DNA strand length

As prepared for *Molecular Simulation*

5.1 Introduction

DNA functionalisation is an attractive route to programme the assembly of nanoparticles into target nanostructures because of the specificity and reversibility of DNA hybridisation. A single DNA strand consists of nucleotides, each of which has a sugar, a phosphate group and a nitrogenous base (adenine (A), guanine (G), cytosine (C), or thymine (T)). According to the Watson-Crick base pairing, complementary bases specifically form hydrogen bonds with each other (A with T and G with C). It is through this Watson-Crick base pairing that a sequence of nucleotides in a single-stranded DNA (ssDNA) hybridises specifically with another ssDNA with a complementary sequence of nucleotides. This hybridization leads to a double-stranded DNA (dsDNA) whose stability at a given temperature is known to be strongly dependent on the strand length and sequence. As the temperature increases above the melting temperature, the dsDNA separates into the two-constituent ssDNA. Using this thermoreversible and specific nature of hybridization of the ssDNA grafted on nanoparticles, one can assemble DNA-grafted nanoparticles into nanoclusters. Strands grafted on one particle hybridise with complementary strands on another particle either in a binary system in which one set of particles is grafted with strands that are complementary to the strands grafted on another set of nanoparticles[1-11] or in a single population of particles in which the ssDNA sequence is self-complementary (e.g.

ACGT)).[12, 13] Alternatively, strands on two or more particles hybridise via free linker strands which when added to the system of DNA-grafted particles induce nanoparticle assembly.[14-22] Current synthetic capabilities allow for design of DNA-functionalised nanoparticles[19, 23-25] and colloids[17, 26, 27] with a desired ssDNA sequence, length and composition to tailor nanoparticle/colloid assembly into target nano/microstructures. Many computational and experimental studies provide a fundamental understanding of the effect of various parameters (ssDNA length, sequence, grafting density, G/C content) on the thermodynamics and kinetics of colloidal and nanoparticle assembly. For example, past studies have established that as the length of the grafted ssDNA increases the hybridisation/melting temperature (T_m) of dsDNA increases and the assembly/dissociation transition temperature of nanoparticles (T_d) increases.[15, 22] As ssDNA strand length increases, the number of base pairs in the dsDNA increases, and in turn, the higher enthalpic gain from the larger number of base pairs drives the T_m and T_d to shift to higher temperatures. Structurally, increasing length of the ssDNA increases the inter-particle spacing within the assembled structure. As grafting density, defined as the number of grafted strands per unit particle surface area, increases, T_d increases because the large enthalpic gain upon hybridisation from an increased number of complementary bases easily overcomes the loss in translational entropy of particles and conformational entropy of the densely grafted DNA strands upon hybridisation. Similarly, as the particle size increases at constant grafting density the number of grafted strands increases, and as a result the T_d increases and melting transition sharpens.[5, 22, 28, 29] With regard to strand content or composition, defined as the percentage of the strand that contains G or C bases, it is well understood that the higher the percentage of G/C bases in the strand, the stronger the drive for hybridisation between the complementary strands. This is because of the three hydrogen bonds in a G-C pair in contrast to two hydrogen bonds in

an A-T pair. This increased enthalpic gain from G-C base pairing leads to higher T_m between the complementary single strands, and as a result higher T_d of the nanocluster assembled through hybridisation of strands containing higher G/C content.[29] One could tune the strength of binding between two oligonucleotide strands by varying the G/C content or by incorporating 'non-hybridizing' spacer bases in the strand between the G/C bases.

In most of the above studies, the DNA-grafted nanoparticles consist of particles of a given diameter grafted uniformly with ssDNA that all have the same features (composition, sequence and length) and accordingly, affect the structure and thermodynamics of assembly homogeneously. For example all grafted ssDNA have a specific length that leads to a specific inter-particle spacing in the assembled nanoparticle cluster or have a specific G/C content which causes the particles to assemble at a specific temperature. Recent synthetic advances have made it possible to have asymmetric functionalisation by demonstrating control over grafting a desired number of ssDNA on desired locations on the particle.[30-34] Precision in functionalising particles with a desired number of strands in specific locations leads to the ability to program into the building blocks unique assembly instructions, such as dimensionality of the assembled nanoparticle structure (e.g. 1D nanowires to 2D sheets to 3D gels or crystals). For example, Ohya and coworkers[33] achieved formation of nanowires by synthesising building blocks with ssDNA grafted at diametrically opposed locations on a particle surface. Particles lightly grafted with ssDNA which have variations in strand lengths and placed in precise locations on the particle allow one to create unique finite-sized nanoclusters, e.g. dimers and trimers, where the trimers can be linear or triangular,[35] pyramids,[36] or satellite structures where small particles grafted with one long strand each hybridize only with a central larger particle.[34] In this paper, we systematically vary bidispersity in DNA strand length, in DNA-functionalised nanoparticles to

understand how the choice of two DNA strand lengths on the same particle affects the assembly of such nanoparticles.

We use coarse-grained molecular dynamics simulations to study a system of a single population of DNA-functionalised nanoparticles that assemble (without linkers) through hybridisation of complementary grafted strands in an implicit solvent. Our goal is to understand the effect of bidispersity in strand lengths on the structure and thermodynamics of the assembly at varying number of grafts and number of G/C beads at constant particle size and particle concentration. At constant number of grafts and number of G/C beads, as bidispersity in strand lengths increases the average number of nanoparticles that assemble into a cluster as well as the radius of gyration of the cluster increases and the average number of neighbors a nanoparticle has in a cluster also increases. Low bidispersity in strands lengths produces relatively anisotropic clusters, whereas high bidispersity in strand lengths produces relatively isotropic clusters. When number of G/C beads is constant and thus the enthalpic drive for assembly is constant, the presence of long strands in the bidisperse systems helps alleviate the entropic losses seen in tightly packed particles by hybridizing with the longer strands on neighboring particles and increasing the inter-particle spacing. Inter-particle spacing in the clusters assembled from particles with bidisperse strand lengths depends on the relative frequency of the three possible ssDNA:ssDNA hybridization between particles, e.g. short strand hybridizing to another short strand (short-short), short strand hybridizing to a long strand partially (short-long), or long strand hybridizing to another long strand (long-long). In the case of small number of grafts there are fewer short-short hybridization and mostly short-long and long-long hybridization. In the case of larger number of grafts there are negligible short-short hybridization and higher frequency of long-long hybridization versus short-long. As the number of grafts increase, long strands

hybridize to other long strands in preference to short-long hybridization so that particle surface separation is increased to minimize entropic loss. While higher number of grafts systems have negligible short to short strand connections, particles are able to have short inter-particle distance via partial hybridization of strands. As we increase the number of G/C beads at constant number of grafts, nanoparticles have a higher propensity to cluster, due an increase in the enthalpic driving force in the strands. At high number of G/C beads, an increase in number of grafts causes a sharp increase in the number of nanoparticles that cluster.

The paper is organized as follows. In section 5.2, we provide details of our model and the simulation method, as well as analysis techniques we use and the table of parameters we studied. In section 5.3, we present results of the assembly of DNA-functionalised nanoparticles as a function of ssDNA strand length bidispersity. In section 5.4, we conclude with the key observed results, limitations of this work, and future directions.

5.2 Method

5.2.1 Model and Simulation

We modelled a system of DNA-functionalised nanoparticles in an implicit solvent using a coarse-grain model. This coarse-grained model is capable of capturing the timescale and length scale of DNA hybridisation-driven assembly of many nanoparticles[12, 13] that atomistically detailed models would not be able to capture. In our model, hard spherical nanoparticles of diameter D are grafted with ssDNA strands at fixed locations and symmetrically on the nanoparticle surface. The strands were modelled as semi-flexible chains composed of N_{bases} number of 'monomer' beads of diameter σ_{mon}, where σ_{mon} ~1 nm, as each monomer bead represents a complete nucleotide (sugar, phosphate and A, C, G, or T base). Each monomer bead

contains an attractive site that mimics hydrogen bonding. This attractive hydrogen bonding site is restricted to interact with another hydrogen bonding site on a complementary monomer bead, thus mimicking Watson-Crick base pairing. This model of DNA-functionalised nanoparticles is adapted from a recent simulation study on DNA dendrimers.[12, 13] We note that while in those studies the DNA dendrimers are modelled with a tetrahedral hub to which ssDNA are bound, we model the nanoparticle as a hard core of a given diameter.

All non-bonded pair-wise interactions (nanoparticle–nanoparticle, nanoparticle–monomer, monomer–monomer, hydrogen bonding site–monomer, hydrogen bonding site–nanoparticle, and hydrogen bonding site– hydrogen bonding site) were modelled using a truncated and shifted Lennard-Jones (LJ) potential:

$$U(r) = U_{LJ}(r) - U_{LJ}(r_c) - (r - r_c) \cdot \left. \frac{dU_{LJ}(r)}{dr} \right|_{r=r_c} \quad (1)$$

where $U_{LJ} = 4 \cdot \varepsilon \cdot \left[\left(\frac{\sigma}{r}\right)^{12} - \left(\frac{\sigma}{r}\right)^{6} \right]$, σ is the sum of the radii of the interacting spheres, ε is the energetic well depth, r_c is the distance where the potential is truncated, and r represents the centre-to-centre distance between the coarse-grained beads of interest. All pair-wise interactions involving nanoparticle–nanoparticle, nanoparticle–monomer, monomer–monomer, hydrogen bonding site–monomer, hydrogen bonding site–nanoparticle, and non-complementary hydrogen bonding site–non-complementary hydrogen bonding site were modelled as repulsive interactions with $r_c = 2^{1/6} \cdot \sigma$. The pair-wise interactions between complementary hydrogen bonding sites include both the repulsive and attractive portion of the potential, with $r_c = 2.5 \cdot \sigma$. The reduced value of ε in Equation (1) is assigned as follows: $\varepsilon_{nanoparticle}=1$, $\varepsilon_{monomer}=1$, $\varepsilon_{hydrogen\ bonding\ site}=1$ for hydrogen bonding sites on monomer beads representing A or T nucleotides, and $\varepsilon_{hydrogen\ bonding}$

$_{site}$=1.5 for hydrogen bonding sites on monomer beads representing G or C nucleotides. All energies are represented in terms of ε_{mon} (LJ energy parameter for the monomer spheres), where ε_{mon} ~8 kT. The value of pair-wise interaction between two sites is the geometric average of the individuals forming the pair, $\varepsilon=(\varepsilon_1\varepsilon_2)^{1/2}$. The value of σ in Equation (1) is assigned as follows: $\sigma_{nanoparticle}=2\cdot\sigma_{mon}$ or $5\cdot\sigma_{mon}$, $\sigma_{monomer}=1$ and $\sigma_{hydrogen\ bonding\ site}=0.35\cdot\sigma_{mon}$ where σ_{mon} is the diameter of the monomer spheres and σ_{mon} ~1 nm.

Bonded interactions between various beads were simulated using a Finitely Extensible Non-linear Elastic (FENE) potential:

$$U_{FENE} = -\frac{K\cdot R_0^2}{2}\cdot\ln\left[1-\left(\frac{r}{R_0}\right)^2\right] \qquad (2)$$

where $K = (30*\varepsilon_{FENE})/\sigma^2$ and $R_0 = 1.5*\sigma$, K is the force constant, R_o is the maximum extension of the bond, ε_{FENE} is an energy parameter which is equal to ε_{mon}, and the values of σ and r depend on the type of beads involved in the bond. For a bond between a nanoparticle and the first monomer of a DNA strand, σ is defined as the radius of the monomer and r is defined as the distance between the center of the monomer and the surface of the nanoparticle. For a bond between two monomers, σ is defined as the sum of the two monomer radii and r is defined as the distance between the monomer centers. Finally, a pseudo-bond between a hydrogen bonding site and the host monomer uses σ equivalent to the diameter of the hydrogen bonding site and r is defined as the centre-to-centre distance of the hydrogen bonding site and the host monomer. The equilibrium position of the hydrogen bonding sites is such that the surface of the hydrogen bonding site protrudes $0.02\cdot\sigma_{mon}$ from the surface of the host monomer.

A three-body potential between bonded monomer beads along the ssDNA regulates the characteristic stiffness of the DNA strands:

$$U_{3-\text{body}} = \frac{1}{2} \cdot K \cdot (\theta - \theta_0)^2 \quad (3)$$

where K is a stiffness factor equal to $2\varepsilon_{3\text{-}body}$, where $\varepsilon_{3\text{-}body}$ is 10 times ε_{mon}, θ is the angle made by the three adjacent monomer beads, and θ_0 is the ideal angle equal to 180° for the preferred linear orientation of DNA. Hydrogen bonding sites are not subject to three-body interactions. A three body interaction is also applied between the nanoparticle and the first two monomers of each chain to keep the monomer chains oriented perpendicular to the surface of the nanoparticle. Lastly, a three-body interaction was applied between the first monomer of each DNA graft, the nanoparticle, and the first monomer of every other DNA strand on the same nanoparticle, and the θ_0 value for this three-body interaction was set to force the DNA grafts to the desired relative positions on the surface of the nanoparticle which allowed us to ensure the grafts were placed symmetrically on the particle surface.

The above model was incorporated into a locally authored MD code in the NVT ensemble, in which the temperature is controlled via Nosé-Hoover thermostat.[37, 38] We refer the reader to the supplementary information for other details of the reduced model parameters and validation of the code.

5.2.2 Analysis

Thermodynamics. We characterised the thermodynamics of DNA-functionalised nanoparticle assembly by calculating the assembly/dissociation transition of the nanoparticles as a function of reduced temperature.

As the temperature is lowered and the strands hybridise the functionalised particles assemble into a cluster. We define a cluster as two or more particles with minimum of one base pair hybridized between DNA strands of adjacent nanoparticles. Free nanoparticles are those whose grafted ssDNA have not hybridized with any strand at that time step. We track the average number of free nanoparticles as a function of temperature. We define the assembly/dissociation transition temperature, T_d, as the temperature at which the number of free nanoparticles is half the total number of particles.

Structure. For each nanoparticle, we calculated a coordination number, Z, defined as the average number of particle neighbours the nanoparticle has within the cluster. Two particles are neighbours if they have at least one base pair hybridized between their DNA strands. The coordination number curve at each temperature is a distribution of the number of neighbours each nanoparticle has in a given system at that temperature. We average the coordination number distribution to obtain $\langle Z \rangle$ of the system at a specific temperature. We also calculate the ensemble average number of nanoparticles in a cluster, $<N>$, as a function of reduced temperature. We calculate the nanoparticle–nanoparticle number profile, $N(r)$ in the simulation box. We calculate an ssDNA:ssDNA hybridization histogram by counting in the final assembled structure the number of dsDNA connections between particles that consist of 2 short strands, one short strand and one long strand, and 2 long strands.

We determine the average shape of the cluster at varying temperatures using relative shape anisotropy (RSA) parameter.[39] The RSA of a cluster is 0 when the particles are arranged perfectly isotropic (i.e. spherical symmetry) and 1 when the particles are perfectly anisotropic (i.e. rod-like) in their arrangement. We apply the RSA calculation to the coordinates of the

particles of a cluster and not on the monomer beads of the DNA. We first translate the center of mass of the particles' coordinates of a cluster to the origin and calculate the average radius of gyration tensor for a cluster containing N particles:

$$S = \frac{1}{N}\sum_{i=1}^{N} r_i r_i^{\boldsymbol{T}} \qquad (5)$$

where r_i is the translated coordinate vector of particle *i,* and $r_i^{\boldsymbol{T}}$ is the transpose of this coordinate vector. Then S is diagonalized as

$$\boldsymbol{S} = V^{\boldsymbol{T}} S\, V \qquad (6)$$

where V is a 3x3 matrix with columns that correspond to the three eigenvectors of S. The traceless part of $\boldsymbol{S}$ is then calculated

$$\widehat{\boldsymbol{S}} = \boldsymbol{S} - \frac{1}{3} tr(\boldsymbol{S}) I \qquad (7)$$

where I is the 3x3 identity matrix, and $tr(\boldsymbol{S})$ is the trace of $\boldsymbol{S}$. The RSA, relative shape anisotropy, of the cluster of particles is then defined as

$$RSA = \frac{3}{2}\frac{tr(\widehat{\boldsymbol{S}}\widehat{\boldsymbol{S}})}{tr(\boldsymbol{S})^2} \qquad (8)$$

We note that as our systems are at significantly low concentration, these RSA calculations are conducted on small values of N (=10-20 particles). RSA calculations are significantly more reliable when applied to systems with large N. Therefore, we have restricted our RSA analysis to trends within a system with changing temperature, rather than placing quantitative or qualitative emphasis on RSA variation between systems with varying parameters.

5.2.3 Parameters

We study 10 DNA-functionalised nanoparticles in simulation box size of $(100\ \text{nm})^3$, corresponding to a dilute concentration of c=0.00001 particles/nm^3. The nanoparticles are of diameter, $D=4\cdot\sigma_{mon}$ with σ_{mon} ~1 nm, as described in the model section. We vary the number of grafts from N_g=8 to 16, which on particles of D=4 nm correspond to a grafting density of σ=0.16 and 0.32 chains/nm^2, respectively. We graft on each particle 50% short strands and 50% long strands. All strands in a system have number of G/C beads the length of the short strands, N_{short}, and arranged in a diblock sequence. For long strands, $N_{long} > N_{short}$, the G/C segment of the strand is located on the outermost portion of the strand (farthest from the particle surface). The remaining bases are Adenine, serving as spacers. We vary the number of G/C beads relative to the particle diameter N_{short}/D=1, 1.5 to 2. We vary the ratio of short to long strand length, N_{short}:N_{long}=1:1.5, 1:2 to 1:3. The sequences that correspond to each bidisperse N_{short}:N_{long} ratio per N_{short}/D are summarized in Table 5.1.

Table 5.1 Sequences studied for each ratio of short to long strand length, N_{short}:N_{long} and G/C content of N_{short} relative to the particle diameter, N_{short}/D. Strands are grafted to the particle surface starting from the left nucleotide of each sequence.

	N_{short}:N_{long}	No.	Sequences (N_{short}/N_{long})
N_{short}/D=1.0:	4 : 6	**(1)**	GGCC/AAGGCC
	4 : 8	**(2)**	GGCC/AAAAGGCC
	4 : 12	**(3)**	GGCC/AAAAAAAAGGCC
N_{short}/D=1.5:	6 : 9	**(4)**	GGGCCC/AAAGGGCCC
	6 : 12	**(5)**	GGGCCC/AAAAAAGGGCCC
	6 : 18	**(6)**	GGGCCC/AAAAAAAAAAAAGGGCCC
N_{short}/D=2.0:	8 : 12	**(7)**	GGGGCCCC/AAAAGGGGCCCC
	8 : 16	**(8)**	GGGGCCCC/AAAAAAAAGGGGCCCC
	8 : 24	**(9)**	GGGGCCCC/AAAAAAAAAAAAAAAAGGGGCCCC

5.3 Results

5.3.1 Effect of bisdispersity in DNA strand length at constant number of grafts and number of G/C beads

In Figure 5.1a, we show the effect of increasing bidispersity in strand lengths on the *thermodynamics* of cluster formation for 10 particles in a $(100\ nm)^3$ simulation box, with particles of diameter D=4 nm each grafted with N_g=8 number of strands, an equal number of short, N_{short}, and long, N_{long}, strands, number of G/C beads relative to the particle diameter, N_{short}/D=1, and sequences **1-3** of Table 5.1. We also show the monodisperse case corresponding to N_{short}=4 (black filled squares, solid line) and N_{long}=12 (black filled circles, solid line). For all systems, as temperature decreases, the DNA-grafted nanoparticles assemble into a cluster. The cluster dissociation temperature, T_d, for all systems is T^*=0.096, except for the monodisperse N_{short}=4 case which has a cluster dissociation temperature of T^*=0.094. Nanoparticle assembly is driven by a balance of maximizing enthalpically favorable contacts of the grafted DNA strands as well as minimizing the entropic loss of particle translation and rotation with particles packing closely. Since sequences with the same G/C content per strand have the same enthalpic drive for hybridization, we expect the differences in entropy losses in these systems to contribute more to the differences in assembly of the particles. T_d does not vary significantly with the bidispersity in these conditions because all systems have the same G/C content and thus the same enthalpic drive for hybridization and assembly. Since T_d is similar for the bidisperse systems, we expect that the entropic losses are similar for the bidisperse cases and lower than for the particles grafted with monodisperse short strands. We note that for the case of monodisperse short strands, there remain free nanoparticles by T_{low}=0.08, which we discuss in the following paragraph.

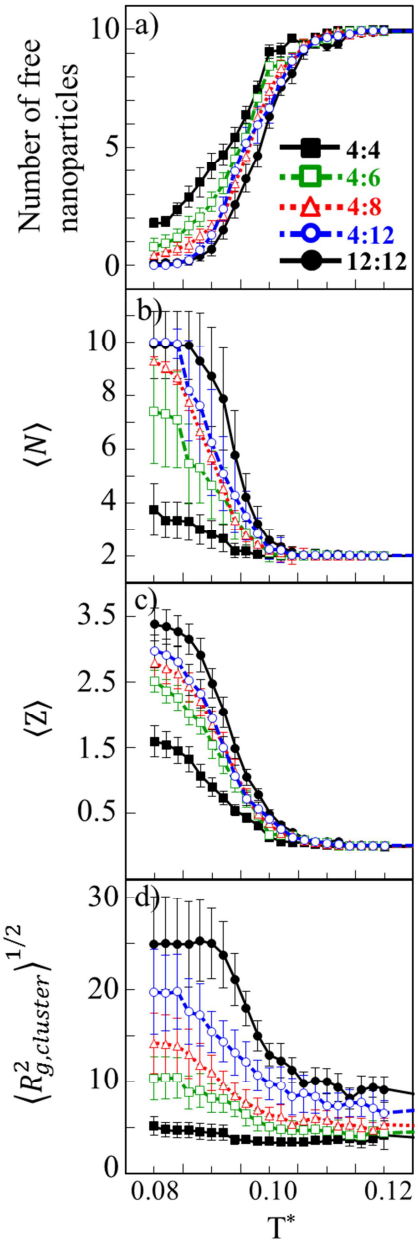

Figure 5.1 (a) Number of free nanoparticles, (b) ensemble average number of nanoparticles per cluster, <*N*>, (c) average coordination number, <*Z*>, and (d) radius of gyration of cluster as a function of reduced temperature, T^*, for 10 particles, in a $(100\ \text{nm})^3$ box, each of diameter D=4 nm and grafted with N_g=8 strands of with bidisperse strand length ratio shown in legend (sequences listed in Table 5.1 for N_{short}/D=1). Also shown are monodisperse case for N_{short} (GGCC) and N_{long} (AAAAAAAAGGCC). Error bars are calculated from the average of 10 trials.

Next we characterize the *structure* of the assembled nanoclusters as a function of bidispersity in strand lengths. Figure 5.1b presents the ensemble average number of nanoparticles per cluster, $<N>$, at each temperature. Below T_d, the increase in $<N>$ with increasing bidispersity can be explained by the presence of the long strands in the bidisperse systems, which alleviate the entropic frustration seen in the case of monodisperse short strands that assemble particles are closer distances. For example, in the absence of long strands, for the monodisperse short strands, all of the particles in the system are unable to cluster together even at the lowest temperature we investigate here (number of free nanoparticles = 1.8 +/- 0.2 at T_{low}=0.08 and $<N>$=3.8 +/- 1.0). The enthalpic gain of the monodisperse short strands at these temperatures is insufficient to overcome the entropic loss of close packing of the particles. In Figure 5.1c, we show the average coordination number, $<Z>$, at each temperature. For the monodisperse short strands case which forms relatively small clusters, the average number of neighbors per particle in the cluster is low ($<Z>$=1.6 +/- 0.2). As larger clusters form with increasing bidispersity in strand lengths, $<Z>$ increases from 2.5 +/ 0.2 for N_{short}:N_{long}=4:6 to 3.0 +/- 0.2 for N_{short}:N_{long}=4:12. The number of strands hybridized is less than the number of grafts available because as the number of strands hybridized increases, so does the crowding, thus making it more difficult for a particle to have all N_g strands hybridize to form N_g neighbors. In our previous study, we found that nanoparticles grafted with monodisperse ssDNA at dilute concentrations formed clusters with a number of neighbors per particle less than N_g. Accordingly, we would expect the bidisperse systems to form clusters with number of neighbors fewer than N_g available strands to reduce crowding of the particles. From Figure 5.1, we see that as bidispersity in strand lengths increases at T_{low}, both the average number of nanoparticles per cluster and the average number of neighbors per nanoparticle in a cluster increase. In Figure 5.1d we observe that the

radius of gyration of the cluster increases as well for increasing bidispersity in strand length at T_{low}. As N_{long} increases, we would expect nanoparticles are spaced farther apart, which in combination with increasing <N> leads to size of the cluster to increase. From the relative shape anisotropy, we see how the cluster size and shape vary from T_{high} to T_{low}. For the systems that form clusters with less than ten particles (Figure S.5.1a-c), cluster shape is relatively anisotropic, even after T_d. In systems that form clusters of all nanoparticles, clusters are relatively isotropic, evident from the low <RSA> at T_{low} for Figures S.5.1d and e.

To further understand how bidispersity in strand lengths affects strand hybridization within the assembled cluster, we present in Figure 5.2, the frequency of inter-particle distances in a cluster with increasing bidispersity in strand lengths (upper panels) as well as the ssDNA:ssDNA hybridization histogram for the dsDNA connections between particles (lower panels).

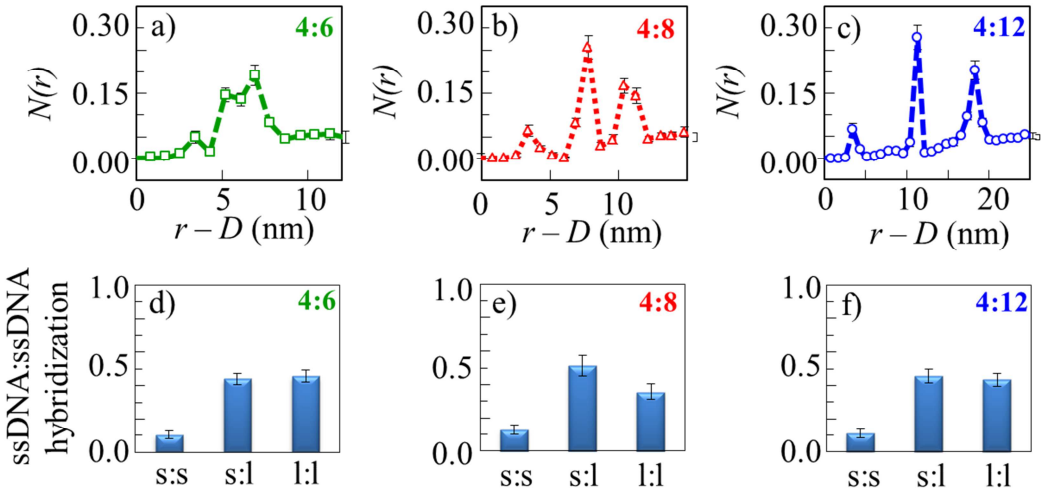

Figure 5.2 (a-c) Nanoparticle-nanoparticle number profile, $N(r)$ versus r-D and (d-f) ssDNA:ssDNA hybridization histogram at T_{low}=0.08 for 10 particles, in a (100 nm)^3 box, each of diameter D=4 nm and grafted with N_g=8 strands of with bidisperse strand length ratio shown in upper right corner of each plot (sequences listed in Table 5.1 for N_{short}/D=1). Error bars are calculated from the average of 10 trials. For (d-f), x-axis s:s denotes short to short strand hybridization, s:l denotes short strand to long strand hybridization and l:l denotes a long strand to long strand hybridization.

The ssDNA:ssDNA hybridization histogram shows the frequency of dsDNA in the assembled clusters that are short strand hybridizing to another short strand (short-short), short strand hybridizing to a long strand partially (short-long), or long strand hybridizing to another long strand (long-long). In Figure 5.2a for N_{short}:N_{long}=4:6, we observe a small peak in *N(r)* at *r–D*=4 nm which corresponds to a distance between surface of particles that have short strand hybridized to another short strand, and a broader peak at *r–D*=5-7 nm which corresponds to a distance between surface of particles that have short strand hybridized to a long strand partially and long strand hybridized to another long strand. The histogram in Figure 5.2d presents the frequency of short-short, short-long and long-long hybridization. At low number of grafts, N_g=8, short-short hybridization is still possible without steric hindrance to the remaining strands on each particle. When bidispersity in strand lengths ratio, N_{short}:N_{long} is 4:8 (Figure 5.2b), we see the *N(r)* peaks separate into inter-particle distances that correlate to the possible ssDNA:ssDNA hybridization. We again observe a small peak of *r–D*=4 nm which corresponds to a distance between surface of particles with short-short hybridization, a larger peak at *r–D*=7-8 nm which corresponds to a distance between surface of particles with short-long hybridization, and a large peak of *r–D*=10-11 nm, which corresponds a distance between surface of particles with long-long hybridization. We note that the ssDNA:ssDNA hybridization histogram shows a similar distribution of strand bonding (Figure 5.2e). Short-long and long-long hybridizations are dominant over short-short, as we would expect as N_{long} increases and particles most easily make short-long and long-long connections. For bidispersity in strand lengths ratio, N_{short}:N_{long}=4:12 (Figure 5.2c), the *N(r)* has peaks of *r–D*=4 nm, *r–D*=11, and *r–D*=18 nm, which correspond to short-short, short-long, and long-long hybridization, respectively and ssDNA:ssDNA hybridization histogram shows a similar distribution in strand bonding (Figure 5.2f). In Figure

5.3, we compare explicitly bidisperse systems with monodisperse systems. We show the $N(r)$ for the case of bidispersity in strand lengths ratio N_{short}:N_{long}=4:12 as well as the monodisperse cases of N_{short}=4 and N_{long}=12. The monodisperse short strands has a single peak of r–D=4 nm which corresponds to a distance between surface of particles with short-short hybridization and the monodisperse long strands has a single peak r–D=18 nm which corresponds to a distance between surface of particles with long-long hybridization. The bidisperse case has the additional peak at r–D=11, which as previously discussed corresponds to short-long hybridization. Bidisperse systems have a distribution of inter-particle distances that are not possible in monodisperse ssDNA grafted nanoparticle clusters.

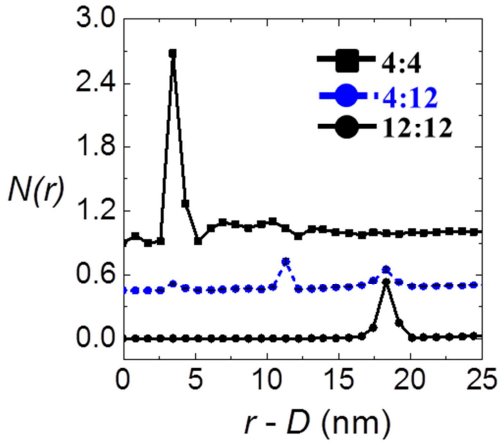

Figure 5.3 Nanoparticle-nanoparticle number profile, $N(r)$, versus r-D at T_{low}=0.08 for 10 particles, in a (100 nm)^3 box, each of diameter D=4 nm and grafted with N_g=8 strands of with bidispersity in strand lengths ratio N_{short}:N_{long}=4:12 (sequence listed in Table 5.1 for N_{short}/D=1) as well as monodisperse N_{short} (GGCC) and N_{long} (AAAAAAAAGGCC). Each curve is shifted 0.45 units along the y-axis from the previous curve for clarity, started from bidispersity in strand lengths ratio 4:12. Error bars are calculated from the average of 10 trials.

5.3.2 Effect of varying number of G/C beads at constant number of grafts

We next determine the effect of bidispersity in DNA strand lengths at varying number of G/C beads for 10 particles in a $(100\ nm)^3$ simulation box, with particles of diameter D=4 nm each grafted with N_g=8 number of strands, number of G/C beads relative to particle diameter N_{short}/D=2, and sequences **7-9** of Table 5.1. We also show the monodisperse case corresponding to N_{short}=8 (black filled squares, solid line). At higher number of G/C beads, cluster dissociation temperature, T_d, occurs at T^*=0.11 for all bidisperse systems and T^*=0.107 for the monodisperse short system (Figure 5.4a). The T_d for the higher number of G/C beads (Figure 5.4a) is higher than for the lower G/C beads (T^*=0.096 in Figure 5.1a) at constant number of grafts. In our previous study where we varied the G/C content at constant number of grafts, we found that T_d increases as G/C content increases because of the increased enthalpic drive for assembly.

Figure 5.4b-d presents $<N>$, $<Z>$, and radius of gyration of the cluster for monodisperse N_{short}=8 and increasing bidispersity in strand lengths systems at higher number of G/C beads. In contrast to the systems at lower number of G/C beads (Figure 5.1), we observe that the higher G/C beads systems form clusters of all 10 nanoparticles by T_{low} (Figure 5.4b). Average number of neighbors per particles, $<Z>$, for all systems is ~3.5 (Figure 5.4c). Also, as bidispersity in strand lengths increases, the radius of gyration of the assembled clusters increases (Figure 5.4d), with the value of radius of gyration of the cluster at T_{low} higher for the higher number of beads systems than for the lower number of beads. For example, the radius of gyration of the cluster for bidisperse case of 4:6 is ~10 nm at low number of G/C beads, Figure 5.1d, versus ~18 for higher number of G/C beads, Figure 5.4d. For all systems at high number of G/C beads, the clusters become relatively isotropic by T_{low} (Figure S.5.2).

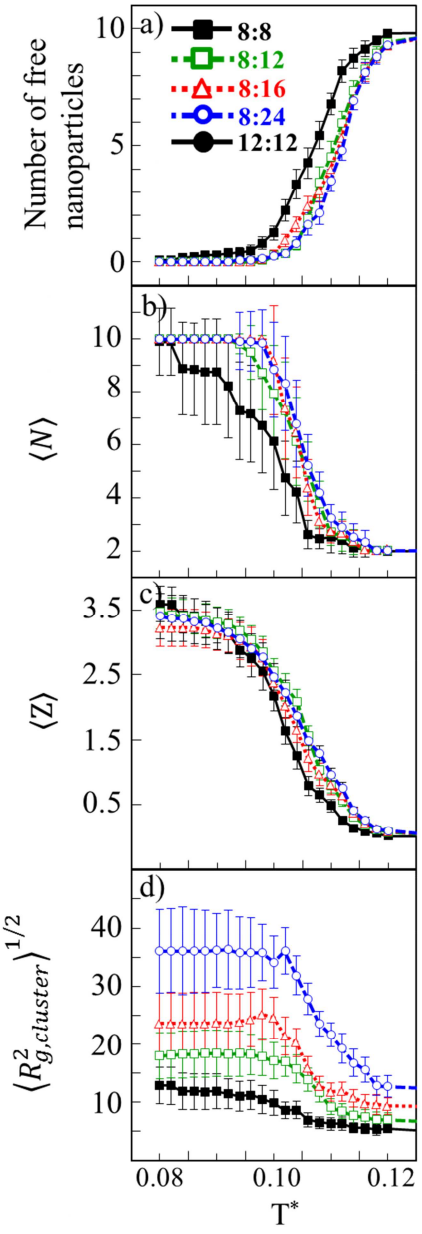

Figure 5.4 (a) Number of free nanoparticles, (b) ensemble average number of nanoparticles per cluster, <*N*>, (c) average coordination number, <*Z*>, and (d) radius of gyration of cluster as a function of reduced temperature, T^*, for 10 particles, in a (100 nm)^3 box, each of diameter D=4 nm and grafted with N_g=8 strands of with bidisperse strand length ratio shown in legend (sequences listed in Table 5.1 for N_{short}/D=2). Also shown are monodisperse case for N_{short} (GGGGCCCC) and N_{long} (AAAAAAAAAAAAAAAGGGGCCCC). Error bars are calculated from the average of 10 trials.

At higher number of G/C beads, nanoparticles have a higher propensity to cluster, due an increase in the enthalpic driving force in the strands as well as a decrease in entropic losses. The lower entropic loss for higher number of G/C beads arises from the increased inter-particle distances that result from the increase in length of strands. When we compare the inter-particle distances of clusters formed from lower number of G/C beads to higher number of G/C beads (Figure 5.5), the primary difference we see is that in the latter case, the bidispersity in strand lengths ratio of 8:12 (Figure 5.5a) produces 3 discernible peaks, which correspond to short-short, short-long, and long-long hybridization, with a noticeable increase in short-long hybridization. Because a higher number of G/C beads results in a larger distance between surface of particles, an increase in short-long hybridization occurs with less entropic loss. As we would expect for the higher bidisperse systems (Figures 5.5b and c), inter-particle distances between surface of particles correspond to short-short, short-long, or long-long hybridization.

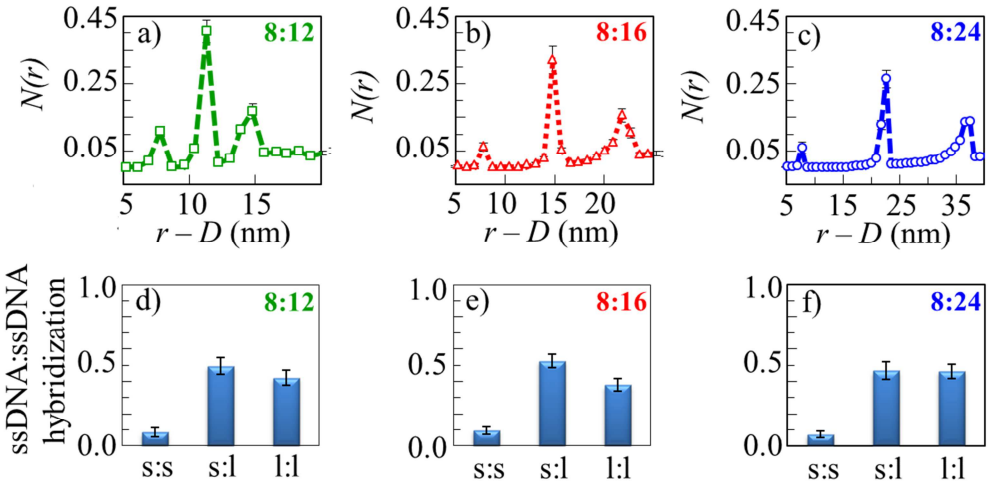

Figure 5.5 (a-c) Nanoparticle-nanoparticle number profile, *N(r)*, versus *r-D* and (d-f) ssDNA:ssDNA hybridization histogram at T_{low}=0.08 for 10 particles, in a (100 nm)^3 box, each of diameter D=4 nm and grafted with N_g=8 strands of with bidisperse strand length ratio shown in upper right corner of each plot (sequences listed in Table 5.1 for N_{short}/D=2). Error bars are calculated from the average of 10 trials. For (d-f), x-axis s:s denotes short to short strand hybridization, s:l denotes short strand to long strand hybridization and l:l denotes a long strand to long strand hybridization.

5.3.3 Effect of varying number of grafts at constant number of G/C beads

Next we examine the effect of increasing number of grafts from N_g=8 to N_g=16 while maintaining number of G/C beads the same. In Figure 5.6a, we present the number of free nanoparticles for bidisperse systems at N_g=8 (dashed lines) and N_g=16 (solid lines). We observe that the T_d for higher number of grafts is shifted to higher temperature than for the lower number of grafts. We expect the increase in T_d as a higher number of G/Cs hybridize between particles in cases of higher number of grafts, requiring a higher temperature for the clusters to dissociate.

With regard to the structure of clusters at higher number of grafts, we observe that the $<N>$ (Figure 5.6b) increases in a similar fashion at higher number of grafts to lower number of grafts, although the higher number of grafts systems begin to assemble at the higher T_d. The $<Z>$ in Figure 5.6c is similar for each bidisperse case by T_{low} at low and high number of grafts, except for at the highest bidispersity in strand lengths ratio where the increase in N_g allows for increased particle neighbors in the assembled clusters. Finally, in Figure 5.6d we see that the size of the clusters for each bidisperse case at low and higher number of grafts is nearly identical. The relative shape anisotropy for the higher number of grafts (Figure S.5.3) shows minimal differences between that for the lower number of grafts (Figure S.5.2) except that in the former case, we see that clusters form at higher temperatures due to the higher T_d for higher number of grafts. In Figure 5.7, we show the inter-particle distances in the assembled clusters as well as the ssDNA:ssDNA hybridization histograms for higher number of graft systems. We observe in all cases a higher frequency of long-long hybridization and negligible short-short hybridization for higher number of grafts (Figure 5.7) as compared to the lower number of grafts (Figure 5.5).

Hybridization of long strands helps to reduce entropic losses of tightly packed clusters by increasing inter-particle separation.

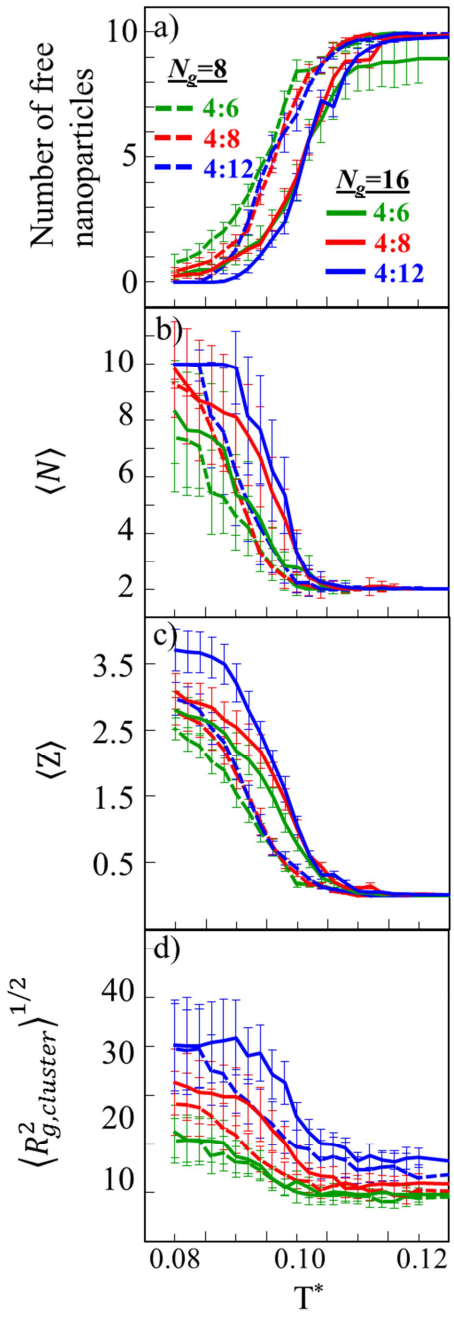

Figure 5.6 (a) Number of free nanoparticles, (b) ensemble average number of nanoparticles per cluster, <*N*>, (c) average coordination number, <*Z*>, and (d) radius of gyration of cluster as a function of reduced temperature, T^*, for 10 particles, in a $(100\ nm)^3$ box, each of diameter D=4 nm and grafted with N_g=8 strands (dashed lines) and N_g=16 (solid lines) of with bidisperse strand length ratio shown in legend (sequences listed in Table 5.1 for N_{short}/D=1 and 2). Error bars are calculated from the average of 10 trials.

Short-short hybridization requires small inter-particle distances, both reducing particle translation and rotation and reducing strand conformational entropy of strands adjacent to the hybridizing strands. Thus in the higher number of grafts systems, increasing bidispersity relieves the entropic frustration of close particle packing by increasing the number of long to long strand hybridization, but the high density of strands on the particle makes it difficult for short strands to hybridize with one another to assemble the particles due to the steric hindrance the remaining strands would have.

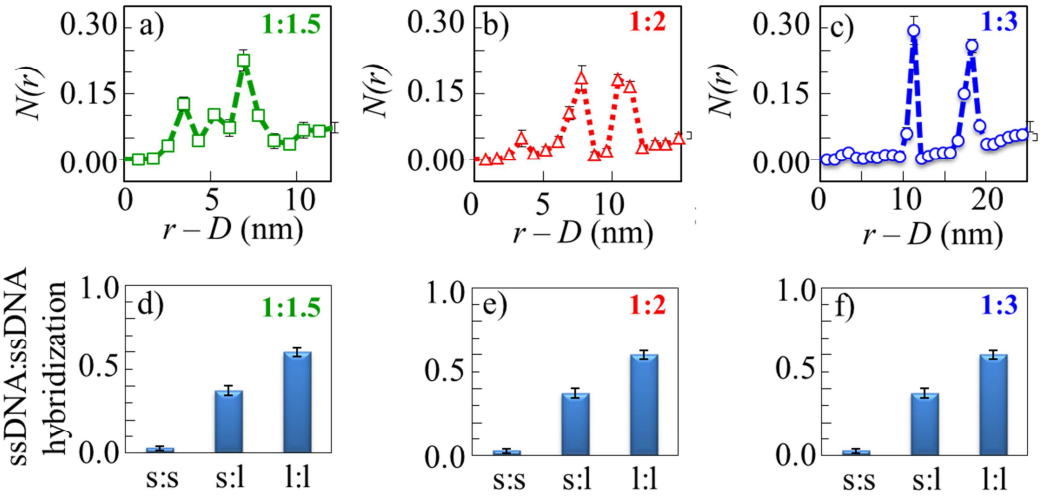

Figure 5.7 (a-c) Nanoparticle-nanoparticle number profile, *N(r)*, versus *r-D* and (d-f) ssDNA:ssDNA hybridization histogram at T_{low}=0.08 for 10 particles, in a (100 nm)^3 box, each of diameter D=4 nm and grafted with N_g=8 strands of with bidisperse strand length ratio shown in upper right corner of each plot (sequences listed in Table 5.1 for N_{short}/D=1). Error bars are calculated from the average of 10 trials. For (d-f), x-axis s:s denotes short to short strand hybridization, s:l denotes short strand to long strand hybridization and l:l denotes a long strand to long strand hybridization.

We see that the $N(r)$ for N_{short}:N_{long}=4:6 and 4:8 (Figure 5.7a and b) have peaks at r–D ~4 nm, but the absence of short-short hybridization in the ssDNA:ssDNA hybridization histogram of Figure 5.7d and e indicates that particles with higher number of grafts assemble by forming partial bonds between strands of neighboring particles at close range. Simulation snapshots (Figure 5.8) confirm that higher number of graft systems at low bidispersity in strand lengths form both complete and partial hybridization between strands.

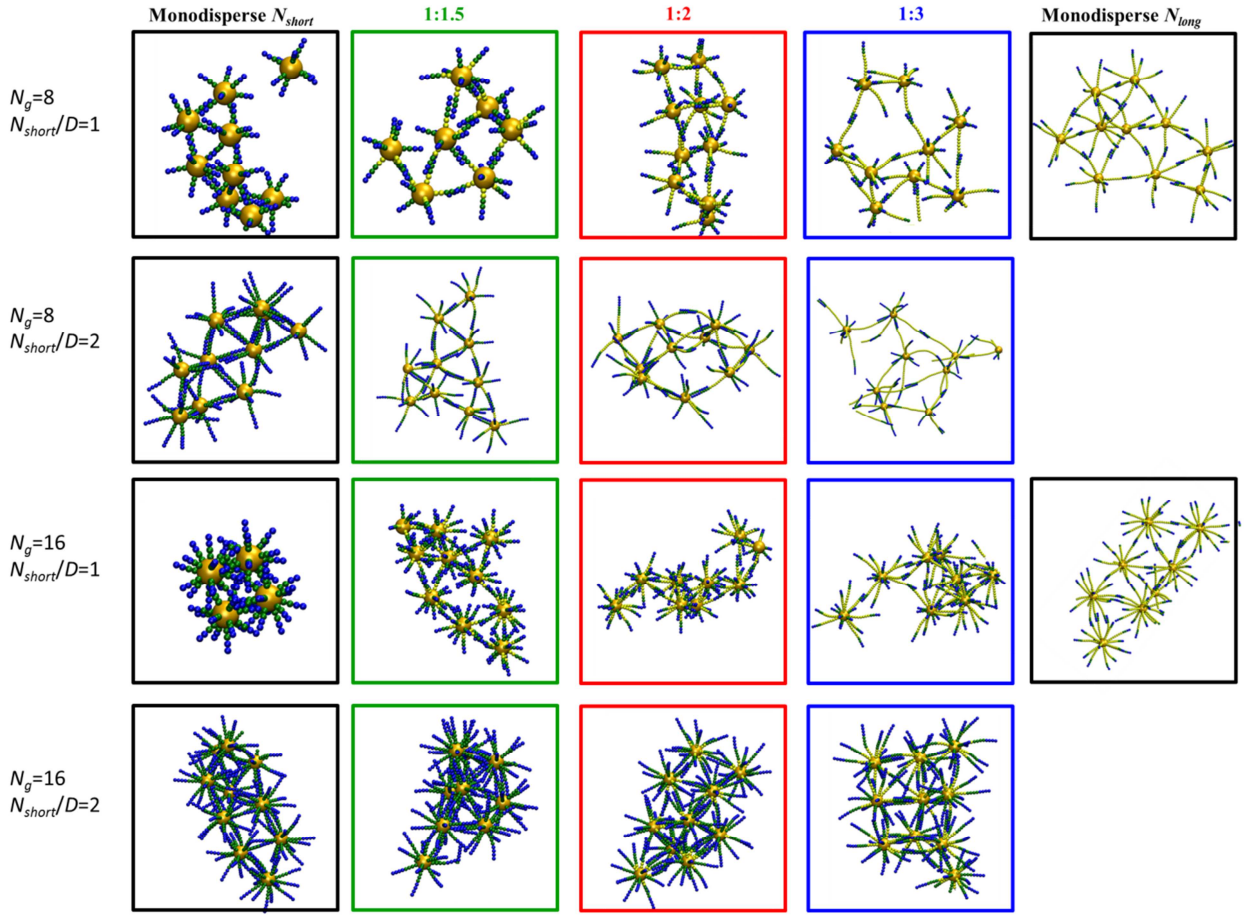

Figure 5.8 Simulation snapshot from one of the trials at T_{low}=0.08 for assembly of 10 particles in a (100 nm)^3 simulation box, with particles of diameter D=4 nm each grafted with N_g=8 (top 2 rows) or N_g=16 (bottom 2 rows) number of strands, an equal number of short, N_{short}, and long, N_{long}, strands, number of G/C beads=4 (rows 1 and 3) or 8 (rows 2 and 4) for strand length ratio indicated at top of each column.

The presence of both complete and partial hybridization induces inter-particle spacing to be at expected distances based on possible ssDNA:ssDNA hybridization (short-short, short-long, long-long) in the case of complete hybridization or inter-particle spacing to be short in the case of partial hybridization. The peak positions in the *N(r)* for higher number of grafts (Figure 5.7a-c) are similar as those for lower number of grafts (Figure 5.2a-c), but the magnitude of long to long connections increases for higher number of grafts systems as we would expect given the increase in long-long hybridization in the ssDNA:ssDNA hybridization histogram (Figure 5.7d-f). By comparing the structure of clusters formed at increasing number of strands and constant bidispersity in strand lengths ratio and number of G/C beads, we observe how particles minimize entropic losses by either forming both short-long and long-long hybridization (to reduce particle entropy losses) in the case of low number of grafts or increasing long-long hybridization (to reduce both particle entropy losses and strand conformational entropy losses) in the case of high number of grafts.

5.3.4 Effect of varying number of G/C beads and number of grafts

When we increase number of grafts at higher number of G/C beads, we observe beginning at the T_d a sharp increase in $<N>$ (Figure 5.9b) for higher number of grafts (solid lines) versus lower number of grafts (dashed lines). As clusters begin to form at higher temperature for the higher number of grafts systems, both the $<Z>$ and radius of gyration of the cluster increase for all bidisperse ratios (Figures 5.9c and d). At a higher number of G/C beads the particle distances between surfaces in the assembled cluster is higher than in the case of lower number of G/C beads. The ability of the particles to assemble at larger distances as well as the presence of more G/Cs due to a higher number of grafts helps the higher number of grafts systems to form clusters more rapidly than for the lower number of grafts systems. The higher number of grafts and the

higher number of G/C beads synergistically promote a sharp cluster dissociation transition, an effect we do not observe simply with higher number of grafts.

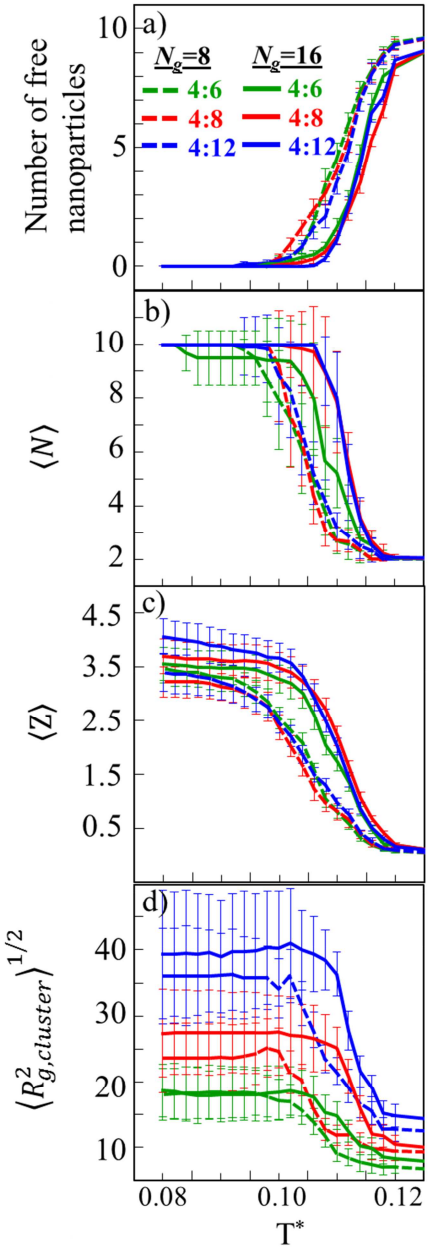

Figure 5.9 (a) Number of free nanoparticles, (b) ensemble average number of nanoparticles per cluster, <*N*>, (c) average coordination number, <*Z*>, and (d) radius of gyration of cluster as a function of reduced temperature, T^*, for 10 particles, in a (100 nm)^3 box, each of diameter D=4 nm and grafted with N_g=8 strands (dashed lines) and N_g=16 (solid lines) of with bidisperse strand length ratio shown in legend (sequences listed in Table 5.1 for N_{short}/D=1 and 2). Error bars are calculated from the average of 10 trials.

5.4 Conclusion

We have studied using molecular dynamics simulations systems of DNA-functionalized nanoparticles that assemble through hybridization of the grafted DNA strands, and demonstrated how the bidispersity in strand lengths induces structural changes in assembled clusters as a function of number of grafts as well as G/C content. We find that the number of grafts along with the number of G/C beads signficantly impacts the structure of the assembled nanoclusters for increasing bidispersity in strand lengths, depending on how the DNA-functionalized nanoparticle building blocks can maximize favorable enthalpic contacts while minimizing entropic losses that arise when particles pack closely (nanoparticle translation and rotation restricted and strand conformations minimized). As bidispersity in strand lengths increases at constant number of grafts and number of G/C beads, number of nanoparticles that cluster as well as number of neighbors per particle in the cluster increases. When number of G/C beads is constant and thus the enthalpic drive for assembly is constant, the presence of long strands in the bidisperse systems helps alleviate the entropic losses seen in tightly packed particles by hybridizing with the longer strands on neighboring particles and increasing the inter-particle spacing. At low number of grafts there are fewer short-short hybridization and mostly short-long and long-long hybridization, whereas at high number of grafts there are negligible short-short hybridization and higher frequency of long-long hybridization versus short-long. As the number of grafts increase, long strands hybridize to other long strands in preference to short-long hybridization so that particle surface separation is increased to minimize entropic loss. At high number of G/C beads, an increase in number of grafts causes a sharp increase in the number of nanoparticles that assemble.

We note a few limitations of the model used in this study. One limitation is that these systems mimic cases where the electrostatic interactions are completely screened. Without explicit counter ions, it is difficult for us both to replicate experimental findings on the effect of salt concentration on the assembly and to determine differences in the secondary structure of the DNA. Another limitation is that the DNA strands in our model are fixed at specific locations, while synthesis of DNA-functionalized gold nanopartiles is often done using Au-thiol non-covalent binding that allows strands to move on the surface.

Despite the limitations, our study outlines the parameters that can be tuned in bidispersity in strand lengths systems to achieve a target assembly. How each system balances enthalpy and entropy depends strongly on the ratio of bidispersity of strand lengths as well as number of grafts and number of G/C beads of the grafted strands. Bidispersity of grafted strands can be an exciting parameter experimentalists can tune to create novel structures from DNA-functionalized building blocks.

5.5 References

1. C. W. Hsu, F. Sciortino and F. W. Starr, *Physical Review Letters*, 2010, **105**.
2. D. Nykypanchuk, M. M. Maye, D. van der Lelie and O. Gang, *Nature*, 2008, **451**, 549-552.
3. R. Dreyfus, M. E. Leunissen, R. J. Sha, A. V. Tkachenko, N. C. Seeman, D. J. Pine and P. M. Chaikin, *Physical Review Letters*, 2009, **102**.
4. R. Dreyfus, M. E. Leunissen, R. Sha, A. Tkachenko, N. C. Seeman, D. J. Pine and P. M. Chaikin, *Physical Review E*, 2010, **81**.
5. O. Padovan-Merhar, F. V. Lara and F. W. Starr, *Journal of Chemical Physics*, 2011, **134**.
6. B. M. Mognetti, M. E. Leunissen and D. Frenkel, *Soft Matter*, 2012, **8**, 2213-2221.
7. W. Dai, S. K. Kumar and F. W. Starr, *Soft Matter*, 2010, **6**, 6130-6135.
8. M. R. Jones, R. J. Macfarlane, B. Lee, J. A. Zhang, K. L. Young, A. J. Senesi and C. A. Mirkin, *Nature Materials*, 2010, **9**, 913-917.

9. E. Auyeung, J. I. Cutler, R. J. Macfarlane, M. R. Jones, J. S. Wu, G. Liu, K. Zhang, K. D. Osberg and C. A. Mirkin, *Nature Nanotechnology*, 2012, **7**, 24-28.
10. W. B. Rogers and J. C. Crocker, *Proceedings of the National Academy of Sciences of the United States of America*, 2011, **108**, 15687-15692.
11. T. Li, R. Sknepnek, R. J. Macfarlane, C. A. Mirkin and M. O. de la Cruz, *Nano Letters*, 2012, **12**, 2509-2514.
12. F. W. Starr and F. Sciortino, *Journal of Physics-Condensed Matter*, 2006, **18**, L347-L353.
13. J. Largo, F. W. Starr and F. Sciortino, *Langmuir*, 2007, **23**, 5896-5905.
14. R. C. Jin, G. S. Wu, Z. Li, C. A. Mirkin and G. C. Schatz, *Journal of the American Chemical Society*, 2003, **125**, 1643-1654.
15. J. J. Storhoff, A. A. Lazarides, R. C. Mucic, C. A. Mirkin, R. L. Letsinger and G. C. Schatz, *Journal of the American Chemical Society*, 2000, **122**, 4640-4650.
16. T. R. Prytkova, I. Eryazici, B. Stepp, S. B. Nguyen and G. C. Schatz, *Journal of Physical Chemistry B*, 2010, **114**, 2627-2634.
17. P. L. Biancaniello, A. J. Kim and J. C. Crocker, *Physical Review Letters*, 2005, **94**.
18. R. T. Scarlett, M. T. Ung, J. C. Crocker and T. Sinno, *Soft Matter*, 2011, **7**, 1912-1925.
19. S. Y. Park, A. K. R. Lytton-Jean, B. Lee, S. Weigand, G. C. Schatz and C. A. Mirkin, *Nature*, 2008, **451**, 553-556.
20. C. H. Kiang, *Physica A*, 2003, **321**, 164-169.
21. B. D. Smith, N. Dave, P. J. J. Huang and J. W. Liu, *Journal of Physical Chemistry C*, 2011, **115**, 7851-7857.
22. Y. Sun, N. C. Harris and C. H. Kiang, *Physica A*, 2005, **354**, 1-9.
23. C. A. Mirkin, R. L. Letsinger, R. C. Mucic and J. J. Storhoff, *Nature*, 1996, **382**, 607-609.
24. A. P. Alivisatos, K. P. Johnsson, X. G. Peng, T. E. Wilson, C. J. Loweth, M. P. Bruchez and P. G. Schultz, *Nature*, 1996, **382**, 609-611.
25. D. Nykypanchuk, M. M. Maye, D. van der Lelie and O. Gang, *Langmuir*, 2007, **23**, 6305-6314.
26. A. J. Kim, R. Scarlett, P. L. Biancaniello, T. Sinno and J. C. Crocker, *Nature Materials*, 2009, **8**, 52-55.
27. V. T. Milam, A. L. Hiddessen, J. C. Crocker, D. J. Graves and D. A. Hammer, *Langmuir*, 2003, **19**, 10317-10323.
28. D. B. Lukatsky and D. Frenkel, *Journal of Chemical Physics*, 2005, **122**.
29. N. Geerts and E. Eiser, *Soft Matter*, 2010, **6**, 4647-4660.
30. D. Zanchet, C. M. Micheel, W. J. Parak, D. Gerion, S. C. Williams and A. P. Alivisatos, *Journal of Physical Chemistry B*, 2002, **106**, 11758-11763.
31. D. Zanchet, C. M. Micheel, W. J. Parak, D. Gerion and A. P. Alivisatos, *Nano Letters*, 2001, **1**, 32-35.
32. W. J. Parak, T. Pellegrino, C. M. Micheel, D. Gerion, S. C. Williams and A. P. Alivisatos, *Nano Letters*, 2003, **3**, 33-36.
33. M. N. Ohya Y., Hashizume M., Tamaki T. , Uehara T., Shingubara S., and Kuzuya A., *Small*, 2012.
34. X. Y. Xu, N. L. Rosi, Y. H. Wang, F. W. Huo and C. A. Mirkin, *Journal of the American Chemical Society*, 2006, **128**, 9286-9287.

35. C. J. Loweth, W. B. Caldwell, X. G. Peng, A. P. Alivisatos and P. G. Schultz, *Angewandte Chemie-International Edition*, 1999, **38**, 1808-1812.
36. A. J. Mastroianni, S. A. Claridge and A. P. Alivisatos, *Journal of the American Chemical Society*, 2009, **131**, 8455-8459.
37. D. Frenkel and B. Smit, *Understanding Molecular Simulation: From Algorithms to Applications*, Academic Press, San Diego, 2002.
38. G. J. Martyna, D. J. Tobias and M. L. Klein, *Journal of Chemical Physics*, 1994, **101**, 4177-4189.
39. D. N. Theodorou and U. W. Suter, *Macromolecules*, 1985, **18**, 1206-1214.

5.6 Supplementary Information

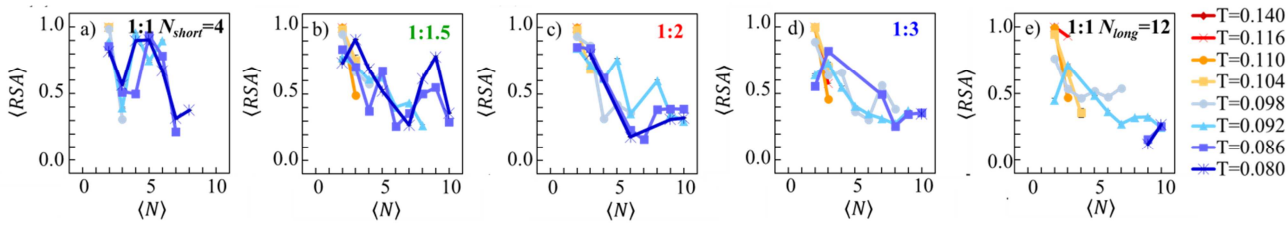

Figure S.5.1 Relative shape anistropy, <*RSA*>, as a function of ensemble average number of nanoparticles per cluster, <*N*>, for 10 particles, in a (100 nm)^3 box, each of diameter D=4 nm and grafted with N_g=8 strands of with bidisperse strand length ratio shown in legend (sequences listed in Table 1 for N_{short}/D=1). Also shown are monodisperse case for N_{short} (GGCC) and N_{long} (AAAAAAAAGGCC). Error bars are calculated from the average of 10 trials.

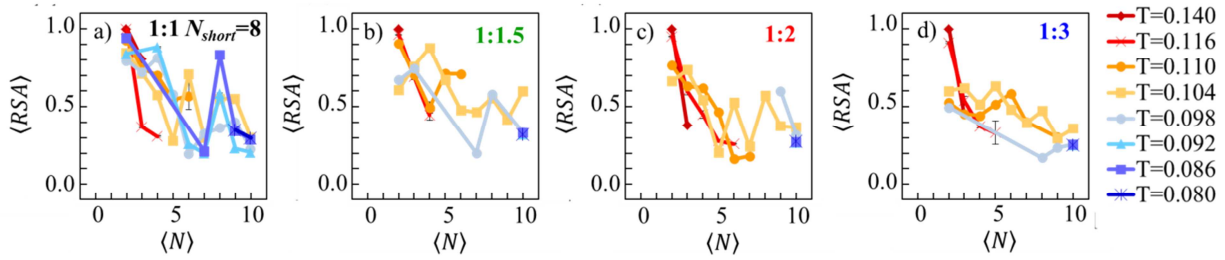

Figure S.5.2 Relative shape anistropy, <*RSA*>, as a function of ensemble average number of nanoparticles per cluster, <*N*>, for 10 particles, in a (100 nm)^3 box, each of diameter D=4 nm and grafted with N_g=8 strands of with bidisperse strand length ratio shown in legend (sequences listed in Table 1 for N_{short}/D=2). Also shown is monodisperse case for N_{short} (GGGGCCCC). Error bars are calculated from the average of 10 trials.

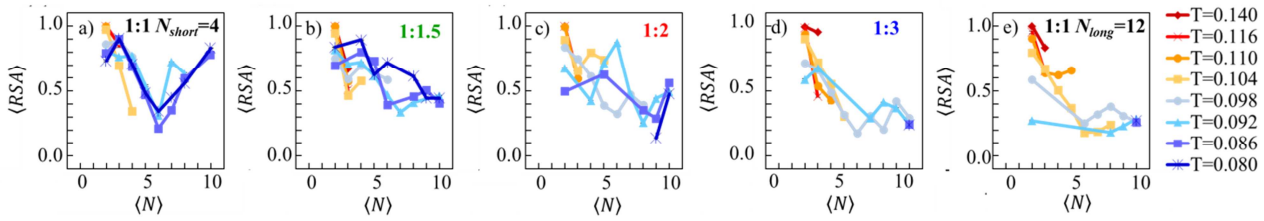

Figure S.5.3 Relative shape anistropy, <*RSA*>, as a function of ensemble average number of nanoparticles per cluster, <*N*>, for 10 particles, in a (100 nm)^3 box, each of diameter D=4 nm and grafted with N_g=16 strands of with bidisperse strand length ratio shown in legend (sequences listed in Table 1 for N_{short}/D=1). Also shown are monodisperse case for N_{short} (GGCC) and N_{long} (AAAAAAAAGGCC). Error bars are calculated from the average of 10 trials.

Chapter 6

Conclusions and Future Directions

6.1 Copolymer-functionalized nanoparticle assembly

Summary of work in this thesis. In the first part of this thesis we have examined the utility of copolymer ligands to assemble copolymer-functionalized nanoparticles. We initially studied the conformations of copolymers grafted to a single nanoparticle and found that the sequence and chemistry of the copolymers had a non-trivial effect on the chain conformations at varying particle size, grafting density and copolymer chain length. We found on the smallest spherical particle we studied that the radius of gyration varies non-monotonically with increasing blockiness of the monomer sequence, and the copolymers have both intrachain and interchain monomer aggregation. At larger particle diameters, however, the grafted chains transition to being mostly intrachain monomer aggregation and the radius of gyration varies monotonically with monomer sequence. From this first study, we selected the two sequences with the most different chain conformations—alternating and diblock—and studied the effect of the sequence and a range of monomer chemistries of the copolymer on the characteristics of assembly of multiple copolymer-functionalized nanoparticles. We find that the alternating sequence produces nanoclusters that are relatively isotropic, whereas diblock sequence tends to form anisotropic structures that are smaller and more compact when the block closer to the surface is attractive and larger loosely held together clusters when the outer block is attractive.

Limitations. In the study on the assembly of copolymer-functionalized nanoparticle assembly, we maintained particle-particle interactions and particle-monomer interactions as athermal to

isolate the effect of grafted monomer chemistry on the nanoparticle assembly. At low to intermediate grafting densities the nanoparticle surface can be covered or exposed, depending on the conformations of the grafted copolymer. Introducing both particle-monomer and particle-particle interactions is important to understand how the presence of those interactions can affect the assembly of copolymer-functionalized nanoparticles. Determining the effect of particle-monomer interactions has been the focus of a recent study by Martin, McKinney and Jayaraman.

Future directions. The first part of this thesis focused on equilibrium properties with respect to copolymer functionalization—in Chapter 2, we determined equilibrium conformations of copolymers grafted to a single nanoparticle, and in Chapter 3, we analyzed the characteristics of equilibrium structures of multiple copolymer-functionalized nanoparticles. Future work of assembly of nanoparticles using copolymer functionalization could include studies of the dynamics of the assembled nanoparticles. In Chapter 3, we observed that the sequence and chemistry of the copolymer affected both the shape (isotropic versus anisotropic) and the inter-particle distances within the assembled cluster (e.g. compact clusters versus large loosely held-together clusters). The shape and inter-particle distances in the assembled clusters could change when extracting nanoclusters from solution to use in a given application. Understanding how nanocluster structure changes under processing conditions is important for applications such as metamaterials where shape and inter-particle distance of the assembled clusters affect the material properties. One can imagine that compact clusters are more rigid than large loosely held-together clusters, but the extent to which each cluster can sustain deformation without the structure changing significantly might depend on chemistry and sequence of the copolymers as well as particle size and grafting density. To a first approximation, one could measure the rigidity of the particles by monitoring the nanoparticle fluctuations from the center of mass of

each cluster. For structures of different rigidity, one could then apply shear to the solution to determine what parameters produce clusters that can maintain a consistent structure.

6.2 DNA-functionalized nanoparticle assembly

Summary of work in this thesis. In the second part of this thesis we used DNA ligands which have specific interactions through Watson-Crick base pairing to evaluate the role the directionality of ligands has on the control over nanoparticle assembly. We primarily investigated two features of the DNA strands: chemical and physical heterogeneity. We studied the effect of grafted DNA strand composition (e.g. G/C content, placement and sequence) (chemical heterogeneity) and bidispersity in DNA strand lengths (physical heterogeneity) on the thermodynamics and structure of assembly of functionalized nanoparticles. Understanding how these strand features affect the structure and thermodynamics of assembly is non-trivial. Our study provides valuable guidance to experimentalists on how chemical or physical heterogeneity (or both) can be tailored for target assembly. We find that at constant grafting density and G/C content, nanoparticles assemble more readily when the G/C blocks are placed on the outer (far from the particle surface) or middle portions of the strands than in the inner portion (closest to the particle surface) because of entropic frustration in the latter case. Also, at constant G/C content, as the G/C placement along the strand shifts closer to the particle surface the "valency" of the particle decreases. As particle size decreases at constant grafting density and G/C placement the minimum G/C content needed for assembly increases. With regards to bidispersity in strand lengths, we find that at constant number of grafts and number of G/C beads, as bidispersity in strand lengths increases the average number of nanoparticles that assemble into a cluster as well as the radius of gyration of the cluster increases and the average number of

neighbors a nanoparticle has in a cluster also increases. When number of G/C beads is constant and thus the enthalpic drive for assembly is constant, the presence of long strands in the bidisperse systems helps alleviate the entropic losses seen in tightly packed particles by hybridizing with the longer strands on neighboring particles and increasing the inter-particle spacing. As the number of grafts increase, long strands hybridize to other long strands in preference to short-long hybridization so that particle surface separation is increased to minimize entropic loss.

Limitations. Analogous to the limitation of our copolymer work, in the study on DNA functionalization, we have not modeled non-specific interactions between the bases and the surface, which could have an effect on the structure and thermodynamics of the assembled clusters. Additionally we have not included electrostatic interactions to mimic purely a high salt concentration condition where electrostatic interactions are screened. Changing salt concentration will need explicit electrostatic interactions, and tuning the strand flexibility. Modeling explicit electrostatics is crucial when determining the secondary structure of DNA. On the other hand, omitting electrostatic interactions is a simplification that reduces computational expense and is applied in cases where one is interested qualitatively in DNA-functionalized nanoparticle assembly induced by DNA hybridization, and not quantitatively in the secondary structure of the DNA grafts.

Future directions. Some of the future directions could involve tackling these limitations. To understand the effect of non-specific binding of the bases to the surface, one could systematically vary attractions of each base to the surface to determine how the hybridization of the grafted DNA affects nanoparticle assembly. The model should be modified to include base stacking interactions so that when a base non-specifically adsorbs to a particle, the structure of the DNA

changes accordingly, altering the sequence available for hybridization based on which base has an attraction for the surface. For electrostatic interactions, the model should be modified not only to include explicit counterions but also to have additional detail of the DNA (or less coarse grained). One model of DNA that would be effective in studying the secondary structure of DNA in the presence of counterions is a three-bead per nucleotide model,[1] where the beads represent the sugar, phosphate group and base of a nucleotide. Interactions between the phosphate group, which along a DNA backbone is negatively charged, and a counterion would change the conformation of the DNA, which can be captured with the three-bead model. Lastly, this thesis has focused only on spherical particles; therefore, a natural next step would be to study DNA-functionalized particles of various shapes (e.g. prisms, octahedral, and rhombic dodecahedral) at varying grafting density and DNA chemical and physical heterogeneity. Current synthetic capabilities allow one to functionalize nanoparticles densely with DNA strands.[2] When particles of non-spherical shapes are densely grafted with DNA, the resulting assemblies can be 1D, 2D, or 3D, as the facets of the nanoparticles can inform the dimensionality of the structure. One limitation to precise assembly using DNA-grafted particles is that the dense coating of DNA causes uniform attractions of the nanoparticles.[3] Thus, if one wanted to create a structure of a finite size with a desired dimensionality, for example for a metamaterials application, using particles with uniform attractions may encourage more cluster formation than desired. For more control over the assembly of non-spherical nanoparticles, one could functionalize the nanoparticles with a low number of DNA strands anisotropically on the facets. Recent synthetic advances demonstrating control over grafting a desired number of DNA strands on desired locations onto spherical nanoparticles[4-7] may soon be extended to non-spherical particles. Thus

studying how nanoparticles assemble given different particle shapes at various low, anisotropic grafting is timely.

6.3 References

1. T. A. Knotts, N. Rathore, D. C. Schwartz and J. J. de Pablo, *Journal of Chemical Physics*, 2007, **126**.
2. M. R. Jones, R. J. Macfarlane, B. Lee, J. A. Zhang, K. L. Young, A. J. Senesi and C. A. Mirkin, *Nature Materials*, 2010, **9**, 913-917.
3. Y. W. Y. Wang, D.R. Breed, V.N. Manoharan, L. Feng, A.D. Hollingsworth, M. Weck, and D.J. Pine, *Nature*, 2012, doi:10.1038/nature11564.
4. D. Zanchet, C. M. Micheel, W. J. Parak, D. Gerion and A. P. Alivisatos, *Nano Letters*, 2001, **1**, 32-35.
5. D. Zanchet, C. M. Micheel, W. J. Parak, D. Gerion, S. C. Williams and A. P. Alivisatos, *Journal of Physical Chemistry B*, 2002, **106**, 11758-11763.
6. W. J. Parak, T. Pellegrino, C. M. Micheel, D. Gerion, S. C. Williams and A. P. Alivisatos, *Nano Letters*, 2003, **3**, 33-36.
7. X. Y. Xu, N. L. Rosi, Y. H. Wang, F. W. Huo and C. A. Mirkin, *Journal of the American Chemical Society*, 2006, **128**, 9286-9287.

Chapter 7

Bibliography

1 P. Akcora, H. Liu, S. K. Kumar, M. J., Y. Li, B. C. Benicewicz, L. S. Schadler, D. Acehan, A. Z. Panagiotopoulos, V. Pryamitsyn, V. Ganesan, J. Ilavsky, P. Thiyagarajan, R. H. Colby and J. F. Douglas. Anisotropic self-assembly of polymer-decorated spherical nanoparticles. *Nature Materials*, 2009, 8, 354-359.

2 P. Akcora, S. K. Kumar, V. G. Sakai, Y. Li, B. C. Benicewicz and L. S. Schadler. Segmental Dynamics in PMMA-Grafted Nanoparticle Composites. *Macromolecules*, 2010, 43, 8275-8281.

3 A. P. Alivisatos, K. P. Johnsson, X. G. Peng, T. E. Wilson, C. J. Loweth, M. P. Bruchez and P. G. Schultz. Organization of 'nanocrystal molecules' using DNA. *Nature*, 1996, 382, 609-611.

4 J. C. Araque, A. Z. Panagiotopoulos and M. A. Robert. Lattice model of oligonucleotide hybridization in solution. I. Model and thermodynamics. *Journal of Chemical Physics*, 2011, 134.

5 E. Auyeung, J. I. Cutler, R. J. Macfarlane, M. R. Jones, J. S. Wu, G. Liu, K. Zhang, K. D. Osberg and C. A. Mirkin. Synthetically programmable nanoparticle superlattices using a hollow three-dimensional spacer approach. *Nature Nanotechnology*, 2012, 7, 24-28.

6 A. C. Balazs, I. C. Sanchez, I. R. Epstein, F. E. Karasz and W. J. Macknight. Effect of Sequence Distribution on the Miscibility of Polymer Copolymer Blends. *Macromolecules*, 1985, 18, 2188-2191.

7 A. C. Balazs and M. T. Demeuse. Miscibility in Ternary Mixtures Containing a Copolymer and 2 Homopolymers - Effect of Sequence Distribution. *Macromolecules*, 1989, 22, 4260-4267.

8 P. L. Biancaniello, A. J. Kim and J. C. Crocker. Colloidal interactions and self-assembly using DNA hybridization. *Physical Review Letters*, 2005, 94, 058302.

9 M. A. Carignano and I. Szleifer. Structural and thermodynamic properties of end-grafted polymers on curved surfaces. *Journal of Chemical Physics*, 1995, 102, 8662-8669.

10 V. Causin, B. X. Yang, C. Marega, S. H. Goh and A. Marigo. Structure-property relationship in polyethylene reinforced by polyethylene-grafted multi-walled carbon nanotubes. *Journal of Nanoscience and Nanotechnology*, 2008, 8, 1790-1796.

11 E. R. Chan, X. Zhang, C. Y. Lee, M. Neurock and S. C. Glotzer. Simulations of tetra-tethered organic/inorganic nanocube-polymer assemblies. *Macromolecules*, 2005, 38, 6168-6180.

12 E. R. Chan, L. C. Ho and S. C. Glotzer. Computer Simulations of Block Copolymer Tethered Nanoparticle Self-Assembly. *Journal of Chemical Physics*, 2006, 125, 064905.

13 Y. Chang, W. C. Chen, Y. J. Sheng, S. Y. Jiang and H. K. Tsao. Intramolecular janus segregation of a heteroarm star copolymer. *Macromolecules*, 2005, 38, 6201-6209.

14 T. L. Chantawansri, A. W. Bosse, A. Hexemer, C. H. D., C. J. Garcia-Cervera, E. J. Kramer and G. H. Fredrickson. Self-consistent field theory simulations of block copolymer assembly on a sphere. *Physical Review E*, 2007, 75, 031802.

15 S. Chen, Y. Li, C. Guo, J. Wang, J. H. Ma, X. F. Liang, L. R. Yang and H. Z. Liu. Temperature-responsive magnetite/PEO-PPO-PEO block copolymer nanoparticles for controlled drug targeting delivery. *Langmuir*, 2007, 23, 12669-12676.

16 J. J. Chiu, B. J. Kim, E. J. Kramer and D. J. Pine. Control of nanoparticle location in block copolymers. *Journal of the American Chemical Society*, 2005, 127, 5036-5037.

17 M. K. Corbierre, N. S. Cameron, M. Sutton, K. Laaziri and R. B. Lennox. Gold nanoparticle/polymer nanocomposites: Dispersion of nanoparticles as a function of capping agent molecular weight and grafting density. *Langmuir*, 2005, 21, 6063-6072.

18 P. J. Costanzo and F. L. Beyer. Thermally driven assembly of nanoparticles in polymer matrices. *Macromolecules*, 2007, 40, 3996-4001.

19 J. C. Crocker. Nanomaterials: Golden handshake. *Nature*, 2008, 451, 528-529.

20 W. Dai, S. K. Kumar and F. W. Starr. Universal two-step crystallization of DNA-functionalized nanoparticles. *Soft Matter*, 2010, 6, 6130-6135.

21 A. K. Dasmahapatra, G. Kumaraswamy and H. Nanavati. Collapse transition in random copolymer solutions. *Macromolecules*, 2006, 39, 9621-9629.

22 A. K. Dasmahapatra, H. Nanavati and G. Kumaraswamy. Pathway to copolymer collapse in dilute solution: Uniform versus random distribution of comonomers. *Journal of Chemical Physics*, 2007, 127, 234901.

23 K. A. Dill, S. Bromberg, K. Z. Yue, K. M. Fiebig, D. P. Yee, P. D. Thomas and H. S. Chan. Principles of Protein-Folding - a Perspective from Simple Exact Models. *Protein Science*, 1995, 4, 561-602.

24 R. Dreyfus, M. E. Leunissen, R. J. Sha, A. V. Tkachenko, N. C. Seeman, D. J. Pine and P. M. Chaikin. Simple Quantitative Model for the Reversible Association of DNA Coated Colloids. *Physical Review Letters*, 2009, 102.

25 R. Dreyfus, M. E. Leunissen, R. Sha, A. Tkachenko, N. C. Seeman, D. J. Pine and P. M. Chaikin. Aggregation-disaggregation transition of DNA-coated colloids: Experiments and theory. *Physical Review E*, 2010, 81.

26 C. C. DuFort and B. Dragnea, in *Annual Review of Physical Chemistry*, Vol 61, 2010, vol. 61, pp. 323-344.

27 J. A. Fan, C. H. Wu, K. Bao, J. M. Bao, R. Bardhan, N. J. Halas, V. N. Manoharan, P. Nordlander, G. Shvets and F. Capasso. Self-Assembled Plasmonic Nanoparticle Clusters. *Science*, 2010, 328, 1135-1138.

28 D. Frenkel and B. Smit, Understanding Molecular Simulation: From Algorithms to Applications, Academic Press, San Diego, 2002.

29 N. Geerts and E. Eiser. DNA-functionalized colloids: Physical properties and applications. *Soft Matter*, 2010, 6, 4647-4660.

30 S. C. Glotzer, M. A. Horsch, C. R. Iacovella, Z. L. Zhang, E. R. Chan and X. Zhang. Self-assembly of anisotropic tethered nanoparticle shape amphiphiles. *Current Opinion in Colloid & Interface Science*, 2005, 10, 287-295.

31 S. C. Glotzer and J. A. Anderson. NANOPARTICLE ASSEMBLY Made to order. *Nature Materials*, 2010, 9, 885-887.

32 V. Goel, T. Chatterjee, L. Bombalski, K. Yurekli, K. Matyjaszewski and R. Krishnamoorti. Viscoelastic properties of silica-grafted poly(styrene-acrylonitrile) nanocomposites. *Journal of Polymer Science Part B-Polymer Physics*, 2006, 44, 2014-2023.

33 N. C. Harris and C. H. Kiang. Disorder in DNA-linked gold nanoparticle assemblies. *Physical Review Letters*, 2005, 95, 046101-046104.

34 S. E. Harton and S. K. Kumar. Mean-field theoretical analysis of brush-coated nanoparticle dispersion in polymer matrices. *Journal of Polymer Science Part B-Polymer Physics*, 2008, 46, 351-358.

35 J. Havrankova, Z. Limpouchova and K. Prochazka. Monte Carlo study of heteroarm star copolymers in good and selective solvents. *Macromol Theor Simul*, 2003, 12, 512-523.

36 J. Havrankova, Z. Limpouchova, M. Stepanek and K. Prochazka. Self-assembly of heteroarm star copolymers - A Monte Carlo study. *Macromolecular Theory and Simulations*, 2007, 16, 386-398.

37 H. D. Hill, R. J. Macfarlane, A. J. Senesi, B. Lee, S. Y. Park and C. A. Mirkin. Controlling the lattice parameters of gold nanoparticle FCC crystals with duplex DNA linkers. *Nano Letters*, 2008, 8, 2341-2344.

38 M. Himmi, M. Benhamou, A. Bettachy and M. Daoud. Interaction force between colloidal particles clothed by end-grafted polydisperse polymer chains in solution. *Journal of Molecular Liquids*, 2003, 102, 347-363.

39 M. A. Horsch, Z. L. Zhang and S. C. Glotzer. Self-assembly of polymer-tethered nanorods. *Physical Review Letters*, 2005, 95, 056105.

40 M. A. Horsch, Z. Zhang and S. C. Glotzer. Self-assembly of laterally-tethered nanorods. *Nano Letters*, 2006, 6, 2406-2413.

41 C. W. Hsu, F. Sciortino and F. W. Starr. Theoretical Description of a DNA-Linked Nanoparticle Self-Assembly. *Physical Review Letters*, 2010, 105.

42 S. J. Hurst, H. D. Hill and C. A. Mirkin. "Three-Dimensional Hybridization" with polyvalent DNA-gold nanoparticle conjugates. *Journal of the American Chemical Society*, 2008, 130, 12192-12200.

43 C. R. Iacovella, M. A. Horsch, Z. Zhang and S. C. Glotzer. Phase Diagrams of Self-Assembled Mono-Tethered Nanospheres from Molecular Simulation and Comparison to Surfactants. *Langmuir*, 2005, 21, 9488-9494.

44 C. R. Iacovella, A. S. Keys, M. A. Horsch and S. C. Glotzer. Icosahedral packing of polymer-tethered nanospheres and stabilization of the gyroid phase. *Phys. Rev. E.*, 2007, 75, 040801.

45 C. R. Iacovella and S. C. Glotzer. Complex Crystal Structures Formed by the Self-Assembly of Ditethered Nanospheres. *Nano Letters*, 2009, 9, 1206-1211.

46 A. Jayaraman and K. S. Schweizer. Structure and Assembly of Dense Solutions and Melts of Single Tethered Nanoparticles. *J. Chem. Phys.*, 2008, 128, 164904.

47 A. Jayaraman and K. S. Schweizer. Effective Interactions, Structure, and Phase Behavior of Lightly Tethered Nanoparticles in Polymer Melts. *Macromolecules*, 2008, 41, 9430-9438.

48 A. Jayaraman and K. S. Schweizer. Effect of the number and placement of polymer tethers on the structure of dense solutions of hybrid nanoparticles. *Langmuir*, 2008, 24, 11119-11130.

49 A. Jayaraman and K. S. Schweizer. Effective Interactions and Self-Assembly of Hybrid Polymer Grafted Nanoparticles in a Homopolymer Matrix. *Macromolecules*, 2009, 42 pp 8423-8434.

50 A. Jayaraman and K. S. Schweizer. Liquid state theory of the structure and phase behaviour of polymer-tethered nanoparticles in dense suspensions, melts and nanocomposites. *Mol Simulat*, 2009, 35, 835-848.

51 X. M. Jiang, B. Zhao, G. J. Zhong, N. X. Jin, J. M. Horton, L. Zhu, R. S. Hafner and T. P. Lodge. Microphase Separation of High Grafting Density Asymmetric Mixed Homopolymer Brushes on Silica Particles. *Macromolecules*, 2010, 43, 8209-8217.

52 R. C. Jin, G. S. Wu, Z. Li, C. A. Mirkin and G. C. Schatz. What controls the melting properties of DNA-linked gold nanoparticle assemblies? *Journal of the American Chemical Society*, 2003, 125, 1643-1654.

53 M. R. Jones, R. J. Macfarlane, B. Lee, J. A. Zhang, K. L. Young, A. J. Senesi and C. A. Mirkin. DNA-nanoparticle superlattices formed from anisotropic building blocks. *Nature Materials*, 2010, 9, 913-917.

54 M. Kar, P. S. Vijayakumar, B. L. V. Prasad and S. Sen Gupta. Synthesis and Characterization of Poly-L-lysine-Grafted Silica Nanoparticles Synthesized via NCA Polymerization and Click Chemistry. *Langmuir*, 26, 5772-5781.

55 C. H. Kiang. Phase transition of DNA-linked gold nanoparticles. *Physica A*, 2003, 321, 164-169.

56 A. J. Kim, P. L. Biancaniello and J. C. Crocker. Engineering DNA-mediated colloidal crystallization. *Langmuir*, 2006, 22, 1991-2001.

57 A. J. Kim, R. Scarlett, P. L. Biancaniello, T. Sinno and J. C. Crocker. Probing interfacial equilibration in microsphere crystals formed by DNA-directed assembly. *Nature Materials*, 2009, 8, 52-55.

58 B. J. Kim, J. Bang, C. J. Hawker and E. J. Kramer. Effect of areal chain density on the location of polymer-modified gold nanoparticles in a block copolymer template. *Macromolecules*, 2006, 39, 4108-4114.

59 B. J. Kim, G. H. Fredrickson and E. J. Kramer. Effect of polymer ligand molecular weight on polymer-coated nanoparticle location in block copolymers. *Macromolecules*, 2008, 41, 436-447.

60 J. U. Kim and M. W. Matsen. Interaction between Polymer-Grafted Particles. *Macromolecules*, 2008, 41, 4435-4443.

61 J. U. Kim and M. W. Matsen. Positioning Janus nanoparticles in block copolymer scaffolds. *Physical Review Letters*, 2009, 102, 078303.

62 A. Kiriy, G. Gorodyska, S. Minko, M. Stamm and C. Tsitsilianis. Single molecules and associates of heteroarm star copolymer visualized by atomic force microscopy. *Macromolecules*, 2003, 36, 8704-8711.

63 S. Kirkpatrick, C. D. Gelatt and M. P. Vecchi. Optimation with Simulated Annealing. *Science*, 1983, 220, 671-680

64 Q. Lan, L. F. Francis and F. S. Bates. Silica nanoparticles dispersions in homopolymer versus block copolymer. *Journal of Polymer Science Part B-Polymer Physics*, 2007, 45, 2284-2299.

65 J. Largo, F. W. Starr and F. Sciortino. Self-assembling DNA dendrimers: A numerical study. *Langmuir*, 2007, 23, 5896-5905.

66 C. F. Laub and J. T. Koberstein. Effect of brush polydispersity on the interphase between end-grafted brushes and polymeric matrices. Macromolecules, 1994, 27, 5016-5023.

67 A. A. Lazarides and G. C. Schatz. DNA-linked metal nanosphere materials: Structural basis for the optical properties. *Journal of Physical Chemistry B*, 2000, 104, 460-467.

68 J. Y. Lee, A. C. Balazs, R. B. Thompson and R. M. Hill. Self-Assembly of Amphiphilic Nanoparticle-Coil "Tadpole" Macromolecules. *Macromolecules*, 2004, 37, 3536-3539.

69 M. E. Leunissen, R. Dreyfus, R. J. Sha, T. Wang, N. C. Seeman, D. J. Pine and P. M. Chaikin. Towards self-replicating materials of DNA-functionalized colloids. *Soft Matter*, 2009, 5, 2422-2430.

70 C. Li, J. Han, C. Y. Ryu and B. C. Benicewicz. A versatile method to prepare RAFT agent anchored substrates and the preparation of PMMA grafted nanoparticles. *Macromolecules*, 2006, 39, 3175-3183.

71 T. Li, R. Sknepnek, R. J. Macfarlane, C. A. Mirkin and M. O. de la Cruz. Modeling the Crystallization of Spherical Nucleic Acid Nanoparticle Conjugates with Molecular Dynamics Simulations. *Nano Letters*, 2012, 12, 2509-2514.

72 C. J. Loweth, W. B. Caldwell, X. G. Peng, A. P. Alivisatos and P. G. Schultz. DNA-based assembly of gold nanocrystals. *Angewandte Chemie-International Edition*, 1999, 38, 1808-1812.

73 D. B. Lukatsky and D. Frenkel. Surface and bulk dissolution properties, and selectivity of DNA-linked nanoparticle assemblies. *Journal of Chemical Physics*, 2005, 122.

74 D. B. Lukatsky, B. M. Mulder and D. Frenkel. Designing ordered DNA-linked nanoparticle assemblies. *Journal of Physics-Condensed Matter*, 2006, 18, S567-S580.

75 K. T. Marla and J. C. Meredith. Simulation of Interaction Forces Between Nanoparticles: End-Grafted Polymer Modifiers. *Journal of Chemical Theory and Computation*, 2006, 2, 1624-1631.

76 G. J. Martyna, D. J. Tobias and M. L. Klein. Constant-Pressure Molecular-Dynamics Algorithms. *Journal of Chemical Physics*, 1994, 101, 4177-4189.

77 A. J. Mastroianni, S. A. Claridge and A. P. Alivisatos. Pyramidal and Chiral Groupings of Gold Nanocrystals Assembled Using DNA Scaffolds. *Journal of the American Chemical Society*, 2009, 131, 8455-8459.

78 G. Mattei, P. Mazzoldi and H. Bernas, in Materials Science with Ion Beams, 2010, vol. 116, pp. 287-316.

79 N. Metropolis, A. W. Rosenbluth, M. N. Rosenbluth, A. H. Teller and E. Teller. Equation of State Calculations by Fast Computing Machines. *Journal of Chemical Physics*, 1953, 21, 1087-1092.

80 V. T. Milam, A. L. Hiddessen, J. C. Crocker, D. J. Graves and D. A. Hammer. DNA-driven assembly of bidisperse, micron-sized colloids. *Langmuir*, 2003, 19, 10317-10323.

81 S. T. Milner, T. A. Witten and M. E. Cates. Effects of polydispersity in the end-grafted polymer brush. *Macromolecules*, 1989, 22, 853-861.

82 C. A. Mirkin, R. L. Letsinger, R. C. Mucic and J. J. Storhoff. A DNA-based method for rationally assembling nanoparticles into macroscopic materials. *Nature*, 1996, 382, 607-609.

83 B. M. Mognetti, M. E. Leunissen and D. Frenkel. Controlling the temperature sensitivity of DNA-mediated colloidal interactions through competing linkages. *Soft Matter*, 2012, 8, 2213-2221.

84 N. Nair and A. Jayaraman. Self-Consistent PRISM Theory-Monte Carlo Simulation Studies of Copolymer Grafted Nanoparticles in a Homopolymer Matrix. *Macromolecules*, 2010, 43, 8251-8263.

85 D. Nykypanchuk, M. M. Maye, D. van der Lelie and O. Gang. DNA-based approach for interparticle interaction control. *Langmuir*, 2007, 23, 6305-6314.

86 D. Nykypanchuk, M. M. Maye, D. van der Lelie and O. Gang. DNA-guided crystallization of colloidal nanoparticles. *Nature*, 2008, 451, 549-552.

87 M. N. Ohya Y., Hashizume M., Tamaki T. , Uehara T., Shingubara S., and Kuzuya A. Formation of 1D and 2D Gold Nanoparticle Arrays by Divalent DNA–Gold Nanoparticle Conjugates. *Small*, 2012.

88 S. Ojha, B. Beppler, H. C. Dong, K. Matyjaszewski, S. Garoff and M. R. Bockstaller. Impact of Polymer Graft Characteristics and Evaporation Rate on the Formation of 2-D Nanoparticle Assemblies. *Langmuir*, 2010, 26, 13210-13215.

89 O. Padovan-Merhar, F. V. Lara and F. W. Starr. Stability of DNA-linked nanoparticle crystals: Effect of number of strands, core size, and rigidity of strand attachment. *Journal of Chemical Physics*, 2011, 134.

90 W. J. Parak, T. Pellegrino, C. M. Micheel, D. Gerion, S. C. Williams and A. P. Alivisatos. Conformation of oligonucleotides attached to gold nanocrystals probed by gel electrophoresis. *Nano Letters*, 2003, 3, 33-36.

91 S. Y. Park, A. K. R. Lytton-Jean, B. Lee, S. Weigand, G. C. Schatz and C. A. Mirkin. DNA-programmable nanoparticle crystallization. *Nature*, 2008, 451, 553-556.

92 W. Park and J. Kim. Negative-Index Materials: Optics by Design. *MRS Bulletin*, 2008, 33, 907-911.

93 C. L. Phillips, C. R. Iacovella and S. C. Glotzer. Stability of the double gyroid phase to nanoparticle polydispersity in polymer-tethered nanosphere systems. *Soft Matter*, 2010, 6, 1693-1703.

94 V. Pryamitsyn, V. Ganesan, A. Z. Panagiotopoulos, H. Liu and S. K. Kumar. Modeling the anisotropic self-assembly of spherical polymer-grafted nanoparticles. *Journal of Chemical Physics*, 2009, 131, 221102.

95 T. R. Prytkova, I. Eryazici, B. Stepp, S. B. Nguyen and G. C. Schatz. DNA Melting in Small-Molecule-DNA-Hybrid Dimer Structures: Experimental Characterization and Coarse-Grained Molecular Dynamics Simulations. *Journal of Physical Chemistry B*, 2010, 114, 2627-2634.

96 W. B. Rogers and J. C. Crocker. Direct measurements of DNA-mediated colloidal interactions and their quantitative modeling. *Proceedings of the National Academy of Sciences of the United States of America*, 2011, 108, 15687-15692.

97 M. Rubinstein and R. H. Colby, Polymer Physics, Oxford University Press, 2008.

98 R. T. Scarlett, M. T. Ung, J. C. Crocker and T. Sinno. A mechanistic view of binary colloidal superlattice formation using DNA-directed interactions. *Soft Matter*, 2011, 7, 1912-1925.

99 F. Sciortino, E. Bianchi, J. F. Douglas and P. Tartaglia. Self-assembly of patchy particles into polymer chains: A parameter-free comparison between Wertheim theory and Monte Carlo simulation. *Journal of Chemical Physics*, 2007, 126, 194903.

100 A. Seifpour, P. Spicer, N. Nair and A. Jayaraman. Effect of monomer sequences on conformations of copolymers grafted on spherical nanoparticles: A Monte Carlo simulation study. *Journal of Chemical Physics*, 2010, 132, 164901.

101 J. J. Semler and J. Genzer. Design of random copolymers with statistically controlled monomer sequence distributions via Monte Carlo simulations. *Journal of Chemical Physics*, 2006, 125, 014902.

102 J. J. Semler, Y. K. Jhon, A. Tonelli, M. Beevers, R. Krishnamoorti and J. Genzer. Facile method of controlling monomer sequence distributions in random copolymers. *Advanced Materials*, 2007, 19, 2877-2883.

103 V. M. Shalaev, W. S. Cai, U. K. Chettiar, H. K. Yuan, A. K. Sarychev, V. P. Drachev and A. V. Kildishev. Negative index of refraction in optical metamaterials. *Optics Letters*, 2005, 30, 3356-3358.

104 Y. J. Sheng, C. H. Nung and H. K. Tsao. Morphologies of star-block copolymers in dilute solutions. *Journal of Physical Chemistry B*, 2006, 110, 21643-21650.

105 K. R. Shull. Theory of End-Adsorbed Polymer Brushes in Polymeric Matrices. *Journal of Chemical Physics*, 1991, 94, 5723-5738.

106 S. Si, A. Kotal and T. K. Mandal. One-dimensional assembly of peptide-functionalized gold nanoparticles: An approach toward mercury ion sensing. *Journal of Physical Chemistry C*, 2007, 111, 1248-1255.

107 S. Si and T. K. Mandal. pH-controlled reversible assembly of peptide-functionalized gold nanoparticles. *Langmuir*, 2007, 23, 190-195.

108 A. Sikorski and P. Romiszowski. Motion of chains in polypeptide brushes. *Physica a-Statistical Mechanics and Its Applications*, 2005, 357, 364-370.

109 J. M. Slocik, F. Tam, N. J. Halas and R. R. Naik. Peptide-assembled optically responsive nanoparticle complexes. *Nano Letters*, 2007, 7, 1054-1058.

110 B. D. Smith, N. Dave, P. J. J. Huang and J. W. Liu. Assembly of DNA-Functionalized Gold Nanoparticles with Gaps and Overhangs in Linker DNA. *Journal of Physical Chemistry C*, 2011, 115, 7851-7857.

111 G. D. Smith and D. Bedrov. Dispersing Nanoparticles in a Polymer Matrix: Are Long, Dense Polymer Tethers Really Necessary? *Langmuir*, 2009, 25, 11239-11243.

112 F. W. Starr and F. Sciortino. Model for assembly and gelation of four-armed DNA dendrimers. *Journal of Physics-Condensed Matter*, 2006, 18, L347-L353.

113 M. Stepanek, P. Matejicek, J. Humpolickova, J. Havrankova, K. Podhajecka, M. Spirkova, Z. Tuzar, C. Tsitsilianis and K. Prochazka. New insights on the solution behavior and self-assembly of polystyrene/poly(2-vinylpyridine) 'hairy' heteroarm star copolymers with highly asymmetric arms in polar organic and aqueous media. *Polymer*, 2005, 46, 10493-10505.

114 M. M. Stevens, N. T. Flynn, C. Wang, D. A. Tirrell and R. Langer. Coiled-coil peptide-based assembly of gold nanoparticles. *Advanced Materials*, 2004, 16, 915-918.

115 J. J. Storhoff, A. A. Lazarides, R. C. Mucic, C. A. Mirkin, R. L. Letsinger and G. C. Schatz. What controls the optical properties of DNA-linked gold nanoparticle assemblies? *Journal of the American Chemical Society*, 2000, 122, 4640-4650.

116 A. Striolo. Controlled assembly of spherical nanoparticles: Nanowires and spherulites. *Small*, 2007, 3, 628-635.

117 Y. Sun, N. C. Harris and C. H. Kiang. The reversible phase transition of DNA-linked colloidal gold assemblies. *Physica A*, 2005, 354, 1-9.

118 V. Talanquer. Phase transitions in DNA-linked nanoparticle assemblies: A decorated-lattice model. *Journal of Chemical Physics*, 2006, 125, 194701.

119 V. A. Tamma, J. H. Lee, Q. Wu and W. Park. Visible frequency magnetic activity in silver nanocluster metamaterial. *Applied Optics*, 2010, 49, A11-A17.

120 D. N. Theodorou and U. W. Suter. Shape of Unperturbed Linear-Polymers - Polypropylene. *Macromolecules*, 1985, 18, 1206-1214.

121 A. V. Tkachenko. Morphological diversity of DNA-colloidal self-assembly. *Physical Review Letters*, 2002, 89, 148303.

122 D. Trombly and V. Ganesan. Interactions between Polymer-Grafted Particles and Bare Particles for Biocompatibility Applications. *Journal of Polymer Science Part B-Polymer Physics*, 2009, 47, 2566-2577.

123 D. M. Trombly and V. Ganesan. Curvature effects upon interactions of polymer-grafted nanoparticles in chemically identical polymer matrices. *Journal of Chemical Physics*, 2010, 133.

124 N. Tsubokawa. Surface grafting of polymers onto nanoparticles in a solvent-free dry-system and applications of polymer-grafted nanoparticles as novel functional hybrid materials. *Polymer Journal*, 2007, 39, 983-1000.

125 T. A. Witten and P. A. Pincus. Colloid Stabilization by long grafted polymers. *Macromolecules*, 1986, 19, 2509-2513.

126 H. M. Xiong, M. Y. Sfeir and O. Gang. Assembly, Structure and Optical Response of Three-Dimensional Dynamically Tunable Multicomponent Superlattices. *Nano Letters*, 2010, 10, 4456-4462.

127 X. Y. Xu, N. L. Rosi, Y. H. Wang, F. W. Huo and C. A. Mirkin. Asymmetric functionalization of gold nanoparticles with oligonucleotides. *Journal of the American Chemical Society*, 2006, 128, 9286-9287.

128 Y. Y. Yuan, X. Q. Liu, Y. C. Wang and J. Wang. Gold Nanoparticles Stabilized by Thermosensitive Diblock Copolymers of Poly(ethylene glycol) and Polyphosphoester. *Langmuir*, 2009, 25, 10298-10304.

129 D. Zanchet, C. M. Micheel, W. J. Parak, D. Gerion and A. P. Alivisatos. Electrophoretic isolation of discrete Au nanocrystal/DNA conjugates. *Nano Letters*, 2001, 1, 32-35.

130 D. Zanchet, C. M. Micheel, W. J. Parak, D. Gerion, S. C. Williams and A. P. Alivisatos. Electrophoretic and structural studies of DNA-directed Au nanoparticle groupings. *Journal of Physical Chemistry B*, 2002, 106, 11758-11763.

131 X. Zhang, E. R. Chan and S. C. Glotzer. Self-assembled morphologies of monotethered polyhedral oligomeric silsesquioxane nanocubes from computer simulation. *Journal of Chemical Physics*, 2005, 123, 184718.

132 Z. Zhang, M. A. Horsch, M. H. Lamm and S. C. Glotzer. Tethered Nano Building Blocks: Toward a Conceptual Framework for Nanoparticle Self-Assembly. *Nano Letters*, 2003, 3, 1341-1346.

133 Z. L. Zhang and S. C. Glotzer. Self-assembly of patchy particles. *Nano Letters*, 2004, 4, 1407-1413.

134 Y. L. Zhao and S. Perrier. Synthesis of well-defined homopolymer and diblock copolymer grafted onto silica particles by Z-supported RAFT polymerization. *Macromolecules*, 2006, 39, 8603-8608.

135 X. M. Zhu, L. Q. Wang, J. P. Lin and L. S. Zhang. Ordered Nanostructures Self-Assembled from Block Copolymer Tethered Nanoparticles. *ACS Nano*, 2010, 4, 4979-4988.